85

CRANFIELD INSTITUE OF TECHNOLOGY

SCHOOL OF MECHANICAL ENGINEERING

PhD THESIS

Academic Year 1983-4

F ALAMDARI

BSc,MSc

Convective Heat Transfer within Mechanically-ventilated Building Spaces

Supervisor G P Hammond

April 1984

This thesis is dedicated

To the memory of my late father Dr. A. Alamdari

and

To my wife Fariba

SUMMARY

A hierarchy of interacting and interdependent approaches have been developed for calculating internal surface convective heat transfer coefficients within mechanically-ventilated rooms. A 'high-level' computer code is developed for non-buoyant and buoyant flow based on the 'elliptic' code of Pun and Spalding (1977), in which 'upwind' finite-difference approximations to the governing partial-differential equations for continuity, momentum and thermal energy are formulated in terms of 'primitive' pressure-velocity variables. Closure of these time-averaged, elliptic equations is obtained via transport equations for both the turbulence kinetic energy and its dissipation rate. The high-level code solves the difference equations for a predetermined size, staggered grid in an iterative 'line-by-line' manner using a guess-and-correct procedure.

An 'intermediate-level' computer code (the ROOM-CHT program) has also been developed for the above purpose, which employs 'informed' estimates of the flow and thermal field based on the known mean flow properties of wall-jets. The corresponding heat transfer distribution across the room surface is calculated using wall-jet profile analysis or improved data correlations for buoyancy-driven convection as appropriate.

Computations are presented for a room into which air is injected through a low or high side wall register. The supply of air governed by both cyclic and modulating control was examined. The intermediate-level code is advocated as being the most appropriate for meeting the requirements of dynamic building thermal models. This code was verified by comparison with the high-level code and with experimental measurements. The computed heat transfer coefficients from the intermediate-level code were found to be in good agreement with that of the high-level code. Both indicate significantly higher values than those which would be obtained from established design guides. These high values suggest errors in building thermal models based on guide data, including substantial under-estimation of preheat times.

ACKNOWLEDGEMENTS

The author wishes to thank his supervisor, Mr. G. P. Hammond for his support and constructive guidance, which has been of immense and invaluable assistance at all stages of this research. He would also like to thank Mr. P. Verey and Mr. R. D. G. Watson , the previous and present GEC computer site managers at Cranfield for their assistance. Further thanks are due to his colleague Mr. C. Melo, who tested the sensitivity of the NBSLD response factor program to changes in convection data as discussed in Chapter 5. The equations have been typed by Miss D. Berryman and Mrs. A. Walshe and the author wishes to thank them for this cooperative assistance.

The present work was supported by UK Science and Engineering Research Council Grants GR/B/5010.2, GR/C/0184.9 and GR/C/2419.0, and form part of the Council's specially promoted programme on 'Energy in Buildings'. The author is pleased to have an opportunity to express his gratitude for this support.

CONTENTS

TABLES

FIGURES

NOTATION

a	Coefficients in finite-difference equations, Eq.(3.17)
a_1, a_2, a_3, a_4	Coefficients in quatric wake function equation, Eq.(2.25)
a_c, b_c	Empirical coefficients in buoyancy-driven correlating equation, Eq.(4.37)
a_i, b_i, c_i, d_i	Coefficients in finite-difference (TDMA) for block-correction equation, Eq.(3.64)
A	Area of the control volume face (m^2)
Ag	Grille area (m^2)
A_j, B_j, C_j	Coefficients in finite-difference equations (TDMA), Eq.(3.58)
A'_j, B'_j	Transformed Coefficients (TDMA), Eq.(3.60)
A_s	Surface area (m^2)
b	The source term in finite-difference equation, Eq.(3.17)
b_u, b_θ	2D wall-jet velocity and temperature half width respectively (m), Eq.(4.1,4.8)
b_z	3D wall-jet spanwise half width (m), Eq.(4.25)
B , B_θ, B', B'_θ	Log-law constants, Eq.(4.1,4.8,4.14)
C_1, C_2, C_D, C_μ, C'	Coeffients in turbuence models, Eq.(2.17-2.21)
C_f	Skin friction coefficient, Eq.(2.24)
C , C_θ	Velocity and temperature wake function coefficients, Eq.(4.1,4.8)
d	Coeffient of pressure-difference term, Eq.(3.43)
D	Diffusion terms, Eq.(3.19)
D , D_θ	Wall-jet velocity and temperature width ratio, Eq.(4.3,4.10)

F	Mass flow rate through a control volume (Kg/s), Eq.(3.14)
g	Gravitational acceleration (m/s^2), Eq.(2.41)
G_B	Buoyancy production, Eq.(2.41)
G_k	Generation rate of turbulence energy, Eq.(2.16)
h	Instantanous specific enthalpy (J/Kg)), Eq.(2.3)
h_c	Convective heat transfer coefficient (W/ m^2K), Eq.(4.35)
H	Time-averaged enthalpy (J/Kg), Eq.(2.31), also room height (m)
Hg	Grille height (m)
J	Total (convection+diffusion) flux, Eq.(3.9), also diffusion flux Eq.(2.6)
K	Turbulent kinetic energy, Eq.(2.15)
lm	Mixing length (m), Eq.(2.14)
L	Length scale, Eq.(2.17), also room Length (m)
L_S	Surface length (m), Eq.(4.38)
L_ε	Dissipation length scale (m), Eq.(2.29)
N	Number of air changed per hour (ACH), Eq.(5.2)
p	Instantanous static pressure (bar), Eq.(2.2)
p´	Pressure-correction term (bar), Eq.(3.39)
P	Time-averaged static pressure (bar), Eq.(3.39)
P*	Gussed pressure (bar), Eq.(3.39)
Pe	Peclet number, Eq.(3.20)
P_s	Surface perimeter (m)
q	Heat flux (W/m^2), Eq.(2.36)
Q	Total heat load (W), Eq.(5.3)

R	Residual source, Eq.(3.69)
Re	Reynolds number at inlet
Rm	Maximum Reymolds number, Eq.(2.26)
S_b	Buoyancy source term, Eq.(2.10)
S_i	Slot inlet height (m), Eq.(2.31)
S_P	Constant part of linearized source term, Eq.(3.11)
$S_P^{'}$	Coefficient of Φ_P in linearized source expression, Eq.(3.11)
S_ϕ	General source term, Eq.(3.11)
St	Stanton number, Eq.(4.12)
t	Time (s), Eq.(2.1)
T	Temperature (K), Eq.(4.8)
T_τ	'Friction temperature' (K), Eq.(4.8)
u , u_1	x-direction velocity component (m/s), Eq.(2.1)
u' , u_1'	Fluctuating componenet of x-direction velocity (m/s), Eq.(2.10)
U , U_1	Time-averaged x-direction velocity (m/s), Eq.(2.9)
U*	x-direction velocity based on the gussed pressure P^*(m/s), Eq.(3.38)
$\hat{U}$	x-direction pseudo-velocity (m/s), Chapter 6
U_m, U_{mo}	Maximum and centreline maximum velocity respectively (m/s), Eq.(2.24,4.24)
U_τ	'Friction velocity' (m/s), Eq.(4.2)
v , u_2	y-direction velocity component (m/s), Eq.(2.1)
v' , u_2'	Fluctuating component of y-direction velocity (m/s), Eq.(2.10)
V , U_2	Time-averaged y-direction velocity component (m/s), Eq.(2.9)
V*	y-direction velocity based on the gussed pressure P^*(m/s), Eq.(3.38)

$\hat{V}$	y-direction pseudo-velocity (m/s), Chapter 6
$\dot{V}$	Volume flow rate (m^3/s), Eq.(5.3)
W	Weighting function, Eq.(3.4), also room width (m)
Wg	Grille width (m)
x,y,z (x_1,x_2, x_3)	Cartesian coordinates
x_c	Potential core length (m), Eq.(4.31)
Xsp ,Ysp	Location and width of the starting profiles (m), Eq.(2.23)
Y^+	Dimensionless distance from the wall, Eq.(4.1)

Greek Symbols

α	A large number (for example 10^{30}), Eq.(3.57)
β	Coefficient of thermal expansion, Eq.(2.41)
Γ	Diffusion coefficient, Eq.(2.40)
δ	Wall-jet velocity or temperature width, Eq.(2.28), and also the distance between near boundary and boundary node (m), Eq.(3.49)
δx, δy	Inter-nodal distances, Eq.(3.19)
Δx, Δy	Dimensions of the computational cell, Eq.(3.10)
ε	Rate of dissipation of K, Eq.(2.17)
κ -E	Log-law constants, Eq.(2.34)
θ	Excess temperature (K), Eq.(2.41)
λ	Convergence criteria, Eq.(3.70)
μ	Fluid dynamic viscosity (Kg/ms), Eq.(2.5)
ν	Fluid kinematic viscosity (m^2/s), Eq.(4.2)
ξ	Relaxation factor, Eq.(3.73)

ρ	Fluid density (Kg/m^3), Eq.(2.1)
σ	Prandtl/Schmidt number, eq.(2.6)
τ	Stress-tensor, Eq.(2.5)
τ_w	Wall shear-stress, Eq.(2.34)
ϕ	Instantanous general scalar property, Eq.(2.4)
ϕ'	Fluctuating value of ϕ , Eq.(2.8)
Φ	Time-averaged value of ϕ , Eq.(2.7)

Subscripts

a	Ambient condition
e	Inlet condition
eff	Effective value
e, w, n, s	Control valume faces
P, E, W, N, S	Central node and its neighbours
ij	Components in cartesian tensor notation
i, j	Location of point in cartesian grid
ℓ	Laminar flow condition
m	Maximum value
o	Centreline and also reference value
r	Room condition
ref	Referece value
t	Turbulent flow condition
w	Condition at wall
1,2	Cartesian directions

Superscripts

+	Dimensionless value
−	Average value
~	Approximate solution
^	Pseudo-velocities
*	Previous iteration value, also velocities based on gussed pressure
'	Correction to starred values, also fluctuations relative to the time-averaged values

Special Symbol

Max (A , B)	The biger of A and B

PART I

INTRODUCTION

CHAPTER 1
ENERGY CONSERVATION AND THE BUILT ENVIRONMENT:

1.1 DYNAMIC THERMAL PERFORMANCE OF BUILDING:

It has become apparent, following the 'energy crisis' of the mid-1970's, that the world's reserves of fossil fuel are exhaustible. Consequantlty, it is necessary to make the most effective use of energy, thereby extending the available time for developing alternative energy suplies. The world consumption is accelerating towards the energy 'bankruptcy' (see Fig 1.1), instead of reducing or at least maintaining steady-state. In many countries the energy used in domestic and commercial buildings is a large proportion of total energy consumption. Most energy consumed in buildings is used for space heating, cooling and ventilation, so that saving in these areas are of great importance.

In the last decade it has been become increasingly recognised that in order to develop realistic methods for the energy-conscious design of buildings it is necessary to model the dynamic thermal response of the system. These dynamic models normally require computational solution { as noted in the reviews by Clarke (ref 1) and Day (ref 2); the latter summarising the efforts of the U.K Science and Engineering Research Council to stimulate research in this area}, in constrast to the manual calculation methods used with steady-state procedures. However, progress in this direction has been hindered by uncertainties in some of the input data, particularly ventilation rates and surface heat transfer coefficients.

The convective heat transfer data currently available to the designer is certainly inadequate for modern requirements. ASHRAE (ref 3) seem to iqnore the possibility of forced convective heating, and employ only buoyancy-driven convective internal surface coefficients to obtain fabric 'U-values'. The recent edition of the CIBS guide (ref 4) provides an approximate correction factor to buoyancy-driven data when air velocity over individual surfaces has non-zero values. Unfortunately this practice is not very helpful as the designer generally has no means of determining this velocity a priori. In any case, such a procedure neglects variations in surface coefficients due to different heating system/room configurations. In a field study of over thirty rooms of various shapes and sizes heated by a fan 'convector', Yaneske and Forrest (ref 5) found the room-averaged convection coefficient to be 6.31 W/m^2K, but with a wide scatter: the standard deviation of their data was 4.77 W/m^2K. They also showed that, when selecting heater capacity, the use of a surface coefficient appropriate to buoyancy-driven convection ($\sim$3.00 W/m^2K), instead of a forced value, would result in substantial increase in preheat times. More recently, Waters (ref 6) has similarly shown that the accuracy of building thermal models for

mechanically-ventilated rooms are strongly dependent on the choice of convection coefficient. He reached this conclusion using an implicit finite-difference model having a relatively fine time-space grid. The time step adopted was only about 5 minutes, in contrast to the 60 minute steps typically employed in response factor programs. Irving (ref 7) has noted, when reviewing the achievements of the International Energy Agency (IEA) Annex 1 validation studies, that uncertainties in input data currently limit the level of sophistication to which it is worthwhile developing the overall building thermal model.

Warm air heating system, probably incorporating a ventilation capability, have many potential advantages for low energy housing of the future. These benefits include a good energy efficiency (70-75% over heating season), and ease of control with rapid response to load changes. In practice, the operation of the circulating fan in conventional warm air heating systems is controlled by an on-off thermostat, and therefore the warm-air is injected into room intermittently (ref 8-9). The rate of heat transfer at room internal surfaces will alternate between those corresponding to forced and buoyancy -driven convection. An alternative modulating control system may be utilised, in which a variable-speed fan is operated continuosly, except at low load when cyclic operation again occurs. Pimbert (ref 8) has shown, on the basis of laboratory tests using a 'Comfy-test' meter, that modulating control results in an improved thermal environment at the most frequently experienced loads. The room heat transfer coefficient under this control system correspond to forced convection, although their magnitude will vary with fan speed and supply air temperature as the heating load changes.

1.2 ROOM AIR MOVEMENT AND THERMAL COMFORT:

The air-movement within mechanicaly ventilated enclosures is a complex, jet-induced turbulent flow which gives rise to a recirculation pattern and therefore uncertainty in thermal comfort variables such as velocity, pressure and temperature distribution. Human discomfort could arise due to draught sensation if the air velocity exceed about 0.15 to 0.24 m/s depends on the prevalling temperature (ref 10-17). Conversely a feeling of stuffiness may be caused if the air velocity falls below about 0.05 m/s (ref 8-9).

In warm air systems, discomfort may arise due to the re-establishment of infiltration draughts during the 'off' period of the control cycle (ref 18). Indeed this discomfort has inhibited the introduction of warm-air systems despite their potential for 'low energy housing'. The influence of this intermittent operation on the character of the injected jet and subsequent room air-movement has received little attention in the published literature.

1.3 THE AIM OF THE PRESENT WORK:

The present work was originally aimed at developing a computer program which would be capable of predicting the convective heat transfer coefficient over the internal surface of two-dimensional, mechanically-ventilated enclosures. However 'intermediate-level' calculation procedure for three-dimensional enclosures was subsequently developed. It was also hoped that such a program would facilitate a better understanding of physics of the flow generated by domestic warm-air heating systems. In this way the rquirements of building thermal modellers for input heat transfer coefficients of known uncertainty would be met.

1.4 APPROPRIATE CALCULATION METHODS FOR THERMO-FLUID PROBLEMS RELATING TO BUILDINGS:

Thermo-fluid calculation methods can , according to Hammond (ref 19) be classified in one of the following categories:

a) 'Lower-level' Methods

This category uses analytical solutions and emperical data for simple shear flows, and thus apply to a very narrow class of flows or range of calculations. An examples of this category are the profile analysis of wall-jets and improved data correlation for buoyancy-driven convection in rooms which are outlined in part III and appendix A of the present work.

b) 'Higher-level' Methods

The arguably most sophisticated approach is the development of 'higher-level' computer-based flow models (one is described in detail in part II), which involve the solution of the governing equations of the flow. The model used for the present study used the 'elliptic' finite-difference computer code of Professor Spalding and his co-workers, together with a two-equation turbulence closure. Unfortunately, such high-level flow models are unsuitable for providing direct input data into the current generation of building thermal models. This is because the models are very costly in terms of computer time and storage, and are rather user 'unfriendly' , due to their complexity.

c) 'Intermediate-level' Method

In order to overcome the practical limitation of 'higher-level' methods , an 'intermediate-level' calculation procedure has been developed by Alamdari and Hammond (ref 20) and incorporated into a computer code called the ROOM-CHT (Room Convective Heat Transfer) program. This program was envisaged as a 'bolt-on' package to building thermal models, and is outlined in part III of the present work.

1.5 LAYOUT OF THE THESIS;

The present work concentrates mainly on the development of 'high-level' and 'intermediate-level' computational methods for convection within mechanically-ventilated enclosures, and these are discribed in part II (Chapters 2 & 3) and part III (Chapter 4) of this thesis respectively.

Chapter 2 lays the mathematical foundation for the high-level approach, while Chapter 3 deals with the numerical solution procedure for the governing flow equations.

Chapter 4 explains the physical basis of the intermediate-level calculation method.

The computed heat transfer coefficients and the experimental validation of the predictions for both the high-level and intermediate-level methods are discussed in Chapter 5 (part IV). The results of both the two and three-dimensional versions of the intermediate-level method are compared. The results of a parametric studies using the two-dimensional version of the intermediate-level program for the case of commercial office air-conditioning via linear or slot 'diffusers' are then presented. In the final section of Chapter 5 the sensitivity of building models to convection data is assessed. In the final chapter of this thesis (Chapter 6) general conclusions are drawn concerning the validity of the various calculation methods 'levels', and recommendations are made for further research.

PART II

A HIGHER-LEVEL COMPUTER BASED MATHEMATICAL MODEL

CHAPTER 2
MATHEMATICAL FRAMEWORK FOR HIGHER-LEVEL MODEL

2.1 INTRODUCTION:

'Higher-level' mathematical models of the type employed here were developed in the early 1970's for predicting complex elliptic flows in practical configurations. These methods solve numerically the differential equations for continuity, momentum and thermal energy in order to generate field values for the velocity components, the static pressure and the enthalpy or temperature. The mathematical statement of the physical laws which govern the flows, and the way that the problem is formulated in terms of physical differential equations for laminar and turbulent flow regimes are briefly discribed in this Chapter.

2.2 OUTLINE OF THE CALCULATION PROCEDURE:

2.2.1 Previous Work:

In recent years there has been considerable progress in the application of numerical computation procedures for fluid flow and heat transfer problems, although relatively few studies have been related to ventilation and heat transfer problems in building spaces. However, in the mid-1970's Neilsen (ref 21) developed a model for the prediction of two-dimensional, isothermal flow in rooms, by using an early stream-function and vorticity procedure (ref 22) , and employing the two-equation, K-ε model of turbulence (ref 23-24) in order to close the governing time-averaged equations. In this method the stream-function and vorticity act as a main dependent variables instead of the velocity components, thereby eliminating the pressure gradient terms which appear in the momentum equations. This method cannot be extended to three-dimensional flows, and the scheme has a poor convergence performance.

Neilsen et al (ref 25-27) have more recently solved the same problem as above but using the velocity components as dependent variables, thereby enabling extension to three-dimensional flows. Neilsen et al (ref 26) also attempted to model the effect of buoyancy , by introducing the buoyancy terms into the y-direction momentum , and turbulence energy and dissipation rate equations, through their source terms. They examined the case of cool-air injection with a predominant 'through-flow' , and relatively small buoyancy effects. The through-flow geometry is an idealisation which greatly assists convergence, but is rarely found in practice.

Hjertager and Magnussen (ref 28) have used the Patankar and Spalding (ref 29) 'SIMPLE' algorithm in order to predict three-dimensional turbulent flow in a ventilated room for both isothermal and buoyant flows, again with the two-equation, K-ε model of turbulence. The influence of buoyancy was introduced into the problem only through the y-direction momentum source terms. A cooled jet (11 K lower than the averaged room temperature, Tr=293K) was emitted horizontally from a rectangular nozzle placed just under the ceiling with nearby outlets extracting the flow vertically to the ceiling cavity. Part of the floor and far-wall (the wall opposite to the jet) were heated in the case of buoyant flow, which is again rare in domestic and comercial office spaces in the UK.

Sakamoto and Matsuo (ref 30) also examined a three-dimensional turbulent flow in a ventilated room, but for isothermal flows only. It seems their aim was mainly to evaluate the use of different turbulence models. The geometry which they considered was a cubic room with a square nozzle inlet at the centre of the ceiling and outlet at the one of the walls closed to the floor.

2.2.2 The Present Work:

In the present work a modified version of the 'elliptic' computer code of Pun and Spalding (ref 31) has been used as the basis for a 'higher-level' flow model for mechanically-ventilated, 'two-dimentional' rooms. In this code, 'upwind' finite-difference approximations to the governing elliptic equations are formulated in terms of primitive pressure-velocity variables for a predetermined size, staggered grid. The SIMPLE (Semi-Implicit Method for Pressure-Linked Equations) algorithm (ref 29,32) was used in the code to solve the finite-difference equations in a 'line-by-line' manner with nearly-exact adjustment of terms. The original continuity (mass conservation) adjustment technique used by Pun and Spalding (ref 31) was found to be unsuitable for the present case of severe flow recirculation together with prescribed jet inlet conditions. It was therefore replaced by a 'block-correction' procedure, which also applied in a line-by-line manner, after each iteration. The jet inlet conditions were specified in a similar manner to that recommended by Nielsen et al (ref 25-26), but using wall-jet empirical data and results of profile analysis of Hammond (ref 33-34). The present work has concentrated on the problem of handling flows involving complete recirculation of the room air-flow which is a much more severe test of the model than the geometry studied by Neilson et al (ref 25-26). The present study also examined flows with significant buoyancy, which gives rise to additional problems of ensuring numerical stability and in turbulent modelling.

The treatment of turbulence is made by way of mathematical model (ref 23), in which the transport of momentum by the

turbulent motions is related to a turbulent viscosity, and transport of scalar quantities. The Launder & Spalding (ref 24) version of 'K-ε' model has been used, in which the turbulent viscosity and diffusivity are evaluated from two local properties of turbulence, namely time-averaged kinetic energy 'K' and dissipation rate 'ε'.

The buoyancy-influenced terms have been introduced into the y-direction momentum, and turbulence energy and dissipation rate equations in the similar to those adopted by Nielsen (ref 26), Markatos and Cox (ref 35) and Kumar and Cox (ref 36). The latter two studies concerned fire spread within an enclosure, which is driven by large buoyancy forces.

2.3 GOVERNING EQUATIONS AND THEIR FINITE-DIFFERENCE ANALOQUE:

The higher-level numerical solution procedure is based on the laws which governing the physics of the flow field in terms of partial differential equations (pdes), which govern the conservation of mass, momentum and thermal energy for any laminar and turbulent regime. The time-averaged pdes for a turbulent flow are the same as the laminar ones, except that effective transport properties are employed. The dependent variable of these equations are usually specific properties, and are based on a unit-volume.

2.3.1 The Continuity, Momentum and Energy Conservation Equations:

The conservation equations which govern the buoyancy-driven and forced convection of mass, momentum and thermal energy may be expressed in cartesian tensor notation as follows (ref 37-39):

a) Mass conservation or continuity equation:

$$\frac{\partial \rho}{\partial t} + \frac{\partial}{\partial x_j} (\rho u_j) = 0 \qquad (2.1)$$

b) Momentum or Navier-Stokes equations for direction i:

$$\frac{\partial}{\partial t}(\rho u_i) + \frac{\partial}{\partial x_j}(\rho u_i u_j) = \frac{\partial}{\partial x_j}(\tau_{ij}) - \frac{\partial p}{\partial x_i} + S_{b,i} \qquad (2.2)$$

c) Thermal energy equation:

$$\frac{\partial}{\partial t}(\rho h) + \frac{\partial}{\partial x_j}(\rho h u_j) = \frac{\partial}{\partial x_j}(J_{h,j}) + S_h \qquad (2.3)$$

where

i & j	are components in cartesian tensor notation, both can take the values of 1 and 2 denoting the directions x_1 and x_2 in two space coordinates. When a subscript is repeated in a term, a summation of two terms is implied,
x_1 & x_2	are x and y components in cartesian coordinate,
ρ	is the fluid density,
t	is the time,
u	is the instantanous velocity,
p	is the instantanous static pressure,
S_b	is buoyancy force,
τ	is the stress-tensor (see Section 2.3.3),
h	is the instantanous specific enthalpy,
J_h	is the heat-flux tensor and
S_h	is the source/sink of h (negligible unless chemical reaction is present).

Equations (2.1),(2.2)and (2.3) are in fact a closed set of equations which must be solved simultaneously, by a finite-difference method in the present study, in order to obtain the velocity, pressure and enthalpy in the field.

2.3.2 The Conservation Equation For A General Scalar Property:

It is convenient to write a conservation or transport equation for a general scalar property of the flow such as enthalpy/temperature. It will be shown later that the turbulence kinetic energy 'K' and its dissipation rate 'ε', have similar transport equations, since they obey the generalized conservation principle. If the dependent variable is denoted by 'ϕ' the general differential equation is:

$$\frac{\partial}{\partial t}(\rho\phi) + \frac{\partial}{\partial x_j}(\rho\phi\, u_j) = \frac{\partial}{\partial x_j}(J_{\phi,j}) + S_\phi \qquad (2.4)$$

where S_ϕ is the source/sink of ϕ and J_ϕ is the scalar property flux.

2.3.3 The Auxilary Relations:

The molecular diffusion of momentum, τ , and the scalar property flux, J_ϕ , in equations (2.2) and (2.4) have not yet been defined. They can be related to gradient of velocity components and scalar properties respectively. For uniform density flows these relations may be written as follows (ref 22).

$$\tau_{ij} = \mu\left(\frac{\partial u_i}{\partial x_j} + \frac{\partial u_j}{\partial x_i}\right) \qquad (2.5)$$

$$J_{\phi,j} = \frac{\mu}{\sigma_\phi}\left(\frac{\partial \phi}{\partial x_j}\right) \qquad (2.6)$$

where μ and σ_ϕ are the dynamic viscosity and molecular Prandtl/Schmidt number of the fluid respectively.

2.4 TIME-AVERAGED EQUATION FOR TURBULENT FLOW:

The calculation of turbulent flows via the exact time-dependent forms of the governing equations is possible, although it is limited to very low Reynolds numbers and requires an excessively fine grid, which renders this approach uneconomic (ref 40). It is therefore necessary to utilise the time-averaged version of these equations, in which the instantaneous properties of the flow are replaced by mean values with fluctuating values

superimposed upon them (ref 40,41). For a general property or variable, ϕ (ie. u, p, h, etc....):

$$\Phi = \frac{1}{t} \int_{o}^{t} \phi \, dt \qquad t \to \infty \tag{2.7}$$

$$\phi = \Phi + \phi' \tag{2.8}$$

where

Φ and ϕ' are the time-averaged component and fluctuating component of the variable respectively.

By substituting equation (2.7) into equations (2.1),(2.2) and (2.4), and thereafter time-averaging (ref 42), the following differential equations will result which govern the mean motion of 'steady' (strictly statistically stationary) turbulent flow:

a) Continuity:

$$\frac{\partial}{\partial x_j} (\rho U_i) = 0 \tag{2.9}$$

b) Momentum:

$$\frac{\partial}{\partial x_j} (\rho U_i U_j) = \frac{\partial}{\partial x_j} \left\{ \mu \left(\frac{\partial U_i}{\partial x_j} + \frac{\partial U_j}{\partial x_i} \right) - \rho u'_i u'_j \right\} - \frac{\partial P}{\partial x_i} + S_{b,i} \tag{2.10}$$

c) General Scalar Property :

$$\frac{\partial}{\partial x_j} (\rho \Phi U_j) = \frac{\partial}{\partial x_j} \left\{ \frac{\mu}{\sigma_\phi} \left(\frac{\partial \Phi}{\partial x_j} \right) - \rho \phi' u'_j \right\} + S_\phi \tag{2.11}$$

where

U is the time-averaged velocity,

P is the time-averaged static pressure,

Φ is the time averaged general scalar property,

S_b is the time-averaged buoyancy force,

S_ϕ is the time-averaged source/sink of ϕ,

u' is the fluctuating value of u,

p' the fluctuating value of p,

ϕ' is the fluctuating value of ϕ,

and τ & J_ϕ have been replaced with relations (2.5) and (2.6) respectively.

The 'Reynolds' stress-tensor ($-\rho u'_i u'_j$) and heat-flux tensor ($-\rho_\phi' u'_j$) are unknowns and therefore before any solution can be obtained they must be expressed in terms of known or calculable quantities.

2.5 TURBULENCE MODELS:

The task of expressing the unknown fluxes ($-\rho u'_i u'_j, -\rho \phi' u'_j$) in equations (2.10)and (2.11) in terms of the mean properties of the flow is known as the turbulence closure problem. Mathematical expressions which perform this function are called 'turbulence models'.

The applicability, economy and accuracy of a turbulence model are the main factors which determine its choice. Many turbulence models are available, and some of the more popular ones are described briefly in this Section. However, a more detailed description of them can be found in (ref 23),(ref 41-45) or elsewhere. There is no ideal classification scheme for turbulence models , but the one suggested by Reynolds (ref 41), and used below, provides a systematic basis for describing the various models.

2.5.1 The Classification Of Turbulence Models:

a) Zero-equation models:

The zero-equation models are those in which no partial differential, or transport, equations for turbulence quantities are used. An example of such models the classical Prandtl mixing length hypothesis ,which employs the Boussinesq eddy viscosity formulation (ref 45). In this approach, the turbulent transport is related to the gradients of mean flow quantities, for example in thin shear layers:

$$- \rho \overline{u_1' u_2'} = \mu_t \left(\frac{\partial U}{\partial x_2}\right) \qquad (2.12)$$

$$- \rho \overline{u_2' \phi'} = \frac{\mu_t}{\sigma_t} \left(\frac{\partial \Phi}{\partial x_2}\right) \qquad (2.13)$$

where μ_t and σ_t are the turbulent viscosity and Prandtl/ Schmit number respectively.

The Prandtl mixing length hypothesis calculate the distribution of the turbulent viscosity , μ_t, by relating it to the local mean velocity gradient:

$$\mu_t = lm^2 \left| \frac{\partial U}{\partial x_2} \right| \qquad (2.14)$$

where lm, is the mixing length, and must be discribed over the flow field empirically.

b) <u>One-equation model</u>

These models use one partial differential equation (pde) relating to some turbulence velocity scale. Usually the scale is the square route of the kinetic energy of turbulence , $\sqrt{K}$. The modelling proposal of Launder and Spalding (ref 23) and others lead to the following equation for K, valid for high Reynolds number flows (i.e. when the effect of molecular viscosity can be neglected).

$$\frac{\partial}{\partial x_j} (\rho K U_j) = \frac{\partial}{\partial x_j} \left(\frac{\mu_t}{\sigma k} \frac{\partial K}{\partial x_j}\right) + G_k - \rho\varepsilon + S_{b,k} \qquad (2.15)$$

and

$$G_k = \mu_t \left\{ \frac{\partial U_i}{\partial x_j} \left(\frac{\partial U_i}{\partial x_j} + \frac{\partial U_j}{\partial x_i} \right) \right\} \qquad (2.16)$$

where

ε is the dissipation rate,

σ_k is Prandtl/Schmidt number for K and

G_k is the generation term.

In these models, the dissipation rate is usually determined from:

$$\varepsilon = C' K^{3/2} / L \qquad (2.17)$$

where

L is length scale and must be prescribed via empirical information similar to that for lm, and

C′ is a constant value.

The eddy viscosity concept can be used here to relate the turbulence stresses to the turbulence kinetic energy determind from equation 2.14. This approach yields the so-called Kolmogorov-Prandtl expression (ref 45):

$$\mu_t = C_\mu \rho K^{\frac{1}{2}} L \qquad (2.18)$$

where

C_μ is a constant

Bradshaw et al (ref 46) developed a popular one-equation model without using the eddy-viscosity concept. They have converted the turbulence kinetic energy equation into a transport equation for the shear stress ($\rho u'_i u'_j$) by assuming a direct link between K and $\rho u'_i u'_j$. They also assumed the diffusion flux of K to be proportional to a bulk velocity.

c) Two-equation models

Two-equation models employed pde′s for both the turbulence velocity and length scales, this overcomes the need to specify the length scale empirically, which is difficult in complex, recirculating flows. However, the length scale itself is not normally used as the dependent variable in a pde. One successful model used the turbulence energy dissipation rate in place of the length scale equation, and is thus known as K-ε model of turbulence. In this model the Reynolds stress($-\rho u'_i u'_j$) is again related to mean velocity via an eddy viscosity which is calculated from the kinetic energy, K, and its dissipation rate ,ε, via the Kolmogorov-Prandtl expression.

$$-\rho\, u'_i\, u'_j = \mu_t \left(\frac{\partial U_i}{\partial x_j} + \frac{\partial U_j}{\partial x_i} \right) \qquad (2.19)$$

$$\mu_t = C_D\, \rho^2\, K^2/\varepsilon \qquad (2.20)$$

where

C_D is an empirical constant.

The transport equation for the dissipation rate , ε, for high Reynolds numbers is as following (ref 23),

$$\frac{\partial}{\partial x_j} (\rho\varepsilon\, U_j) = \frac{\partial}{\partial x_j} \left(\frac{\mu_t}{\sigma_\varepsilon} \frac{\partial \varepsilon}{\partial x_j} \right) + C_1\, G_k\, \frac{\varepsilon}{K} - C_2\, \rho\, \frac{\varepsilon^2}{K} + S_{b,\varepsilon} \qquad (2.21)$$

where

C_1 and C_2 are empirical constants, and

σ_ε is an effective Prandtl / Schmidt number.

d) Stress-equation models

Models which are based on eddy-viscosity/diffusivity concept such as the K-ε model, are valid only under certain conditions. In these models the eddy viscosity is assumed to be the same for all turbulent stresses, although in complex flows or flows with turbulence influenced by strong body forces acting in preferred directions, such as buoyancy forces, it may be anisotropic. The local state of turbulence is also characterized in these models by one velocity scale , $\sqrt{K}$, and individual stresses are related to this scale. However, in reality, each stress component may develop quite differently in the flow.

In order to account for the different development of individual stress components pde's for all components of turbulence stresses are necessary. These models are often called second-order closure schemes, and a variety of such models have been proposed by different investigators (ref 44,47-49). The pde's for these models are complex and lengthy , and have the general form as follows:

$$D(\rho\acute{u}_i u'_j)/Dt = \text{Production} + \text{Dissipation} + \text{Redistribution} \qquad (2.22)$$

e) Large-eddy simulations models:

In 1973 the group at Stanford University under Professor W. C. Reynolds with close co-oporation from the NASA-Ames laboratory began to develop this approach, and considerable success has been achived since that time. However, the method is not able to be used for complex problem, but it might after considerable development, eventually be useful to handel problems as such.

The basic idea of this approach is that a numerical computation of the time-dependent Navier-Stokes equations is performed for the large-eddy structure while a sub-grid effective viscosity is used for the small scales turbulence. A more detailed discription of the progress in large-eddy simulation is given by Reynolds (ref 41).

2.5.2 The Turbulence Model Adopted For Present Study:

Zero-equation models have been used widely for simple shear layer problems, where the upstream 'history' of turbulent transport is not important and a mixing length distribution can be prescribe realisticly. In one-equation models a pde for turbulent kinetic energy is solved, and thus these transport effects can be taken into account. However, the problem of specifying the length scale distribution in complex flows remains. Therefore, zero-equation and one-equation models are not suitable for the present work, where the flow patterns are complex and description of mixing length or length scale is difficult.

The stress-transport models appear to be potentially more accurate and 'universal', but they require much more computer time than two-equation models, since there are more pdes to be solved. The validation studies that have compared the two-equation models with stress-transport models, such as that by Pope and Whitelaw (ref 50), have shown that the predictions of the latter models display little improvement. The two-equation model was therefore adopted for the present study simply because it is capaible of handling complex recirculating flows without the need to prescribe any length scale, and it uses much less computer time than the stress-transport models.

The present work has concentrated on 'K-ε' ,two-equation model of turbulence since it has been tested widely in many different flows and found to have an accuracy sufficient for practical purposes. The values of the turbulence model constants (i.e. C_1, C_2, C_D, σ_k, σ_ε) employed here are those adopted in the elliptic code of Pun and Spalding (ref 31), and are given in table 2.1. The basis for the determination of these constants is

explained by Launder and Spalding (ref 23).

Table 2.1; Constants in turbulence model

C_1	C_2	C_D	σ_k	σ_ε
1.43	1.92	0.09	1	1.3

2.6 BOUNDARY CONDITIONS:

A two-dimensional room (see Fig 2.1) is typically modelled in the present work with a low side 'linear' slot wall register. Thus the solution domain is bounded by walls, the floor, the ceiling, and slot inlet and outlet planes.

The condition at any point in the flow can be influenced by other points, because of 'elliptic' nature of the flow. Therefore it is necessary to supply boundary conditions for variables at all the boundaries of the flow domain, these boundaries could be specified value of the variable or value of the associated flux, or a relation between the variable and the flux. Since the velocities and pressures are inter-dependent, where velocities are prescribed pressure need not. Therefore the variables for which boundary conditions are supplied are U, V, H, K and ε .

The boundary conditions specified for the present study are as follows:

2.6.1 At Jet Inlet and Outlet:

Particular difficulties arises with the use of numerical finite-difference methods in a large room with a very small slot inlet, due to the large number of grid nodes that would be required in the slot. In the present study inlet conditions were specified in a similar manner to those recommended by Nielsen et al (ref 25), but using wall-jet empirical data and the results of profile analysis of Hammond (ref 33,34). In this way an arbitrary inlet and outlet have been prescribed in the fully developed region of the wall-jet (as shown in Fig 2.1). The location of the starting profile, Xsp, is unimportant, provided that is kept small compared to the length of the room. In the present calculation the distance Xsp is located at the nearest grid line to the 1/4 of the room length. The width of the starting zone, Ysp, can be then estimated from the growth of the jet (Hammond private communication, 1981):

$$Ysp = 0.1825\ Xsp + 1.4783\ Si \tag{2.23}$$

where Si is the height of the slot inlet. The actual value of the width Ysp corresponds to distance to the next farthest grid line away from floor beyond that given by equation 2.23.

2.6.1.1 Starting profiles:

a) Velocity profile in x-direction

Using complete velocity profile formula and associated data correlations given by Hammond (ref 33,34),(see also part III) gives:

$$U = Um \left(\frac{C_f}{2}\right)^{\frac{1}{2}} \left\{ \frac{1}{\kappa} \ell n \left[R_m \left(\frac{C_f}{2}\right)^{\frac{1}{2}} \left(\frac{b_u}{y_m}\right) \left(\frac{y}{b_u}\right) \right] + B + C\,\omega\left(\frac{y}{b_u}\right) \right\} \tag{2.24}$$

A quartic wake function was adopted:

$$\omega\left(\frac{y}{b_u}\right) = \sum_{1}^{n=4} a_n \left(\frac{y}{b_u}\right)^n \tag{2.25}$$

where

U	is the velocity component in x-direction,
U_m	is the maximum velocity,
C_f	is the local skin friction coefficient,
y	is the normal distance from the wall,
b_u & y_m	are defined in fig 2.1,
B	is the log-law constant (=5.2, see part III),
C	is the wake function coefficient (see part III)

Hammond (ref 34) presented approximate values for the coefficients, a_n , as power-law functions of the local, wall-jet Reynolds number ($R_m = \rho U_m y_m / \mu$):

$$a_1 = 0.841\ R_m^{-0.1040}$$

$$a_2 = 0.223\ R_m^{\ 0.0917}$$

$$a_3 = -0.18\ R_m^{\ 0.0627}$$

$$a_4 = 0.030\ R_m^{\ 0.0555} \qquad (2.26)$$

These approximate relations are used to specify the U-component starting profile.

b) Velocity Profile in y-direction

It is assumed that the flow is fully developed and the velocity component in direction y is zero:

$$V=0 \qquad (2.27)$$

c) Turbulence kinetic energy profile

Hammond (private communication, 1981) has derived an empirical expression for the turbulence kinetic energy profile across a wall-jet, which may be written in the form:

$$K = \left\{ U\ k_1 \left[k_2 \left(\frac{y}{\delta}\right)^2 + 1 \right] \right\}^2 \qquad (2.28)$$

where δ is the velocity width and the values of k_1 and k_2 are 0.175 and 7.10 respectively.

d) Energy dissipation profile

Energy dissipation profile for wall-jet may be obtained via the mixing length hypothesis. Hammond (private communication, 1981) has derived a dissipation length scale expression for plane wall-jets in the form:

$$\frac{L_\varepsilon}{\delta} = 0.44 + 0.68\left(1 - \frac{y}{\delta}\right)^2 - 1.12\left(1 - \frac{y}{\delta}\right)^4 \qquad (2.29)$$

where L_ε is the dissipation length scale. The dissipation rate may then be obtained from the definition:

$$\varepsilon = \frac{K^{3/2}}{L_\varepsilon} \qquad (2.30)$$

e) Enthalpy/ Temperature profile

The rather limited data for heated wall-jets on a adiabatic surfaces suggest (Hammond private communication, 1981):

$$\frac{H_m - H_a}{H_e - H_a} = 4.09\left(\frac{X_{sp}}{S_i}\right)^{-0.5} \qquad (2.31)$$

$$\frac{H - H_a}{H_m - H_a} = 1 - \frac{y}{\delta} \qquad (2.32)$$

where

H is the time-averaged enthalpy/temperature,

H_e is the enthalpy/temperature at slot inlet,

H_a is the ambient enthalpy/temperature and

H_m is the maximum enthalpy/temperature.

2.6.1.2 Boundary condition for Xsp and outlet

Along the line Xsp and the room outlet plane a zero streamwise gradient was imposed to all the variables except U at Xsp and V at the outlet, which were specified as zero. Thus,

$$\begin{aligned} &\text{at the outlet:} && \partial\Phi/\partial x = 0 && \text{and} && V=0 \\ &\text{and at Xsp:} && \partial\Phi/\partial y = 0 && \text{and} && U=0 \end{aligned} \qquad (2.33)$$

2.6.2 At Walls, Floor and Ceiling:

In the present work the solid surfaces are stationary and impervious so the velocity components are specified zero. The enthalpy/ temperature is therefore given a prescribed value. However, the kinetic energy and its dissipation rate requires special treatment as discribed in the next section.

2.7 WALL FUNCTION:

The simple boundary specification of zero velocity components at a stationary, non-slip and impermeable wall is valid, but with difficulties in numerical calculations when the flow is turbulent. Viscous and turbulent stresses are of the same order of magnitude near the wall. Thus the effective viscosity and other transport properties, fall to their laminar values and the result is a steep, non-linear variation with distance from the wall in velocities, scalar properties, turbulent viscosity and their gradients. It is still possible to compute these variations by packing the grid nodes into regions of steep gradient changes, close enough for accurate numerical calculation. However, this necessitates both a large computer and running costs. Also those functions appearing in turbulence model equations must properly represent the influences of the local Reynolds number of turbulence μ_{eff}/μ_ℓ , which for the type of turbulence model used in the present work is inappropriate. Fortunately, very close to the wall, one-dimensional 'Couette flow' behaviour is observed, which offers a way around this dilemma in the form of a 'bridging-over' across the near wall region, via the introduction of 'wall-functions'. These functions are often expressed in the form of algebric equations. It is therefore convenient to use a 'wall-function' to connect the flux of Φ to the wall with the local Φ - difference across the Couette flow region and with other relevent quantities.

The wall function adopted for the present work is the same as the one Pun and Splading (ref 31) have incorporated in their elliptic code, which is described in some detail by Launder and Spalding (ref 24).

a) Momentum flux near the wall

The velocity variation is assumed to conform to the following modified form of the logarithmic law:

$$U^+ = \frac{U}{U_\tau} = \frac{1}{\kappa} \ln (E\ Y^+) \qquad (2.34)$$

where

U	is the velocity parallel to the wall at a distance y from the wall,
U_τ	is the socalled 'friction' velocity ($\equiv (\tau_w/\rho)^{\frac{1}{2}} \simeq \tau_w/\rho C_D^{\frac{1}{4}} K^{\frac{1}{2}}$)
κ & E	are the law of the wall constants, whose values are 0.41 and 8.4 respectively (ref 33),
Y^+	is the dimensionless distance from the wall ($\equiv \rho\ U_\tau\ y/\mu_\ell \simeq C_D^{\frac{1}{4}}\ \rho\ K^{\frac{1}{2}}\ y/\mu_\ell$)
τ_w	is the wall shear stress

b) Heat flux near the wall

The distribution of enthalpy is assumed to be analogous to that for velocity given by equation 2.34. It may be written in the form:

$$H^+ = \sigma_t\ (U^+ + P) \qquad (2.35)$$

where H^+ is defined in terms of the enthalpy near the wall (H), enthalpy at the wall (H_w) and the local flux to the wall (qw) as follows:

$$H^+ = \frac{(H - H_w)\quad C_D^{\frac{1}{4}}\ K^{\frac{1}{2}}}{q_w} \qquad (2.36)$$

and P is the viscous sublayer 'resistance'. Jatatilleke (ref 51) evaluated the P-function from experimental data for moderate to high molecular Prandtl numbers, and found that it is well represented by:

$$P = 9.0 \left(\frac{\sigma_\ell}{\sigma_t} - 1\right)\left(\frac{\sigma_\ell}{\sigma_t}\right)^{-\frac{1}{4}} \qquad (2.37)$$

where σ_ℓ and σ_t are the laminar (molecular) and turbulent Prandtl numbers.

c) Kinetic energy near the wall

The kinetic energy is obtainable from its 'pde', but with the diffusion of K to the wall set to zero, thus:

$$\left(\frac{\partial K}{\partial y}\right)_{wall} = 0 \qquad (2.38)$$

The generation and dissipation terms are modified to be consistent with the known results for a Couette flow region. Details will be given in chapter 3.

d) Dissipation rate near the wall

Near the wall the length scale is assumed proportional to the distance from the wall, thus the dissipation rate can be expressed as:

$$\varepsilon = \frac{C_D^{\frac{3}{4}} K^{\frac{3}{2}}}{\kappa y} \qquad (2.39)$$

using a variation on equation (2.30).

2.8 THE GENERALIZED FORM OF THE EQUATIONS TO BE SOLVED:

The equations to be solved can be expressed by a single equation of the form:

$$\underbrace{\frac{\partial}{\partial x_j}(\rho\Phi U_j)}_{\text{Convection terms}} = \underbrace{\frac{\partial}{\partial x_j}\left(\Gamma_\phi \frac{\partial \Phi}{\partial x_j}\right)}_{\text{diffusion terms}} + \underbrace{S_\phi}_{\text{Source terms}} \qquad (2.40)$$

The expressions for diffusion coefficient, Γ_ϕ , and source term, S_ϕ , corresponding to a particular variable Φ are given in table 2.2, and the buoyancy production (ref 26,35,36,52-54) is given by:

$$G_B = - \beta g \frac{\mu_t}{\sigma_t} \frac{\partial \theta}{\partial y} \qquad (2.41)$$

The effective viscosity μ_{eff} is defined by:

$$\mu_{eff} = \mu_\ell + \mu_t \qquad (2.42)$$

and the effective exchange coefficient for H is given by:

$$\Gamma_{h,eff} = \frac{\mu_\ell}{\sigma_\ell} + \frac{\mu_t}{\sigma_t} \qquad (2.43)$$

where

θ	is the excess temperature (T-To),
To	is some reference value,
β	is coefficient of thermal expansion and
g	is gravitational acceleration.

Conserved property	Φ	Γ_ϕ	S_ϕ
Continuity	1	0	-
x-direction momentum	U	μ_{eff}	$-\frac{\partial P}{\partial x} + \frac{\partial}{\partial x}\left(\mu_{eff}\frac{\partial U}{\partial x}\right) + \frac{\partial}{\partial y}\left(\mu_{eff}\frac{\partial V}{\partial x}\right)$
y-direction momentum	V	μ_{eff}	$-\frac{\partial P}{\partial y} + \frac{\partial}{\partial x}\left(\mu_{eff}\frac{\partial U}{\partial y}\right) + \frac{\partial}{\partial y}\left(\mu_{eff}\frac{\partial V}{\partial y}\right) + \rho\beta g\theta$
Thermal energy	H	$\Gamma_{h,eff}$	S_h
Turbulence energy	K	μ_{eff}/σ_k	$G_k - \rho\varepsilon + G_B$
Dissipation rate	ε	$\mu_{eff}/\sigma\varepsilon$	$\frac{\varepsilon}{K}\{(G_k + G_B)C_1 - C_2 \rho\varepsilon\}$

Table 2.2: Exchange Coefficients and Source Terms

CHAPTER 3
NUMERICAL SOLUTION PROCEDURE FOR THE HIGHER-LEVEL METHOD

3.1 INTRODUCTION:

The 'elliptic' governing partial differential equations obtained in Chapter 2 are complex and strongly inter-linked with no obvious equation available for the static pressure that appears in the momentum equations. An analytical solution is therefore not possible, and it is necessary to use numerical methods of solution. There are two main numerical solution techniques for the type of elliptic equations encountered in the present problem: 'finite-difference' and 'finite-element' methods. The main differences between these two methods concern the manner in which the discretized equations are derived. The benefit of finite-element methods (FEM) lies in its ability to fit irregular boundaries fairly readily , although difficulties have been experienced in bridging the steep property gradients encountered near walls in turbulent flows. There are a number of other technical difficulties in using the FEM for fluid flow (as opposed to solid mechanic) problems, and these are discussed by Patankar (ref 55). Fortunately, the flow domains considered here are all rectangular, and the finite-difference approach has been adopted.

3.2 FORMULATION OF THE FINITE-DIFFERENCE EQUATIONS:

3.2.1 Derivation Methods:

There are several ways to obtaining finite-difference equations (FDE's) from differential equations, some of the most common methods are briefly described below, and further details are given by Patankar (ref 55):

a)Taylor-series formulation:

In this method, the derivaties in the differential equations are obtained via a truncated Taylor series expansion. An assumption that the variation of Φ in a particular direction may be represented by polynomial is also invoked.

The method offers less flexibility and little physical insight into the derivation of the FDE's, and the resultant equations do not always satisfy the conservation requirement.

b)Variational formulation:

Method is based on the calculus of variations. It shows that, the solution of a certain differential equation is equivalent to minimizing a related quantity called 'functional'. This equivalence is known as variational principle. This method is complex and rather limited in applicability.

c)Weighted residuals:

This is a powerful method for solving the differential equations. The method is summerised below, although it is described by Patankar (ref 55) and in more detail by Finlayson (ref 56).

Supposing the differential equation is of the form:

$$L(\Phi) = 0 \tag{3.1}$$

and

$$\tilde{\Phi} = a_o x^0 + a_1 x^1 + a_2 x^2 + ... + a_n x^n \tag{3.2}$$

where a's are parameters. The substitution of equation (3.2) into the equation (3.1) gives a residual, which is defined as:

$$R = L(\tilde{\Phi}) \tag{3.3}$$

This residual should be as small as possible . Let propose that

$$\int WR \, dx = 0 \tag{3.4}$$

where W is a weighting functions. A number of equations can be generated for evaluating the unknown parameters, by first integrating equation (3.4) over the domain of interest, and then choosing a succession of weighting functions. Different versions of the method result from the choice of weighting functions. A simplest weighting function is obtained when W=1. A number of weighting residual equations may be generated by dividing the complete solution domain into subdomains or control-volumes, and setting the weighting function to be unity over one control volume at a time and zero elswhere. This version of weighted residuals is called the 'subdomain' , 'micro-integration' or 'control-volume' method. The advantage of this approach is that the approximations inherent in the discretization process are easily identifiable, and it is easy to ensure that the resulting

FDE's satisfy the conservation requirement. This method has been chosen for the present work.

3.2.2 Computational Grid and Control-Volume:

The first step in the derivation of the FDE's is the establishment of a discritization grid, and the definition of the points at which variables are located. The grid spacing may be non-uniform, to allow the spacing to be small in regions with steep property gradients, such as near walls. The intersection of the grid lines are grid nodes. Each grid node is assumed to be enclosed in its own cell or control volume. The control volume boundaries were taken to be mid-way between the grid nodes in the present study.

Fig. (3.1) illustrates the two-dimensional grid applied in the present work. A typical grid node P and its neigbours N,S,E and W are shown in fig. (3.2) as well as the relevant control volume (i.e., the volume enclosed by the dashed lined). The boundaries of the control volume are labelled with the lower-case version of the lable of the neigbouring nodes (n,s,e and w).

3.2.3 Location of Dependent Variables:

All dependent variables are stored at the grid nodes, except the velocity components which are calculated at 'staggered' locations (i.e. mid-way between adjacent grid nodes), as shown in fig. (3.3). This 'staggered' grid , which was first used by Harlow and Welch (ref 57) and subsequently adopted by Patankar and Spalding (ref 29) in their SIMPLE algorithm, has the advantage of ensuring that the velocities are directly available for calculating the convective fluxes of scalar flow variables as well as lying between the location of the static pressures which 'drive' them. The staggered location and control volume for velocity components are shown in fig. (3.4) and (3.5).

3.2.4 The General Finite-Difference Equations:

The governing differential equations which must be replaced by FDE's are:

(a) Continuity

$$\frac{\partial}{\partial x_j}(\rho U_j) = 0 \qquad (3.5)$$

and,

(b) the general differential equation

$$\frac{\partial}{\partial x_j}\ (\rho\Phi U_j) = \frac{\partial}{\partial x_j}\left(\Gamma_\phi\ \frac{\partial\Phi}{\partial x_j}\right) + S_\phi \qquad (3.6)$$

Both equation (3.5) and (3.6) may be written, for an incompressible flow, in the form:

$$\rho U_j \left(\frac{\partial\Phi}{\partial x_j}\right) = \frac{\partial}{\partial x_j}\left(\Gamma_\phi\ \frac{\partial\Phi}{\partial x_j}\right) + S_\phi \qquad (3.7)$$

Equation (3.6) can alternatively be written in the form:

$$\frac{\partial}{\partial x_j}\ (J_j) = S_\phi \qquad (3.8)$$

where J_j is the total flux in direction j, which defined as:

$$J_j = \rho\Phi U_j - \Gamma_\phi\ \frac{\partial\Phi}{\partial x_j} \qquad (3.9)$$

The integration of equation (3.8) over the control volume shown in Fig (3.2) gives:

$$J_e - J_w + J_n - J_s = S_\phi\ \Delta x\ \Delta y \qquad (3.10)$$

where J_e , J_w , J_n and J_s are the integrated total fluxes over the control-volume faces. The source term, S_ϕ , may simply be written in quasi-linear form as:

$$S_\phi = S_P + S'_P \Phi_P \tag{3.11}$$

where S_P and S'_P are determined from a suitable finite difference approximation of the S_ϕ expression for the particular variabl ϕ. Hence, equation (3.10) becomes:

$$J_e - J_w + J_n - J_s = (S_P + S'_P \Phi_P)\, \Delta x\, \Delta y \tag{3.12}$$

The continuity equation (3.5) may also be integrated over the control volume, and the result can be written in the form:

$$F_e - F_w + F_n - F_s = 0 \tag{3.13}$$

where F_e , F_w , F_n and F_s are the mass flow rate through the control volume faces:

$$\begin{aligned} F_e &= (\rho U)_e\, \Delta y \\ F_w &= (\rho U)_w\, \Delta y \\ F_n &= (\rho V)_n\, \Delta x \\ F_s &= (\rho V)_s\, \Delta x \end{aligned} \tag{3.14}$$

By multiplying the equation (3.13) by Φ_p and substracting from equation (3.12) , the following equation will result:

$$(J_e - F_e \Phi_P) - (J_w - F_w \Phi_P) + (J_n - F_n \Phi_P) - (J_s - F_s \Phi_P) = (S_P + S'_P \Phi_P)\, \Delta x\, \Delta y \tag{3.15}$$

This is in fact the finite-difference equivalent to equation (3.7). According to Patankar (ref 55), terms $(J_e - F_e \Phi_P)$, etc... can be replaced by:

$$
\begin{aligned}
J_e - F_e \Phi_P &= a_E (\Phi_P - \Phi_E) \\
J_w - F_w \Phi_P &= a_W (\Phi_W - \Phi_P) \\
J_n - F_n \Phi_P &= a_N (\Phi_P - \Phi_N) \\
J_s - F_s \Phi_P &= a_S (\Phi_S - \Phi_P)
\end{aligned}
\tag{3.16}
$$

After substituting the relations (3.16) into equation (3.15) and some rearrangement, the FDE has the final form:

$$
a_P \Phi_P = \Big(\sum_{E,W,N,S} a\Phi \Big) + b
\tag{3.17}
$$

where

$$
\begin{aligned}
a_E &= D_e \, L \, (|Pe|)_e + \mathrm{Max}(-F_e, 0) \\
a_W &= D_w \, L \, (|Pe|)_w + \mathrm{Max}(F_w, 0) \\
a_N &= D_n \, L \, (|Pe|)_n + \mathrm{Max}(-F_n, 0) \\
a_S &= D_s \, L \, (|Pe|)_s + \mathrm{Max}(F_s, 0) \\
a_P &= \Big(\sum_{E,W,N,S} a \Big) - S_P' \, \Delta x \, \Delta y \\
b &= S_P \, \Delta x \, \Delta y
\end{aligned}
\tag{3.18}
$$

The D_e , D_w , D_n and D_s are diffusion terms and are defined as:

$$
\begin{aligned}
D_e &= \Gamma_{\phi,e} \, \Delta y \, / \, (\delta x)_e \\
D_w &= \Gamma_{\phi,w} \, \Delta y \, / \, (\delta x)_w \\
D_n &= \Gamma_{\phi,n} \, \Delta x \, / \, (\delta y)_n \\
D_s &= \Gamma_{\phi,s} \, \Delta x \, / \, (\delta y)_s
\end{aligned}
\tag{3.19}
$$

Pe_e , Pe_w , etc... are Peclet numbers representing the ratio of the strenghts of the convection and diffusion terms:

$$Pe_e = (\rho U\ \delta x/\Gamma_\phi)_e = F_e/D_e$$

$$Pe_w = (\rho U\ \delta x/\Gamma_\phi)_w = F_w/D_w$$

$$Pe_n = (\rho V\ \delta y/\Gamma_\phi)_n = F_n/D_n$$

$$Pe_s = (\rho V\ \delta y/\Gamma_\phi)_s = F_s/D_s \qquad (3.20)$$

The exchange coefficients Γ_ϕ at control-volume faces are simply specified as:

$$\Gamma_{\phi,e} = (\Gamma_{\phi,P} + \Gamma_{\phi,E})/2$$

$$\Gamma_{\phi,w} = (\Gamma_{\phi,W} + \Gamma_{\phi,P})/2$$

$$\Gamma_{\phi,n} = (\Gamma_{\phi,P} + \Gamma_{\phi,N})/2$$

$$\Gamma_{\phi,s} = (\Gamma_{\phi,S} + \Gamma_{\phi,P})/2 \qquad (3.21)$$

L(|Pe|) is a function related to the particular differencing scheme adopted for the finite-difference procedure. The Max(A,B) denotes the greater of A and B.

3.2.5 The Differencing Schemes:

In order to illustrate the choice of differencing schemes, a steady one-dimensional situation in which only the convection and diffusion terms exist will be considered. The governing differential equation then simplifies to:

$$\frac{d}{dx}(\rho U\Phi) = \frac{d}{dx}\left(\Gamma_\phi \frac{d\Phi}{dx}\right) \qquad (3.22)$$

and the continuity equation to:

$$\frac{d}{dx}(\rho U) = 0 \quad \text{or} \quad \rho U = \text{const.} \tag{3.23}$$

The corresponding grid nodes are illustrated in figure (3.6). Finally, the integration of equation (3.22) over the control volume in figure 3.6 yields:

$$(\rho U\Phi)_e - (\rho U\Phi)_w = \left(\Gamma_\phi \frac{\partial\Phi}{\partial x}\right)_e - \left(\Gamma_\phi \frac{\partial\Phi}{\partial x}\right)_w \tag{3.24}$$

a) Central Difference Scheme

In this scheme a piecewise-linear variation for Φ is assumed between the grid nodes, therefore the value of Φ at an interface is specified as:

$$\Phi_e = (\Phi_E + \Phi_P)/2$$

$$\Phi_w = (\Phi_P + \Phi_W)/2 \tag{3.25}$$

and the diffusion terms are given in the form:

$$\left(\Gamma_\phi \frac{d\Phi}{dx}\right)_e = \Gamma_{\phi,e} \frac{\Phi_E - \Phi_P}{(\delta x)_e}$$

$$\left(\Gamma_\phi \frac{d\Phi}{dx}\right)_w = \Gamma_{\phi,w} \frac{\Phi_P - \Phi_W}{(\delta x)_w} \tag{3.26}$$

Thus, equation 3.24 may be written in the form:

$$\tfrac{1}{2}(\rho U)_e (\Phi_E + \Phi_P) - \tfrac{1}{2}(\rho U)_w (\Phi_P + \Phi_W) =$$

$$\Gamma_{\phi,e}(\Phi_E - \Phi_P)/(\delta x)_e - \Gamma_{\phi,w}(\Phi_P - \Phi_W)/(\delta x)_w \tag{3.27}$$

After some rearrangement, and using equation 3.23, the finite-difference form of equation 3.22 becomes:

$$a_P \Phi_P = a_E \Phi_E + a_W \Phi_W \qquad (3.28)$$

where

$$a_E = D_e - F_e/2$$

$$a_W = D_w + F_w/2$$

$$a_P = a_E + a_W \qquad (3.29)$$

According to Patankar (ref 55), Runchal (ref 58), and others for given values of Φ_E and Φ_W the central difference scheme yields accurate results only when $P_e < 2$. Outside this limit the scheme may become inaccurate and, with an iterative method of solution, instability may ensue (ref 22,55,58,59).

b) Upwind Scheme

In this scheme the formulation of diffusion term is the same as with central difference scheme, except that the convection term is calculated in a different way (ref 55,60). The value of Φ at an interface is assumed to be equal to the value of Φ at the grid node on the 'upstream' or 'upwind' side of the face: for example

$$\Phi_e = \Phi_P \quad \text{if} \quad F_e > 0$$

$$\Phi_e = \Phi_E \quad \text{if} \quad F_e < 0 \qquad (3.30)$$

When equations (3.25) is replaced by this definition, the a's coefficients in equation 3.28 become:

$$a_E = D_e + \text{Max}\ (-F_e, 0)$$

$$a_W = D_w + \text{Max}\ (F_w, 0) \qquad (3.31)$$

The upwind scheme gives realistic and stable behaviour at all Peclet numbers. It is also superior to central difference scheme in terms of accuracy for $Pe > 2$, but slightly inferior for smaller values (ref 58).

c) Hybrid Scheme

This is a combination of central difference and upwind schemes. It employs the central difference scheme for, $-2 \leq Pe \leq 2$, and the upwind scheme, in which the diffusion has been set equal to zero for outside this range. For example

$$\frac{a_E}{D_e} = -Pe_e \qquad \text{if} \quad Pe_e < -2$$

$$\frac{a_E}{D_e} = 1 - \frac{Pe_e}{2} \qquad \text{if} \quad -2 \leq Pe_e \leq 2$$

$$\frac{a_E}{D_e} = 0 \qquad \text{if} \quad Pe_e > 2 \qquad (3.32)$$

In combined form, the coefficient a_E and a_W have the form:

$$a_E = \text{Max}\left(-F_e, D_e - \frac{F_e}{2}, 0\right)$$

$$a_W = \text{Max}\left(F_w, D_w + \frac{F_e}{2}, 0\right) \qquad (3.33)$$

d) Power-Law Scheme

According to Patankar (ref 55,61) the departure of the hybrid scheme from the exact result is large at $Pe=\pm 2$ (see fig 3.7). He felt that the setting of the diffusion terms to zero as soon as $|Pe|$ exceeds 2 as rather premature, and therefore proposed a power-law scheme which may be written in the form:

$$\frac{a_E}{D_e} = -Pe_e \qquad \text{if} \quad Pe_e < -10$$

$$\frac{a_E}{D} = (1 + 0.1\,Pe_e)^5 - Pe_e \qquad \text{if} \quad -10 \leq Pe_e < 0$$

$$\frac{a_E}{D_e} = (1 - 0.1\,Pe_e)^5 \qquad \text{if} \quad 0 \leq Pe_e \leq 10$$

$$\frac{a_E}{D_e} = 0 \qquad \text{if} \quad Pe_e > 10 \qquad (3.34)$$

In a combined form thus may be written as:

$$a_E = D_e \text{ Max}\{0, \left(1 - \frac{0.1\ |F_e|}{D_e}\right)^5\} + \text{Max}\ (0, -F_e)$$

$$a_W = D_w \text{ Max}\{0, \left(1 - \frac{0.1\ |F_w|}{D_w}\right)^5\} + \text{Max}\ (0, F_w)$$

(3.35)

It is now possible to specify the function $L(|Pe|)$, which appears in equations 3.18 , from the various schemes outlined above. These are summarised in table 3.1 below.

Table 3.1 : The function L(|Pe|) for different schemes

Scheme	L (| Pe |)
Central difference	$1 - 0.5\ \|Pe\|$
Upwind	1
Hybrid	$\text{Max}(0, 1-0.5\|Pe\|)$
Power law	$\text{Max}\{0, (1-0.1\|Pe\|)^5\}$

All schemes discussed above give a physically realistic solution except the central differencing scheme, which requires a very fine grid in order to yield reasonable solution for $Pe < 2$. The upwind scheme is adopted in the present work, as it appears to exhibit a reasonable balance between accuracy and economy. However, the other differencing schemes have been incorporated into the program structure, and could readily be used if greater numerical accuracy is required.

3.2.6 Special Attention On Momentum Equations:

The momentum equations can be obtained from equation 3.17 for the general variable Φ , where Φ now stands for the relevent velocity components and Γ_ϕ and S_ϕ are given in table 2.2. The only compilcation arises due to the use of staggered grid and control volume (see fig. 3.3-3.5) for U and V components. The use of staggered grid allows the pressure differences ($P_P - P_E$ & $P_P - P_N$) to be employed directly to calculate the pressure force acting

on the control volume for each velocity component. The resulting U-momentum and V-momentum equations have the form:

$$a_P U_P = \left(\sum_{E,W,N,S} aU\right) + b + A_e (P_P - P_E)$$

$$a_P V_P = \left(\sum_{E,W,N,S} aV\right) + b + A_n (P_P - P_N) \qquad (3.36)$$

The source term ,b, is defined in the same manner as in equations 3.18 ,where the pressure gradient is not included in the source term quantities (S_P & S_P'). The pressure gradients $A_e(P_P - P_E)$ & $A_n(P_P - P_N)$ are acting in the U and V control volume respectively, where:

$$A_e = \Delta y \times 1 \quad , \quad A_n = \Delta x \times 1 \qquad (3.37)$$

The momentum equations cannot be solved unless the pressure field is given or estimated, and the resulting velocities will not satisfy the continuity equation unless they are based on the correct pressure field. However, 'imperfect' velocity components may be estimated from guessed pressures, P*, from the solution of the following equations:

$$a_P U^*_P = \left(\sum_{E,W,N,S} aU^*\right) + b + A_e (P^*_P - P^*_E)$$

$$a_P V^*_P = \left(\sum_{E,W,N,S} aV^*\right) + b + A_n (P^*_P - P^*_N) \qquad (3.38)$$

where U* and V* are called 'starred' velocity components.

3.2.7 The Pressure and Velocity Corrections:

The guessed or starred pressure P* must be improved in such a way that more accurate starred velocity components (U* and V*) are produced, and therefore get closer to satisfying the continuity equation. Correction quantities such as P' , U' and V' whose purpose is to bring the continuity and momentum equation into balance, may be determined as follows:

$$P = P^* + P'$$

$$U = U^* + U'$$

$$V = V^* + V' \qquad (3.39)$$

The substitution of equations 3.39 into equations 3.38, and the substraction from 3.36, leads to:

$$a_P U'_P = \left(\sum_{E,W,N,S} aU'\right) + A_e (P'_P - P'_E)$$

$$a_P V'_P = \left(\sum_{E,W,N,S} aV'\right) + A_n (P'_P - P'_N) \qquad (3.40)$$

In the SIMPLE algorithm of Patankar and Spalding (ref 29) adopted here, the terms $\sum aU'$ and $\sum aV'$ are neglected from the above equations, for the reason given in section 3.2.8. Equation 3.40 then becomes:

$$a_P U'_P = A_e (P'_P - P'_E)$$

$$a_P V'_P = A_n (P'_P - P'_N) \qquad (3.41)$$

or

$$U'_P = d_e (P'_P - P'_E)$$

$$V'_P = d_n (P'_P - P'_N) \qquad (3.42)$$

where

$$d_e = A_e/a_P \quad , \quad d_n = A_n/a_P \qquad (3.43)$$

The substitution of equations 3.42 into equations 3.39 yield:

$$U_P = U^*_P + d_e (P'_P - P'_E)$$

$$V_P = V^*_P + d_n (P'_P - P'_N) \qquad (3.44)$$

3.2.8 The Pressure-Correction Equation

The substitution of equations 3.44 into the continuity equation (3.13) , and rearranging yields the desired equation for the pressure-correction ,P´:

$$a_P P'_P = \left(\sum_{E,W,N,S} a\, P' \right) + b \qquad (3.45)$$

where

$$a_E = \rho_e\, d_e\, A_e$$

$$a_W = \rho_w\, d_w\, A_w$$

$$a_N = \rho_n\, d_n\, A_n$$

$$a_S = \rho_s\, d_s\, A_s$$

$$a_P = a_E + a_W + a_N + a_S$$

$$b = (\rho U^* A)_w - (\rho U^* A)_e + (\rho V^* A)_s - (\rho V^* A)_n \qquad (3.46)$$

Where

$$A_e = A_w = \Delta y$$
$$A_n = A_s = \Delta x \qquad (3.47)$$

and ρ_e , ρ_w, ρ_n and ρ_s can be calculated by interpolation from the value of the densities at the grid nodes.

The source term in equation 3.46 ,b, represents a mass balance on the control volume based on the preliminary velocities in the calculation domain. The purpose of pressure correction is to reduce this ´mass source´ to zero. Since the mass-source and pressure corrections will become zero after the velocities and the pressure satisfy the momentum and continuity equations, the final solution will be independent of the terms $\sum aU'$ and $\sum aV'$ neglected from equations 3.40.

Equation 3.45 has the same form as 3.17 and can be solved in a similar manner. The resulting pressure-correction may then be used to adjust the velocity components from equations 3.44 and pressure from equation 3.39.

3.3 THE INSERTION OF BOUNDARY CONDITIONS:

The FDE's are not applicable for boundary nodes since they refer to the points which lying outside the calculation domain. The control volumes for different variables near to boundary are shown in fig 3.8 . This arrangement has the advantage for meeting the conservation requirement and facilitating the flux calculation.

A particular expression for Φ_N (see fig 3.9), which coincides with the face n of the adjoining control volume can be inserted to break the normal link between Φ_P and Φ_N in the FDE's. This link breakes simply by specifying the appropriate coefficient in FDE to zero (for example $a_N=0$).

The boundary appropriate to the present study were outlined in Section 2.6. The special practice which are required to incorporate the appropriate boundary conditions for the various flow variables in the wall region will be outlined in this Section.

3.3.1 Tangential Velocity:

The tangential velocity for the node next to the wall (for example, U_P in fig 3.9b) can be obtained from the usual FDE for momentum. However, U_P follows the logarithmic law of the wall (equation 2.34), which relates it to friction velocity U_τ . It is necessary to incorporate the correct shear stress into the FDE. The shear stress may be introduced into the FDE by breaking the link between the node on the wall and the adjacent grid node, and by modifying the source terms in FDE. For example, for nodes P and N shown in fig 3.9b

$$a_N = 0 \qquad (3.48)$$

If point P is within the turbulent region ($Y^+ > 11.5$), the correct shear stress can then be determined via the logarithmic law, equation 2.34:

$$\tau_w = \kappa C_D^{1/4} \rho U_P K_P^{1/2} / \ell n (E \rho \delta K^{1/2} C_D^{1/4} / \mu_\ell) \quad (3.49)$$

where

$$Y^+ = C_D^{1/4} \rho K_P^{1/2} y / \mu_\ell \quad (3.50)$$

However, if point P is within the viscous sublayer ($Y^+ \leqslant 11.5$), then the shear stress may be simply evaluated from:

$$\tau_w = \mu_\ell U_P / \delta \quad (3.51)$$

The appropriate form of τ_w obtained from either of these expressions can then be inserted into the FDE via the source terms as follows (ref 31):

$$S_P = 0$$

$$S_P' = - \tau_w A_n / U_P \quad (3.52)$$

It should be noted that no special treatment is required for the velocity normal to the wall.

3.3.2 Heat Flux Near The Wall:

The enthalpy boundary condition can be introduced to the thermal energy FDE in a similar manner to that for velocity. Equation 2.36 can also be written in terms of the wall shear stress as follows (ref 31):

$$St \equiv \frac{- q_w}{(H_P - H_N)\rho |U_P|} = \frac{\tau_w / (\rho U_P^2)}{\sigma_t \{1 + P\sqrt{\tau_w / (\rho U_P^2)}} \quad (3.53)$$

where, if the node P lies within the turbulent region, τ_w is evaluated from equation 3.49, or, if it is within the viscous sublayer, from equation 3.51. The FDE coefficient a_N is first set to zero (see fig 3.9a),and the heat flux is then incorporated into the FDE through the source terms as before (ref 31):

$$S_P = |St\ \rho\ U_P\ A_n|\ H_N$$

$$S'_P = |St\ \rho\ U_P\ A_n|$$

3.3.3 Turbulence Kinetic Energy:

To achieve the conditions which are mentioned in Section 2.7(c), it is necessary again to set a_N to zero (see fig 3.9a). Due to the steep velocity gradients near the walls, the source terms are best expressed through shear stress (ref 31). These terms may therefore be written in the form:

$$S_k = G_k - \rho\varepsilon$$

$$= \tau_w \frac{\partial U}{\partial y} - \frac{C_D\ \rho^2\ K^2}{\mu_t}$$

$$= \tau_w \frac{\partial U}{\partial y} - \frac{C_D\ \rho^2\ K^2}{\tau_w} \frac{\partial U}{\partial y}$$

the integration of S_k over the control volume shown in fig 3.9a yields:

$$\iint S_k dV = \tau_w\ U_s\ A_n - C_D\ \rho^2\ K_P^2\ U_S\ A_n/\tau_w \qquad (3.54)$$

hence,

$$S_P = \tau_w\ U_S\ A_n$$

$$S'_P = C_D\ \rho^2\ K_P\ A_n/\tau_w \qquad (3.55)$$

3.3.4 The Dissipation Rate:

The dissipation rate ε_p (see fig 3.9a) is obtained directly from the expression 2.39, thus;

$$\varepsilon_P = \frac{C_D^{3/4} K_P^{3/2}}{\kappa \delta} \qquad (3.56)$$

The value of ε_P is incororated into the FDE for the near-wall node through the source terms (ref 31,55):

$$S_P = \alpha \varepsilon_P$$

$$S_P' = - \alpha \qquad (3.57)$$

where α is a very large number (eq 10^{30}).

3.4 THE SOLUTION OF THE FINITE-DIFFERENCE EQUATIONS:

Equations 3.17 and 3.36 must be solved to obtain U, V, K, ε, H and P' for all the grid nodes in the calculation domain. These equations must be solved simultaneously and, since they are non-linear and inter-linked, it is necessary to employ an iterative solution procedure. The particular iterative method adopted in the present work is a combination of 'line-by-line' iteration with a 'block' line adjustment applied to each line. For each grid node on a line considered (see fig 3.10) the FDE's can be expressed as:

$$\Phi_j = A_j \Phi_{j+1} + B_j \Phi_{j-1} + C_j \qquad (3.58)$$

where j denotes the position along a particular line, in the range from j=2 to j=n-1. The boundary conditions (i.e., node positions j=1 and j=n) are incorporated in C_j. With respect to equation 3.17:

$$\Phi_j = \Phi_P \ , \ \Phi_{j+1} = \Phi_N \ , \ \Phi_{j-1} = \Phi_S$$

and

$$A_j = \frac{a_N}{a_P} \quad , \quad B_j = \frac{a_S}{a_P}$$

$$C_j = \frac{a_W \Phi_W + a_E \Phi_E + b}{a_P} \qquad (3.59)$$

Equations 3.58 for nodes on a line are solved simultaneously by matrix-inversion procedure. While the Φ values on a line are being solved, the Φ values on both sides of the line are kept unchanged. The computer code employed in the present study has been developed from that of Pun and Spalding (ref 31), who adopted the Tri-Diagonal Matrix Algorithm (TDMA), based on an elimination procedure derived by successive substitution (ref 62) for solving elliptic FDE sets.

An alternative way of rewriting equation 3.58, obtained by elimination, is:

$$\Phi_j = A'_j \Phi_{j+1} + B'_j$$

$$j = n-1 , n-2 , ... , 2 \qquad (3.60)$$

and the transformed coefficients A'_j & B'_j are given by the recurrence relations:

$$A'_j = A_j / (1 - A'_{j-1} B_j)$$

$$B'_j = (C_j + B'_{j-1} B_j) / (1 - A'_{j-1} B_j) \qquad (3.61)$$

3.4.1 The Block-adjustment Procedure:

The block-adjustment procedure is used in an effort to successfully obtain a converged solution. The idea is to add a uniform increment $\delta\Phi$ to the values of variables Φ in each line, although the increment is varied from line to line. This

increment is applied in such a way that, after adjustment, all the lines satisfy the overall conservation requirement. Thus equation 3.17 can be written as:

$$A^P_{ij}\,\Phi_{ij} = A^E_{ij}\,\Phi_{i+1,j} + A^W_{ij}\,\Phi_{i-1,j} + A^N_{ij}\,\Phi_{i,j+1} + A^S_{ij}\,\Phi_{i,j-1} + B_{ij} \qquad (3.62)$$

where the subscripts i and j denote the position in the x and y directions respectively (see fig 3.10).

If the prevailing solution procedure by line iteration is denoted by $\tilde{\Phi}_{ij}$, then a uniform increment $\delta\Phi_i$ is added to the interior nodes on each line, changing the equation 3.62 as follows:

$$\sum_j A^P_{ij}\,(\tilde{\Phi}_{ij} + \delta\Phi_i) = \sum_j \left(A^E_{ij}\,\tilde{\Phi}_{i+1,j} + A^W_{ij}\,\tilde{\Phi}_{i-1,j} + A^N_{ij}\,\Phi_{i,j+1} + A^S_{ij}\,\tilde{\Phi}_{i,j-1} + B_{ij} \right)$$

$$+ \sum_j \left(A^N_{ij} + A^S_{ij} \right) \delta\Phi_i$$

Except boundary

$$+ \sum_j A^E_{ij}\,\delta\Phi_{i+1} + \sum_j A^W_{ij}\,\delta\Phi_{i-1} \qquad (3.63)$$

Further manipulation of equation 3.63 results in the following equation for the $\delta\Phi$'s:

$$d_i\,\delta\Phi_i = a_i\,\delta\Phi_{i+1} + b_i\,\delta\Phi_{i-1} + C_i$$

$$i=2,3,4,\ldots,n-1 \qquad (3.64)$$

where

$$a_i \equiv \sum_j A^E_{ij} \quad , \quad b_i \equiv \sum_j A^W_{ij}$$

$$C_i \equiv -\sum_j \left(A^P_{ij}\,\tilde{\Phi}_{ij} - A^E_{ij}\,\tilde{\Phi}_{i+1,j} - A^W_{ij}\,\tilde{\Phi}_{i-1,j} - A^N_{ij}\,\tilde{\Phi}_{i,j+1} - A^S_{ij}\,\tilde{\Phi}_{i,j-1} - B_{ij} \right)$$

$$d_i \equiv \sum_j \left(A^P_{ij} - A^N_{ij} - A^S_{ij}\right) \qquad (3.65)$$

The equation 3.64 can be solved by TDMA with the increments $\delta\Phi$'s set to zero at boundaries. The coefficient C_j is in fact the sum of residual sources from equation 3.17 for a line and, when C_j is zero, $\delta\Phi$ will be zero.

3.4.2 The Algorithm and the Sequence of Solution:

The solution procedure adopted for the present work is similar to the SIMPLE algorithm of Patankar and Spalding (ref 29), and more recently described by Patankar (ref 32), except that:

i) all variables are solved on a line before advancing the sweep, as advocated by Pun and Spalding (ref 31), and
ii) a block-adjustment procedure is employed to ensure continuity.

The sequence in which the FDE's are solved is as follows:

a) Variables are initialized.

b) A line is considered.

c) Exchange coefficients Γ_ϕ are defined (via equation 3.21).

d) Convection and diffusion terms are calculated (from equations 3.14 and 3.19).

e) The finite-difference coefficients are evaluated (from equation 3.18).

f) The FDE's (equations 3.17 and 3.36) are solved by TDMA.

g) Block-adjustment coefficients are calculated (equation 3.65).

h) The steps b-g are repeated for all the variables except P'.

i) U* and v* are used to calculate the coefficients in pressure-correction equation (equation 3.46).

j) Pressure-correction equation (equation 3.45) is solved using the TDMA.

k) The resulting pressure corrections are used to update the pressure and velocity components in the manner indicated by equations 3.39 and 3.44.

l) The cycle of steps b-k represents one iteration. At the end of each iteration the equation for block-adjustment (equation 3.64) is solved by TDMA.

m) The increments $\delta\Phi$ are added to the corresponding Φ's on each line.

h) Steps b-m are repeated until a converged solution is achieved.

3.5 NUMERICAL CONSIDERATIONS:

3.5.1 Convergence:

Equation 3.17 may also be written in the form:

$$\Phi_P = \frac{\sum_{E,W,N,S} a\,\Phi}{a_P} + \frac{b}{a_P} \qquad (3.66)$$

According to Scarborough (ref 63), as discussed by Gosman et al (ref 22) and Patankar (ref 55), a successive substitution method ensures the convergence of a linear equation of a type such as equation 3.66 (i.e. when a's and b are constants) if:

$$\frac{\sum_{E,W,N,S} |a|}{|a_p|} \begin{cases} \leq 1 & \text{for all equations} \\ < 1 & \text{for at least one equation} \end{cases} \qquad (3.67)$$

All equations to be solved must satisfy this condition, thus:

$$a'_s > 0$$

$$a_P \geq \sum_{E,W,N,S} a \qquad (3.68)$$

However, in the present work the coefficients are not constant, and indeed they vary from one iteration to another. Fortunately Scarborough's criterion (Eq 3.67) is known to be a sufficient rather than a necessary condition for convergence and, when the above criteria are obeyed, it may be possible to solve non-linear equations. In an iterative method of solution, it is necessary to examine how the current solution approximates to the exact solution of the FDE's at the end of each iteration, for each dependent variable. The convergence criteria applied in the present work is based on the residual-sources of the FDE's. The residual source for equation 3.17, is defined by:

$$R_\phi = a_P \Phi_P - \sum_{E,W,N,S} a\Phi + b \qquad (3.69)$$

For an exact solution, R_ϕ must be zero to satisfy the FDE, but for an inexact or nearly exact solution the normalized residual-source can be defined as:

$$\frac{\sum R_\phi}{R_{\phi,\,ref}}\ \text{for all field} \leqslant \lambda \qquad (3.70)$$

where λ is a constant. $R_{\phi,ref}$ is a reference residual-source that is specified relative to an appropriate property at entrance of the flow. In the present study, the value for the convergence criteria λ was typically set at less than 0.005.

The residual-source for pressure correction equation (3.45) was defined as the mass balance on the relevant control volume (i.e. b in equation 3.46).

3.5.2 Stability:

The equations to be solved are non-linear and strongly interlinked, and must be solved simultaneously. They are therefore prone to numerical instability. Since iterative solution of linear and non-linear equations using the Scarborough criteria will normally converge, the instability must be due to the interlinkage between the dependent variables. The result of numerical instability is the non-satisfaction of the mass conservation on a local and overall basis. This leads to an oscillation of the residual-sources rather than convergece. Such oscillations are particularly prevalent in the case of the buoyant flow.

The major sources for instability identified in the present study were:

- non-linearity of the equations,
- velocity-pressure interlinkage of the momentum equations,
- buoyancy-linkage of momentum and thermal energy equations,
- buoyancy-linkage of K , ε and thermal energy equations,
- buoyancy-linkage of μ_t through the K and ε equations.

The following techniques may reduce the numerical instability, although they proved only of rather limited success in buoyant flows.

(a) Under-relaxation

The use of some form of under-relaxation is very useful when solving non-linear equations. It reduces the magnitude of current error level in the field, while preventing the divergence in the iterative solution of equations. The way in which the dependent variables were under-relaxed in the present study is as follows:

Equation 3.17 may be written in the form :

$$\Phi_P = \frac{\left(\sum_{E,W,N,S} a\Phi\right)_+ b}{a_P} \qquad (3.71)$$

Supposing Φ_P^* is the value of Φ_P from the previous iteration, then by subtracting Φ_P^* from both sides of equation 3.71, it becomes:

$$\Phi_P - \Phi_P^* = \frac{\left(\sum_{E,W,N,S} a\Phi\right)_+ b}{a_P} - \Phi_P^* \qquad (3.72)$$

Thus the right-hand side of the above equation gives the change in the variable between the current and previous iteration. This change can be modified by introducing a relaxation factor, ξ , as follows:

$$\Phi_P - \Phi^*_P = \xi \left(\frac{\left\{ \sum_{E,W,N,S} a\Phi \right\} + b}{a_P} - \Phi^*_P \right) \qquad (3.73)$$

By rearrangement of the terms, equation 3.73 becomes:

$$\frac{a_P}{\xi} \Phi_P = \sum_{E,W,N,S} a\Phi + b + (1 - \xi) \frac{a_P}{\xi} \Phi^*_P \qquad (3.74)$$

where

$0 < \xi < 1$ implies under-relaxation, and

$\xi = 1$ means no relaxation

The value of the relaxation factors for the different variables adopted in the present work are similar to those which were used by Pun and Spalding (ref 31) for the computation of turbulent flow through a sudden enlargement in a circular pipe. These relation factors are listed in table 3.2.

Table 3.2 Under-relaxation factors

Variable	U	V	K	ε	H	P	μ
Under-relaxation	0.3	0.3	0.5	0.5	1.0	0.5	0.5

(b) Linearization:

The FDE source terms may induce the divergence of the iteration solution, if they are not properly linearized. The general approach to the linearization of the source terms was indicated by equation 3.11. The quantity S_p must be either zero or negative. Thus in the K & ε equations, the negative source terms are incorporated into S'_p . If some part of the source terms may change sign (such as the buoyancy source terms in the V, K & ε equations) a suitable arrangement would be;

$$S_p \approx \text{Max}\ (\ \text{STERM}\ ,\ 0.)+.....$$
$$S_p \approx -\text{Max}\ (\ -\text{STERM}\ ,\ 0.)-..... \qquad (3.75)$$

where STERM can be negative or positive.

(c) Line-traverse:

Increasing the number of TDMA traverses on a line might possibly yield a more complete solution of the equations during each iteration. In the present study, the maximum number of traverses on a line for all variables specified was two. However, if the largest of the absolute value of the algebraic sums of the residual sources for any variable on the line is smaller than a criteria value (say , 0.001) no more TDMA traverse were made on that line.

(d) Initialization:

Specifying realistic initial field values for all variables can be an important factor in ensuring both fast convergence and stability. In the present study the wall-jet profile analysis of Hammond (ref 33,34) has been used to initialize the fields values for all variables (see fig 3.11) prior to the first iteration of the initial run. The converged solution for a 21 X 21 grid with an expansion between adjacent nodes of 1.1 on both the x and y directions is obtained after approximatly 300 iterations, in the non-buoyant case. However, for subsequent runs, the results of previous computations can be used to initialize the field values for all variables, and this procedure reduces the number of iterations needed to obtain a converged solution to 30-200. The exact number of iterations depends on the degree of change in the input data from the previous run.

(e) Grid adjustment:

Generally the number of the grid lines must be sufficient to ensure numerical accuracy. In the case of a non-uniform grid, special attention must be paid to the ratio between two adjacent grid lines and the ratio between the cell walls. A series of tests for grid-dependence is therefore necessary, including a test of the influence of the number of grid nodes and one of the expansion ratio between neighbouring grid lines. These tests were conducted using various grids having between 225 and 729 nodes, and expansion rations of 1.1 to 1.3 in both x and y directions. The results of these tests are presented in figures 3.12 to 3.14, where for the computations shown in figures 3.12 and 3.13 the expansion ratio between the grid lines was held at 1.1. It is clear that, although coarse 15 X 15 and 17 X 17 grids led to a converged solution, they differ from the results for the other, more refined grids. These differences are particularly significant in regard to the convective heat transfer coefficient (fig 3.12), but much less so in regard to the velocity field

(fig 3.13). Apart from the coarse 15 X 15 and 17 X 17 grids, the results obtained using the various meshes are quite similar for most the variables in the field.

All the subsequent computed results presented in this thesis were obtained using a 21 X 21 finite-difference grid, as this gave rise to reasonable balance between rapid convergence and numerical accuracy when an expansion ratio of 1.1 was employed (see fig 3.14). A converged solution was typically achieved after 300 iterations for non-buoyant flows using a guessed initialization of the field variables. This corresponds to a central processor time of about 3300 seconds on the Cranfield GEC 4085 mini-computer.

3.5.3 Accuracy:

The accuracy of the solution obtained with the present method depends on the following factors:

i- The degree to which the solution satisfies the FDE's: this can be assessed by the level of the residual-sources defined by equation 3.69.

ii- The degree to which the solution depends on the grid arrangement: a grid independence test must be sought by increasing the number of grid lines, or concentrating them into regions where large variations in the variables occur, such that no significant change is observed with further increase.

iii- The conditions imposed at boundaries; the realistic adjustment of the variables at boundaries improves the degree of accuracy in the prediction.

iv- The adequacy of the turbulence model: the correctness of the turbulence model is open to question, and that may have a large influence to the accuracy of the problem.

Attempts have been made to reduce to a certain extent the errors due to factors i, ii and iii which are computation factors in origin, but no modifications have been made to the popular, K-ε turbulence model.

3.6 THE FLOW DIAGRAM FOR THE HIGHER-LEVEL COMPUTER PROGRAM:

Figure 3.15 shows the flow diagram for the present higher-level computer program (the elliptic code). It indicates the sequence of operations , the inter-connections between the various parts of the program, and briefly indicates their function.

PART III

AN INTERMEDIATE-LEVEL CALCULATION METHOD

CHAPTER 4
BASIS OF THE CALCULATION PROCEDURE

4.1 INTRODUCTION:

Unfortuately the 'high-level' computer-based flow model which is discribed in part II above, is unsuitable for providing direct input data into the current generation of building thermal models. This is because the model is very costly in terms of computer time and storage, and is rather user 'unfriendly', due to its complexity. In order to overcome this practical limitation, an 'intermediate-level' calculation procedure have been developed by Alamdari and Hammond (ref 20), and incorporated into a computer code which the authors have called the ROOM-CHT (Room Convective Heat Transfer) program. This program was envisaged as a 'bolt-on' package to building thermal models, and is outlined below.

4.1.1 Requirements of Building Thermal Modellers:

The present generation of building thermal models require surface-averaged convection coefficients for individual room elements: ceilings, floors, walls and windows. Many employ a relatively large time step (~ 60 minutes) and also need these coefficients to be time-averaged over the heating system control cycle. In any case, computing cost would usually prohibit small time step (~ 5 minutes) in design studies even for those models capable of using them {see, for example, Waters (ref 6)}. Thus, the normal requirement for multiple averaging suggests that detailed variations in heat transfer distributions across surfaces will have only a minor influence on the final coefficient. This implication of the averaging process lies behind the development of the ROOM-CHT program.

4.2 PHYSICAL BASIS OF THE CALCULATION METHOD:

4.2.1 Profile Analysis of Wall-jets:

Wall-jets are the normal means of air distribution in buildings with forced convective heating systems. The characteristics of these jets are similar to those of classical plane wall-jet in 'stagnant' surroundings over much of their development. In order to calculate forced convective heat tranfer the present method makes 'informed' estimates of the flow and thermal field based on two and three-dimensional turbulent wall-jet characteristics. These jets are assumed to spread out

from their supply apperture and sequentially flow over all room elements. The mean-flow properties for the two-dimensional wall-jet are calculated from the empirical data reviewed by Hammond (ref 33), while that for its three-dimensional counterpart are taken from Rajaratnam (ref 64). Once the mean-flow feild has been determined, the corresponding heat transfer distributions across the surfaces are calculated from the 'optimum log-law' for wall-jet heat transfer derived by Hammond (ref 34) on the basis of profile analysis.

4.2.1.1 Two-dimensional Wall-jets:

a) Velocity profile:

Coles' (ref 65) velocity profile expressions for plane wall jets in the form used by Hammond (ref 33,66) is adopted here:

$$U^+ = \frac{1}{\kappa} \ell n\ (Y^+) + B + C\ \omega \left(\frac{Y^+}{b_u^+}\right) \qquad (4.1)$$

Where

$$U^+ \equiv \frac{U}{U_\tau}\ ,\quad Y^+ \equiv \frac{U_\tau y}{\nu}\ ,\quad b^+_u \equiv \frac{U_\tau\ b_u}{\nu}$$

and

$$U_\tau \equiv (\tau_w/\rho)^{\frac{1}{2}} \qquad (4.2)$$

The velocity half-width, b_u , and other wall-jet properties are defined in fig 4.1(a). The values recommended by Brederode and Bradshaw (ref 67) for the log-law constants were adopted by Hammond (ref 34), and have also been used in the present work. These values are : κ=0.41 and B=5.2.

Equation (4.1) is essentially the conventional 'log-law' for near wall turbulent shear layers modified by a wake component, $\omega(Y^+/b^+u)$, and is valid outside the viscous sublayer. Hammond (ref 34) also developed a more complex, two-part expression for the complete velocity profile extending from the wall to the free edge of the jet. However, the variation of velocity within the viscous sublayer is unimportant for the present purposes.

By setting $U^+ = 0$ and $\omega(Y^+/b^+_u) = 1$ at $Y^+ = \delta^+$ (see fig 4.1a) in equation (4.1), the wake function coefficient becomes:

$$C = -\left[\frac{1}{\kappa} \ln (D\, b^+_u) + B \right] \tag{4.3}$$

In the present work the value of the width ratio $D \equiv \delta^+/b^+_u = 2.5$ was employed basis on the profile analysis of Hammond (ref 34).

The velocity profile equation 4.1 may be transformed at it's maxima where $Y^+ = Y^+_m$ by noting that,

$$C_f \equiv \tau_w/(\tfrac{1}{2}\, \rho\, U^2_m)$$

$$U^+_m \equiv U_m/U_\tau = (2/C_f)^{\frac{1}{2}}$$

$$Y^+_m \equiv R_m\, (C_f/2)^{\frac{1}{2}}$$

(4.4)

This yields a 'log-law' for skin friction (ref 34) in the form :

$$\left(\frac{2}{C_f}\right)^{\frac{1}{2}} = \frac{1}{\kappa} \ln \left[R_m \left(\frac{C_f}{2}\right)^{\frac{1}{2}} \right] + B + C\ \omega \left(\frac{Y^+_m}{b^+_u}\right) \tag{4.5}$$

The value of the wake-component at the velocity peak may be written for convenience in the form of a power-law relation:

$$\omega \left(\frac{Y^+_m}{b^+_u}\right) = 0.205\ R_m^{-0.1067} \tag{4.6}$$

A consequence of the solution procedure is that:

$$b^+_u = 0.283\ R_m \qquad (4.7)$$

b) Temperature Profile:

Similar expression to equation 4.1 may be obtained for the wall-jet temperature profile ,outside the molecular diffusive sublayer:

$$T^+ = \frac{1}{\kappa_\theta}\ \ell n\ Y^+ + B_\theta + C_\theta\ \omega_\theta \left(\frac{Y^+}{b^+_\theta}\right) \qquad (4.8)$$

where

$T^+ \equiv (T - T_w)/T_\tau$

$b^+_\theta \equiv U_\tau\ b_\theta/\nu$

T is the time-averaged value of the absolute temperature,

T_w is the wall temperature,

T_τ is the socalled 'friction temperature' $\{q_w/(\rho\ C_p\ U_\tau)\}$

q_w is the wall heat flux,

C_p is the specific heat of the fluid,

The temperature half-width, b_θ , and other wall-jet properties are defined in fig 4.1(b). The values recommended by Kader and Yaglom (ref 68) for the log-law constants were adopted by Hammond (ref 34), and have also been used in the present work. These imply a value for turbulent Prandtl number, $\sigma_t = \kappa/\kappa_\theta$ of 0.85, giving κ_θ =0.48. The molecular prandtl number, σ_ℓ , dependence of the corresponding 'additive constant' is given by (ref 68):

$$B_\theta = 12.5\ \sigma_\ell^{\frac{2}{3}} - 5.8 \qquad (4.9)$$

By setting $T^+ = 0$ and $\omega_\theta (Y^+/b^+_\theta) = 1$ at $Y^+ = \delta^+_\theta$ see fig 4.1b) in equation (4.8) the thermal wake component coefficient becomes:

$$C_\theta = \left[\frac{1}{\kappa_\theta} \ln (D_\theta b_\theta^+) + B_\theta \right] \tag{4.10}$$

where the thermal width ratio $D_\theta = \delta^+_\theta / b^+_\theta$ was given the same value as D by Hammond (ref 34).

The wall-jet temperature profile expression, equation 4.8, may also be transformed at it's maxima, where $Y^+ = Y^+_{m\theta}$ $(\equiv U_\tau \, Y^+_{m\theta}/\nu)$, by noting that:

$$S_t \equiv \frac{q_w}{\rho \, C_p \, U_m \, (T_m - T_w)}$$

$$T^+_m \equiv \frac{T_m - T_w}{T_\tau} = \frac{1}{S_t} \left(\frac{C_f}{2}\right)^{\frac{1}{2}}$$

$$Y^+_{m\theta} = R_m \left(\frac{C_f}{2}\right)^{\frac{1}{2}} \left(\frac{Y_{m\theta}}{Y_m}\right) \tag{4.11}$$

This leads to Hammond's optimum log-law for heat transfer:

$$\frac{1}{St} \left(\frac{C_f}{2}\right)^{\frac{1}{2}} = \frac{1}{\kappa_\theta} \ln \left[R_m \left(\frac{C_f}{2}\right)^{\frac{1}{2}} \frac{Y_{m\theta}}{Y^+_m} \right] + B_\theta + C_\theta \, \omega_\theta \left(\frac{Y_{m\theta}}{b^+_\theta}\right) \tag{4.12}$$

Equation (4.12) may be rearranged (ref 34) to yield a complicated relation for the Reynolds analogy factor, $St/0.5 \, C_f)$ $R_m \, (C_f/2)^{\frac{1}{2}}$. This is accomplished by elimination of the terms in equations (4.5) and (4.12), to give:

$$\frac{St}{0.5 \, C_f} = \frac{\kappa_\theta/\kappa}{1 + K_\theta \left(\frac{C_f}{2}\right)^{\frac{1}{2}}} \tag{4.13}$$

The term K_θ is dependent on the molecular Prandtl number and, according to profile analysis, is given by:

$$K_\theta = \frac{1}{\kappa}\left[\ell n \left(\frac{Y^+_{m\theta}}{Y^+_m}\right) + B'_\theta - B' + \kappa_\theta C_\theta \omega_\theta \left(\frac{Y^+_{m\theta}}{b^+_\theta}\right) - \kappa C \omega \left(\frac{Y^+_m}{b^+_u}\right)\right] \quad (4.14)$$

where, $B' = \kappa B$ and $B'_\theta = \kappa_\theta B_\theta$

Recently, Hammond (private communication, 1982) noted that K_θ was relatively independent of R_m, and that it could be more simply represented by:

$$K_\theta = -11.26 + 14.21 \ \sigma_\ell^{0.673} \quad (4.15)$$

This form of K_θ has been used in the ROOM-CHT program, although for air (σ_ℓ =0.71) K_θ has a constant value equal to about 0.025. The variation in the profile peak ratio and thermal wake component may be approximated by:

$$\frac{Y^+_{m\theta}}{Y^+_m} = 1.194 \ \sigma_\ell^{-0.455} \ R_m^{(0.00209 \ \sigma_\ell)} \quad (4.16)$$

$$\omega_\theta \left(\frac{Y^+_{m\theta}}{b^+_\theta}\right) = 0.169 \ \sigma_\ell^{-0.973} \ R_m^{-(0.0894 \ \sigma_\ell^{-0.274})} \quad (4.17)$$

and for air become:

$$\frac{Y^+_{m\theta}}{Y^+_m} = 1.395 \ R_m^{0.0015} \quad (4.18)$$

$$\omega_\theta \left(\frac{Y^+_{m\theta}}{b^+_\theta}\right) = 0.236\ R_m^{-0.0982} \qquad (4.19)$$

The analogy factor is insensitive to the choice of the value for the flow specific parameters $\delta^+_\theta/b^+_\theta$ and b^+_θ/b^+_u . In the present work, Hammond's value of $b^+_u/b^+_\theta = 0.85$ (ref 34) has been adopted.

In order to convert the optimum log-law in terms of the jet's initial conditions, it is necessary to make estimates of the mean flow properties of the jet particularly the peak velocity and temperature decay, and the jet spread. These are conventionally written in the form:

$$\frac{U_m}{U_e} = K_u \left(\frac{x}{S_i}\right)^{-n} \qquad (4.20)$$

$$\frac{T_m - T_e}{T_e - T_a} = K_t \left(\frac{x}{S_i}\right)^{-n} \qquad (4.21)$$

and

$$\frac{b_u}{S_i} = K_b \left(\frac{x}{S_i} + \frac{x_o}{S_i}\right) \qquad (4.22)$$

and the local Reynolds number can be expressed as:

$$R_m = 0.215\ R_e^{0.89} \left(\frac{x}{S_i}\right)^{0.40} \qquad (4.23)$$

where Ue, Te and Re are velocity, temperature and Reynolds number at inlet respectively.

The spread constant, K_b , is equal to the far-field spreading rate $(d\ b_u/dx)$ and x_o/S_i is socalled 'geometric' virtual

origin of the jet (ref 69). The variability observed in the experimental data reviewed by Hammond(ref 34, also private communication, 1982) does not seem to justify a choice for the velocity and temperature decay exponent, n, other than 0.5. Adopting these exponents, permits the constants K_u , K_t , K_b and x_o/Si to be assigned mean values from the data in the experimental literature. These constants are given in table 4.1.

Table 4.1

K_u	K_t	K_b	x_o/S_i
3.73	4.09	4.03	8.10

4.2.1.2 Three-dimensional Wall-jet:

a)Velocity profile

The experimental data reviewed by Rajaratnam (ref 64) suggests that the centreline velocity decay in three-dimensional wall-jet may be expressed in the form:

$$\frac{U_{mo}}{U_e} = 8.325 \left(\frac{x}{\sqrt{Ag}}\right)^{-1} \qquad (4.24)$$

where the outlet area, Ag , is the product of its height, Hg, and width, Wg (see also fig 4.2) and U_{mo} is the maximum velocity in centreline. According to Rajaratnam the spanwise jet spread is well described by the equation:

$$\frac{b_z}{w_g} = 0.20 \left(\frac{x}{w_g}\right) - 1.25 \qquad (4.25)$$

where b_z is the spanwise half-width. Inspection of the available data supports a value for the spanwise width ratio:

$$\frac{\delta_z}{b_z} \simeq 2.50 \tag{4.26}$$

Equation (4.25) breaks down for $x \leqslant 15$ Hg and in this region this spread is better represented by (ref 64):

$$\frac{b_z}{w_g} = 0.12 \left(\frac{x}{w_g}\right) + 0.20 \tag{4.27}$$

Thus, the spanwise jet spread δ_z , may be calculated as follows:

for the far-field:

$$\delta_z = 2.5\ w_g\ \ 0.20 \left(\frac{x}{w_g}\right) - 1.25 \tag{4.28}$$

for the near-field:

$$\delta_z = 2.5\ w_g \left[0.12 \left(\frac{x}{w_g}\right) + 0.20\right] \tag{4.29}$$

The intersection between these two relations actualy occurs at $x/w_g = 18.125$.

The spanwise velocity distribution may be written in the form (ref 64):

$$\frac{U_m}{U_{mo}} = \exp\left[-0.693 \left(\frac{z}{b_z}\right)^2\right] \tag{4.30}$$

and the potential core length as:

$$x_c \simeq 8.235 \sqrt{Ag} \tag{4.31}$$

b) Temperature profile

In the absence of appropriate experimental data for the temperature field, it is assumed the following relations may be applied (Hammond, private communication,1982):

$$\frac{\theta_{mo}}{\theta_e} = 9.125 \left(\frac{x}{\sqrt{Ag}}\right)^{-1} \qquad (4.32)$$

where $\theta = T - T_a$, and T_a is ambient temperature.

The spanwise width ratio may be determined by analogy with Hammond's two-dimensional analysis (ref 34), $b_z/b_{zo} = 0.85$, and then the temperature profile may be given by:

$$\frac{\theta_m}{\theta_{mo}} = \exp\left[-0.693 \left(\frac{z}{b_{zo}}\right)^2\right] \qquad (4.33)$$

in a similar manner to the corresponding velocity profile.

4.3 COMPUTATIONAL PROCEDURE:

The Reynolds analogy formula (4.12) obtained from profile analysis (Hammond, ref 34) gives the dimensionless wall-jet convection coefficient in the form of Stanton number $\{St \equiv h_m/(\rho\, C_p\, U_m)\}$.

$$St = St(R_m\,,\ \sigma_\ell) \qquad (4.34)$$

where, h_m , is heat transfer coefficent $\{ \equiv q_w / (T_m - T_w)\}$.

However, building thermal modellers conventionally use heat transfer coefficients based on the notional room air temperature:

$$h_c = q_w/(T_r - T_w) \qquad (4.35)$$

where, T_r , is the room temperature. Alamdari and Hammond (ref 20) have noted that, this coefficient is related to that of the wall-jet by:

$$h_c = h_m \frac{T_m - T_w}{T_r - T_w} \qquad (4.36)$$

The wall-jet convection coefficient may locally fall below the value corresponding to buoyancy-driven convection at the same room temperature difference. In these situations the calculation method adopts the appropriate heat transfer coefficient for buoyancy-driven convection.

The calculation procedure employs improved data correlations (Alamdari and Hammond, ref 70, see Appendix A for bounded paper) to obtain the buoyancy-driven convection coefficient in dimensional terms. Adopting a mediam 'film temperature', $T_f = (T_a + T_w)/2$, applicable to naturally-ventilated buildings (say 27 C)allows the buoyancy-driven convection coefficient to be in the form:

$$h_c = \left\{ \left[a_c \left(\frac{\Delta T}{L_s} \right) \right]^m + \left[b_c (\Delta T)^q \right]^m \right\}^{\frac{1}{m}} \qquad (4.37)$$

An examination of experimental data for vertical and horizontal surfaces (see Appendix A) suggests an optimal value of the exponent m of 6. The empirical coefficients, a_c and b_c for both vertical and horizontal surfaces are given in table 4.2. In the present work the characteristic length, L_s , has been defined as;

for vertical surfaces $L_s = H_s$

for horizontal surfaces $L_s = 4\ A_s/P_s$

where

H_s is the height of the surface,

A_s is the surface area and

P_s is the perimeter

In the case of stably-stratified convection near horizontal surfaces the following simple correlating equations is used

(ref 70):

$$h_c = 0.60 \left(\frac{\Delta T}{L_s^2}\right)^{1/5} \qquad (4.38)$$

Table 4.2 ; Empirical coefficients in the data correlation for hc

Flow & surface orientation	a_c	b_c	p	q	m
Buoyancy-driven convection over vertical surface	1.50	1.23	1/4	1/3	6
Buoyancy-driven flow on horizontal surface	1.40	1.63	1/4	1/3	6

Thus the ROOM-CHT program calculates the local heat transfer distribution over the room internal surfaces in the manner indicated above. The equations to be solved are generally explicit, algebraic ones, execpt for the wall-jet heat transfer 'log-law' which is implicit and therefore require an iterative solution. In order to avoid the possibility of divergence and to obtain a rapid solution, the Newton-Raphson iteration method (ref 71) has been employed for this equation with convergence being achieved in about three iterations. The computation grid typically employs about 10 uniformly-spaced calculation points per metre length of surface. Once the local heat transfer at mesh nodes was computed, the program performs multiple averaging by successive numerical integrations as required.

The ROOM-CHT program was run with a 45 X 27 uniform solution mesh (its local calculation are automatically grid-independent), and needed a corresponding central processor time of 54 seconds on the Cranfield GEC 4085 mini-computer.

4.4 THE FLOW DIAGRAM FOR THE INTERMEDIATE-LEVEL PROGRAM:

The flow diagram for the intermediate-level (ROOM-CHT) program isshown in figure 4.3. The diagram discribes the sequence of the operations and the way different parts of program are connected. It also indicates briefly the functions of various call statements.

PART IV

OBSERVATION AND DEDUCTIONS

CHAPTER 5
COMPUTATIONS AND COMPARISONS

5.1 INTRODUCTION:

This chapter, which presents the major contribution of the present work, is devoted to the comparisons between the results of the higher-level method (the elliptic code) and those of the intermediate-level method (the ROOM-CHT program), which were described in detail in Parts II & III respectively. The validation process consists of comparison with the experimental data obtained in a mechanically-ventilated test room by Alamdari, Chan and Hammond (ref 72). The results of the three-dimensional version of the ROOM-CHT program have been compared with the equivalent two-dimensional version. A parametric study is also reported in which the two-dimensional version of the ROOM-CHT program is used to generate internal surface convection coefficients for some of the most common space heating and air-conditioning geometries used in the UK. 96 different configurations/thermal conditions were examined, in all of which the air supply jet emanated from a linear slot beneath the ceiling. The sensitivity of modern building thermal models to input values for the convective coefficients were studied by Alamdari, Hammond and Melo (ref 81), using a well-tested dynamic model developed by the US National Bureau of Standard. A summery of their findings is presented here.

5.2 WALL-JET STARTING PROFILE COMPARISONS:

In order to overcome the problems associated with using a numerical finite-difference method to compute the jet-induced flow in a large room supplied from a small slot inlet (see Section 2.6.1), specified 'starting profiles' were employed at a downstream station (see figure 2.1). In this section, the wall-jet empirical data and Hammond's profile analysis results (ref 33,34), which have been used to generate these starting profiles, are compared with the predicted values obtained from a fine-grid elliptic code for the wall-jet region. Some comparisons are also made with the computations of Ljuboja and Rodi (ref 73,74) using a 'boundary layer' or 'parabolic' code. The latter code incorporated an algebraic stress turbulence model in which the standard K-ε model, Kolmogorov-Prandtl eddy viscosity constant was replaced by a algebraic expression derived from modelled Reynolds stress transport equations. This more complex model retains a wall damping correction to the Reynolds stress pressure-strain model. In the following comparisons of predicted wall-jet development, two versions of elliptic code were used, one with the standard K-ε turbulence model and the other with an algebric stress model, similar to that of Ljuboja and Rodi (73,74).

The inlet section of room was modelled (see figure 2.1) with boundary conditions similar to the one's described in Sections 2.6, 2.7 & 3.3, except at the slot inlet, which were prescribed in an analogous manner to that of Pun and Spalding (ref 31) for inlet flow: i.e.

$$U = U_e$$
$$V = 0$$
$$H = H_e$$
$$K = 0.00135\ U_e^2$$
$$\varepsilon = C_D\ K_e^{3/2} / (0.03\ S_i) \qquad (5.1)$$

The inlet Reynolds number in this particular study was given a value of 7.35×10^3, with a domain length, L/Si=200, where L is the length of the wall. Predictions were obtained with a non-uniform 31 X 31 grid with an expansion ratio of 1.1 in both x and y directions. The converged solution for this case was obtained after about 650 iterations using the standard K-ε turbulence model, corresponding to a central processor time of about 18000 sec on Cranfield GEC 4085 mini-computer.

5.2.1 Velocity Field:

The streamwise development the wall-jet velocity field is indicated in figures 5.1 to 5.5. Generally good agreement can be seen between the results of wall-jet profile analysis and empirical data of Hammond (ref 33,34) ,and turbulence model predictions with both the elliptic code and the parabolic code used by Ljuboja and Rodi. In figure 5.2 the two turbulence models used with the elliptic code are seen to yield velocity profiles that are very close for $y/b_u <$ 1.30, but differ slightly nearer the free edge of the jet. By comparison, the profile analysis of Hammond exhibits a 'fuller' profile when $y/b_u <$ 1.0, and vice versa. The standard K-ε model version of the elliptic code displays a growth, $d\ b_u/dx$, that is 15% higher than suggested by empirical data (see figure 5.3), whereas the algebraic stress model predicts a 9% lower rate. The velocity vectors and velocity profiles presented in figure 5.5 are proportional to the local resultant and x-direction velocity component respectively, but have not been scaled.

5.2.2 Temperature field:

Figures 5.6-5.8 show the corresponding streamwise development of the temperature field. Although the empirical data for temperature is based on only a very limited number of data sets, reasonable agreement with predictions of the standard K-ε and algebraic stress turbulence models is indicated in figures 5.6-5.8. In a similar manner to the cross-stream profile of velocity (figure 5.2), the profile analysis for the cross-stream temperature profile (figure 5.7) exhibits a fuller profile when $y/b_\theta < 1.0$ and vice versa. The agreement between the standard K-ε and algebraic stress model predictions for the growth of the wall-jet thermal field, b_θ/S_i, (figure 5.8) is closer than that for b_u/S_i in figure 5.3. The standard K-ε model gives about 2% lower growth rate than the empirical data suggests, while algebraic stress model yields 7% lower values.

5.2.3 Remarks:

It can clearly be seen in the above comparisons that the difference between the two turbulence models is small in this type of configuration. However, the algebraic stress model required over 100 iterations more than the standard K-ε one. Therefore for the main computations in the whole room, the standard K-ε model of turbulence was adopted.

The close agreement between the wall-jet empirical data reviewed by Hammond, and his profile analysis, with the predictions of both the elliptic and parabolic codes gives confidence in the formers' use. They were therefore employed to specify the starting profiles in the whole room computations.

5.3 COMPARISONS BETWEEN INTERMEDIATE AND HIGH LEVEL METHODS:

5.3.1 Warm-air Heating of Rooms:

5.3.1.1 Choice of simulated operating conditions:

A corner, ground floor domestic living room, having dimensions 4.75m length, 2.45m height and 2.45m width (i.e. L/H=1.94, W/H=1) was modelled (see Fig. 5.9). These dimensions are similar to those used by Sidaway, Hammond and Probert (ref 9) and Sidaway (ref 75). The operating conditions chosen are similar to those used by Alamdari and Hammond (ref 20) to demonstrate the

capabilities of the ROOM-CHT program , and conform with those recommended in the British design manual for gas-fired warm-air heating (ref 76). The two external walls, incorporating single-glazed windows (1.45m X 1.00m in the far-wall and 1.80m X 1.00m in the side-wall), and the floor were given inside surface temperatures estimated on the basis of the best current British practice U-value (ref 20,77). These temperatures are given in table 5.1 as a function of three representative heat loads. A notional room air temperature of 21 C was adopted, while the surface temperature of the internal walls and ceiling were similarly assumed to remain constant at 20 C over the heating season. The commonest terminal device used in warm-air heating practice is the low-side wall register. This was the device studied initially by Alamdari and Hammond (ref 20), and also modelled in the present work. Calculations have been performed for a linear slot spanning the bottom of the wall, with a height of 0.0175m (Si/H=0.007). This is the same slot height as modelled by Alamdari et al (ref 72), Sidaway et al (ref 9) and Sidaway (ref 75). A two-dimensional or plane wall-jet (ref 33,34,64), forms when warm-air is injected into the room. The size adopted for the supply register gives a supply ventilation rate of 8 air-changed per hour (ACH), based on the size of the room and the face velocity (~ 1.5 m/sec). This is higher than the more realistic domestic ventilation rate of 3.5 ACH adopted by Alamdari and Hammond (ref 20), and is used here only to permit comparison between the two computer codes. The supply conditions for cyclic and modulating control corresponding to the three representative heat loads are given in table 5.2 and 5.3 respectively. The control cycles given for intermittent warm-air heating (see table 5.2) are typical of normal operation (ref 20). In the case of modulating control, the supply air temperature will modulate very slightly, but, in accordance with Pimbert's measurments (ref 8), it was maintained constant with time in the calculations at each successive load.

Table 5.1 ; Demand-dependent Temperatures

Demand	Load	Outside Temp. (C)	Internal Surface Temperature	
			Exterior Walls	Windows
High	Full	-1	16	6
Inter-mediate	65%	7	18	11
Low	30%	15	20	16

Table 5.2 ; Supply Conditions - Cyclic Control

Case No.	Demand	Supply Air Condition	
		Velocity (m/s)	Temperature (C)
1	High 20min on/6min off (76.9% on)	1.954	65
2	Intermediate 6min on/6min off (50.0% on)	1.954	65
3	Low 6min on/20min off (23.1% on)	1.954	65

Table 5.3 ; Supply Conditions - Modulating Control

Case No.	Demand	Supply Air Condition	
		Velocity (m/sec)	Temperature (C)
1	High	1.503	65
2	Intermediate	1.209	55
3	Low	0.933	39

5.3.1.2 Observations:

The predicted flow pattern represented by the resultant velocity vector and the profile for the x-direction component of velocity, and the computed variation in local heat transfer coefficient, hc, for cyclic and modulating controls corresponding to the three representative heat loads are shown in figures 5.10 to 5.16. The arrows in figure 5.10a represent the resultant velocity vector within the room using the non-buoyant version of elliptic code. The length of the arrows is proportional to the local velocity, but is not scaled. The genral shape of the flow pattern (fig 5.10a) and the U-velocity profiles (fig 5.10b) computed using the non-buoyant elliptic code are much the same for all the heating load profiles and control cycles. Only one example of flow pattern is therefore presented here (in Figure 5.10a). It can clearly be seen from figure 5.10a that the jet has spread out from the slot inlet and sequentially flows over the

floor, far-wall and window, ceiling and lastly the near-wall. This is conforms with the assumption made in developing the intermediate-level ROOM-CHT program (ref 20), except that the higher-level elliptic code is able to account for the effect of corners and the flow extract from outlet. The size of the extract slot is not critical in the calculation of the convective heat transfer coefficient (see fig 5.10c), when using the elliptic code, provided that a reasonable number of grid nodes are employed in this region. In the present work the slot outlet's height was specified to be 0.25 m, which gave 3 grid nodes in slot outlet for 21 X 21 grid with expansion of 1.1 in x and y directions. Figures 5.11a, 5.12a & 5.13a show the flow pattern for the three representative heat load under cyclic control. It is clear from these figures that the reverse flow zone near the window is reduced when the load drops from full to low load. However, this effect is not evident in the case of modulating control (see figures 5.14a, 5.15a, 5.16a) , since the supply air velocity in these cases also decreases, and the influence of cold window becomes relatively greater.

The computed heat transfer distribution is plotted on a logarithmic scale in figures (5.11 to 5.16) for clarity. Its variation over the room surfaces is caused by downstream 'decay' of wall-jet velocities and temperatures, and by differences in the surface temperature and a notional room air temperature. The higher-level elliptic code is clearly better able to simulate the complicated wall heat transfer distribution resulting from the complex, jet induced room air flow. Nevertheless, the only appreciable difference between the computations of non-buoyant version of the higher-level, elliptic code and intermediate-level, ROOM-CHT program occurs near the corners and the outlet. Although the buoyant version of the elliptic code predicts an appreciably different local variation in hc, particularly on the floor and the ceiling. But in reality, deviations of this magnitude from the values computed by ROOM-CHT program will not have any significant effect on the predictions of dynamic building thermal models. The dependence of the overall, room averaged convection coefficient, $\bar{h}_{c,r}$ on the heat load for cyclic and modulating controls are indicated in figures 5.17 and 5.18 respectively. In the calculation of this room average convection coefficient, the values given in tables 5.4-5.6 were used. The local values on the side walls were calculated using the improved data correlations for buoyancy-driven convection (ref 70, Appendix A). In cyclic control, the calculated $\bar{h}_{c,r}$ from ROOM-CHT program is slightly lower than that from the non-buoyant version of the elliptic code, and higher for the buoyant version (see figure 5.17). However, under modulating control the ROOM-CHT value is higher than both versions of elliptic code. The percentage difference between the calculated $\bar{h}_{c,r}$ from the elliptic code and that from the ROOM-CHT program for both cyclic and modulating controls is shown in tables 5.7 and 5.8.

Table 5.4: Internal Surface Convection Coefficients -- Full Heat Load

$(W/m^2 K)$

FULL HEAT LOAD	SURFACE ELEMENT					
	Floor	Far-wall & Window	Ceiling	Near-wall	Side-wall & Window	Side-wall
● Cyclic Control						
ROOM-CHT Program	33.102	5.927	16.023	11.253		
Elliptic Code						
non-buoyant	33.515	5.592	17.046	17.341		
buoyant	29.225	3.656	25.570	17.150		
● Modulating Control					2.396	1.367
ROOM-CHT Pogram	27.359	4.956	13.142	9.225		
Elliptic Code						
non-buoyant	27.406	4.315	12.888	13.263		
buoyant	22.170	3.613	25.246	18.139		

Table 5.5: Internal Surface Convection Coefficients - Intermediate Load

($W/m^2 K$)

INTERMEDIATE HEAT LOAD	SURFACE ELEMENT					
	Floor	Far-wall & Window	Ceiling	Near-wall	Side-wall & Window	Side-wall
● Cyclic Control						
ROOM-CHT Program	51.398	8.162	16.023	11.259		
Elliptic Code						
non-buoyant	52.331	8.142	18.996	18.616		
buoyant	46.356	4.654	28.738	20.255		
					2.067	1.367
● Modulating Control						
ROOM-CHT Pogram	28.982	4.850	8.915	6.285		
Elliptic Code						
non-buoyant	28.826	4.095	8.499	8.464		
buoyant	23.536	3.552	17.645	12.733		

Table 5.6: Internal Surface Convection Coefficients - Low Load

($w/m^2 K$)

LOW HEAT LOAD	SURFACE ELEMENT					
	Floor	Far-wall & Window	Ceiling	Near-wall	Side-wall & Window	Side-wall
• Cyclic Control						
ROOM-CHT Program	142.878	18.712	16.023	11.259	1.535	1.367
Elliptic Code non-buoyant	146.409	20.219	20.942	19.896		
buoyant	132.673	9.852	24.596	18.272		
• Modulating Control						
ROOM-CHT Pogram	36.331	5.267	4.385	3.142		
Elliptic Code non-buoyant	35.823	4.247	3.993	3.898		
buoyant	28.982	3.350	8.284	7.414		

Table 5.7 ; Percentage difference in $\bar{h}_{c,r}$ computed by the elliptic code compared to the ROOM-CHT program - Cyclic control

Demand	% Difference in $\bar{h}_{c,r}$	
	non-buoyant	buoyant
Full	12% higher	6% lower
Intermediate	11% higher	8% lower
Low	9% higher	30% lower

Table 5.8 ; Percentage difference in $\bar{h}_{c,r}$ computed by the elliptic code compared to the ROOM-CHT program - Modulating control

Demand	% Difference in $\bar{h}_{c,r}$	
	non-buoyant	buoyant
Full	18% lower	36% lower
Intermediate	4% lower	20% lower
Low	1% lower	22% lower

5.3.2 Air-conditioning of Commercial Offices:

5.3.2.1 Choice of simulated operating conditions:

A room with the same shape and size as that used above for the heating studies, was again employed when examining the convective heat exchange induced by the air conditioning of comercial offices. However, a high-side wall register was adopted for the terminal device, as these are very common in air-conditioning applications. This arrangement is similar to that studied by Sidaway et al (ref 9), Sidaway (ref 75) and Holmes (ref 78). Two different types of structure were chosen for the exterior walls and windows:

- Type 1 : Cavity wall + Single glazed window
- Type 2 : Insulant-filled cavity wall + Double glazed window

The U-values corresponding to the above structures are given in table 5.9, (ref 3):

Table 5.9 ; U-values

Type of structure	U ($W/m^2 K$)
Single glazed window	summer 5.90 winter 6.20
Double glazed window (13mm)	summer 3.20 winter 2.80
Cavity wall	1.53
Cavity wall (insulant-filled)	0.50
Floor (ground floor + carpet)	0.84

The inside surface temperatures were calculated on the basis of a heat balance , assuming that the outside summer air temperature was 30 C and the inside room air temperature was maintained at 23 C. The surface temperatures corresponding to the structures mentioned earlier are given in table 5.10.

Table 5.10 ; Surface temperature in summer condition (C).

Structure	Room elements			
	Ceiling & Near-wall	Far-wall	Window	Floor
Type 1	23.2	24.3	28.0	23.7
Type 2	23.2	23.4	25.7	23.7

In air conditioning applications the temperature difference between the supply air at inlet and the return air at outlet is

typically less than 10 C (ref 26). In the present study, the diffence between supply air and room air temperatures was assumed to be 12 C in summer season with the corresponding supply air velocity assumed to be 1.75 ms^{-1}. This velocity was also used as the reference velocity for determining the ratio of maximum to minimum flowrate in cases where 'dumping' occures according to the air-conditioning guide tables (ref 78).

5.3.2.2 Observations:

The predicted flow pattern illustrated by velocity vector plots, U-velocity profiles, and the computed convective heat transfer distribution hc, for each structure specified in sub-section 5.3.2.1, are plotted in figures 5.19 to 5.20. A comparison of figures 5.19a and 5.20a, shows that the reverse flow zone near the window is due to the influence of the warm window. It disappears when the single glazed window replaces the double glazed window. Good agreement can be observed for the computed convective heat transfer coefficient predicted by all three programs, particularly for the structure type 2 (see figures 5.19c and 5.20c). The agreement between the two versions of the elliptic codes is very close as shown in figure 5.20c simply because the predicted flow fields (see figure 5.20a) are similar, which in turn is like that assumed for ROOM-CHT program (ref 20).

5.4 EXPERIMENTAL VALIDATION:

In this section, the results of the higher-level and intermediate-level computer programs are compared with the measurements of Alamdari et al (ref 72) for a mechanically-ventilated room.

5.4.1 Operating Conditions:

Alamdari et al (ref 72) have carried out a series of tests in a full-scale environmental test room at Cranfield. The effective internal dimensions of the room were , 4.52m length, 2.52m height and 3.58m width. The terminal device was a high-side wall linear slot register with a height of 0.0175m, and the return air was extracted through a rectangular near-floor outlet. The supply air was provided by a variable speed fan in continous operation. The measured temperatures are given in table 5.11 for various ventilation rates ranging from 3.3 to 7.65 ACH.

Table 5.11 ; Measured Surface Temperatures

ACH	Internal Surface Temperature (C)				
	Ceiling	Far-wall	Floor	Near-wall	Side-walls
3.30	22.5	20.4	19.2	22.4	21.4
3.99	20.1	18.8	17.0	20.2	19.4
5.24	23.9	22.5	21.2	24.0	23.1
6.80	23.1	22.1	21.1	23.6	22.8
7.65	20.5	19.7	19.3	20.4	19.9

The supply, return and room air temperatures are given in table 5.12.

Table 5.12 ; Supply and Room Air Temperatures (C)

ACH	Room air	Supply air	Return air
3.30	22.9	26.5	21.3
3.99	20.4	24.2	19.5
5.24	23.9	26.9	23.6
6.80	23.2	25.2	23.1
7.65	20.5	22.2	20.5

5.4.2 Observations:

Comparisons between the results of the ROOM-CHT program and those of the non-buoyant elliptic code for the mechanically-ventilated test room (ref 72) are shown in figures 5.21 to 5.25.

A typical predicted flow field is presented in figures 5.25b and 5.25c for a mechanical ventilation rate of 7.65 ACH. The dependence of the overall, room-averaged convection coefficients on the mechanical-ventilation rate is shown in figure 5.26, where the calculations of the two computer codes are compared with the measurments of Alamdari et al (ref 72). The large uncertainty band on the experimental data, calculated by the method of Kline and McClintock (ref 80) at 20:1 odds, reflects the problem of

measuring the relatively small temperature differences found in 'real' buildings. Calculations of the ROOM-CHT program with and without the buoyancy-driven convection routine are included in figure 5.26. A good agreement between the latter and the elliptic code can be seen in all figures particularly in figures 5.24 and 5.25 for ventilation rates of 6.8 and 7.65 ACH (see tables 5.11 and 5.12).

5.5 COMPARISON BETWEEN TWO- AND THREE-DIMENSIONAL VERSIONS OF THE ROOM-CHT PROGRAM:

The two- and three-dimensional versions of intermediate-level ROOM-CHT program are compared below in order determine whether realistic results could be obtained by assuming a simplified two-dimensional geometry.

5.5.1 Choice of Simulated Operating Conditions:

The geometry and operating conditions for comparison between the 2D and 3D versions of intermediate-level (ROOM-CHT) computer programs are similar to that used when modelling the warm-air heating of rooms (Section 5.3.1), except that, the calculations have been performed for 3.4 air changed per hour and a rectangular grille (200mm X 120mm , 70% free area) at the bottom centre of the interior wall, and also for equivalent linear slot (7.3mm height) spanning the bottom of the wall. These are similar conditions to those reported by Alamdari and Hammond (ref 20).

5.5.2 Observations:

The forced convective surface distribution generated by the three-dimensional wall-jet are shown in figure 5.27. This gives a dramatic illustration of high local coefficients near the supply aperture, which falls off rapidly away from the register. The effect of averaging such local distributions is shown in figures 5.28 and 5.29 for cyclic and modulating controls, corresponding to the three representative heat loads respectively, where the three- dimensional results have been span-averaged, and compared with the equivalent two-dimensional wall-jet. The three-dimensional flow coefficients have a more uniform variation along the floor, and are substantially below the two-dimensional flow values. The disparity in near-aperture heat transfer distribution is, therefore, the major limitation in the using the simpler, two-dimensional geometry.

Only the floor, far-wall/window and ceiling heat transfer distributions are shown in figure 5.27 as the variation over

remaining surfaces is modest, due to the three-dimensional jet having substantially 'diffused'. In the surface plot for far-wall and window (fig 5.27b) the convection coefficient over the latter is seen to be lower than the surrounding wall. This is simply due to the way in which the coefficients are factored (see equation 4.36), and the window heat flux itself, q_w, will be higher than that of the surrounding wall.

The time-dependent behaviour induced by cyclic heating control for each surface , and the three representative heat loads, are shown in figures 5.30 and 5.31 for two and three-dimensional ROOM-CHT program respectively. In the two-dimensional version of the program, an overshoot 'blip' may be seen on the floor trace (see fig 5.30). This blip displays a very short, but large, convective coefficient associated with the impulsive injection of warm-air. It was calculated on the basis of the experimental data on 'starting' wall-jets obained by Sidaway et al (ref 9). Fortunately, the overshoot has a negligible effect on the time-averaged heat transfer as Alamdari and Hammond (ref 20) first observed, owing to its short duration. The remaining surfaces display a simple rectangular-wave cycle with the dashed line representing the time-averaged coefficients.

The time-averaged heat transfer coefficients are presented in figures 5.32 and 5.33 for cyclic and modulating controls respectively, as a function of the fractional heat load. The rise, at low load, in the convection coefficients for floor and far-wall is another manifestation of their factoring discussed above. The corresponding heat fluxes will in practice be lower, as the temperature differences fall with heat load.

5.5.3 Remarks:

The magnitude of the heat transfer coefficients obtained from three-dimensional version of the ROOM-CHT program are higher than those obtained, for instance, using the CIBS Guide (ref 4) with surface-averaged air velocities calculated via the ROOM-CHT program (see table 5.13). In reality, of course, the designer currently has no means of estimating these velocities (ref 20). The results of the present method are nearer to those that would be expected from the field measurements of Yaneske and Forrest (ref 5), and the building thermal model computational study of Waters (ref 6), although the present results are more detailed.

Table 5.13; Internal Surface Convection Coeffients
(hc, W/m^2K)

	Surface element				
	Floor	Far-wall	Window	Ceiling	Near-wall
●Present Method*					
Cyclic Cont.	8.706	4.844	3.825	9.339	5.661
Modulating cont.	9.031	4.700	3.468	9.758	5.774
●CIBS Guide	1.043	2.572	3.695	1.819	1.470

Notes: Full heat load. *Three-dimensional version

The above version of the ROOM-CHT program yields a notional room-averaged convective heat transfer coefficient at full load of 5.905 and 5.150 W/m^2K for cyclic and modulating control respectively. These values are some 40% higher than those originally given by Alamdari and Hammond (ref 20). The main reasons of this increase can be traced to the revised input data, and the adoption of the improved data correlations for buoyancy-driven convection (ref 70, Appendix A). The input data used in the present study differ from that of Alamdari and Hammond (ref 20). In particular, the surface temperature for the internal walls and ceiling were prescribed higher values, and room length was also slightly longer. The present surface internal temperatures were thought to be more realistic, since they ensure that their values never fall below the exterior surfaces temperature no matter what the heat load. In any case, the need to prescribe surface temperatures for example computations such as these is eliminated when the ROOM-CHT program is directly coupled to a building thermal models (see Section 5.7 below) , and these temperature are calculated simultaneously.

The CIBS approach (ref 4), obtained in a manner indicated above, gave a coefficient of only 2.182 W/m^2K. Yaneske and Forrest (ref 5) have shown that the use of a value as low as the CIBS figure would lead to a substantial under-estimate of the system pre-heat time. The convection coefficients obtained for cyclic control (fig 5.32) are different from those for modulating control (fig 5.33), but the difference is not practically significant. In contrast, the simpler two-dimensional version of the program produced coefficients for floor which are substantially higher(~100%) than its three-dimensional counterpart, for the reasons discussed above. Nevertheless, over all other surfaces, agreement between the two versions of ROOM-CHT program was quite reasonable (ref 20).

5.6 PARAMETRIC STUDIES:

The two-dimensional version of the ROOM-CHT program has been used to generate internal convection coefficients, hc, for rooms of various dimensions commonly found in domestic and commercail building spaces in the UK. The sizes of the rooms studied here are similar to those used by Holmes (ref 78,79), to demonstrate the application of ceiling mounted air terminal devices for cooling and heating duties. The room lengths and heights were varied from 3m to 5m and 2.5m to 3.25m respectively. In these parametric studies, the size of the window in the far-wall was assumed to be 40% of the room height. A high-side wall, linear slot register, was modelled, from which the supply air was discharged towards the far-wall/window. This is one of the cases examined by Holmes (ref 78,79), in his applications guide. For a given velocity (say 1.75 m s^{-1}) the height of the slot is made proportional to the size of the room and the number of air changed per hour:

$$S_i = H\ L\ N\ /(3600\ U_e) \qquad (5.2)$$

where

N is the number of air changed per hour,

H is the room height and

L is the room length

The supply air temperature in warm-air systems may then be calculated as follows (ref 79):

$$T_e = \frac{Q}{1000\ \rho\ \dot{V}} + T_r \qquad (5.3)$$

where

Q is the total design heat load ,

$\dot{V}$ is the volume flowrate (=H L W N/3600)

W is the room width

However, for air-conditioning applications the supply temperature is typically 10 C below the room air temperature.

The internal surface temperatures were calculated on the basis of a heat balance, with the U-values given in table 5.9, and the room air temperature of 21/23 C and the outside air temperature of -1/30 C for the winter/summer seasons respectively. The surface temperatures are given in table 5.14 and 5.15 for winter and summer conditions respectively. Different types of exterior wall and window construction were considered for both summer and winter, as indicated in table 5.16. The internal surface convection coefficients, hc, are presented in tables B.1 and B.2 in Appendix B.

The computed heat transfer coefficient, hc, along the near-aperture surface (in this case the ceiling) is substantially higher than those of other surfaces (see tables B.1 & B.2 in Appendix B). These high values of hc on the near-aperture surface are due to the way in which the coefficients are factored, for the reasons discussed in Section 5.5. The persentage difference in hc between the 'standard' case of a single glazed, cavity wall exterior surface (Cases I-III) and Cases IV-VI, VII-IX and X-XII, are indicated in table 5.17, where the effects of having an insulant-filled cavity and double glazing are indicated.

Table 5.14; Internal surface temperatures (C)- Winter season

Case	Surface element			
	Ceiling	Far-wall	Window	Floor
I-III	20.5	17.0	4.6	18.8
IV-VI	20.5	19.7	4.6	18.8
VII-IX	20.5	17.0	13.6	18.8
X-XII	20.5	19.7	13.6	18.8

Table 5.15; Internal surface temperatures (C)- Summer season

Case	Surface element			
	Ceiling	Far-wall	Window	Floor
I-III	23.2	24.3	28.0	23.7
IV-VI	23.2	23.4	28.0	23.7
VII-IX	23.2	24.3	25.7	23.7
X-XII	23.2	23.4	25.7	23.7

Table 5.16: Type of structure

Case	Exterior surface	
	Wall	Window
I-III	Cavity wall	Single glazed
IV-VI	Insulant-filled Cavity	Single glazed
VII-IX	Cavity wall	Double glazed
X-XII	Insulant-filled Cavity	Double glazed

Table 5.17 ; Percentage difference in $\bar{h}c$, computed for Cases I-III compared to Cases IV-XII.

Condition	% Difference in hc				
	Ceiling	Far-wall	Floor	Near-wall	Window
● Winter					
Case IV-VI	13% lower	61% higher	6% lower	10% lower	Nil
Case VII-IX	28% lower	11% lower	14% lower	23% lower	21% lower
Case X-XII	41% lower	27% lower	20% lower	33% lower	21% lower
● Summer					
Case IV-VI	Nil	133% higher	Nil	Nil	Nil
Case VII-IX	Nil	Nil	Nil	Nil	24% higher
Case X-XII	Nil	133% higher	Nil	Nil	24% higher

5.7 SENSITIVITY ANALYSIS ON A BUILDING THERMAL MODEL:

In the context of the work of Alamdari, Hammond and Melo (ref 81) it was felt desirable to quantify the influence on internal and external convection coeffients by using the ROOM-CHT

and WIND-CHT (another intermediate-level computer code for calculation of external convective heat transfer ,ref 81,82) programs respectively on the predicted heating load in a typical domestic dwelling. A hypothetical, detached house was adopted, broadly based on the multi-layered construction of the 3-bedroomed, terraced houses in Livingston, Scotland studied by Clarke and Forrest (ref 83). In addition, a ground floor insulation slab was included (ref 81) to reflect a 'heavy' (or thermally 'massive') structure, while the height of each room in the two-storey dwelling were assumed to be 2.8 m. The cavity air gaps and the floor slab were subsequently removed in order to loosely simulate the effect of a 'light' structure.

A widely used dynamic model, the NBSLD 'response factor' program developed at the US National Bureau of Standard (ref 84), was used to simulate the performance of the above house. The overall response factors contain terms which are sensitive to surface convection coefficients. A large number of discrete hourly intervals are needed to represent such lumped parameters in the case of a building with thermally heavy weight construction, and vice versa (ref 2,81).

In order to simulate the winter heating load Alamdari et al (ref 81), have adopted the meteorological data for Kew, London (51°28'N, 0°19'W) on the 21st December 1965 . This constitutes part of the data base for the CIBS 'Example Weather Year' (ref 85). An intermittent heating cycle typical of UK practice was assumed (see figure 5.34), with full-load warm-air conditions, similar to those used by Alamdari and Hammond (ref 20). The house has been treated by C. Melo (private communication, 1984) as a five-zone system, with identical thermal conditions in zones adjacent to that being simulated. The ROOM-CHT program was incorporated as an additional subroutine into the NBSLD code, in order to demonstrate the feasibility of direct coupling. The heating load profiles computed by the standard version of the NBSLD program for a city centre location, together with that using the ROOM-CHT program are shown in figure 5.34. The daily energy consumption predicted by the standard program for the heavyweight (lightweight) structure was 382 (432) MJ, and this increased by 7 (11) per cent when the ROOM-CHT code was employed. These computations required corresponding central processor times of 59 and 177 seconds on a Cranfield DEC VAX 11/780 computer, when all five zones were treated sequentially. The heating load profiles shown in this figure display a considerable sensitivity to the internal convection coefficients. The standard version of the NBSLD program employs buoyancy-driven convection coefficients for internal surfaces, and this accounts for the differences in the computed heating load profiles. However, the extend of the impact of the convection model is likely to depend on the conditions prevailing within the particular building being simulated. Nevertheless, the load profile shown in figure 5.34 illustrates the accuracy constraints that are imposed on this building thermal model, and more complex ones, by input internal convection data (ref 81).

CHAPTER 6
CONCLUSIONS AND RECOMMENDATIONS

6.1 CONCLUDING REMARKS:

In an attempt to satisfy the requirements of the new generation building thermal models, a 'hierarchy' of interacting and interdependent approaches have been developed for calculating internal surface convective heat transfer coefficients within mechanically-ventilated rooms. These range from 'lower-level' approaches, such as improved data correlations for buoyancy-driven convection (Appendix A, ref 70) and wall-jet profile analysis (ref 33,34), to the development of a 'high-level' flow model based on finite-difference analogues to the governing 'elliptic' equations for the complex, jet-induced room airflow (Part II): the elliptic code. Both the lower and higher-level models have been used to develop and verify an 'intermediate-level' computer code (Part III, ref 20,81): the ROOM-CHT program.

In the high-level flow model, 'upwind' finite-difference approximation to the governing partial-differential equations are formulated in terms of 'primitive' pressure-velocity variables. Closure of these time-averaged, elliptic equations is obtaind through an isotripic 'eddy' viscosity, or turbulent exchanged coefficient for momentum, calculated via transport equations for both the turbulence kinetic energy and its dissipation rate. The transport of heat is modelled using the effective Prandtl number approach, while 'wall functions' are employed to bridge the steep property gradients in near-wall regions. The code of Pun and Spalding (ref 31) was adopted to solve the difference equations for a predetermined size, staggered grid in an iterative 'line-by-line' manner using the SIMPLE algorithm of Patankar and Spalding (ref 29).

The ROOM-CHT computer code, employs 'informed' estimates of the flow and thermal field based on the known mean-flow properties of wall-jets (ref 33,34,64). The corresponding heat transfer distribution across the room surfaces is calculated using the wall-jet profile analysis, or the improved data correlations for buoyancy-driven convection as appropriate. The program then performs multiple (space and time) averaging by successive numerical integrations as required to meet the needs of building thermal models.

The elliptic code is able to simulate more accurately the complicated wall heat distribution resulting from the complex, jet induced room air-flow. However, this code is rather user unfriendly, since it requires specialist computational thermo-fluids expertise, skill and experience on the part of user. The computational resources for this code are also very high compared with that for the ROOM-CHT program. Alamdari et al

(ref 81) have argued therefore that, the ROOM-CHT program appears to offer the best prospect for meeting the requirements of the new generation of dynamic building thermal models in terms of accuracy, economy and user friendliness. The results of the computations and comparisons of the surface-averaged convection coefficients calculated from ROOM-CHT program, have been shown to be in generally good agreement with those obtained from the elliptic code, and with the limited experimental data. They are also much more realistic than the data currently available to the designer in design guides (see Chapter 5). Nevertheless, ROOM-CHT program for relies its success on the elliptic code which, together with experimental data, provides the basis for its verification. The ROOM-CHT program may therefore be regarded (ref 81) as a means of transfering data in a form appropriate to the needs of building thermal modellers and energy-conscious designers.

6.2 RECOMMENDATIONS FOR FURTHER RESEARCH:

6.2.1 Higher-level Elliptic Code:

The following suggestions for further research should lead to improvements in the accuracy with which the elliptic code is able to predict the flow pattern and surface convective heat transfer within mechanically-ventilated enclosures:

a) The replacement of the upwind finite-difference scheme by Patankar´s power-law scheme (ref 55), which may improve slightly the present results. Although the upwind scheme gives a physically realistic solution, the results of the power-law scheme are much closer to an exact solution, at least for one-dimensional case (see Patankar, ref 55).

b) The rate of te convergence might be improved by a change to the SIMPLE algorithm. According to Patankar (ref 55,61), the approximation made in the derivation of P´ (see Section 3.2.7), by omission of the terms $\sum a U'$ and $\sum a V'$ from equations 3.40, yields to a rather exaggorated pressure correction. Although this pressure-correction is fairly good at correcting the velocities, it is poor at correcting the pressure. Thus, if the pressure-correction is used only to correct the velocities, and some other means be found to obtain an improved pressure field, this might increase the rate of convergence. Patankar (ref 55,61) has proposed a more efficient algorithm, which he terms ´SIMPLER´, for this purpose. In this algorithm, the pressure field is obtained from a FDE similar to that for pressure-correction FDE (Eq. 3.45), except that the starred velocities (U^* & V^*) in the source term, b, are replaced by the so-called pseudo-velocity ($\hat{U}$ & $\hat{V}$), which are defined as:

$$\hat{U}_P = \frac{\left\{\sum_{E,\,W,\,N,\,S} a\,U\right\} + b}{a_P}$$

$$\hat{V}_P = \frac{\left\{\sum_{E,\,W,\,N,\,S} a\,V\right\} + b}{a_P}$$

In this way no approximation is made in the derivation of the pressure equation. Thus, if a correct velocity field is used to calculate the pseudo-velocities, the pressure FDE would at once give the correct pressure.

c) In the case of the buoyant version of the elliptic code, an attempt must be made to increase the rate of convergence, since it was found to be very slow in the present computations. Some improvement might be provided by applying an inertial relaxation method similar to that of Ideriah (ref 52,86). The author attempted to apply Ideriah's relaxation method at an early stage in the development of the buoyancy version of the elliptic code. However, this wasn't very successful at the time, although some variation on this approach might prove more fruitful.

d) Wall-jet profile analysis can be used to specify the starting profiles (see Section 2.6.1) for non-buoyant and/or very weakly buoyant flows with good accuracy. However, this approach is not very suitable for strongly buoyant flows. Improvements in this area are most desirable, since it will not only yield greater accuracy, but might also improve the rate of convergence.

e) The present work was initially based on the belief that a simple, two-dimensional room geometry would probably be adequate for building thermal modelling purposes. However, experience with the ROOM-CHT program, which has been developed with two- and three-dimensional versions, has shown that the development of a three-dimensional version of the elliptic code is desirable. As discussed in Chapter 5, the two-dimensional model produces surface heat transfer coeffients which are substantially too high (~100%) over the surface adjacent to supply aperture (see figures 5.28 & 5.29),although they are quite reasonable over the other surfaces. Unfortunately, the value calculated for the near-supply surfaces has a dominant influence on the overall convective exchange in the room. The Cranfield group under G. P. Hammond are currently engaged in determining the convective heat transfer coefficient over the internal surfaces of three-dimensional, mechanically-ventilated enclosures. Thus the surface coefficients will be obtained by using a high-level, computer-based flow model, together with scale-model experimental measurements, in order to extend and further validate the ROOM-CHT program. The high-level flow model will also facilitate a better understanding of the physics of these complex flows, and permit the calculation of the associated thermal comfort

criteria.

6.2.2 Intermediate-level Code:

The main components of the ROOM-CHT program, wall-jet profile analysis (ref 34) and buoyancy-driven convection correlations (Appendix A), have themselves been fully verified by comparison with experiment. It was implicit in the development of the ROOM-CHT program that multi-averaged surface coefficients would be insensitive to such effects. Nevertheless, this needs to be directly verified, and empirical corrections incorporated into the program if necessary. Hammond's group at Cranfield have established an experimental research programme aimed at obtaining the necessary data. The Cranfield group also plan to extend the ROOM-CHT program to permit the calculation of radiative exchange within enclosures. This would enable it to be used to investigate the relative importance of convective and radiative exchange at high ventilation rates. It is hoped that the extended ROOM-CHT program will then be used as the primary 'vehicle' for generating design data for a wider range of enclosures and air distribution systems. In this way it would seen feasible to meet the requirements of building thermal modellers for internal surfaces heat transfer coefficients over foreseeable future.

REFERENCES

1. CLARKE J A
Computer applications in the design of energy-conscious buildings, Computer-aided Design, Vol 14, 1982, pp 3-9

2. DAY B
Computation of the dynamic thermal performance of buildings, Computer-aided Design, vol 14, 1982, pp 49-54

3. ASHRAE
Handbook of Fundamentals, New York, 1981

4. CIBS GUIDE, C3
Heat transfer, London, 1976

5. YANESKE P P AND FORREST I D
The thermal response of rooms with intermittent, forced convective heating, Building Services Engineer, Vol 46, No 4, 1978, pp 13-17

6. WATERS J R
The experimental verification of a computerised thermal model for buildings, BSER&T, Vol 1, No 2, 1980, pp 76-82

7. IRVING S J
Energy program validation: conclusions of IEA Annex 1, Computer-aided Design, Vol 14, No 1, 1982, pp 33-38

8. PIMBERT S L
Controlling warm air: the thermal environment produced by warm air units fitted with modulating and on/off controls, Gas Marketing, Vol 22, No 8, 1978, pp 6-8

9. SIDAWAY C S , HAMMOND G P AND PROBERT S D
Intermittent air injection into rooms - the isothermal ceiling jet, BSER&T, Vol 1, No 2, 1980, pp 63-70

10. McNALL P E AND NEVINS R G
A critique of ASHRAE comfort standard 55-56, ASHRAE journal, June 1968, pp 99-102

11. McINTYRE D A
A guide to thermal comfort, Appl. Ergonomics, Vol 4, 1973, pp 66-72

12. DIN 1946
Ventilation system (VDI Ventilation Rules), June 1962

13. STRAUB H E
Principles of room air distribution, Heat. Pip. & Air-Condit. ,Vol 41, 1969, pp 122-128

14. RYDBERG J AND NORBACK P
Air distribution and draft, ASHVE Trans., vol 55, 1949, pp 225-240

15. HOUGHTEN F C , GUTBERLET C AND WITKOWSKI E
Draft temperature and velocities in relation to skin temperature and feeling of warmth, ASHVE Trans., Vol 44, 1938, pp 289-308

16. CROOME D J AND ROBERTS B M
Air conditioning and ventilation of buildings, Pergamon Press, Oxford, New York, Toronto, Sydney, Vol 10, 1975

17. STOECKER W F AND JONES J W
Refrigeration and air conditioning, McGraw Hill, Second edition, 1982

18. ETHERIDGE D.W. AND NEVRALA D J
Air infiltration and our thermal environment. Building Services and Environmental Engineer, Vol 1, Pt 7, 1979, pp 10-13

19. HAMMOND G P
'Appropriate' calculation methods for thermo-fluid problems related to buildings, SERC Seminar ; "What Next in Energy in Building Research?", Rodney Lodge, Bristol University, 19-21 September 1982

20. ALAMDARI F AND HAMMOND G P
Time-dependent convective heat transfer in warm-air heated rooms, Proc. 3rd Int. Symp. Energy Conservation in the Built Environment, Vol. 4, pp 209-220,(CIB/An Foras Forbartha, Dublin, 1982)

21. NIELSEN P V
Flow in air-conditioned rooms. English translation of PhD thesis of Technical University Of Denmark (1974), Danfoss A/S, Denmark 1976

22. GOSMAN A D, PUN W M, RUNCHAL A K, SPALDING D B AND WOLFSHTEIN M
Heat and mass transfer in recirculating flows,

Academic Press, London and New York, 1969

23. LAUNDER B E AND SPALDIND D B
Mathematical models of turbulence, Academic Press, London and New York, 1972

24. LAUNDER B E AND SPALDING D B
The numerical computation of turbulent flows, Computer Methods in Applied Mechanics and Engineering , Vol 3, 1974, pp 269-289

25. NIELSEN P V, RESTIVO A AND WHITELAW J H
The velocity characteristics of ventilated rooms, ASME Journal of Fluids Engineering, vol 100,1978, pp 291-298

26. NIELSEN P V, RESTIVO A AND WHITELAW J H
Buoyancy affected flows in ventilated rooms, Numerical Heat Transfer, vol 2, 1979, pp 115-127

27. GOSMAN A D , NIELSEN P V, RESTIVO A AND WHITELAW J H
The flow properties of rooms with small ventilation openings, ASME Journal of Fluids Engineering, Vol 102, 1980, pp 316-323

28. HJERTAGER B H AND MAGNUSSEN B F
Numerical prediction of three-dimensional turbulent buoyant flow in a ventilated room, Heat Transfer and Buoyant Convection, Hemisphere, Washington, Vol 2, 1976, pp 429-441

29. PATANKAR S V AND SPALDING D B
A calculation procedure for heat and mass and momentum transfer in three-dimensional parabolic flows, International Journal of Heat and Mass Tranfer, Vol 15, 1972, pp 1787-1806

30. SAKAMOTO Y AND MATSUO Y
Numerical prediction of three-dimensional flow in a ventilated room using turbulence models, Appl. Math. Modelling, Vol 4, 1980, pp 67-72

31. PUN W M AND SPALDING D B
A general computer program for two-dimensional elliptic flows, Imperial College, Mech. Eng. Dept. , Report HTS/76/2 (Amended 1977)

32. PATANKAR S V
A numerical prediction of three-dimensional flows. Studies in Convection, Volume 1, Academic Press, London, 1975, pp 1-78

33. HAMMOND G P
Complete velocity profile and 'optimum' skin friction formulas for the plane wall-jet, ASME Journal of Fluid Engineering, Vol 104, 1982, pp 59-66

34. HAMMOND G P
Profile analysis of heat/mass across the plane wall-jet, Heat Transfer 1982 :Proc. 7th Int. Heat Transfer Conf. Minich, Vol 3, 1982, pp 349-355, Hemisphere, Washington

35. MARKATOS N C AND COX G
Hydrodynamics and heat transfer in enclosures containing a fire source, PCH PhysicoChemical Hydrodynamics , to be published Jan. 1984

36. KUMAR S AND COX G
The application of a numerical field model of smoke movement to the physical scaling of compartment fires, Numerical Methods in Thermal Problems, Proceeding of the Third International Conference, Seattle, USA, 2nd-5th Aug. 1983, Pineridge press, Swansea, UK, pp 837-848

37. BIRD R B, STREWART W E AND LIGHT FOOT E N
Transport phenomena, John Wiley, New York, 1960

38. CEBECI T AND BRADSHAW P
Momentum transfer in boundary layers. Hemisphere, Washington 1977

39. BATCHELOR G K
An introduction to fluid dynamics. Cambridge University Press , 1970

40. BRADSHAW P
An introducation to turbulence and it's measurement. Pergamon, Oxford, 1971

41. REYNOLDS W C
Computation of turbulent flows. Annual Review of Fluid Mechanics, Vol 8, 1976, pp 183-208

42. HINZE J O
Turbulence, McGraw Hill, New York, 1959

43. LAUNDER B E
On the effects of a gravitational fields on the turbulent transport of heat and momentum, Journal Of Fluid Mechanics. Vol 67, Pt 3, 1975, pp 569-581

44. LAUNDER BE , REECE G J AND RODI W
Progress in the development of Renolds-stress turbulence closure, Journal Of Fluid Mechanics. Vol 68, pt 3, 1975, pp 537-566

45. RODI W
Examples of turbulence models for incompressible flows, AIAA journal, Vol 20, No. 7, 1982, pp 872-879

46. BRADSHAW P , FERRISS D H AND ATWELL N P
Calculation of boundary-layer development using the turbulent energy equation, Journal Of Fluid Mechanics, Vol 28, 1967, pp 593-616

47. GIBSON M M AND LAUNDER B E
Ground effects on pressure fluctuations in the atmospheric boundary layers, Journal of Fluid Mechanics. Vol 86, pt 3, 1978, pp 491-511

48. LUMLEY J L AND KHAJH-NOURI B
Computation of turbulent transport, Advance in Geophysics, Vol A18, 1974, pp 169-192

49. LEWELLEN W S , TESKE M AND DONALDSON C duP
Variable density flows computed by second-order closure description of turbulence, AIAA Journal, Vol 14, 1976, pp 382-397

50. POPE S B AND WHITELAW J H
The calculation of near-wake flows, Journal of Fluid Mechanics, Vol 73, pt 1, 1976, pp 9-32

51. JATALILLEKE C L V
The influence of Prandtl number and surface roughness on the resistance of the laminar sub-layer to momentum and heat transfer, Progress in Heat & Mass Transfer, Vol I, 1969, pp 193-329

52. IDERIAH F J K
Prediction of turbulent cavity flow driven by buoyancy and shear, Journal Mechanical Engineering Science, Vol 22, No 6, 1980, pp 287-295

53. RODI W
Influence of buoyancy and rotation on equations for turbulent length scale, 2nd Symposium on Turbulent Shear Flows, Imperial College, London, July 2-4, 1979

54. MARKATOS N C, MALIN M R AND COX G
Mathematical modelling of buoyancy-induced smoke flow in enclosures, Int. J. Heat Mass Transfer, Vol 25, No 1, 1982, pp 63-75

55. PATANKAR S V
Numerical heat transfer and fluid flow, Hemisphere, Washington, 1980

56. FINLAYSON B A
The method of weighted residual and variational principles, Academic Press, New York, 1972

57. HARLOW F H AND WELCH J E
Numerical calculation of time-dependent viscous incompressible flow of fluid with free surface, Physics of Fluids, Vol 8, 1965, pp 2182-2189

58. RUNCHAL A K
Convergence and accuracy of the three finite-difference schemes for a two-dimensional conduction and convection problem, International Journal for Numerical Methods in Engineering, Vol 4, 1972, pp 541-550

59. SPALDING D B
A novel finite-difference formulation for differential expressions involving both first and second derivatives, International Journal for Numerical Method in Engineering, Vol 4, 1972, pp 551-559

60. RUNCHAL A K AND WOLFSHTEIN M
Numerical integration procedure for steady state Navier-Stokes equations, Journal of Mechanical Engineering Sci., Vol 11, 1969, p 445-453

61. PATANKAR S V
A calculation procedure for two-dimensional elliptic situation. Numerical Heat Transfer, Vol 4, 1981, pp 409-425

62. AMES W F
Nonlinear partial differential equations in engineering. Academic Press, New York and London, 1965

63. SCARBOROUGH J B
Numerical mathematical analysis, 4th ed., The John Hopkins Press, Baltimore, 1958

64. RAJARATNAM N
Turbulent Jets, Elsevier Scientific Publishing Company, Amsterdam, Oxford, New York, 1976

65. COLES D
The law of the wake in the turbulent boundary layer, Journal of Fluid Mechanics, Vol 1, 1956, pp. 191-226

66. HAMMOND G P
Similarity profile analysis of the self-preserving plane wall-jet, Cranfield Institute of Technology, unpublished report, 1981

67. BREDERODE V AND BRADSHAW P
A note on the empirical constants appearing in the logarithmic law for turbulent wall flows, Imperial College , London unversity, Aero Rept 74-03, 1974

68. KADER B A AND YAGLOM A M
Heat and mass transfer laws for fully turbulent wall flows, Int. J. Heat Mass Transfer, Vol 15, 1972, pp 2329-2351

69. FLORA J J AND GOLDSCHMIDT
Virtual origins of a free plane turbulent jet, AIAA Journal, Vol 7, No 12, 1969, pp 2344,2346

70. ALAMDARI F AND HAMMOND G P
Improved data correlations for buoyancy-driven convection in rooms, BSER&T, Vol 4, No 3, 1983, pp 106-112

71. STARK P A
Introduction to numerical methods, London, 1970

72. ALAMDARI F , CHAN J K C AND HAMMOND G P
An intermediate-level model of heat transfer for mechanically-ventilated enclosures with 'linear' supply apertures, Cranfield Institue of Technology Repot SME/J/84/04, in preparation, 1984

73. LJUBOJA M AND RODI W
Calculation of turbulent wall-jets with an algebric Reynolds stress model, Journal of Fluid Engineering, Vol 102, 1980, pp 350-356

74. LJUBOJA M AND RODI W
Prediction of horizontal and vertical turbulent buoyant wall-jets, Journal of Heat

Transfer, Vol 103, 1981, pp 343-349

75. SIDAWAY C S
Intermittent warm-air heating of rooms, PhD thesis, School of Mech. Eng. Cranfield Institute of Technology, 1980

76. WARM AIR GROUP -SBGI
Gas Fired Warm Air Heating : British System Design Manual, London, 1976

77. THE ELECTRICITY COUNCIL
The Medallion Award Specification, EC 4155, 1981

78. HOLMES M J
Designing variable volume systems, for room air-movement, HVRA Application Guide 1/74 , 1974

79. HOLMES M J
Room air-movement with ceiling mounted diffusers: The influence of cold windows, BSRIA Application Guide 2/75

80. KLINE S J AND McCLINTOCK F A
Describing uncertainties in single-sample experiments, Mechanical Engineering, January 1953, pp 3-8

81. ALAMDARI F , HAMMOND G P AND MELO C
Appropriate calculation methods for convective heat transfer from building surfaces, First UK National Heat Transfer Conference, Leeds, 3-5 July 1984, I. Chem. E. Symp. Series No. 86, Paper No. MI08

82. GRANDRILLE T , HAMMOND G P AND MELO C
An intermediate-level of external convective hea transfer from buildings, Cranfield Institute of Technology Report SME/J/84/03, in preparation 1984

83. CLARKE J A AND FORREST I
Validation of the ESP thermal simulation program, Univesity of Strathclyde ABACUS Occasional Paper NO. 61, 1978

84. KUSUDA T
NBSLD: the computer program for heating and cooling loads in buildings, US National Bureau of Standards Report, 1981

85. HOLMES M J AND HITCHIN E R
An example year for the calculation of energy demand in buildings, Building Service Engineer, Vol 45, 1978, pp 186-189

86. IDERIAH F J K
An inertial relaxation method of curing numerical instability in prediction of flows influenced by servere body forces, Journal Mechanical Engineering Science, Vol 22, No 3, 1980, pp 153-156

87. O'CALLAGHAN P W
Design and management for energy conservation, Pergamon Press, Oxford New York , 1981

APPENDIX A

IMPROVED DATA CORRELATION FOR BUOYANCY-DRIVEN CONVECTION IN ROOMS

Summary Improved data correlations have been derived for buoyancy-driven convective heat transfer from the internal surfaces of naturally-ventilated buildings. They cover the full range of laminar, transitional and turbulent airflows, and are based on the mathematical model of Churchill & Usagi (1972). The new correlating equations are presented in a convenient form for incorporating into modern computer programs which simulate the dynamic thermal performance of buildings. They compare favourably with the available exerimental data for isolated surfaces, and are shown to be an improvement on the 'standard' correlations recommended in the CIBS Guide. The factors which affect the accuracy of such data correlations, when used for the energy-conscious design of 'real' buildings, are briefly discussed.

Improved data correlations for buoyancy-driven convection in rooms

F. ALAMDARI, MSc and G. P. HAMMOND, MSc, CEng, MIMechE, MInstR

List of symbols

A, B, C	empirical coefficients in correlating Equations (3) and (5)	
a, b	empirical coefficients in correlating Equation (7)	
A_s	area of heat transfer surface	m^2
C_p	fluid specific heat at constant pressure	J/kgK
g	gravitational acceleration	m/s^2
Gr	Grashof number ($\equiv \rho^2 g \beta \Delta T L^3/\mu^2$)	
h_c	surface-averaged convective heat transfer coefficient	$W/m^2 K$
k_f	fluid thermal conductivity	W/mK
L	characteristic length of heat transfer surface	m
m,n,p,q	exponent in correlating Equations (3), (5) & (7)	
Nu	Nusselt number ($\equiv h_c L/k_f$)	
Pr	Prandtl number ($\equiv C_p \mu/k_f$)	
P_s	perimeter of heat transfer surface	m
q_c	convective heat flux	W/m^2
Ra	Rayleigh number ($\equiv$ Gr Pr)	
T_a	temperature of the quiescent (ambient) air	K
T_f	'film temperature'	K
T_w	'wall' (surface) temperature	K
β	coefficient of cubic expansion ($= T_f^{-1}$ for gases)	K^{-1}
ΔT	($\equiv T_w - T_a$)	K
μ	fluid dynamic viscosity	kg/m s
ρ	fluid density	kg/m^3

1 Introduction

In the last decade it has become increasingly recognised that in order to develop realistic methods for the energy-conscious design of buildings it is necessary to model the dynamic thermal response of the system. These dynamic models normally require computational solution (as noted in the reviews by Clarke[1] and Day[2]; the latter summarising the efforts of the UK Science and Engineering Research Council to stimulate research in this area), in contrast to the manual-calculation methods used with the traditional *steady-state* procedures. Unfortunately, the accuracy of the new generation of building thermal models is presently limited by uncertainties in the input data, particularly for air infiltration and convective heat transfer rates (see, for example, the results of the International Energy Agency (IEA) study reported by Irving[3]). The aim of the present study was therefore to develop improved methods for calculating buoyancy-driven convective heat transfer within naturally-ventilated buildings.

The convective heat flux from a surface may be written, from 'Newton's Law of Cooling', in the form:

$$q_c = h_c \Delta T \qquad (1)$$

The surface-averaged convective heat transfer coefficient, h_c, may then be combined with the corresponding radiative coefficient[4] to yield an internal 'surface resistance' for the building elements. In the case of buoyancy-driven (sometimes, but misleadingly, termed 'free' or 'natural') convection, h_c is itself a function of the temperature difference, ΔT, as well as the length of the surface and the physical properties of the convected fluid. Dimensional analysis may be employed to correlate experimental data reflecting this dependence in terms of dimensionless parameters (defined above in the List of Symbols):

$$Nu = Nu\ (Gr, Pr) \qquad (2)$$

The Nusselt number relation, for fluids with moderate Prandtl numbers ($0.7 < Pr < 70$), may be closely represented by a 'power-law' of the form:

$$Nu = C\ Ra^n \qquad (3)$$

The exponent, n, is found to be about 1/4 for low Rayleigh numbers typically in the range $10^4 < Ra < 10^6$, which correspond to laminar flow induced by short surface lengths and/or small temperature differences. Conversely, for $Ra > 10^{10}$ transition to turbulent flow occurs, and n asymptotes to a value of about 1/3 (except for stable-stratification near horizontal surfaces where diffusion on a molecular scale persists up to quite high

Mr. Alamdari is a Research Officer and Mr. Hammond a Lecturer with the Applied Energy Group, School of Mechanical Engineering, Cranfield Institute of Technology, Bedford.

The paper was first received on 10 March 1983, and in revised form on 11 July 1983.

Rayleigh numbers, and n has a value of about 1/5; see Section 2.3 below). Thus, conventional practice is to calculate h_c via data correlations of the form of Equation (3), using an exponent of 1/4 for Rayleigh numbers less than about 10^8 and 1/3 otherwise. This 'two-part' correlaion, implying an abrupt transition, has been adopted in the CIBS Guide[4]. It was also used by the present authors[5] to model off-cycle, buoyancy-driven heat transfer in their 'intermediate-level' calculation procedure for warm-air heated rooms. When used with dynamic thermal models the two-part correlation Equation (3) is usually close to its intersection point, due to the relatively large size of typical building elements: ceilings, floors, walls and windows. This point corresponds to the location of maximum error in the calculated heat transfer coefficient, and the sudden change in the exponent there may also give rise to numerical instability in building thermal models.* In Section 2 below, a more elaborate set of correlating equations is developed that cover the full range of laminar, transitional and turbulent flows, and avoid the disadvantages of the simpler, 'two part model'. These improved data correlations are presented in a dimensional form that permit the direct calculation of convection coefficients appropriate to buoyancy-induced air movement at conditions typical of those found in the built environment.

2 Development and validation of the improved correlating equations

The problem of obtaining a correlating equation which will fit both laminar and turbulent buoyancy-driven convection is one of a class of problems involving transfer processes in which solutions are known for asymptotically large and small values of an independent variable, namely:

$$y \to A\,x^p \text{ as } x \to 0$$
$$y \to B\,x^q \text{ as } x \to \infty$$

where x and y are the independent and dependent variables respectively. Fortunately, Churchill & Usagi[6] have developed a general solution for this class of problems in the form:

$$y = \left| (Ax^p)^m + (Bx^q)^m \right|^{1/m} \quad (4)$$

where $m > 0$ if $p < q$, and vice versa. They originally applied this formulation to laminar buoyancy-driven convection with $x = Pr$, and to laminar, mixed (combined buoyancy-driven and forced) convection. In the present case of laminar/turbulent buoyancy-driven convection a solution may be obtained in the form of Equation (4) as:

$$Nu = \left| (A\,Ra^p)^m + (B\,Ra^q)^m \right|^{1/m} \quad (5)$$

*J. A. Clarke, private communication, 1981.

An examination of experimental data for vertical and horizontal surfaces (see Sections 2.1 to 2.2 below) suggests an optimal value of the exponent m of 6. The empirical coefficients in Equation (5) were chosen as mean values from the range employed in the 'standard' data correlations for the asymptotic states published in the literature, and these are summarised in Table 1. This equation, together with the latter coefficients, is valid over an extensive range ($10^4 < Ra < 10^{12}$) which encompasses all the conditions of practical significance for the built environment. The physical properties of the convected fluid, air in the case of buildings, may be obtained from standard tables such as those given by Mayhew & Rogers[7]. These properties are primarily dependent on temperature, and their values at the so-called 'film temperature', namely:

$$T_f = (T_a + T_w)/2 \quad (6)$$

are normally employed.

In the context of the built environment the physical properties of air do not vary greatly. It is therefore possible, and obviously convenient, to simplify the 'exact' correlating Equation (5) so that the convection coefficient is recovered in a dimensional form. Adopting a median film temperature applicable to naturally-ventilated buildings (say 27°C) this yields:

$$h_c = \left[\left\{ a \left(\frac{\Delta T}{L} \right)^p \right\}^m + \left\{ b\,(\Delta T)^n \right\}^m \right]^{1/m} \quad (7)$$

where the empirical coefficients, a and b, for both vertical and horizontal surfaces are again given in Table 1. The temperature variations experienced in buildings imply that the convection coefficients obtained from Equations (5) and (7) are unlikely to differ by more than ± 4 per cent. This is small in comparison with the experimental uncertainty in buoyancy-driven convection data which is typically ± 20 per cent.

The experimental data on buoyancy-driven convection reported in the literature were often obtained using fluids, surface lengths and temperature differences which are unlike those found in buildings. It is therefore desirable to check the empirical coefficients in correlating equations from data more appropriate to this case. Thus, the present data correlations, Equations (5) and (7), were validated by comparison with heat transfer measurements from relatively large area surfaces, mainly in air. Only when data for air were found to be too sparse, were selected measurements for water employed. Details of the comparisons for vertical and horizontal surfaces are discussed in Sections 2.1 to 2.3 below. An idealised representation of the resulting buoyancy-induced flow patterns near isolated surfaces are shown in Fig. 1. These diagrams are used below to distinguish the physical nature of each flow pattern. The effect of the room element and flow interactions present in 'real' buildings are briefly discussed in Section 3.

Table 1. Empirical coefficients in the data correlations for Nu and h_c (Equations (5) and (7)).

Flow and surface orientation	A	B	a	b	p	q	m
Buoyancy-driven convection over vertical surfaces	0.58	0.11	1.50	1.23	1/4	1/3	6
Buoyancy-driven flow on horizontal surfaces	0.54	0.14	1.40	1.63	1/4	1/3	6

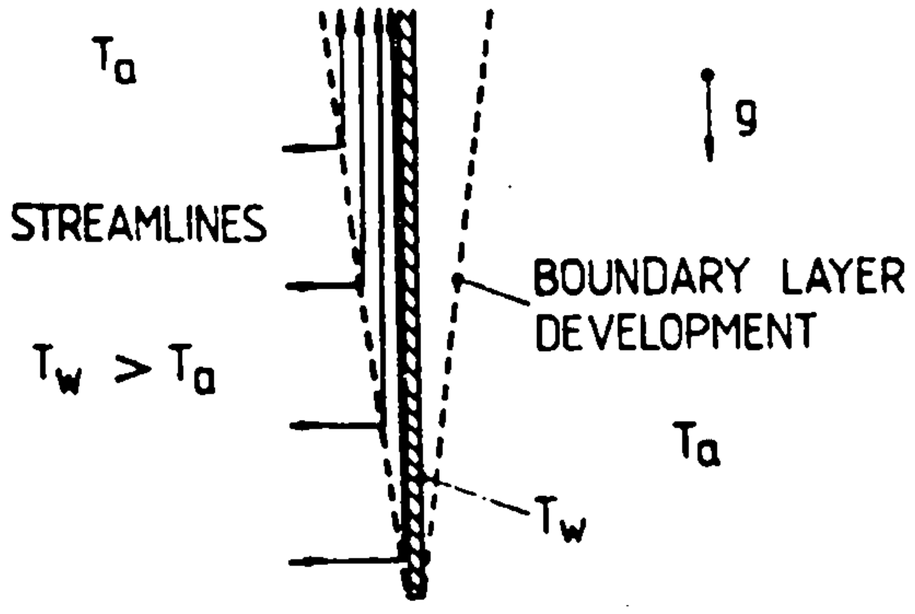

(a) MOTION INDUCED BY A VERTICAL HEATED PLATE

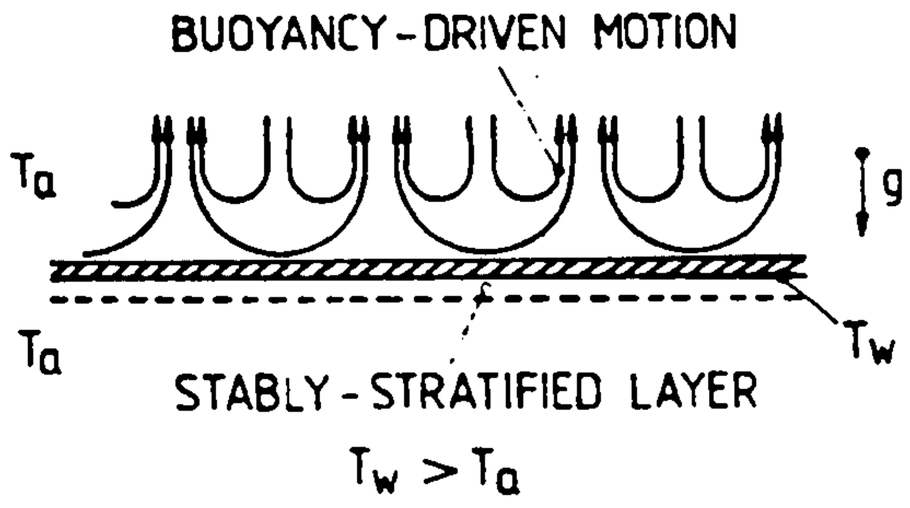

(b) MOTION INDUCED BY A HORIZONTAL HEATED PLATE

Fig. 1. Idealised buoyancy-driven convection near flat surfaces, motion induced (a) by a vertical heated plate, and (b) by a horizontal heated plate.

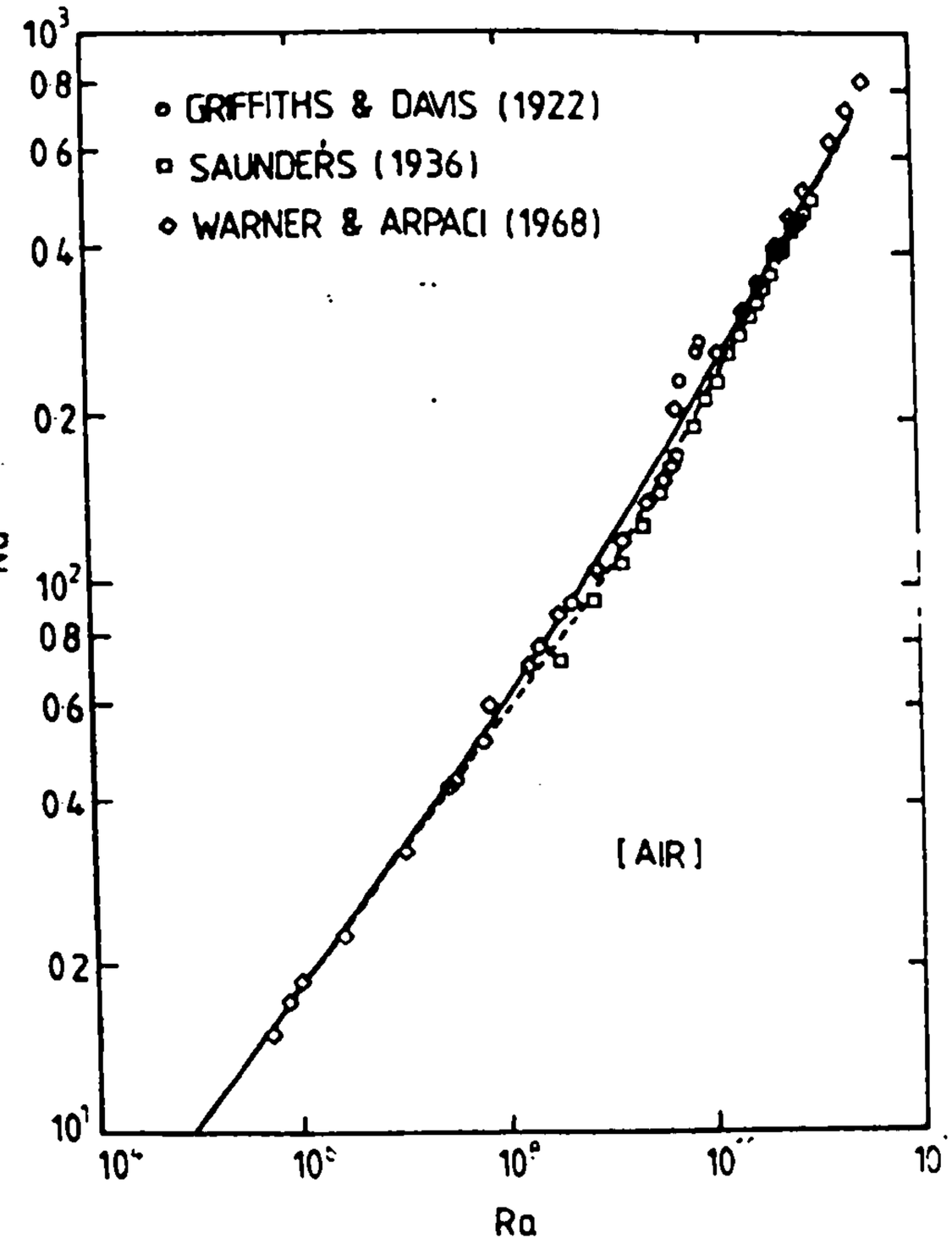

Fig. 2. Nusselt versus Rayleigh number relation for buoyancy-driven convection near vertical surfaces. (Solid line: present correlation. Broken line: asymptotic laminar and turbulent behaviour).

2.1 Buoyancy-driven convection near vertical surfaces

The flow pattern induced by a hot, vertical plate results from the heated, lower density fluid adjacent to the surface rising upward (see Fig. 1a). Conversely, a cold, vertical plate, where $T_w < T_a$, induces a downward motion with a heat flux of similar magnitude, but opposite sign. 'Window downdraught' is an obvious example of the latter motion in the context of buildings. The characteristic length scale, L, associated with these vertical surface flows is the height of the plate. Nusselt number data for air[8-10], scaled on this basis, are compared with the present correlating Equation (5) in Fig. 2. It is evident that the scatter of this data is small, and that the improved data correlation exhibits a good fit throughout the laminar, transitional and turbulent regimes. Not surprisingly, therefore, the recovered data for h_c, shown in Fig. 3, is similarly well represented by Equation (7). (The data in this figure implies a slightly greater scatter, due to uncertainties in recovering heat transfer coefficients. Such a process inevitably involves an element of subjective interpretation.) The height of walls in domestic houses are typically about 2.5 m, which is covered by the data displayed in Fig. 3. It is to be expected that heat transfer would be influenced by three-dimensional flow or 'side-wall' effects if the height/width ratio of the walls were relatively large. However, this aspect ratio varies between about 0.5 and 1 in houses, so that the flow and heat transfer are likely to be essentially two-dimensional.

The CIBS Guide[4] does not provide data for surface-averaged, buoyancy-induced heat transfer in the practical case of transition to turbulent flow on vertical surfaces. Its laminar flow data also falls 10 per cent below the

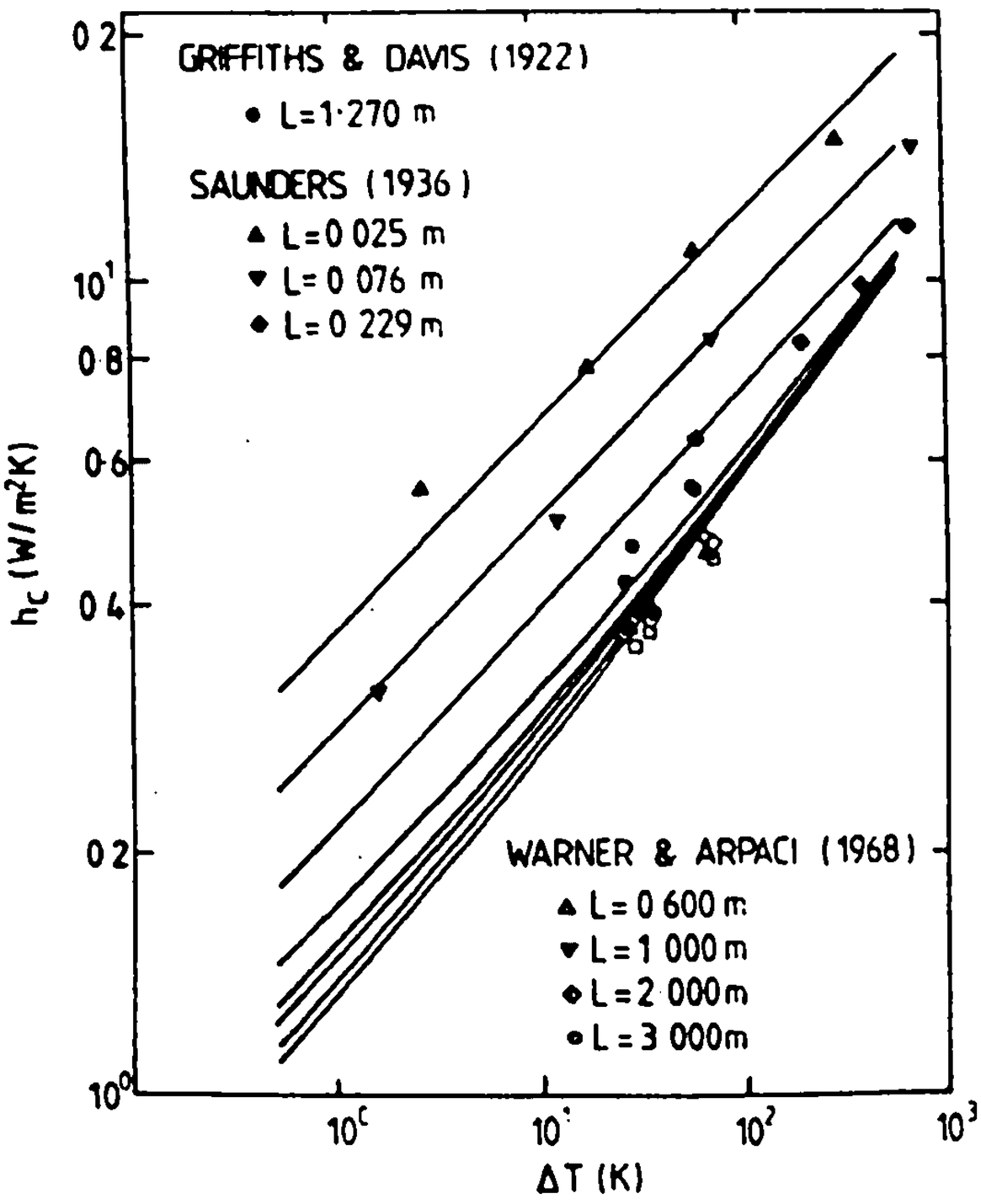

Fig. 3. Heat transfer coefficient for buoyancy-induced air flow near vertical surfaces.

asymptotic Nusselt number given by the present correlating Equation (5). This new expression for convection on vertical surfaces, in the form of Equation (7), therefore provides building thermal modellers with a more accurate and convenient basis for their computations.

When the authors developed the present correlating Equations (5) and (7) they were unaware that later work by Churchill and his co-workers[11] had yielded analogous data correlations for buoyancy-driven motion on vertical surfaces.* Churchill & Chu[11] developed their formulation for the two asymptotic conditions $Ra \to 0$ and $Ra \to \infty$, with an additional requirement that it should reproduce the analytical results of laminar boundary layer theory in the range $10^5 < Ra < 10^8$. This led to the rather complicated expression:

$$Nu^{1/2} = 0.825 + \frac{0.387\ Ra^{1/6}}{[1 + (0.437/Pr)^{9/16}]^{8/27}} \quad (8)$$

Very low Rayleigh numbers ($Ra \to 0$) are only encountered in practice for rather exotic low Prandtl number fluids, such as liquid metals, which are obviously inappropriate to the built environment. Nevertheless, ESDU[12] has simplified Equation (8) for air flow and, over the limited range of temperatures applicable to naturally-ventilated buildings, it becomes:

$$h_c = 0.134\ L^{-1/2} + 1.11\ \Delta T^{1/6} \quad (9)$$

This expression, together with its counterpart, Equation (8), are found to yield heat transfer coefficients which are about 5 per cent higher than the present correlating Equations, (5) and (7), for high temperature differences and long surfaces (high Rayleigh numbers, $10^9 < Ra < 10^{12}$). Conversely, for relatively low temperature differences and short surface lengths ($10^4 < Ra < 10^7$), the Churchill & Chu/ESDU equations imply coefficients that are about 11 per cent lower than those given by the present correlations. Interestingly, Churchill & Chu[11] themselves argued that heat transfer coefficients similar to those yielded by the present correlating Equation (5) are 'more accurate', in the range $10^4 < Ra < 10^7$, than those of Equation (8). Nevertheless, in view of the inherent uncertainty in the experimental data on buoyancy-driven convection noted above, the Churchill & Chu/ESDU correlating equations may be regarded as alternatives to the present ones for vertical surface flows. The present data correlations, however, have the additional merit of being rather simpler in form, and have been extended to horizontal surfaces in the section that follows.

2.2 Buoyancy-driven convection near horizontal surfaces

The motion induced by a heated horizontal surface is illustrated in Fig. 1b. The relatively hot, lighter fluid on the upper surface has a tendency to be convected upwards in the form of 'plumes' or 'thermals', being replaced by colder, more dense fluid from above. This configuration is therefore gravitationally unstable and, for temperature differences above a minimum or 'critical' value, the buoyancy forces will drive the convective motion. The flow pattern shown for the upper surface in Fig. 1b is an idealisation based on the work of the Soviet scientist M. Mikheyev as given by Al-Arabi & El-Riedy[13]. 'Orderly', laminar flow is observed at low Rayleigh numbers ($Ra < 10^6$), but the convective motion undergoes a transition to turbulence at high values ($Ra > 10^9$). A cooled horizontal surface, where $T_w < T_a$, will give rise to a similar flow pattern, although this develops on the underside of the element. Both arrangements involve a downward heat flow. There is a considerable divergence of opinion in the literature regarding the most appropriate length scale to adopt for these horizontal surface flows. In the present study the characteristic length has been defined as:

$$L = 4A_s/P_s \quad (10)$$

where A_s is the surface area and P_s its perimeter. This is analogous to the 'hydraulic diameter' used in fluid mechanics, and for a square surface the length scale simply becomes the length of one side. Equation (10) has the conceptual merit of yielding appropriate length scales for irregular, non-rectangular surfaces, although elements of this type are not usually found in buildings. Experimental Nusselt number data obtained in air[13-15] and corrected for the present length scale are shown in Fig. 4, where they are compared with the new correlating Equation (5). The data of Fujii & Imura[16] for water (considered by Yousef *et al*[15] to be amongst the most accurate) has also been included in Fig. 4 in order to augment the rather sparse air data at high Rayleigh numbers. Data for buoyancy-driven convection on horizontal surfaces is seen to display a greater scatter than that for vertical surfaces. This is in part due to the influence of 'edge' effects which tend to increase the heat transfer rate on relatively small surfaces[13,15]. Nevertheless, the present correlating Equation (5) is seen to be representative of the bulk of this data throughout the laminar, transitional and turbulent regimes. A similar

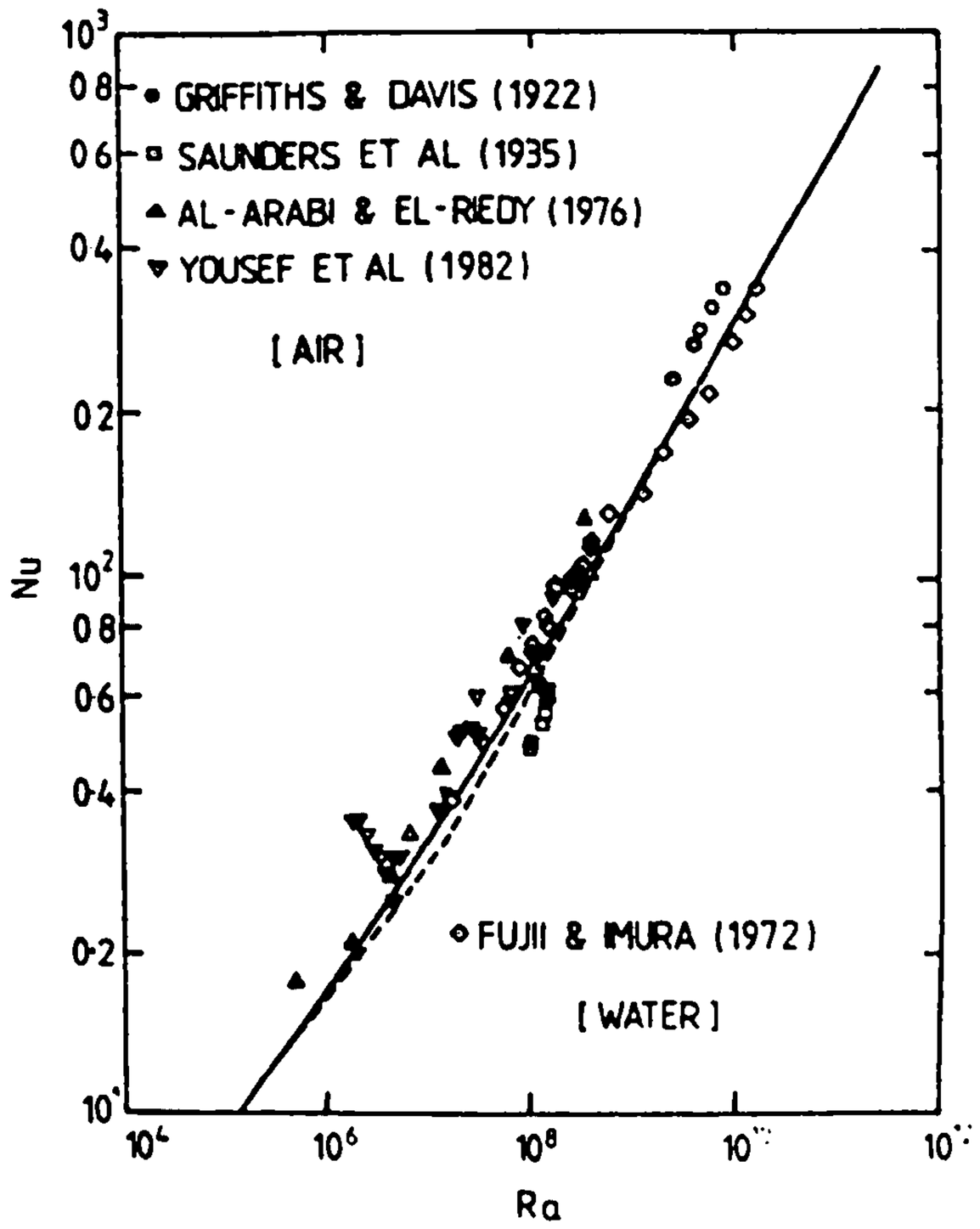

Fig. 4. Nusselt versus Rayleigh number relation for buoyancy-driven convection adjacent to horizontal surfaces. (Solid line: present correlation. Broken line: asymptotic laminar and turbulent behaviour).

*The authors only discovered a reference to the paper of Churchill & Chu[11] when they consulted the Engineering Sciences Data Unit[12] in search of additional data to validate the horizontal surface cases.

conclusion may be drawn in regard to the recovered data for h_c in air plotted on Fig. 5, where they are compared with correlating Equation (7). Yousef *et al*[15] postulated that the very high heat transfer coefficients obtained with their smallest test plate (L_c = 0.1 m) might have been caused by the presence of a single buoyant plume. This explanation for the anomalous data is open to doubt, but this geometry is, in any case, outside the range of interest to the built environment. The data of Saunders *et al*[14] which falls considerably below the present correlation, is generally regarded (see, for example, Yousef *et al*[15] as being among the lowest of the available data sets. It is clear from Fig. 5 that further accurate data for L $\simeq$ 3 m would have been useful for validating the present correlating Equation (7) at conditions directly applicable to buildings.

Both the CIBS Guide[4] and the appropriate ESDU Data Item[12] employ two-part models to correlate data for h_c in air near horizontal surfaces. The former adopts a characteristic length scale equal to the mean value of the two sides of a rectangular surface. This choice is identical to that given by Equation (10) for square surfaces, and differs only slightly for rectangular elements. The length scale adopted by ESDU is equal to 0.25 L as used in the present work. In the laminar regime, the CIBS correlation is almost identical to that given by Equation (7), whereas the ESDU relation yields coefficients which are almost 30 per cent higher. The CIBS and ESDU correlations for the turbulent regime, in contrast, imply coefficients which are not more than 5 per cent above those given by correlating Equation (7).

2.3 Stably-stratified convection near horizontal surfaces

The fluid beneath a heated horizontal surface, such as that illustrated in Fig. 1b, must always be at a lower temperature than that of the surface. This fluid is therefore gravitationally stable, and the layer over which the vertical temperature gradient persists is stably-stratified. A cooled horizontal surface would also give rise to the formation of such a stable layer, but on top of the element. Either configuration may be characterised as having an upward heat flow. Instabilities that would otherwise lead to the onset of turbulence at high Rayleigh numbers are damped under the influence of downward, negative buoyancy forces which restore equilibrium. The analytical results of Singh *et al*[17], based on the solution of the integral boundary layer equations, indicate that the Nusselt number for such laminar stably-stratified layers varies according to a 1/5 power of the Rayleigh number. This differs from the ¼ power-law dependence of buoyancy-driven laminar flow on both vertical and horizontal surfaces. Nevertheless, recent experimental data[16,18,19] has confirmed that the 1/5 power relation holds up to at least Ra $\simeq 10^{11}$, and it is adopted in the present work. Thus, for stable-stratification alone, the standard correlation Equation (3) is used, together with the 1/5 exponent and the empirical coefficient, C, having a value of 0.58. Simplifying this expression for the thermal conditions applicable to naturally-ventilated buildings yields a dimensional formula for the convective heat transfer coefficient:

$$h_c = 0.60 \left(\frac{\Delta T}{L^2}\right)^{1/5} \qquad (11)$$

The choice of the characteristic length scale governing heat transfer across stably-stratified layers has again been the subject of divergent opinions in the literature. Equation (10) has been employed in the present work for the reasons outlined in Section 2.2 above. The experimental Nusselt number data for air[8,14,18,19] which is displayed in Fig. 6 has been scaled using this characteristic length. The early measurements by

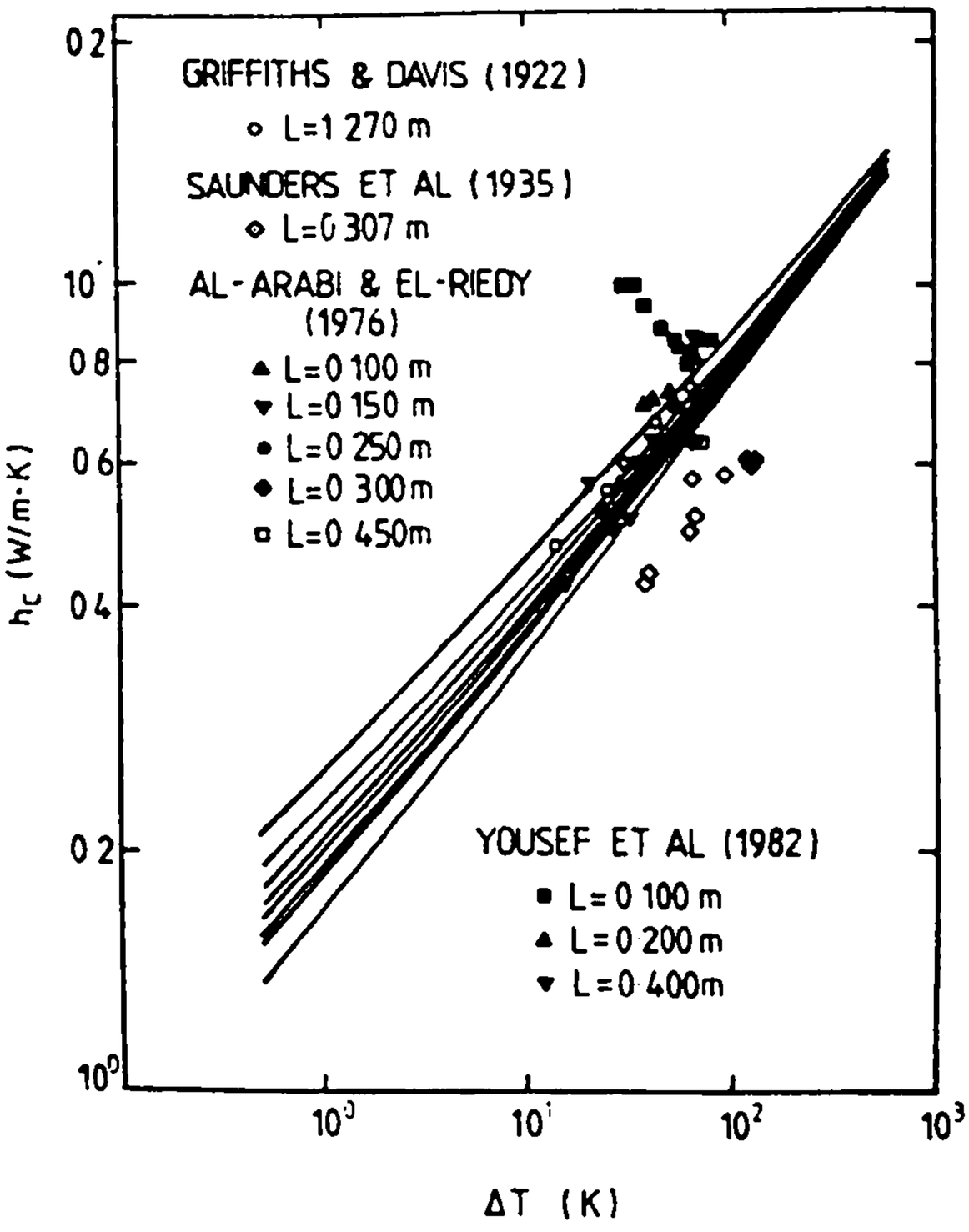

Fig. 5. Heat transfer coefficient for buoyancy-induced air movement adjacent to horizontal surfaces.

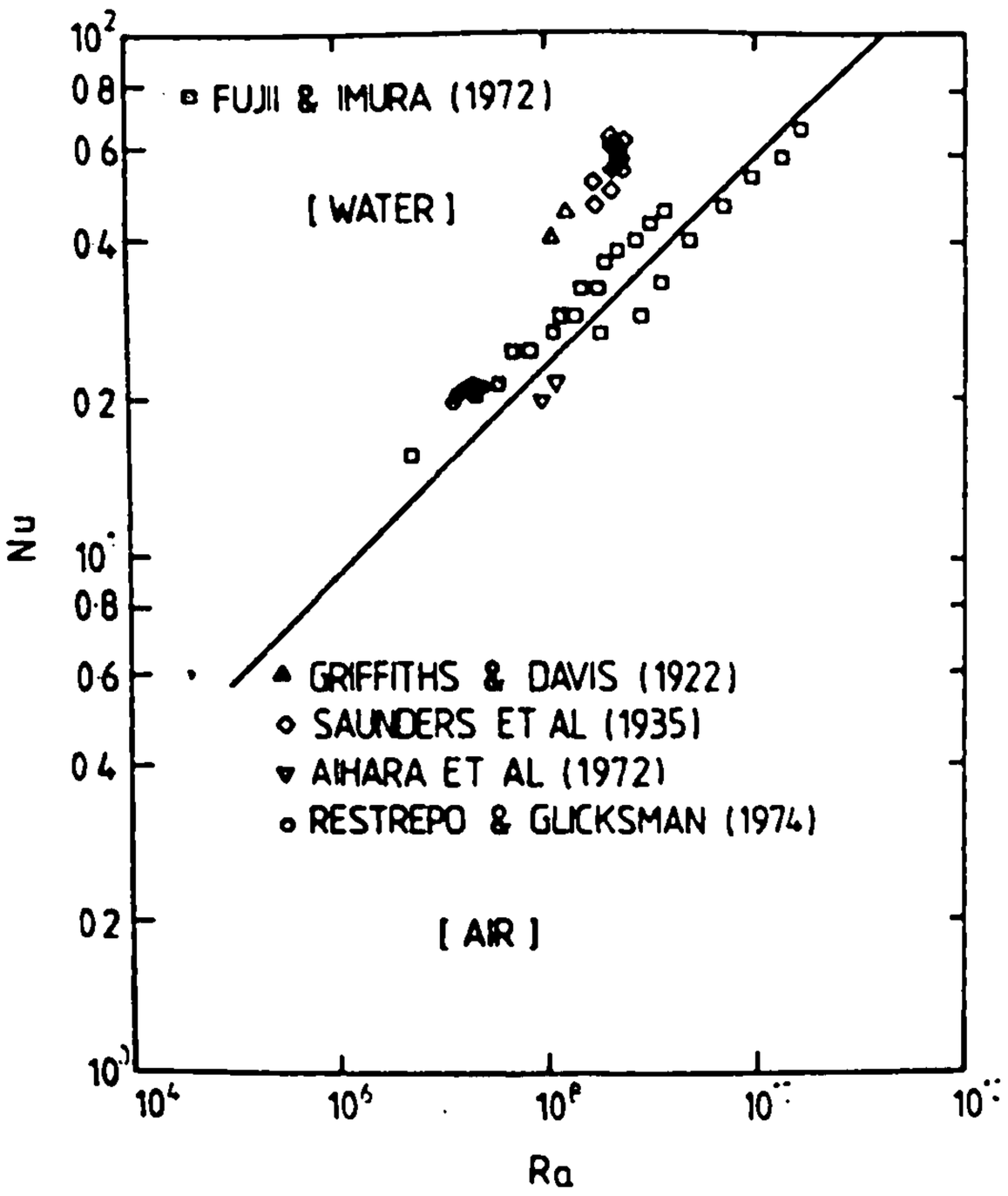

Fig. 6. Nusselt versus Rayleigh number relation for stably-stratified layers near horizontal surfaces.

Saunders *et al*[14], on which the 'standard' data correlations are based[4,12], have been criticised by subsequent investigators[18,19] and are regarded as too high. They used a test plate which simultaneously heated the fluid above and below the surface, so that the flow over the upper surface influenced that near the edges of the lower one[19]. Restrepo & Glicksman[19] have also drawn attention to the influence of the edge thermal boundary conditions (whether they are heated, cooled or insulated) which can alter the heat transfer coefficient by more than ± 20 per cent. In order to give fuller coverage of high Rayleigh number data, the measurements of Fujii & Imura[16] for water have been included in Fig. 6. It can be seen that the present correlating Equation (3) is representative of the more recent measurements, and that the early data of Griffiths & Davis[8] and Saunders[14] are appreciably higher. This is the reason that correlating Equation (11) does not appear to fit the recovered data for h_c in Fig. 7 very closely. In fact the more recent, but rather sparse, data is fairly evenly scattered about the present data correlation.

A data correlation based on the measurements of Saunders *et al*[14] and employing a ¼ power-law dependence has been adopted for both the CIBS Guide[4] and the corresponding ESDU Data Item[12]. These 'standard' correlations, when corrected for the length scale given by Equation (10), are almost identical, but yield heat transfer coefficients which are up to 40 per cent higher than those given by correlating Equations (3) and (11) under conditions typical of the built environment. Indeed the older correlations are over 120 per cent in error at the highest Rayleigh number of their declared range of application. The use of the ¼ power-law is at variance with theoretical results[17] and with recent experimental data[16,18,19], which all suggest a 1/5 power-law dependence for heat transfer in stably-stratified layers. The new correlating Equations (3) and (11) therefore constitute a significant improvement on these older data correlations.

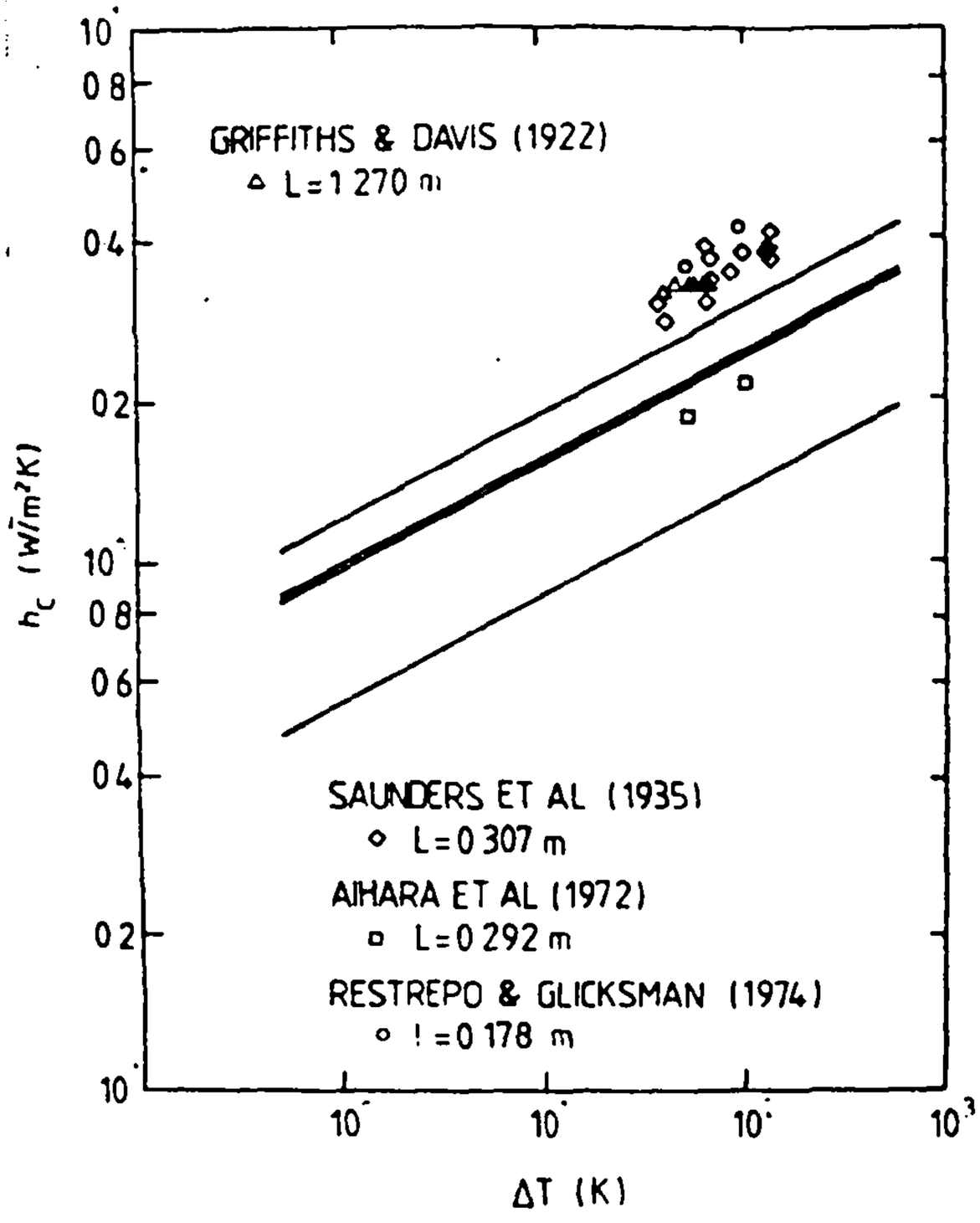

Fig. 7. Heat transfer coefficient for stably-stratified air layers near horizontal surfaces.

3 Concluding remarks

Improved data correlations for buoyancy-driven convection from the internal surfaces of naturally-ventilated buildings have been derived on the basis of the model of Churchill & Usagi[6]. These correlating equations provide a smooth fit to data across the full range of laminar, transitional and turbulent airflows, in contrast to the 'two-part' model employed in 'standard' correlations. The new correlating equations thereby avoid the possibility of inducing numerical instability when used in conjunction with the new generation of dynamic building thermal models. The new data correlations are presented in a simplified and more convenient form, Equation (7), from which the convective heat transfer coefficient may be obtained directly in dimensional terms, rather than via the 'exact' Nusselt number relation. They display generally good agreement with the rather limited experimental data available for conditions typical of the built environment. However, it has been shown that the standard, two-part correlation equations used by the CIBS and the ESDU are, in some cases, significantly in error when compared with recent measurements.

The data on which the improved correlating equations are based was obtained from experiments using isolated surfaces. It is therefore appropriate to consider the extent to which this idealisation is valid in the conditions prevailing in 'real' buildings. The ESDU[12] has identified a number of factors which alter the apparent heat transfer rates implied by correlating equations, and those relevant to buildings include non-uniform surface temperatures, room temperature stratification, room element and flow interactions, and draughts. Surface temperatures in naturally-ventilated buildings are sensibly uniform, and vertical room temperature gradients of 1 °C per metre (dictated by thermal comfort requirements) would also have a negligible effect on surface heat transfer. However, the effect of room element interactions and draughts are more problematic. The data of Griffiths & Davis[8] demonstrates that the interaction between a floor and an adjacent wall boundary layer is negligible, although that between such a layer and a ceiling (for which there appears to be no direct data available) is likely to be significant. The influence of draughts is similarly uncertain. In addition, heat transfer within rooms will be affected by the presence of fixtures* and fittings, as well as surface texture or relative roughness. Fortunately, *surface-averaged* heat transfer coefficients for the large surface areas associated with building elements are generally insensitive to *local* variations such as these. Nevertheless, building thermal modellers should allow for variations of at least ± 20 per cent in the coefficients recommended for correlating Equations (7) or (11) (see Table 1) to account for these disturbances. Despite the obvious limitations in using data for idealised buoyancy-driven convective processes, correlating equations such as those developed here remain arguably the most appropriate calculation method in the absence of field measurements.

Finally, it must be emphasised that the present heat transfer data correlations only apply to buildings that are naturally-ventilated. In order to determine the thermal

*It should be noted, incidentally, that the thermal boundary conditions for the plume above a 'radiator' are different from those associated with the present or standard data correlations. Thus, such correlating equations do not apply in this case, and the error involved in their use cannot be readily evaluated.

performance of buildings using forced convective heating and/or mechanical ventilation, the convection coefficient must be calculated via a more elaborate procedure, such as that recently developed by the present authors[5]. Yaneske & Forrest[20] concluded for example, from a field study of over thirty rooms of various shapes and sizes heated by a fan 'convector', that surface coefficients were much higher than those for buoyancy-driven convection. They demonstrated that the use of the latter when selecting heater capacity for a mechanically-ventilated dwelling could result in substantial increases in preheat times. Waters[21] has likewise shown that the accuracy of his implicit finite-difference building thermal model was strongly dependent on the correct choice of internal heat transfer coefficient when simulating mechanically-ventilated structures.

Acknowledgements

The work reported here was supported by UK Science and Engineering Research Council Grants GR/B/5010.2 and GR/C/0184.9, and forms part of the Council's specially promoted programme on Energy in Buildings. The authors are grateful to Dr. J. A. Clarke (ABACUS, University of Strathclyde) for stimulating their interest in obtaining improved correlating equations for buoyancy-driven convection.

The authors' names appear alphabetically.

References

1 Clarke, J. A., Computer applications in the design of energy-conscious buildings, Computer-aided Design, 14, 3-9 (1982).
2 Day, B., Computation of the dynamic thermal performance of buildings, Computer-aided Design, 14, 49-54 (1982).
3 Irving, S. J., Energy program validation: conclusions of IEA Annex 1, Computer-aided Design, 14, 33-38 (1982).
4 CIBS Guide, C3: Heat Transfer (CIBS, London, 1976).
5 Alamdari, F. & Hammond, G. P., Time-dependent convective heat transfer in warm-air heated rooms, Proc. 3rd Int. Symp. Energy Conservation in the Built Environment, 4, 209-220 (CIB/An Foras Forbartha, Dublin, 1982).
6 Churchill, S. W. & Usagi, R., A general expression for the correlation of rates of transfer and other phenomena, AIChE Journal, 18, 1121-1128 (1972).
7 Mayhew, Y. R. & Rogers, G. F. C., Thermodynamic and Transport Properties of Fluids: SI Units (Blackwell, Oxford, Second Edition, 1969).
8 Griffiths, E. &,Davis, A. H., The transmission of heat by radiation and convection, DSIR Food Investigation Board Special Report No. 9 (HMSO, London, 1922).
9 Saunders, O. A., The effect of pressure upon natural convection in air, Proc. Roy. Soc., A157, 278-291 (1936).
10 Warner, C. Y. & Arpaci, V. S., An experimental investigation of turbulent natural convection in air at low pressure along a vertical heated flat plate, Int. J. Heat Mass Transfer, 11, 397-406 (1968).
11 Churchill, S. W. & Chu, H. H. S., Correlating equations for laminar and turbulent free convection from a vertical plate, Int. J. Heat Mass Transfer, 18, 1323-1329 (1975).
12 ESDU Data Item No. 77031, Heat transfer by free convection and radiation—simply shaped bodies in air and other fluids (ESDU, London, 1979).
13 Al-Arabi, M. & El-Riedy, M. K., Natural convection heat transfer from isothermal horizontal plates of different shapes, Int. J. Heat Mass Transfer, 19, 1399-1404 (1976).
14 Saunders, O. A., Fishenden, M. & Mansion, H. D., Some measurements of convection by an optical method, Engineering, 483-485 (May 1935).
15 Yousef, W. W., Tarasuk, J. D. & McKeen, W. J., Free convection heat transfer from upward-facing isothermal horizontal surfaces, ASME J. Heat Transfer, 104, 493-500 (1982).
16 Fujii, T. & Imura, H., Natural-convection heat transfer from a plate with arbitrary inclination, Int. J. Heat Mass Transfer, 15, 755-767 (1972).
17 Singh, S. N., Birkebak, R. C. & Drake, R. M., Laminar free convection heat transfer from downward-facing horizontal surfaces of finite dimensions, Prog. Heat Mass Transfer, 2, 87-98 (1969).
18 Aihara, T., Yamada, T. & Endo, S., Free convection along the downward-facing surface of a heated horizontal plate, Int. J. Heat Mass Transfer, 15, 2535-2549 (1972).
19 Restrepo F. & Glicksman, L. R., The effect of edge conditions on natural convection from a horizontal plate, Int. J. Heat Mass Transfer, 17, 135-142 (1974).
20 Yaneske, P. P. & Forrest, I. D., The thermal response of rooms with intermittent, forced convective heating, Build. Serv. Eng., 46, 13-17 (1978).
21 Waters, J. R., The experimental verification of a computerised thermal model for buildings, BSER&T, 1, 76-82 (1980).

APPENDIX B

INTERNAL SURFACE CONVECTION COEFFICIENT

(Results of Parametric Studies)

Table B.1 :Internal Surface-averaged Convection Coefficients - Winter Season

Winter Case No. I	● Room length 3.0 (m) ● Single glazed window ● Cavity wall				
Room height (m)	Internal Surface Convection Coefficient (W/m^2K)				
	Ceiling	Far-wall	Floor	Near-wall	Window
2.50	87.539	3.168	2.884	5.453	3.458
2.75	90.688	3.309	2.930	5.551	3.421
3.00	93.638	3.435	2.971	5.638	3.390
3.25	96.489	3.547	3.007	5.715	3.364

Winter Case No. II	● Room length 4.0 (m) ● Single glazed window ● Cavity wall				
Room height (m)	Internal Surface Convection Coefficient (W/m^2K)				
	Ceiling	Far-wall	Floor	Near-wall	Window
2.50	65.861	2.896	2.628	4.751	3.458
2.75	67.949	3.012	2.679	4.848	3.421
3.00	69.906	3.118	2.724	4.936	3.390
3.25	71.809	3.213	2.764	5.017	3.364

Winter Case No. III	● Room length 5.0 (m) ● Single glazed window ● Cavity wall				
Room height (m)	Internal Surface Convection Coefficient (W/m^2K)				
	Ceiling	Far-wall	Floor	Near-wall	Window
2.50	53.588	2.707	2.448	4.273	3.458
2.75	55.087	2.809	2.499	4.366	3.421
3.00	56.496	2.903	2.546	4.451	3.390
3.25	57.872	2.988	2.588	4.530	3.364

Table B.1: -- continue

Winter Case No. IV	● Room length 3.0 (m) ● Single glazed window ● Cavity wall (insulant filled)				
Room height (m)	Internal Surface Convection Coefficient (W/m^2K)				
	Ceiling	Far-wall	Floor	Near-wall	Window
2.50	75.998	5.244	2.685	4.855	3.458
2.75	78.473	5.505	2.723	4.928	3.421
3.00	80.790	5.739	2.756	4.993	3.390
3.25	83.039	5.946	2.785	5.050	3.364

Winter Case No. V	● Room length 4.0 (m) ● Single glazed window ● Cavity wall (insulant filled)				
Room height (m)	Internal Surface Convection Coefficient (W/m^2K)				
	Ceiling	Far-wall	Floor	Near-wall	Window
2.50	57.909	4.629	2.474	4.285	3.458
2.75	59.525	4.830	2.517	4.359	3.421
3.00	61.042	5.013	2.555	4.425	3.390
3.25	62.523	5.178	2.589	4.488	3.364

Winter Case No. VI	● Room length 5.0 (m) ● Single glazed window ● Cavity wall (insulant filled)				
Room height (m)	Internal Surface Convection Coefficient (W/m^2K)				
	Ceiling	Far-wall	Floor	Near-wall	Window
2.50	47.620	4.220	2.322	3.893	3.458
2.75	48.762	4.386	2.367	3.966	3.421
3.00	49.837	4.539	2.407	4.032	3.390
3.25	50.893	4.679	2.444	4.093	3.364

Table B.1: -- Continue

Winter Case No. VII				● Room length 3.0 (m) ● Double glazed window ● Cavity wall	
Room height (m)	Internal Surface Convection Coefficient (W/m^2K)				
	Ceiling	Far-wall	Floor	Near-wall	Window
2.50	62.142	2.778	2.446	4.137	2.808
2.75	63.804	2.886	2.474	4.180	2.800
3.00	65.364	2.981	2.498	4.218	2.787
3.25	66.888	3.065	2.519	4.251	2.769

Winter Case No. VIII				● Room length 4.0 (m) ● Double glazed window ● Cavity wall	
Room height (m)	Internal Surface Convection Coefficient (W/m^2K)				
	Ceiling	Far-wall	Floor	Near-wall	Window
2.50	48.361	2.599	2.288	3.725	2.743
2.75	49.411	2.691	2.322	3.772	2.712
3.00	50.398	2.773	2.351	3.814	2.692
3.25	51.373	2.847	2.378	3.852	2.676

Winter Case No. IX				● Room length 5.0 (m) ● Double glazed window ● Cavity wall	
Room height (m)	Internal Surface Convection Coefficient (W/m^2K)				
	Ceiling	Far-wall	Floor	Near-wall	Window
2.50	40.455	2.469	2.172	3.438	2.743
2.75	41.168	2.552	2.208	3.485	2.708
3.00	41.842	2.627	2.241	3.529	2.679
3.25	42.514	2.694	2.270	3.569	2.653

Table B.1: -- Continue

Winter Case No. X	● Room length 3.0 (m) ● Double glazed window ● Cavity wall (insulant filled)				
Room height (m)	Internal Surface Convection Coefficient (W/m^2K)				
	Ceiling	Far-wall	Floor	Near-wall	Window
2.50	50.602	4.045	2.246	3.538	2.760
2.75	51.589	4.203	2.266	3.557	2.738
3.00	52.516	4.342	2.283	3.573	2.720
3.25	53.436	4.462	2.297	3.586	2.699

Winter Case No. XI	● Room length 4.0 (m) ● Double glazed window ● Cavity wall (insulant filled)				
Room height (m)	Internal Surface Convection Coefficient (W/m^2K)				
	Ceiling	Far-wall	Floor	Near-wall	Window
2.50	40.410	3.716	2.134	3.259	2.743
2.75	40.987	3.841	2.160	3.283	2.708
3.00	41.534	3.953	2.182	3.304	2.679
3.25	42.086	4.052	2.202	3.323	2.655

Winter Case No. XII	● Room length 5.0 (m) ● Double glazed window ● Cavity wall (insulant filled)				
Room height (m)	Internal Surface Convection Coefficient (W/m^2K)				
	Ceiling	Far-wall	Floor	Near-wall	Window
2.50	34.487	3.487	2.047	3.059	2.743
2.75	34.843	3.594	2.076	3.086	2.708
3.00	35.182	3.690	2.102	3.110	2.679
3.25	35.535	3.776	2.125	3.132	2.653

Table B.2: Internal Surface-averaged Convection Coefficients - Summer Season

Summer Case No. I	● Room length 3.0 (m) ● Single glazed window ● Cavity wall				
Room height (m)	Internal Surface Convection Coefficient (W/m^2K)				
	Ceiling	Far-wall	Floor	Near-wall	Window
2.50	132.619	4.310	4.226	7.791	2.941
2.75	140.221	4.578	4.360	8.078	2.974
3.00	147.317	4.823	4.480	8.335	2.989
3.25	154.097	5.044	4.587	8.566	2.989

Summer Case No. II	● Room length 4.0 (m) ● Single glazed window ● Cavity wall				
Room height (m)	Internal Surface Convection Coefficient (W/m^2K)				
	Ceiling	Far-wall	Floor	Near-wall	Window
2.50	121.853	4.303	4.301	8.033	2.824
2.75	128.927	4.565	4.466	8.388	2.878
3.00	135.538	4.808	4.617	8.712	2.916
3.25	142.857	5.032	4.754	9.008	2.940

Summer Case No. III	● Room length 5.0 (m) ● Single glazed window ● Cavity wall				
Room height (m)	Internal Surface Convection Coefficient (W/m^2K)				
	Ceiling	Far-wall	Floor	Near-wall	Window
2.50	114.316	4.267	4.317	8.133	2.726
2.75	121.013	4.525	4.504	8.535	2.793
3.00	127.279	4.768	4.676	8.906	2.845
3.25	133.271	4.994	4.835	9.250	2.884

Table B.2: -- continue

Summer Case No. IV	● Room length 3.0 (m) ● Single glazed window ● Cavity wall (insulant filled)				
Room height (m)	Internal Surface Convection Coefficient (W/m^2K)				
	Ceiling	Far-wall	Floor	Near-wall	Window
2.50	132.619	9.722	4.226	7.791	2.941
2.75	140.221	10.453	4.360	8.078	2.974
3.00	147.317	11.128	4.480	8.335	2.989
3.25	154.097	11.742	4.587	8.566	2.989

Summer Case No. V	● Room length 4.0 (m) ● Single glazed window ● Cavity wall (insulant filled)				
Room height (m)	Internal Surface Convection Coefficient (W/m^2K)				
	Ceiling	Far-wall	Floor	Near-wall	Window
2.50	121.853	9.797	4.301	8.033	2.824
2.75	128.927	10.515	4.466	8.388	2.878
3.00	135.538	11.187	4.617	8.712	2.916
3.25	141.857	11.810	4.754	9.008	2.940

Summer Case No. VI	● Room length 5.0 (m) ● Single glazed window ● Cavity wall (insulant filled)				
Room height (m)	Internal Surface Convection Coefficient (W/m^2K)				
	Ceiling	Far-wall	Floor	Near-wall	Window
2.50	114.316	9.776	4.317	8.133	2.726
2.75	121.013	10.486	4.504	8.535	2.793
3.00	127.279	11.156	4.676	8.906	2.845
3.25	133.271	11.785	4.835	9.250	2.884

Table B.2: -- continue

Summer Case No. VII	● Room length 3.0 (m) ● Double glazed window ● Cavity wall				
Room height (m)	Internal Surface Convection Coefficient (W/m^2K)				
	Ceiling	Far-wall	Floor	Near-wall	Window
2.50	132.619	4.310	4.226	7.791	3.605
2.75	140.221	4.578	4.360	8.078	3.657
3.00	147.317	4.823	4.480	8.335	3.685
3.25	154.097	5.044	4.587	8.566	3.692

Summer Case No. VIII	● Room length 4.0 (m) ● Double glazed window ● Cavity wall				
Room height (m)	Internal Surface Convection Coefficient (W/m^2K)				
	Ceiling	Far-wall	Floor	Near-wall	Window
2.50	121.853	4.303	4.301	8.033	3.472
2.75	127.927	4.565	4.466	8.388	3.553
3.00	135.538	4.808	4.617	8.712	3.612
3.25	141.857	5.032	4.754	9.008	3.651

Summer Case No. IX	● Room length 5.0 (m) ● Double glazed window ● Cavity wall				
Room height (m)	Internal Surface Convection Coefficient (W/m^2K)				
	Ceiling	Far-wall	Floor	Near-wall	Window
2.50	114.316	4.267	4.317	8.133	3.358
2.75	121.013	4.525	4.504	8.535	3.456
3.00	127.279	4.768	4.676	8.906	3.534
3.25	133.271	4.994	4.835	9.250	3.594

Table B.2: -- Continue

Summer Case No. X	● Room length 3.0 (m) ● Double glazed window ● Cavity wall (insulant filled)				
Room height (m)	Internal Surface Convection Coefficient (W/m^2K)				
	Ceiling	Far-wall	Floor	Near-wall	Window
2.50	132.619	9.722	4.226	7.791	3.605
2.75	140.221	10.453	4.360	8.078	3.657
3.00	147.317	11.128	4.480	8.335	3.685
3.25	154.097	11.742	4.587	8.566	3.692

Summer Case No. XI	● Room length 4.0 (m) ● Double glazed window ● Cavity wall (insulant filled)				
Room height (m)	Internal Surface Convection Coefficient (W/m^2K)				
	Ceiling	Far-wall	Floor	Near-wall	Window
2.50	121.853	9.797	4.301	8.033	3.472
2.75	128.927	10.515	4.466	8.388	3.553
3.00	135.538	11.187	4.617	8.712	3.612
3.25	141.857	11.810	4.754	9.008	3.651

Summer Case No. XII	● Room length 5.0 (m) ● Double glazed window ● Cavity wall (insulant filled)				
Room height (m)	Internal Surface Convection Coefficient (W/m^2K)				
	Ceiling	Far-wall	Floor	Near-wall	Window
2.50	114.316	9.776	4.317	8.133	3.358
2.75	121.013	10.486	4.504	8.535	3.456
3.00	127.279	11.156	4.676	8.906	3.534
3.25	133.271	11.785	4.835	9.250	3.594

FIGURES

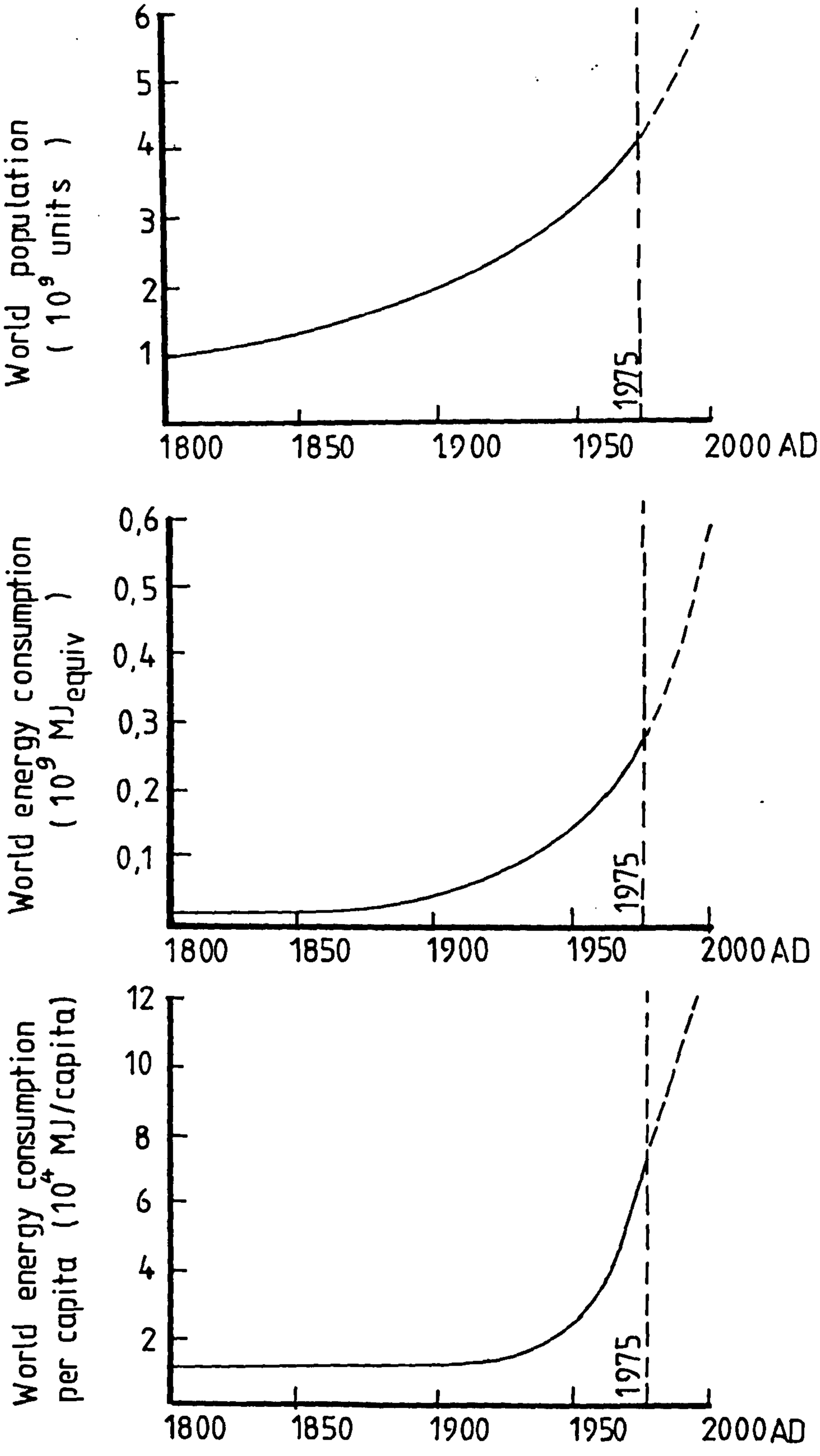

Fig. 1.1: World Population & Rate of Energy Consumption:——— Projections (O'Callaghan, ref 87).

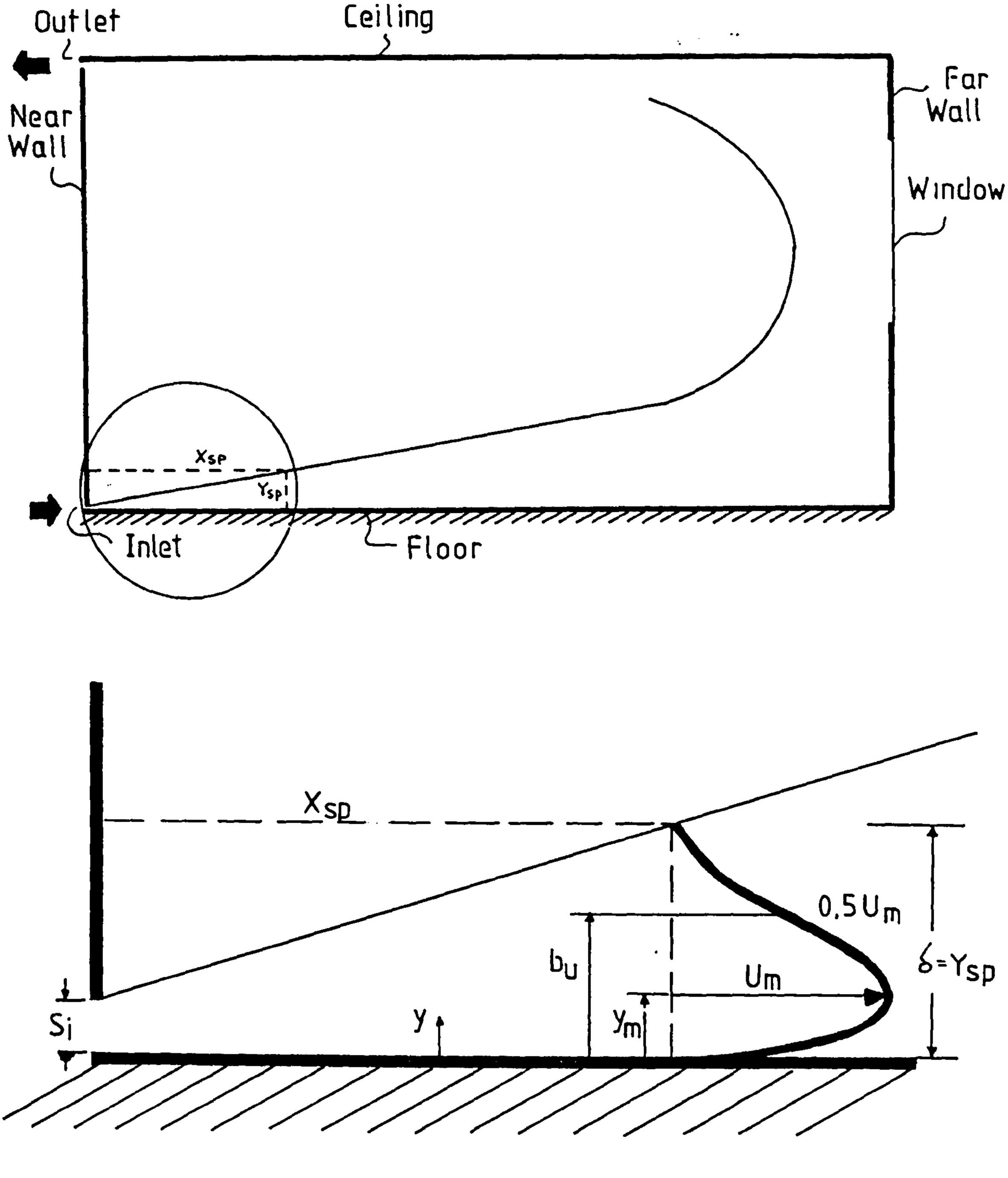

Fig. 2.1: Two-dimensional Room & Starting Wall-jet Profile.

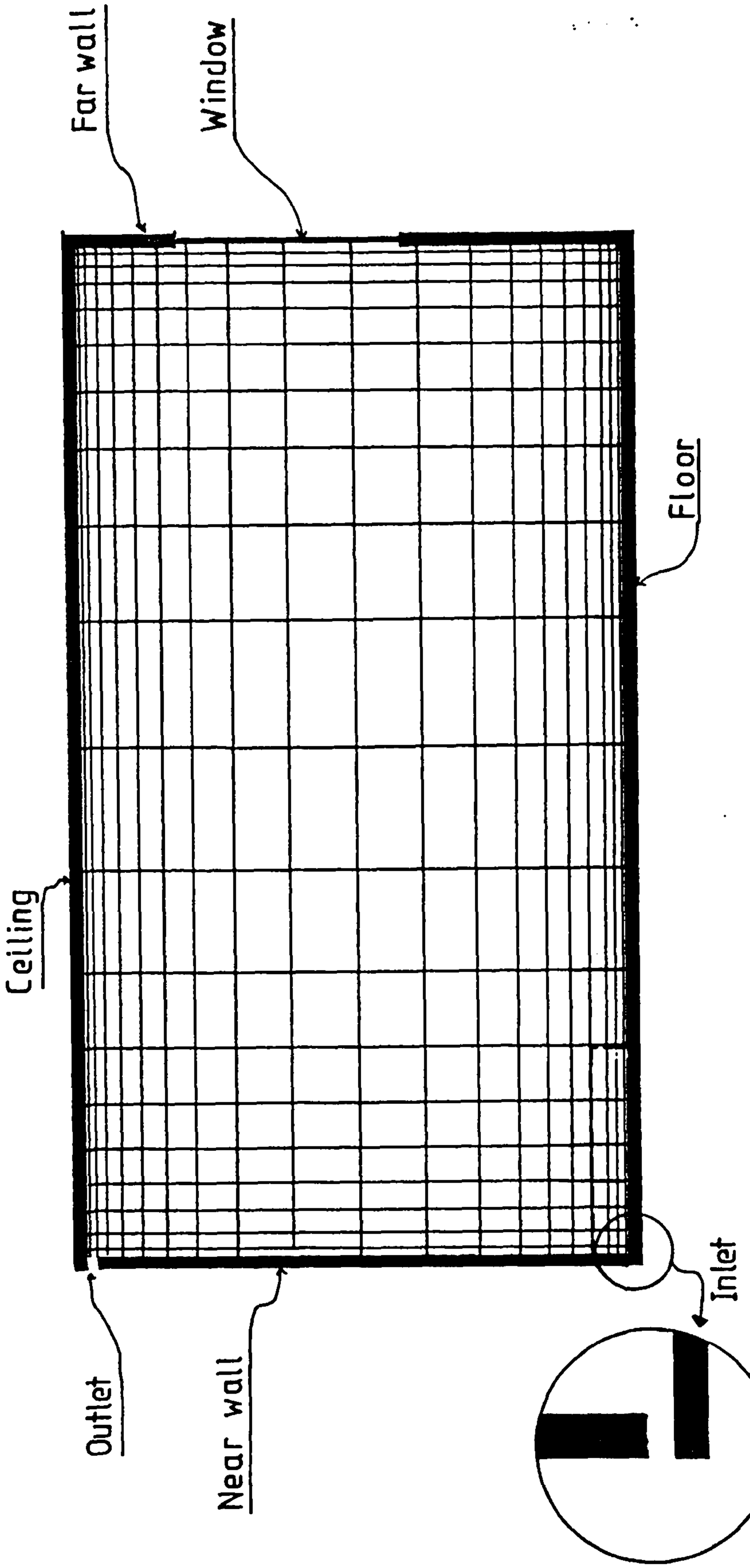

Fig. 3.1: The Illustration of the Two-dimensional 21X21 Grid with Expansion of 1.3.

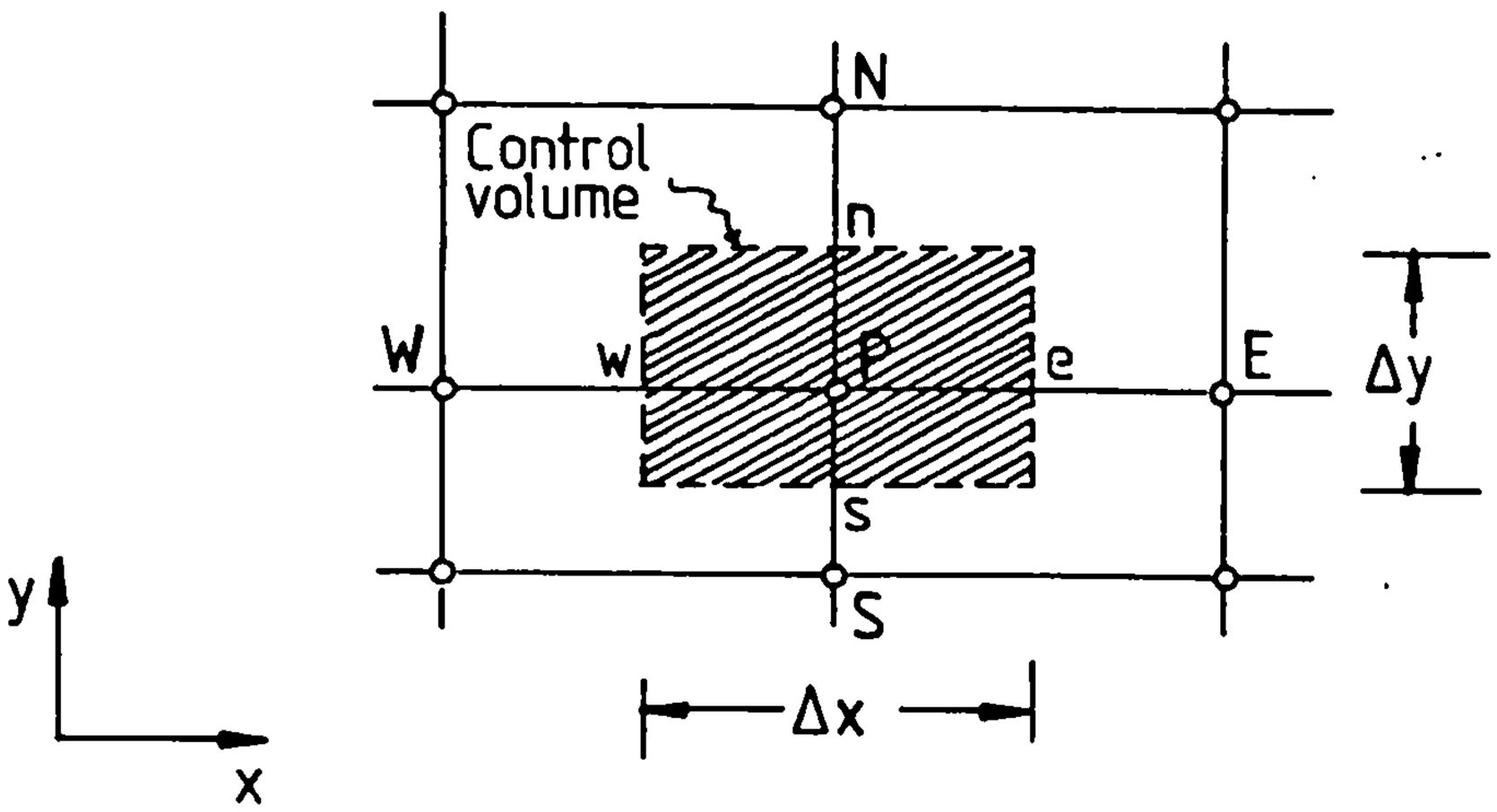

Fig. 3.2: Two-dimensional Control Volume for General Variable Φ.

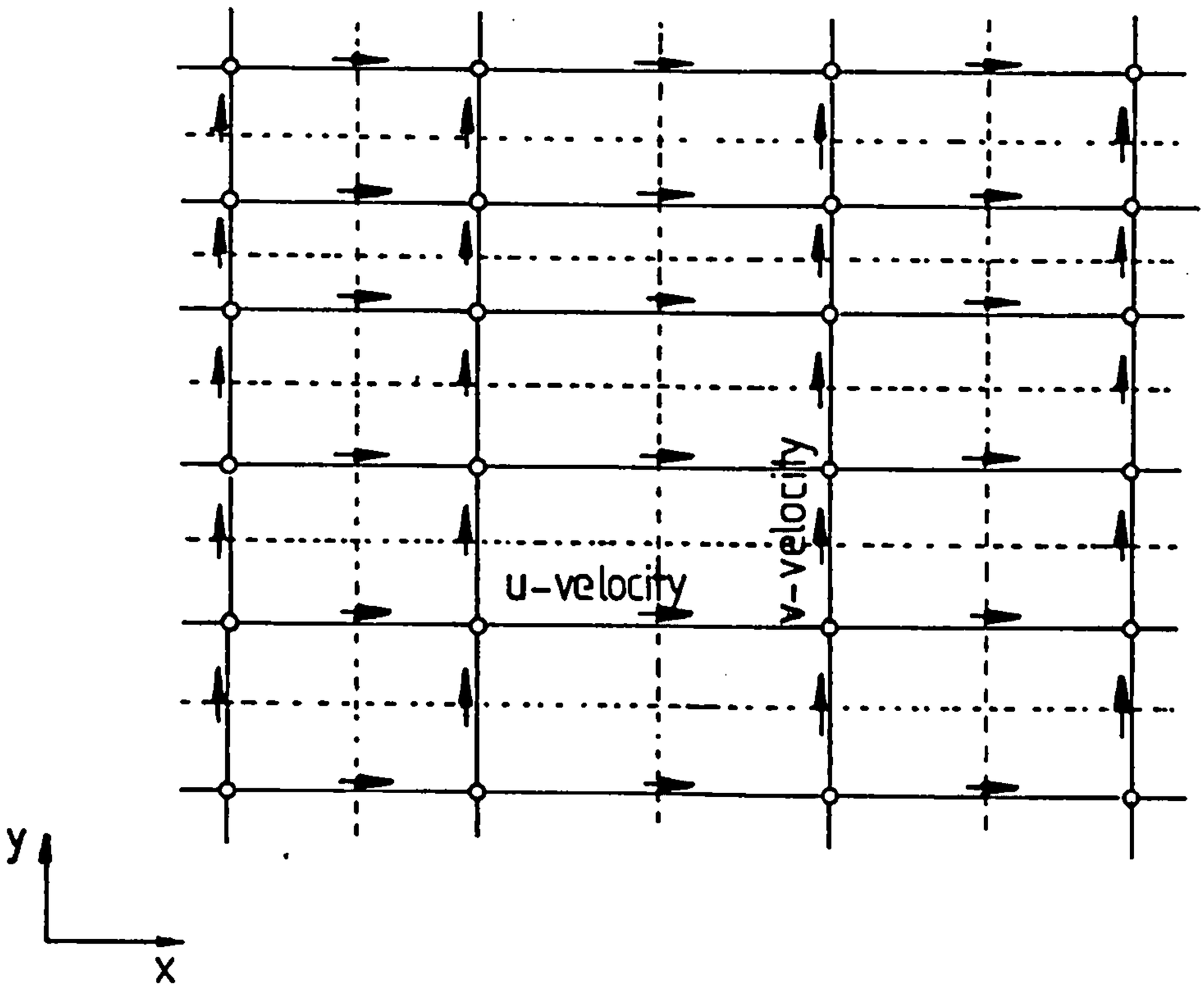

Fig. 3.3: Location of the Dependent Variables;
→ = U-velocity
↑ = V-velocity
o = Other variables.

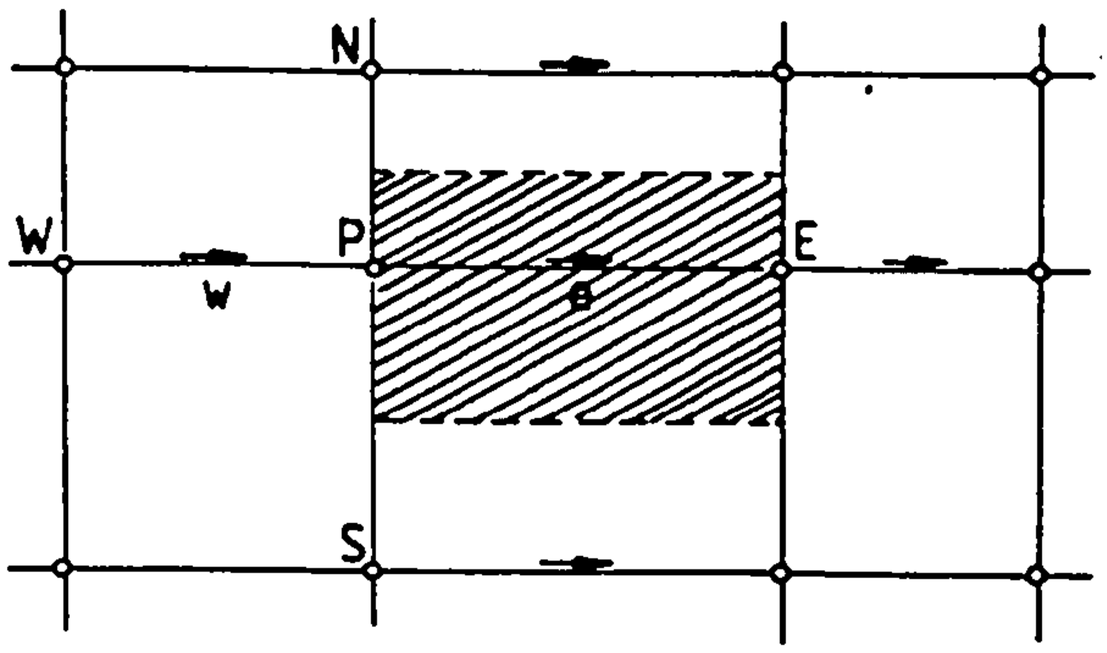

Fig. 3.4: Control Volume and Staggered Locations for U.

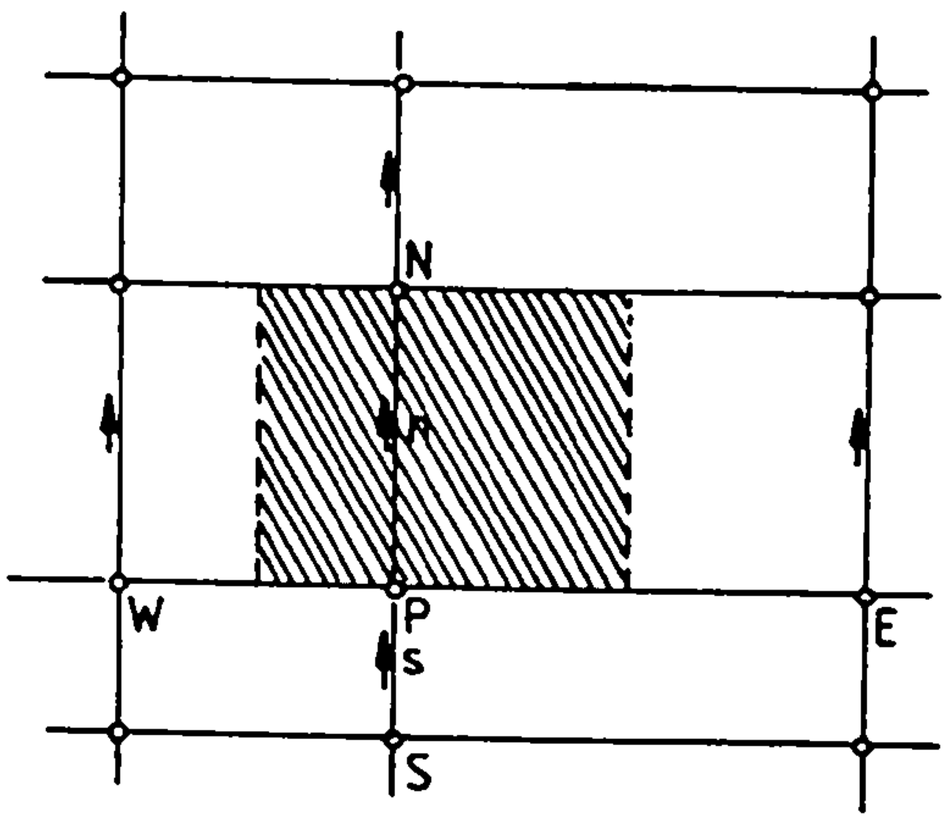

Fig. 3.5: Control Volume and Staggered Locations for V.

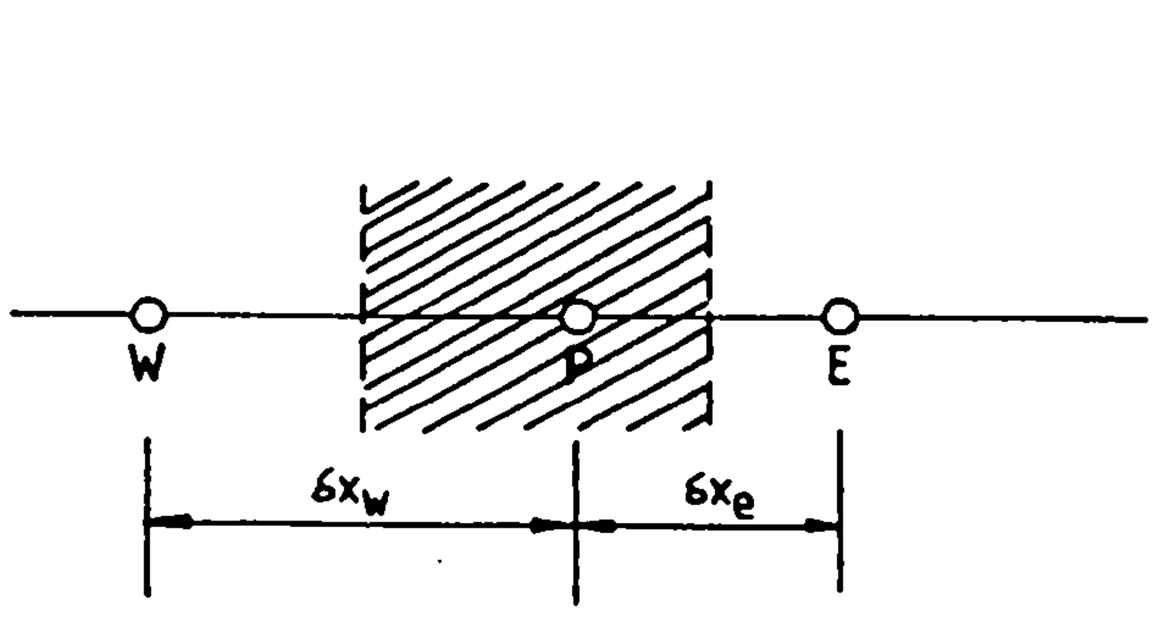

Fig. 3.6: One-dimensional Grid and Control Volume.

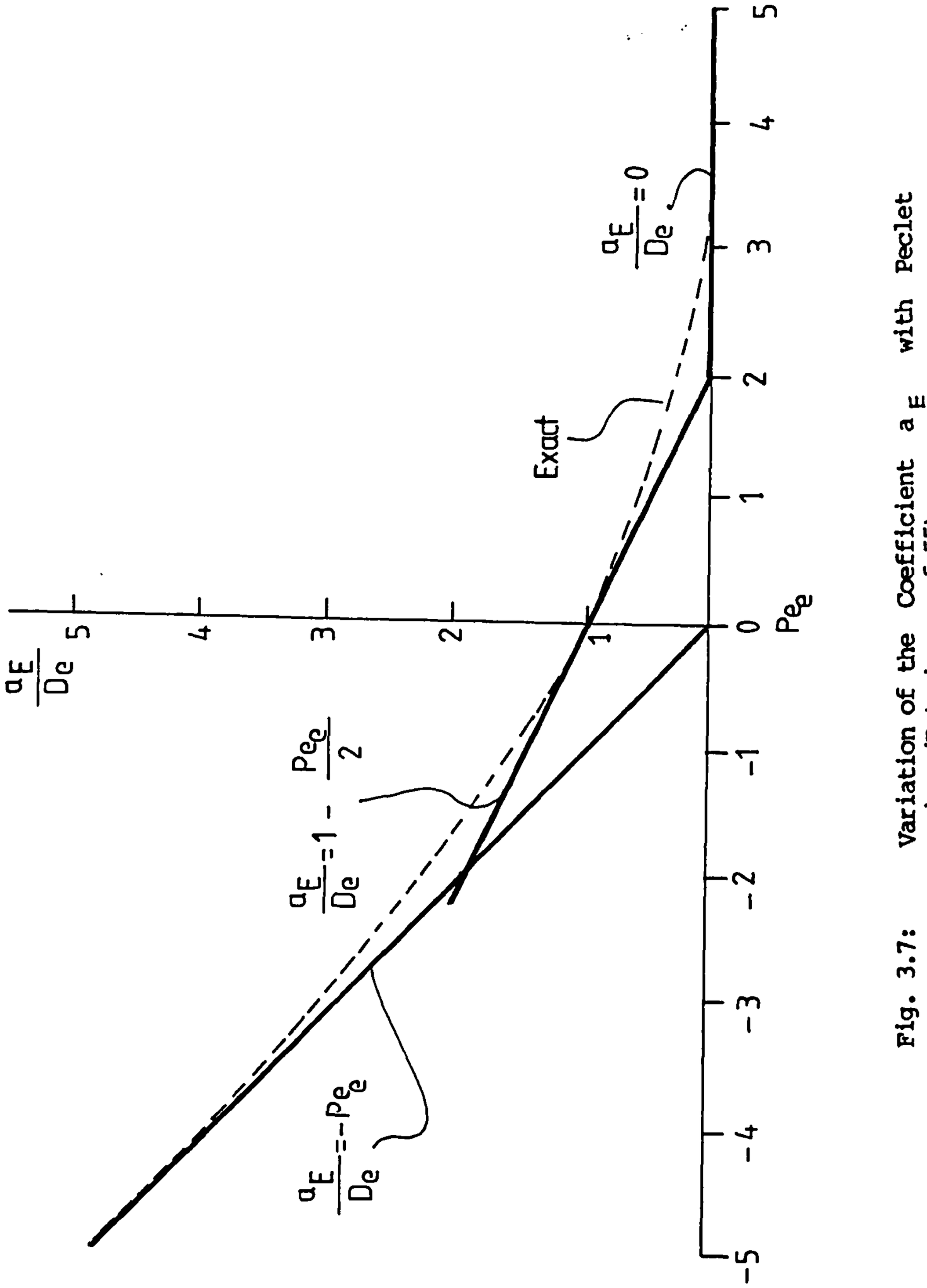

Fig. 3.7: Variation of the Coefficient a_E with Peclet number (Patankar, ref 55).

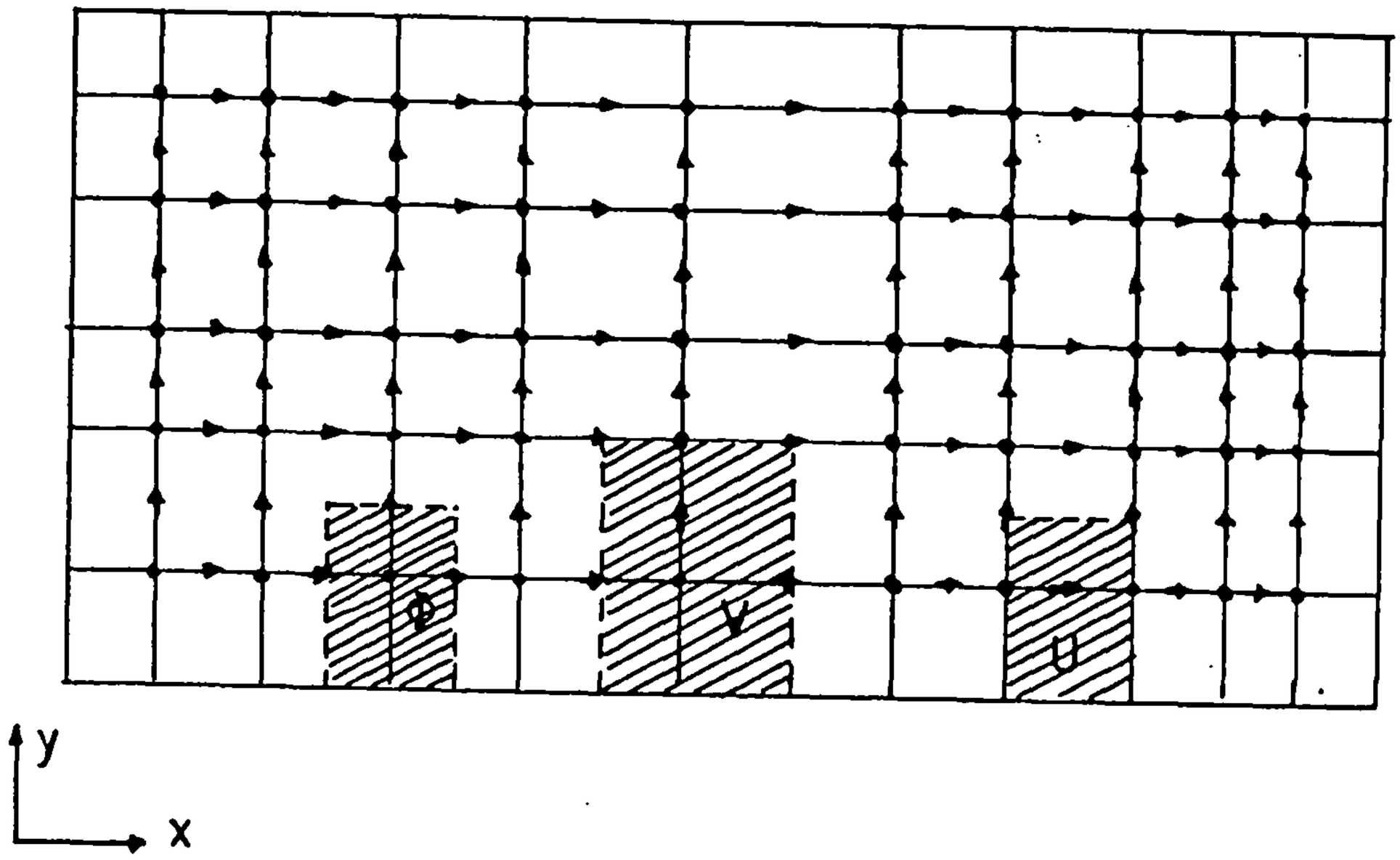

Fig. 3.8: Boundary Control Volume of Variables.

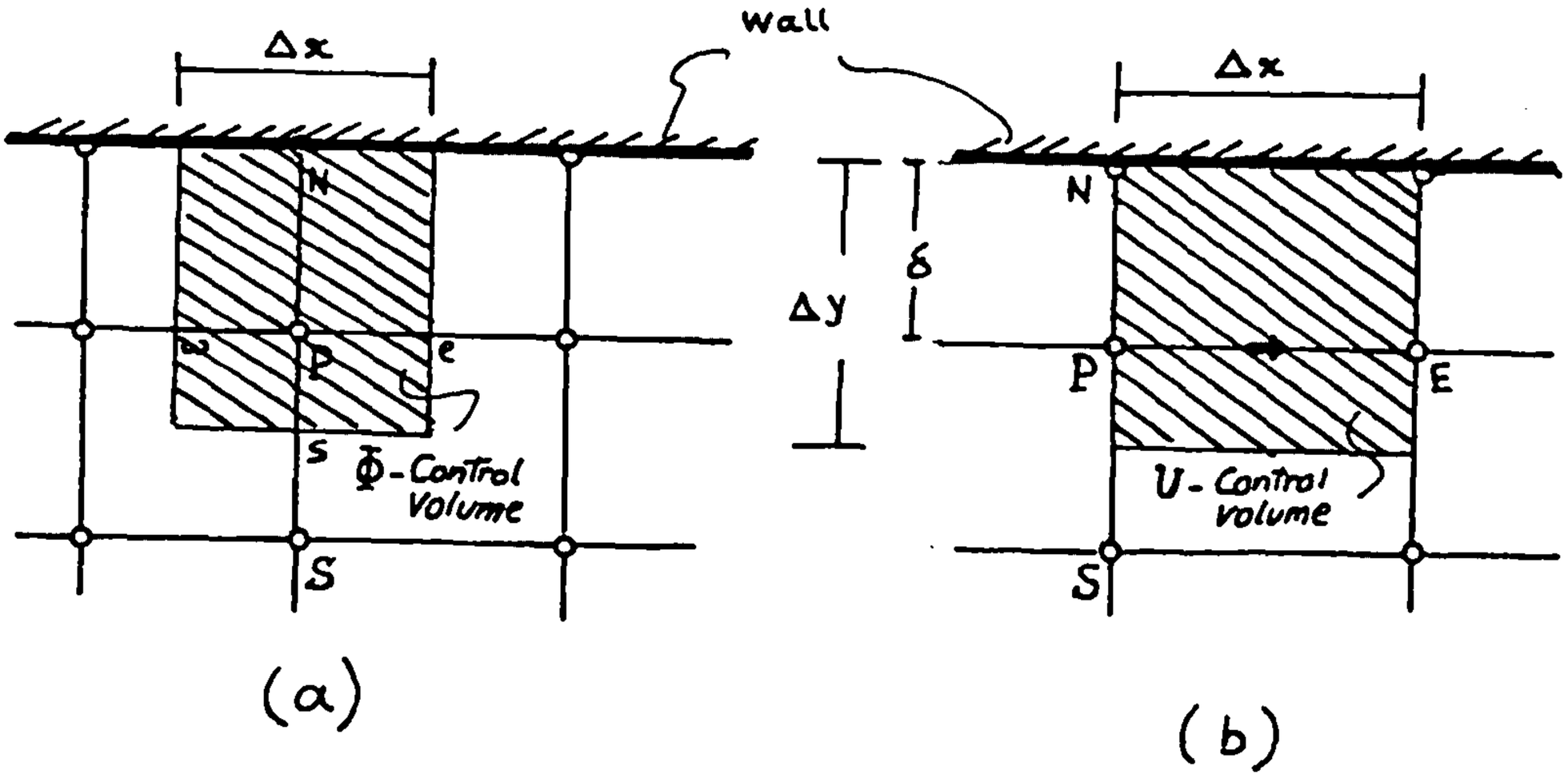

Fig. 3.9: Boundary Control Volume for Φ and U.

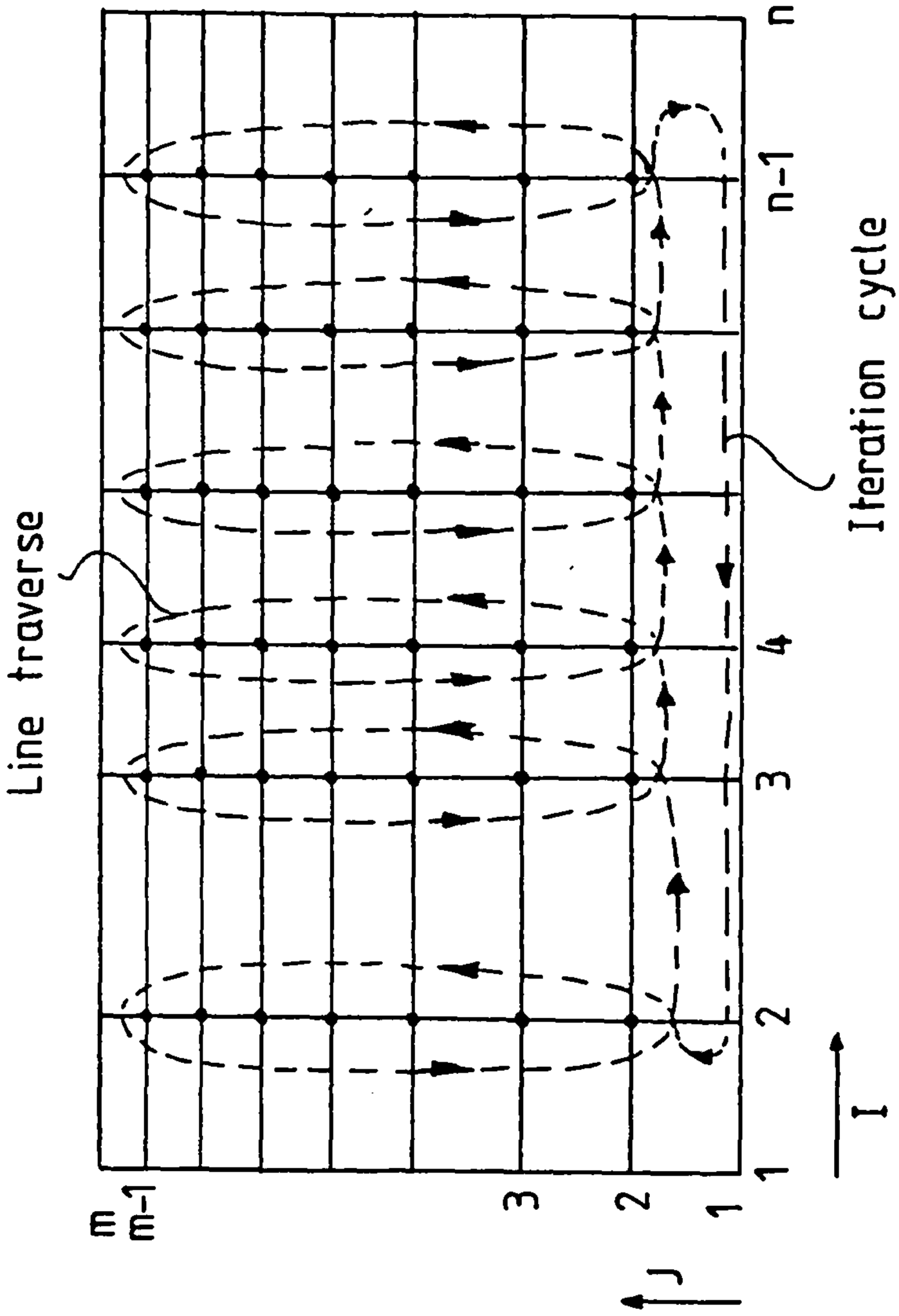

Fig. 3.10: Representation of Line-by-line Iterative Method.

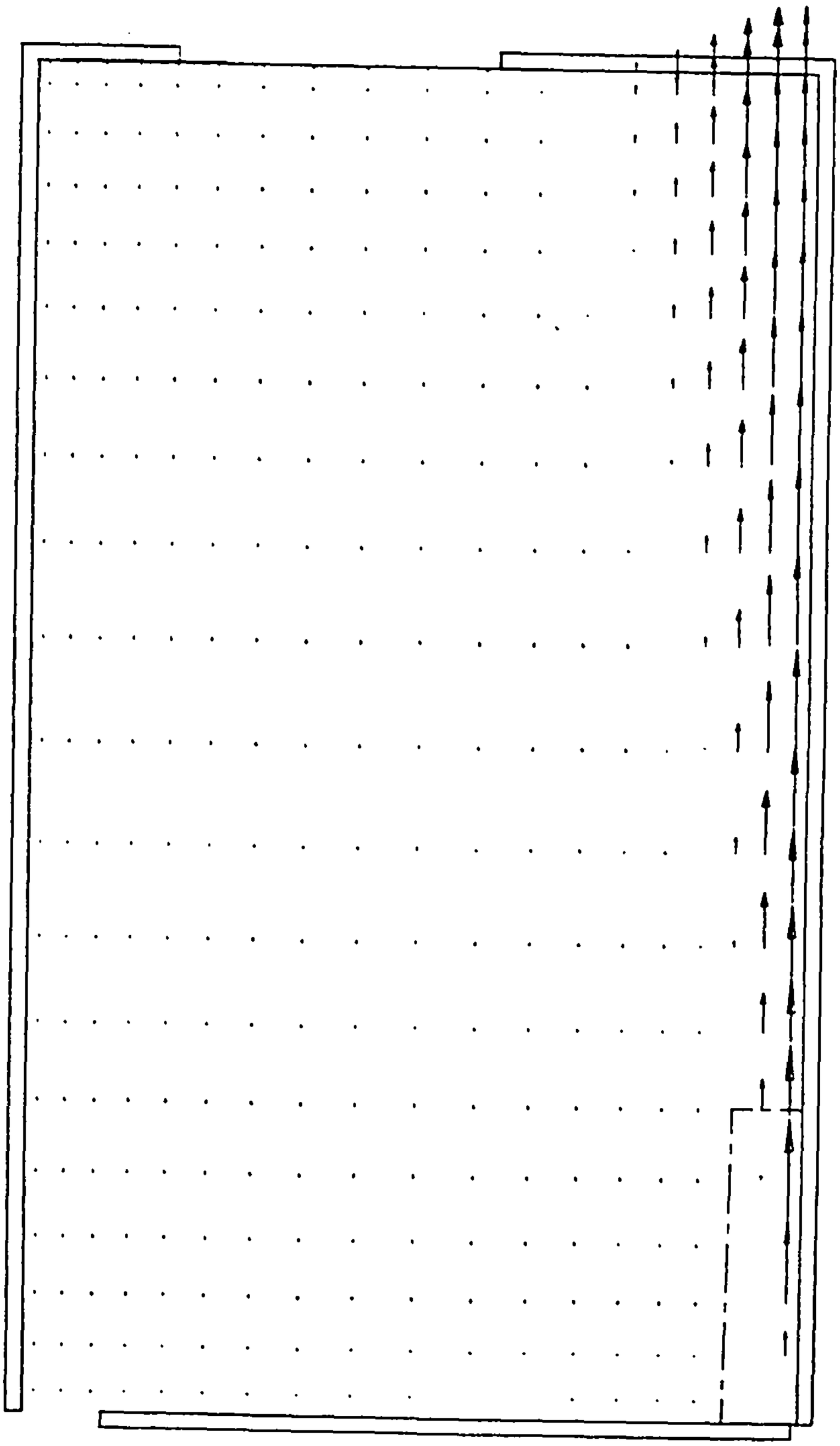

Fig. 3.11: The Initialized U-velocity Prior to the First Iteration of Initial Run.

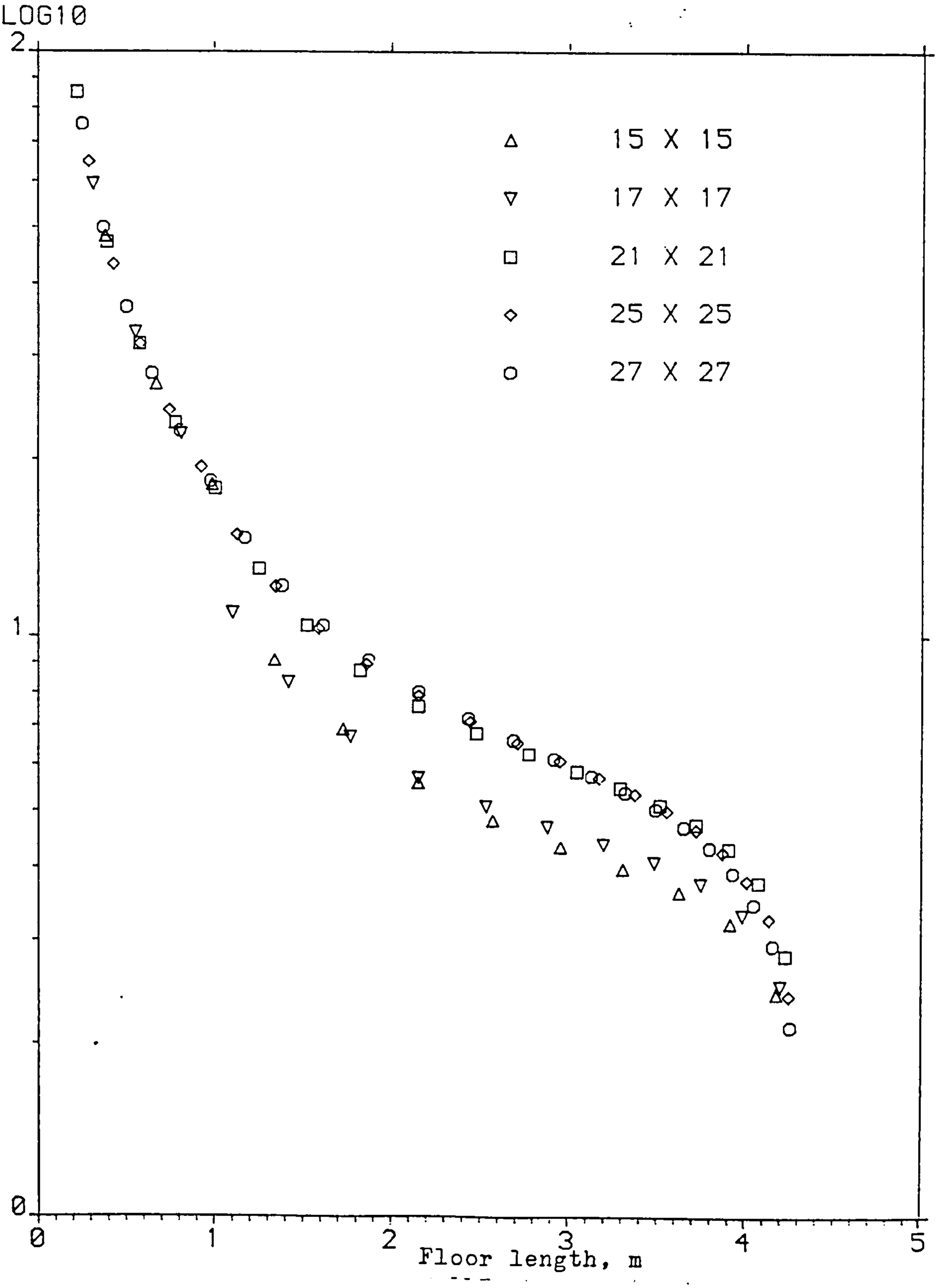

Fig. 3.12: **Computed Local Heat Transfer Coefficients along the Floor (Grid-dependence test).**

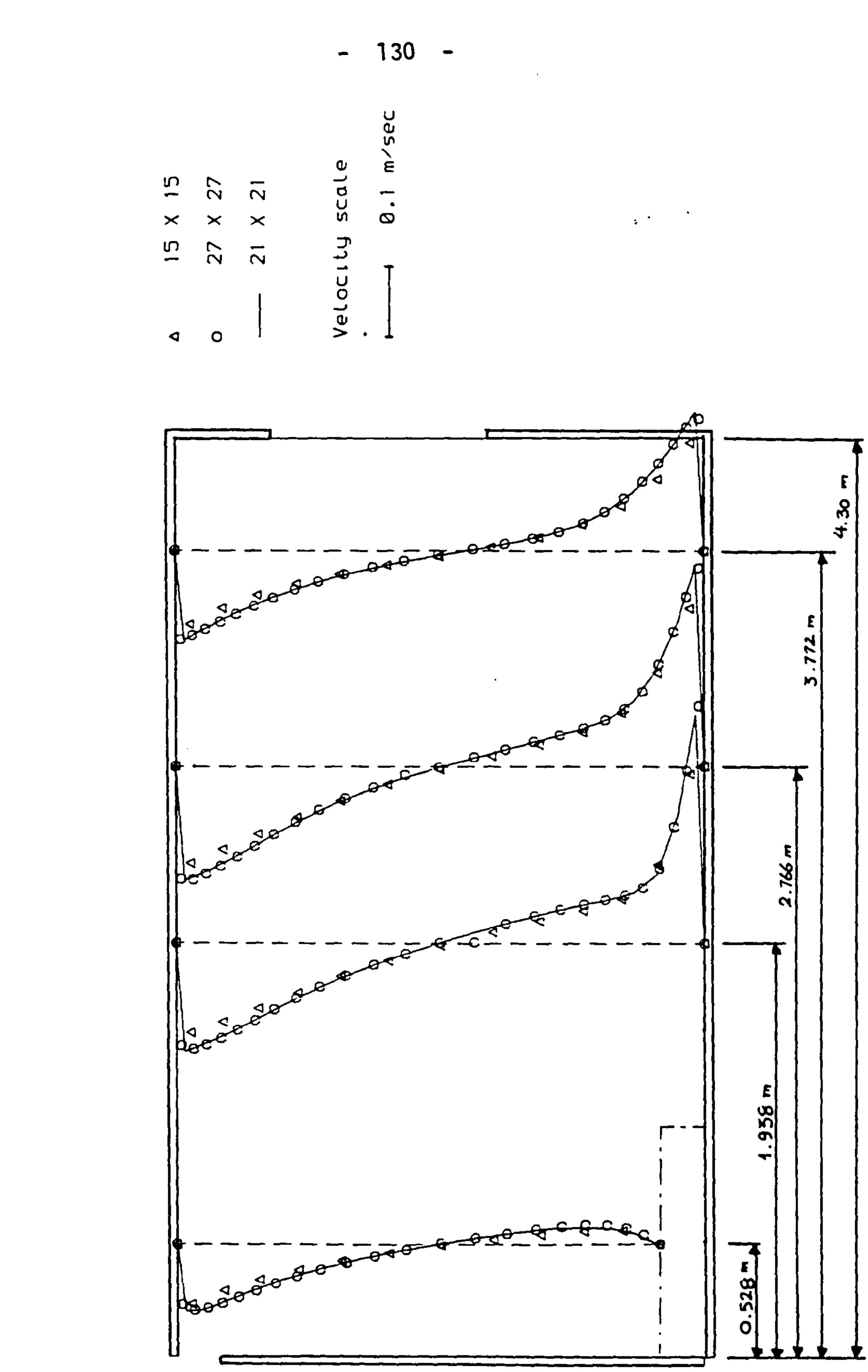

Fig. 3.13: Predicted U-veclocity Profile (Grid-dependence test).

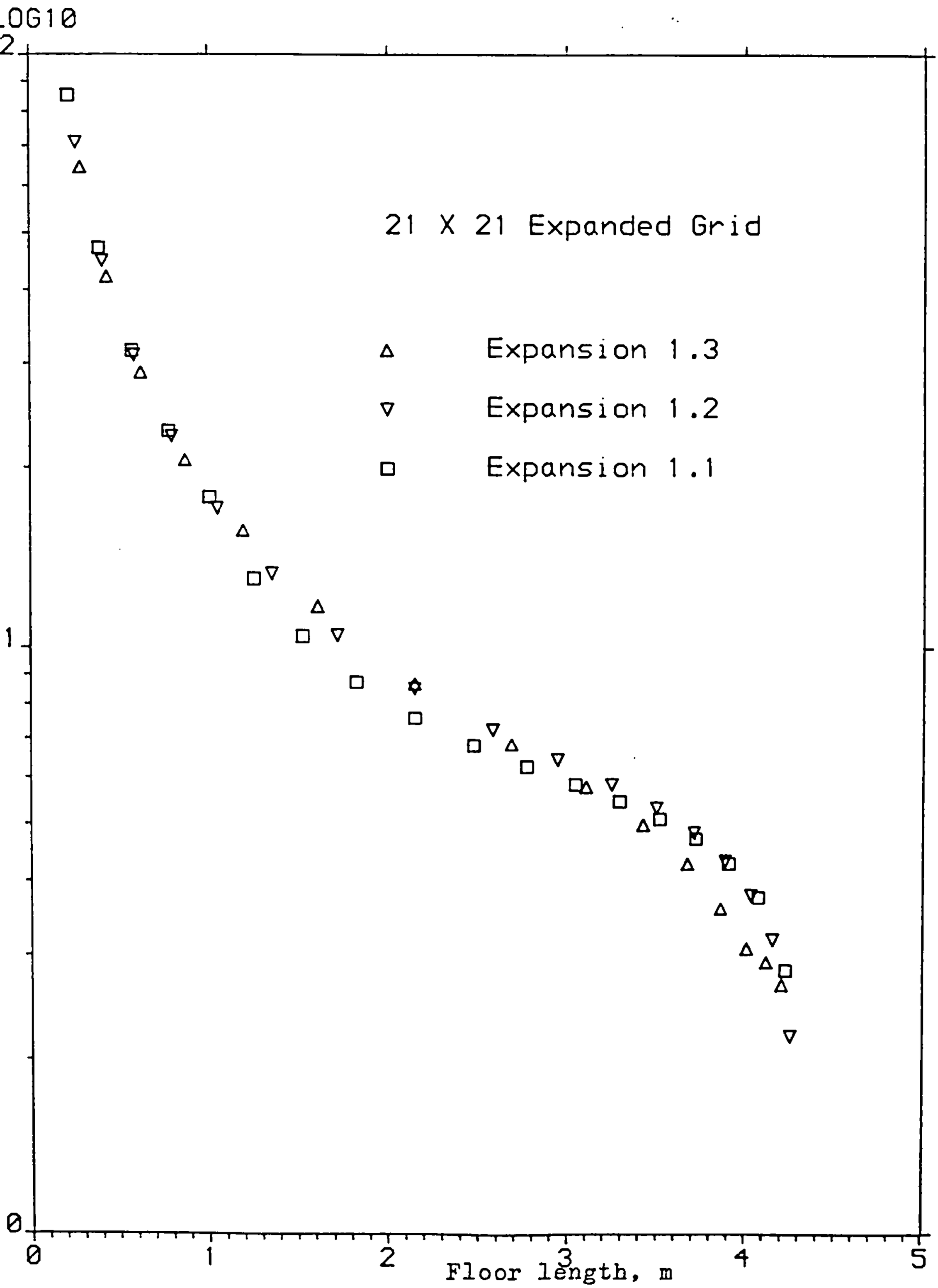

Fig. 3.14a: Computed Local Heat Transfer Coefficients along the Floor, for 21X21 Grid (Grid expansion test).

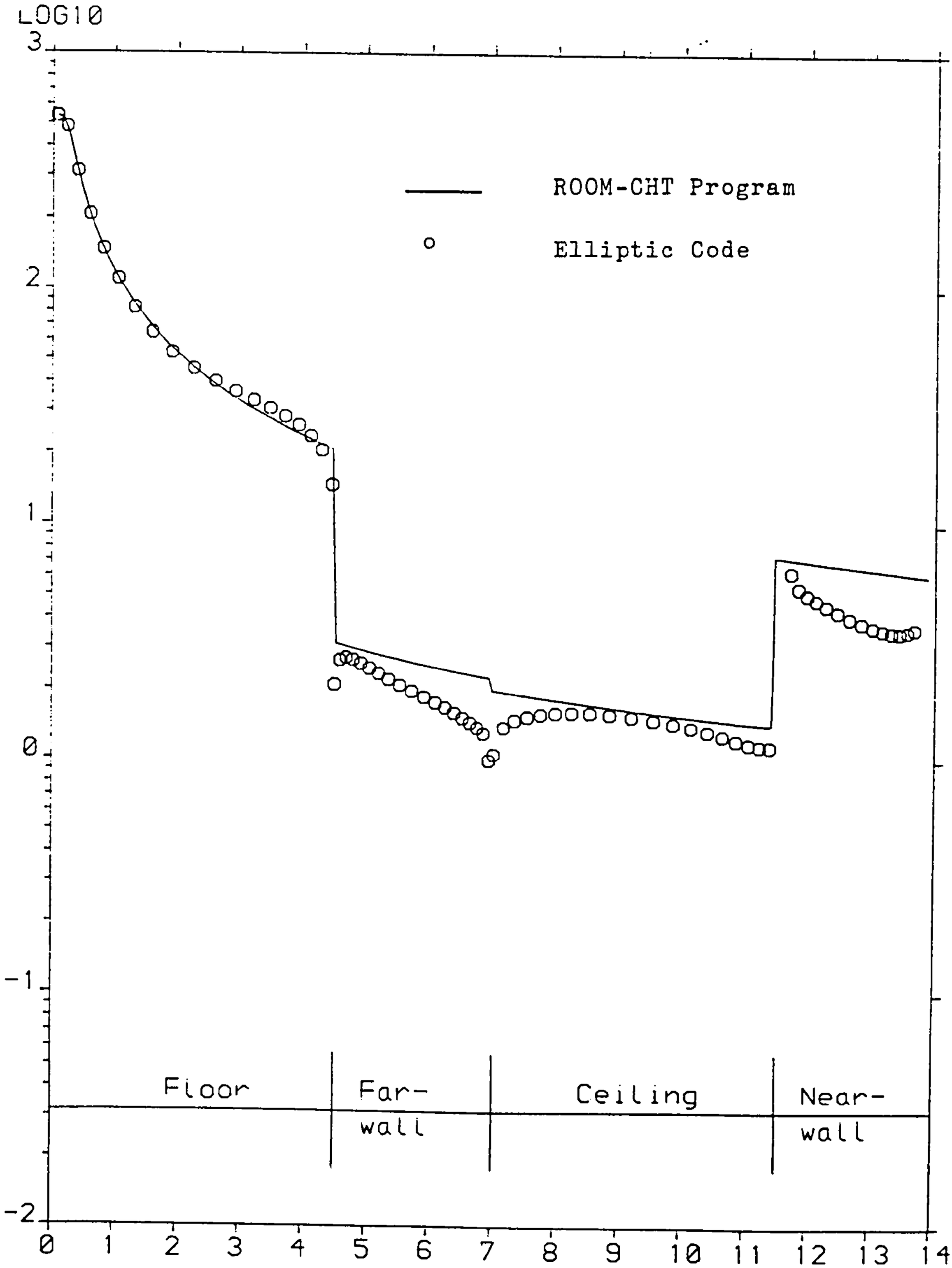

Fig. 3.14b: **Computed Local Heat Transfer Coefficients with 21X21 Grid and Expansion 1.1.**

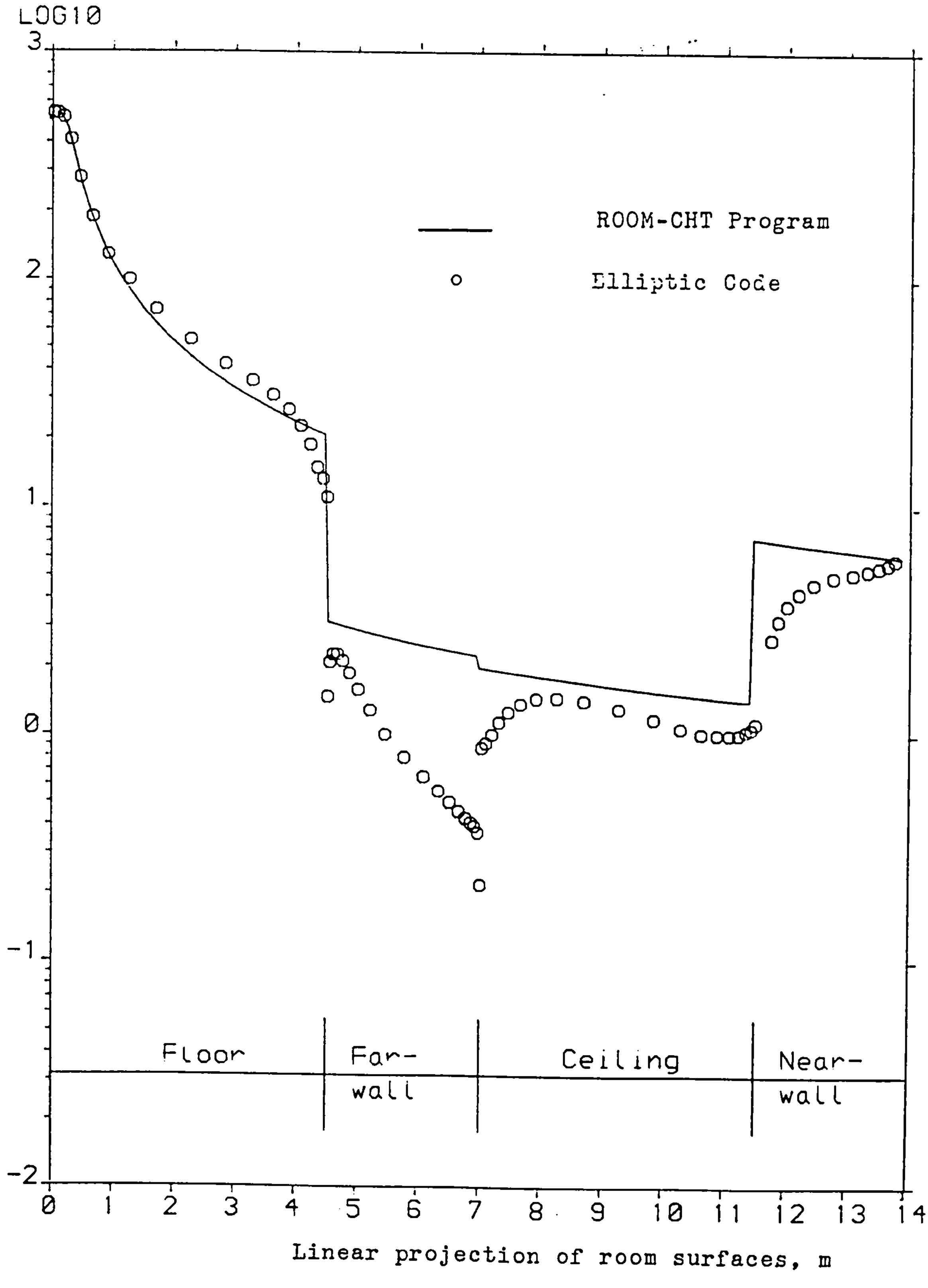

Fig. 3.14c: Computed Local Heat Transfer Coefficients with 21X21 Grid and Expansion 1.3.

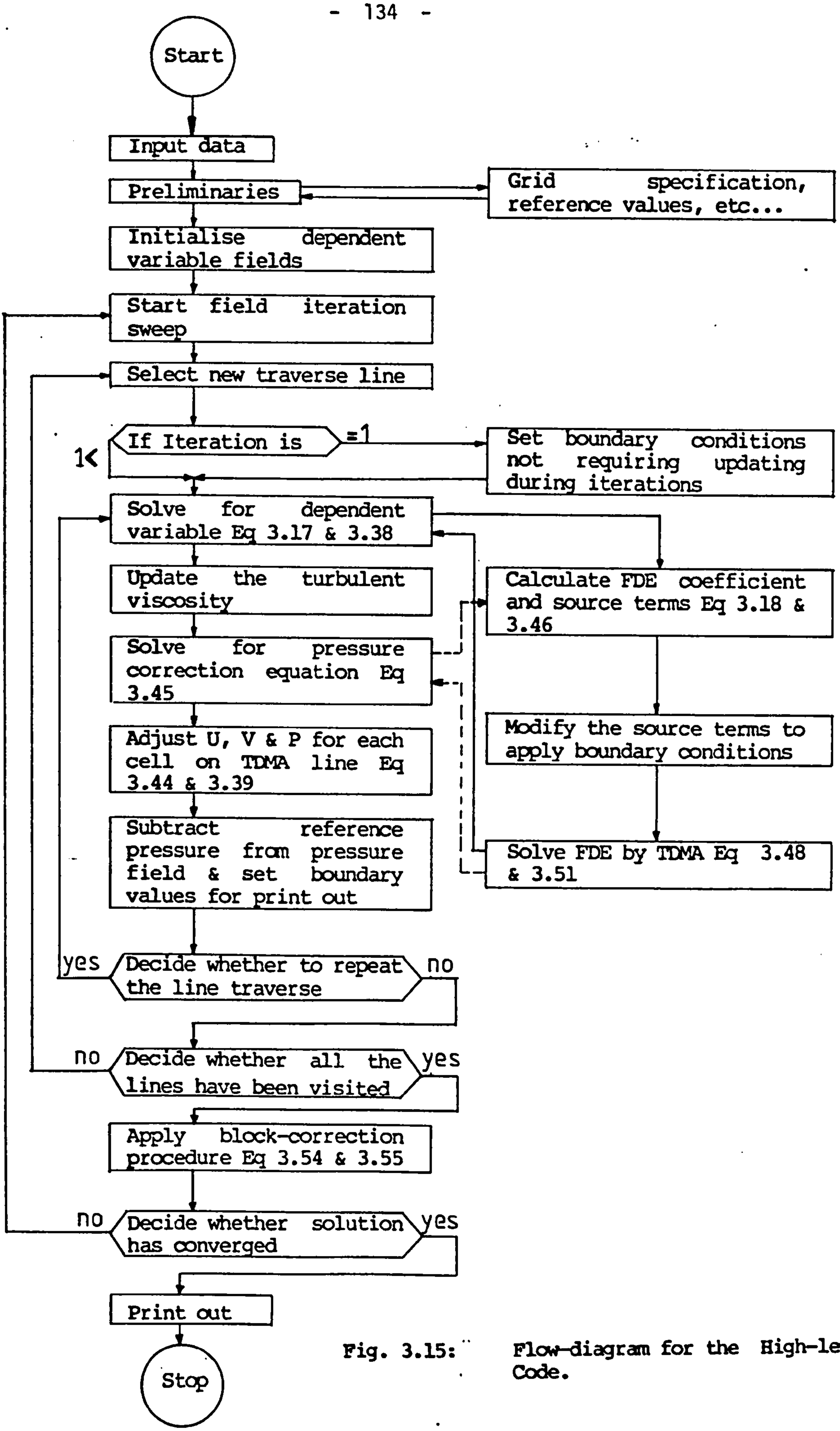

Fig. 3.15: Flow-diagram for the High-level Code.

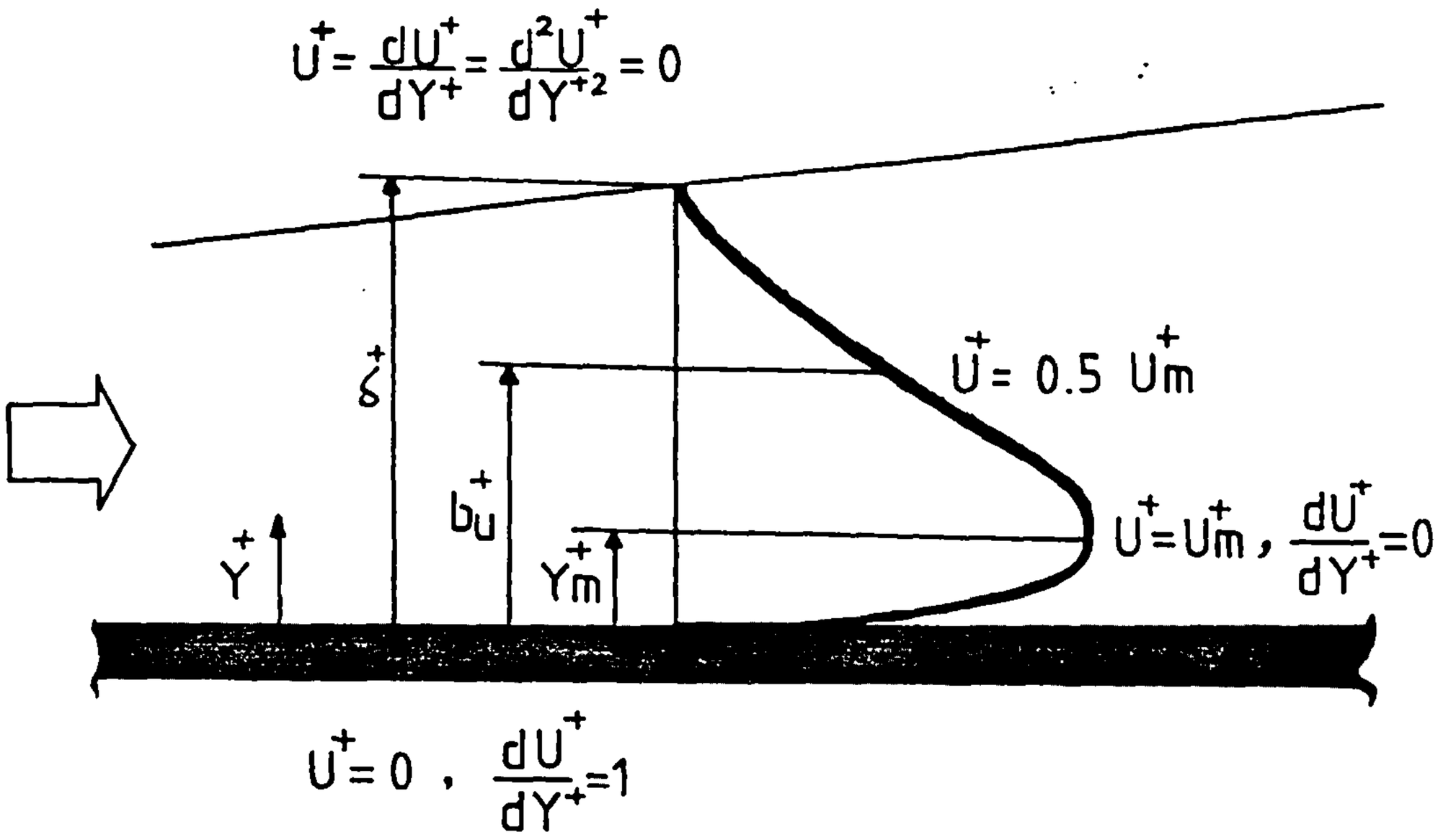

(a)

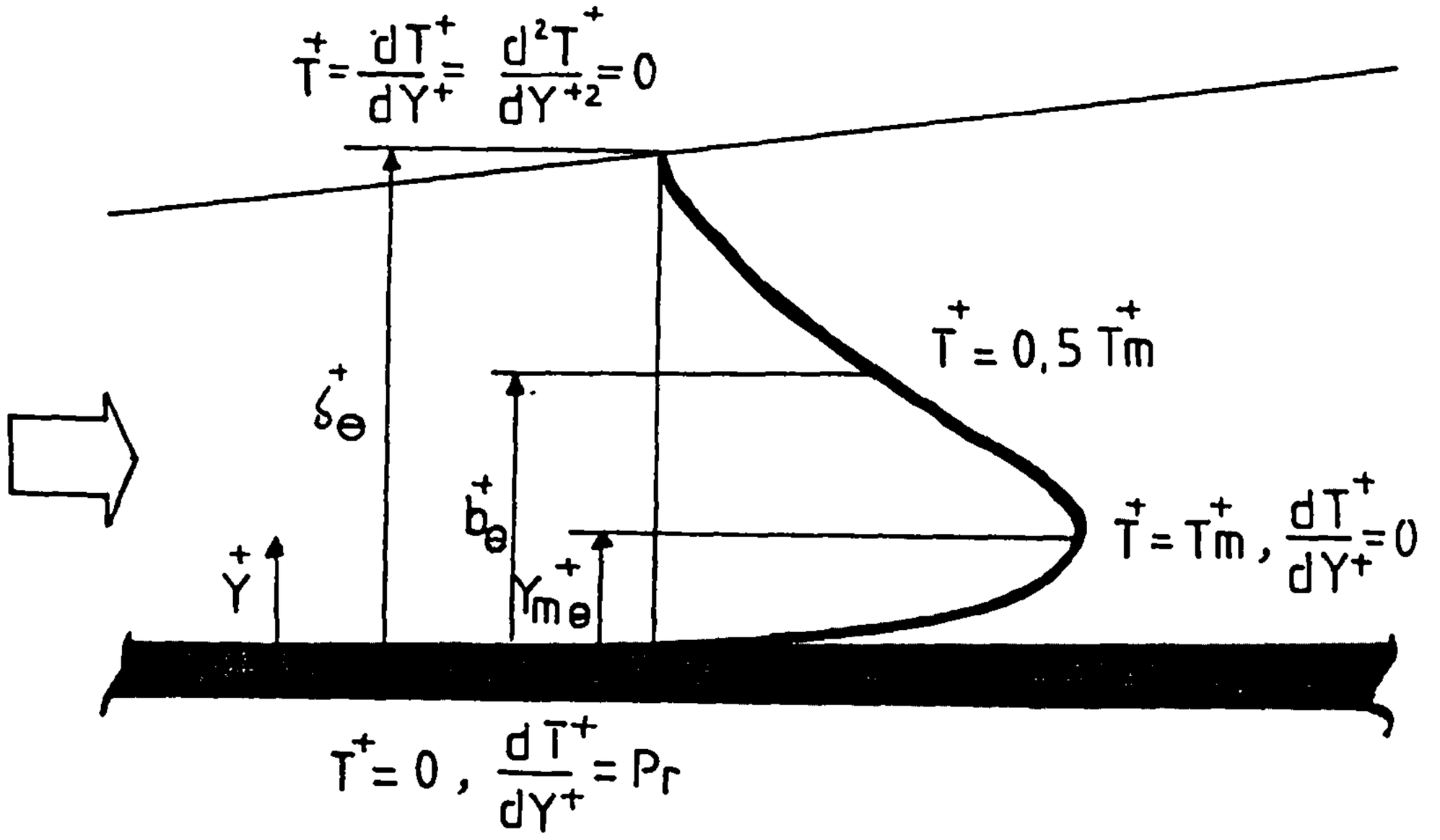

(b)

Fig. 4.1: Wall-jet Notation and Boundary Conditions (Hammond, ref 34).

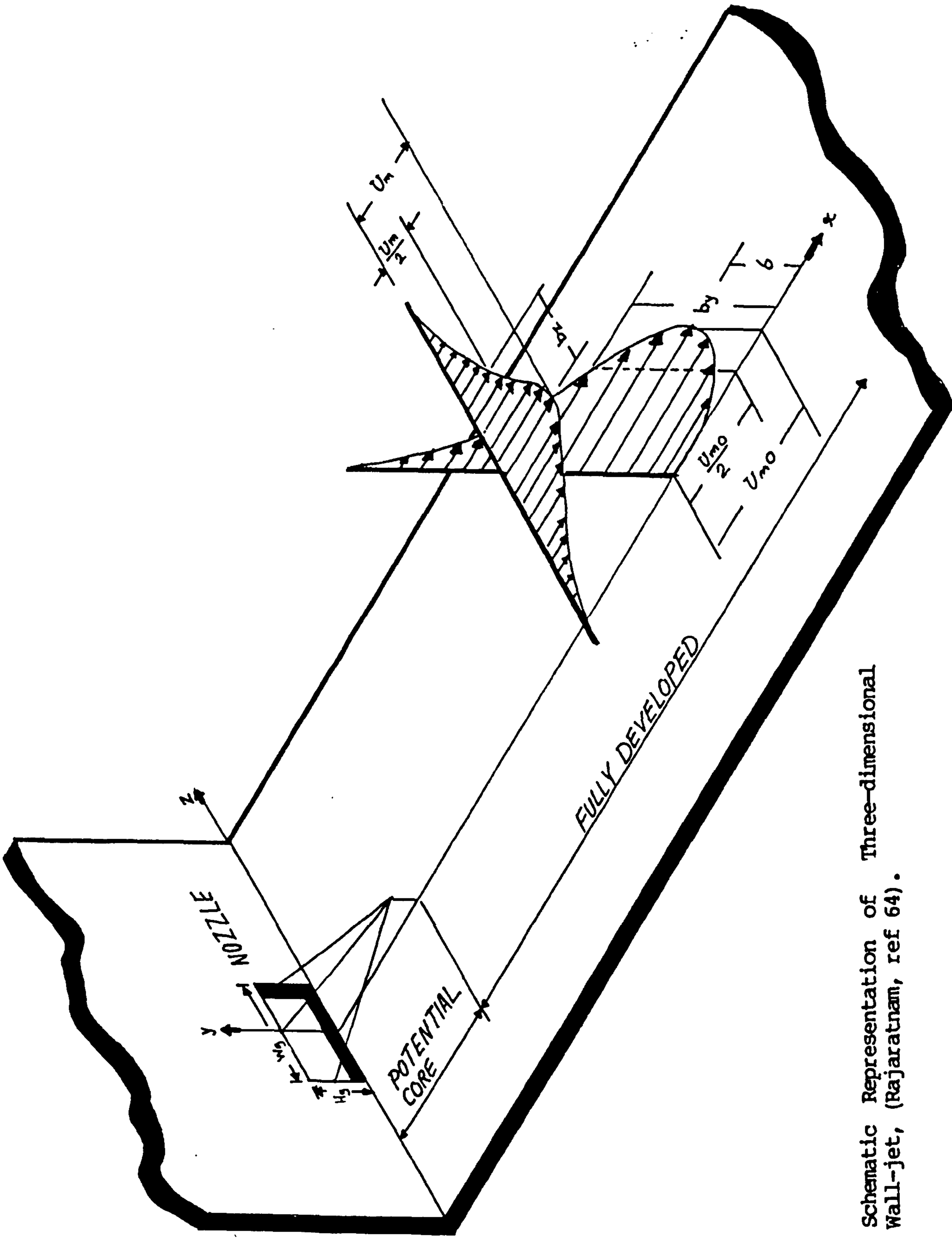

Fig. 4.2: Schematic Representation of Three-dimensional Wall-jet, (Rajaratnam, ref 64).

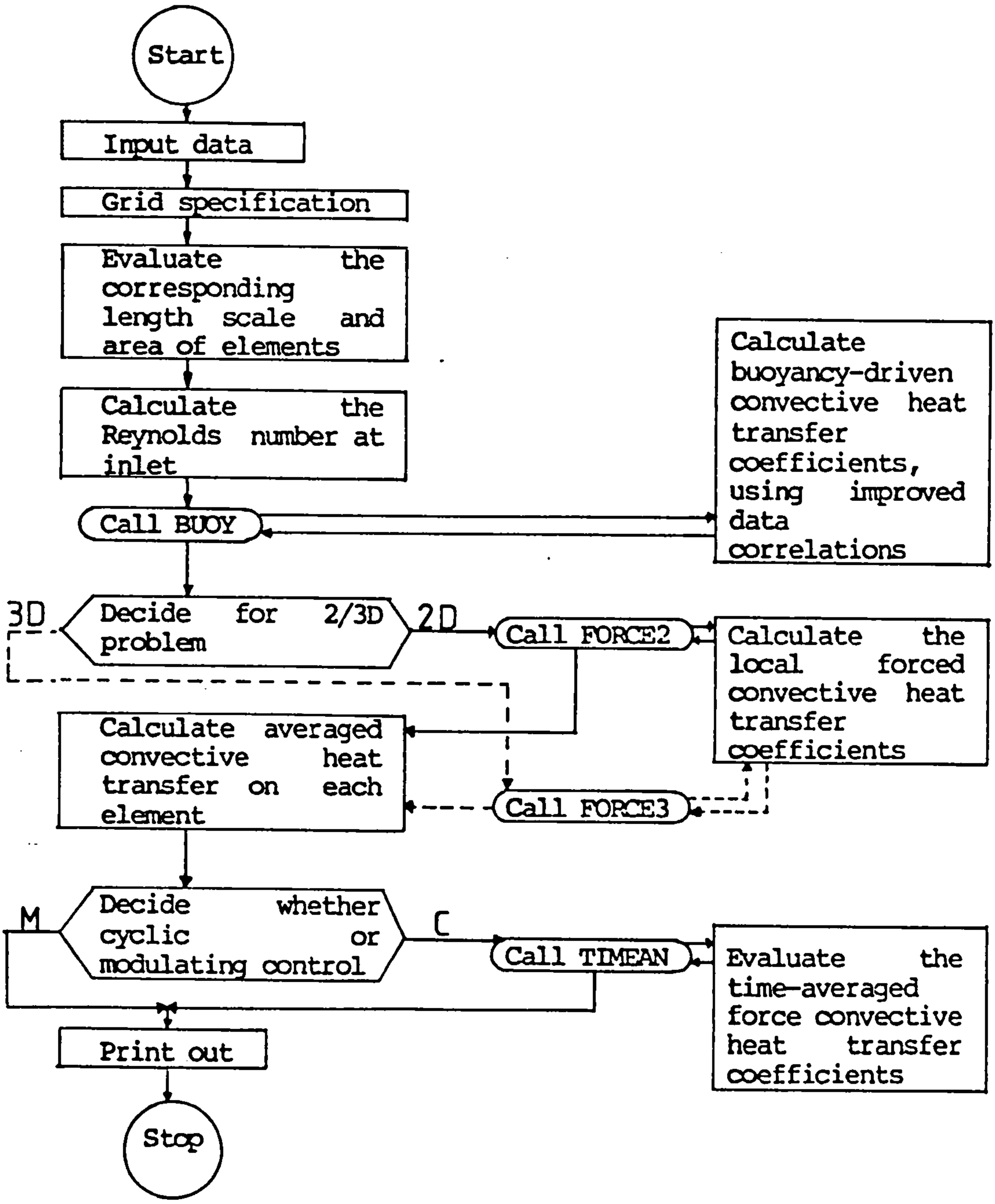

Fig. 4.3: Flow-diagram for the Intermediate-level (the ROOM-CHT) Program.

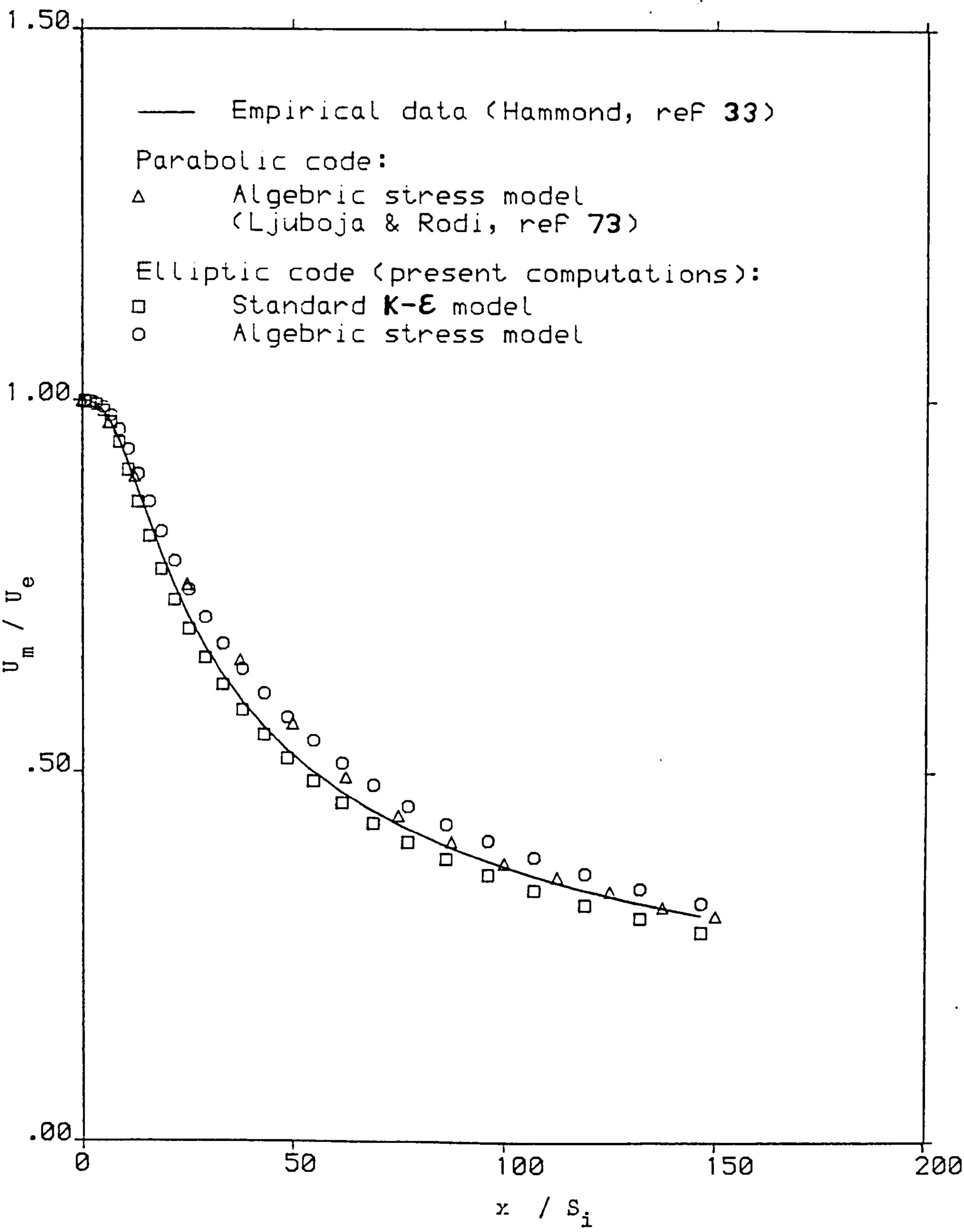

Fig. 5.1: **Streamwise Development of Um/Ue.**

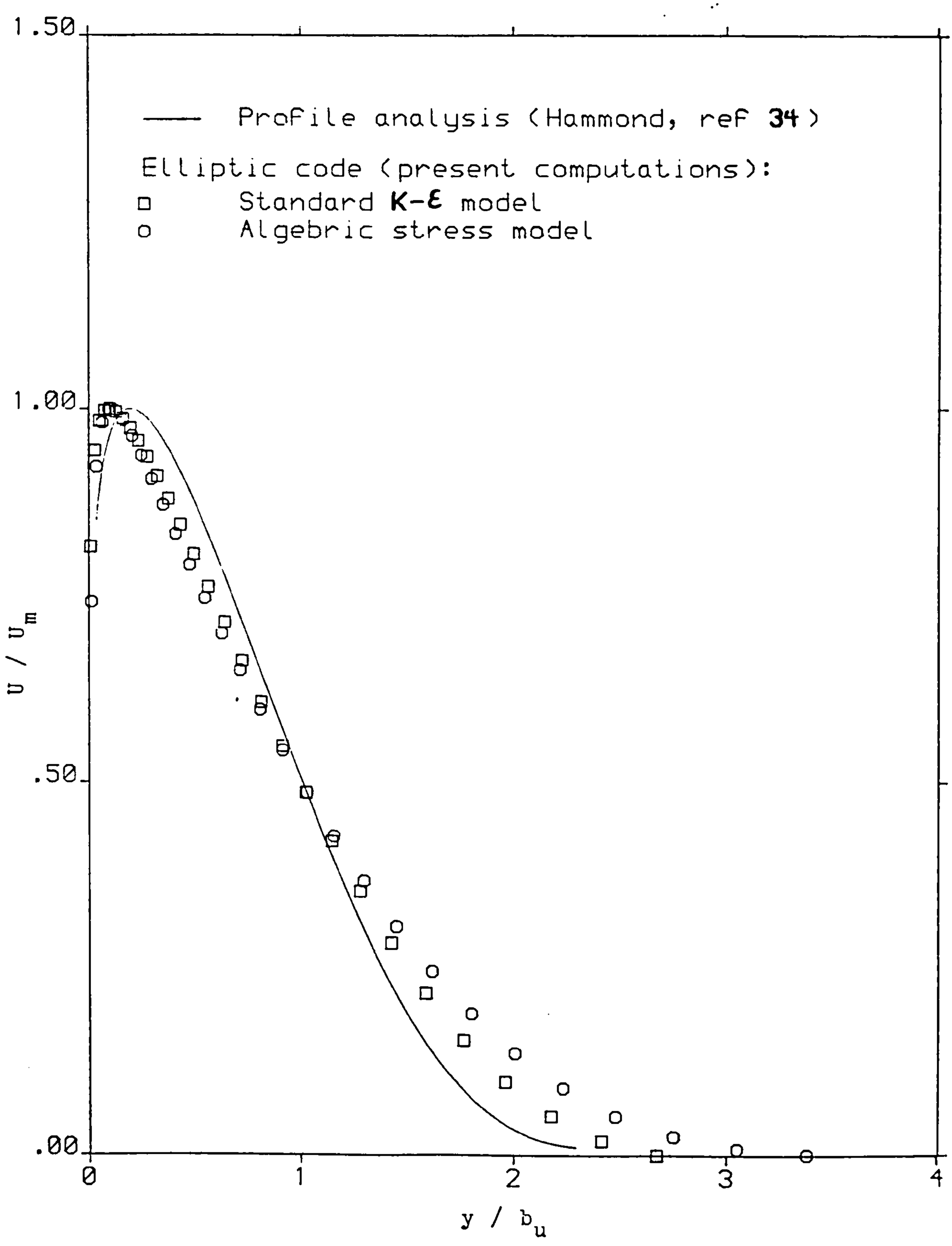

Fig. 5.2: **Cross-stream Distribution of U/Um.**

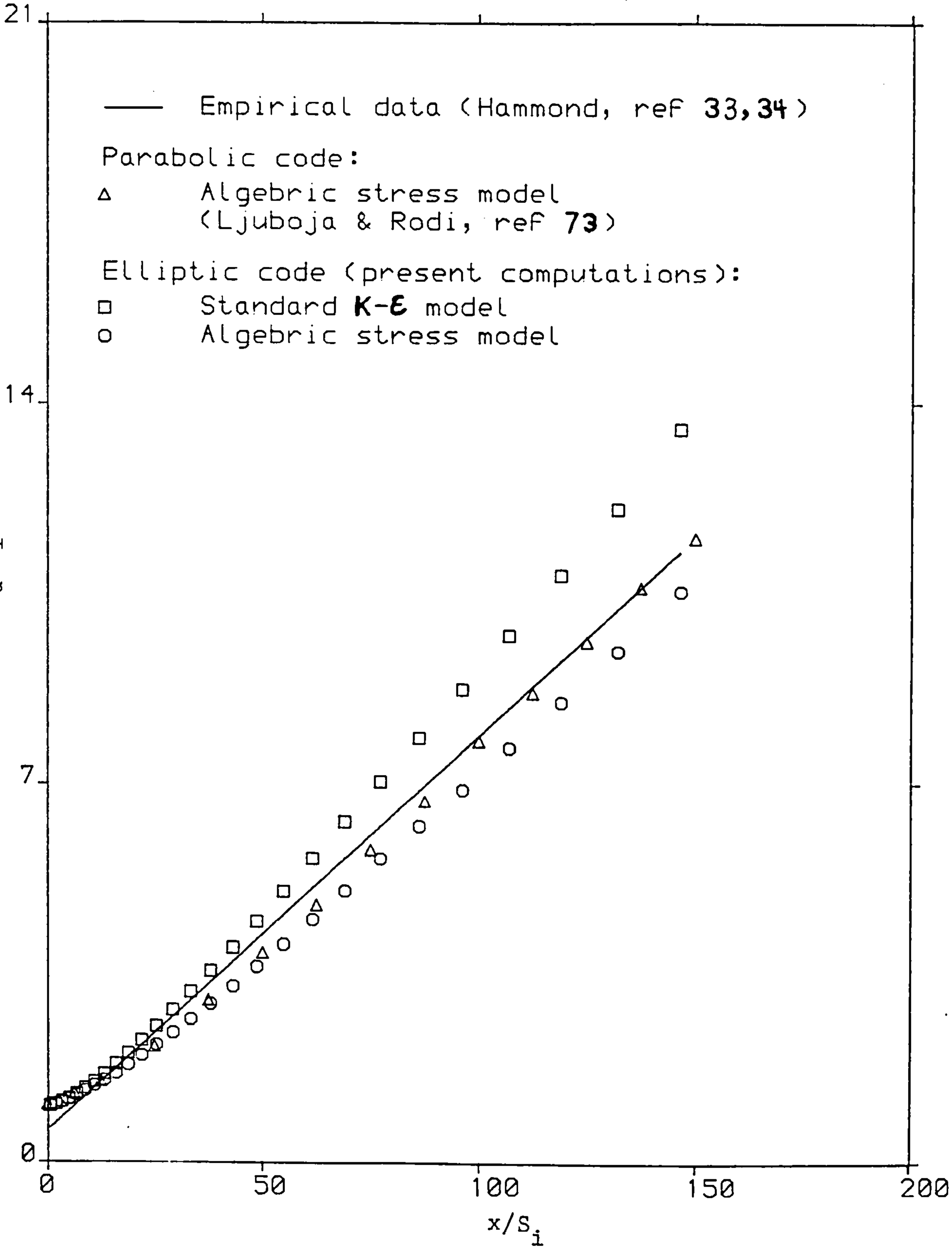

Fig. 5.3: Streamwise Development of b_u/Si.

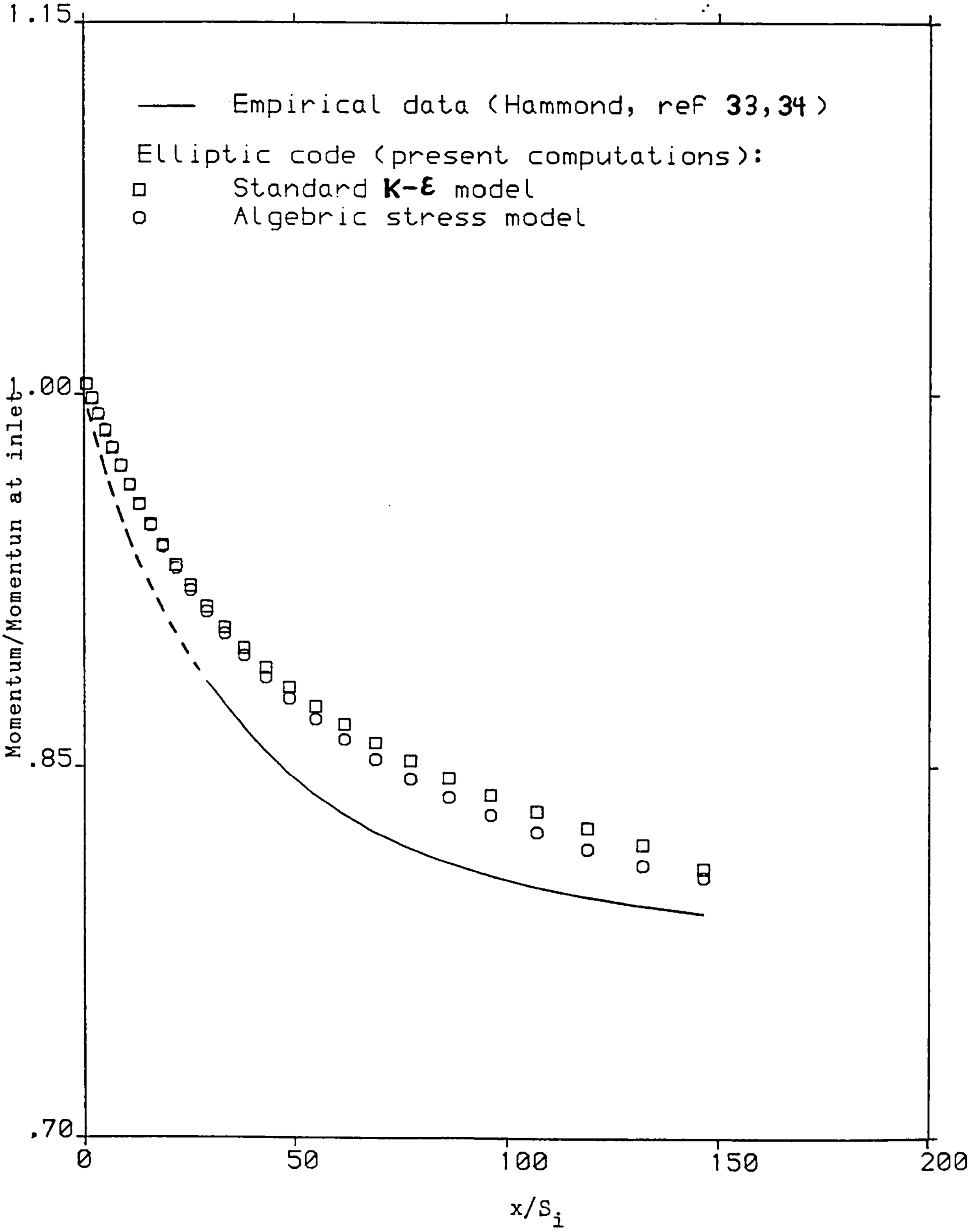

Fig. 5.4: **Streamwise Momentum Distribution.**

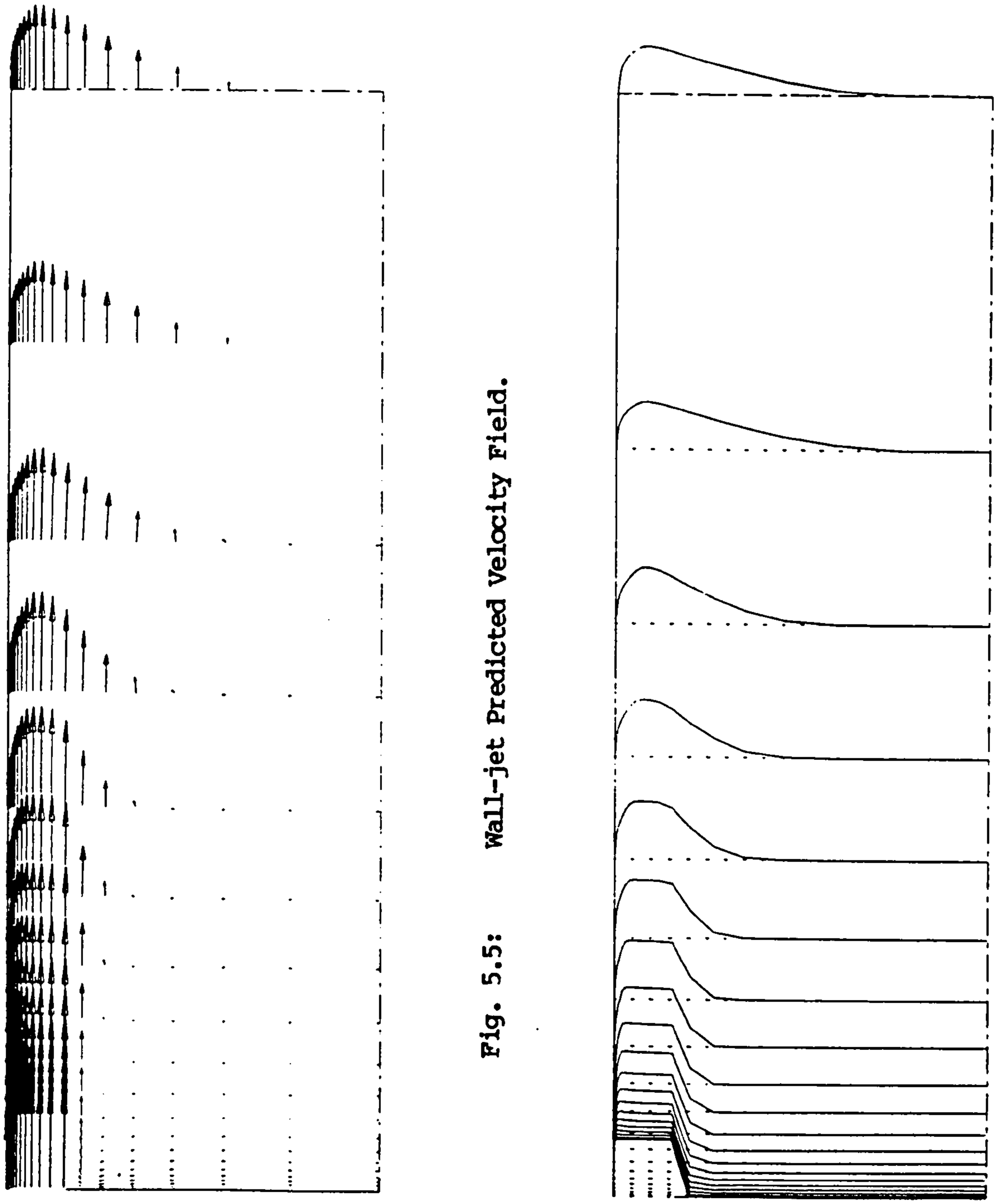

Fig. 5.5: Wall-jet Predicted Velocity Field.

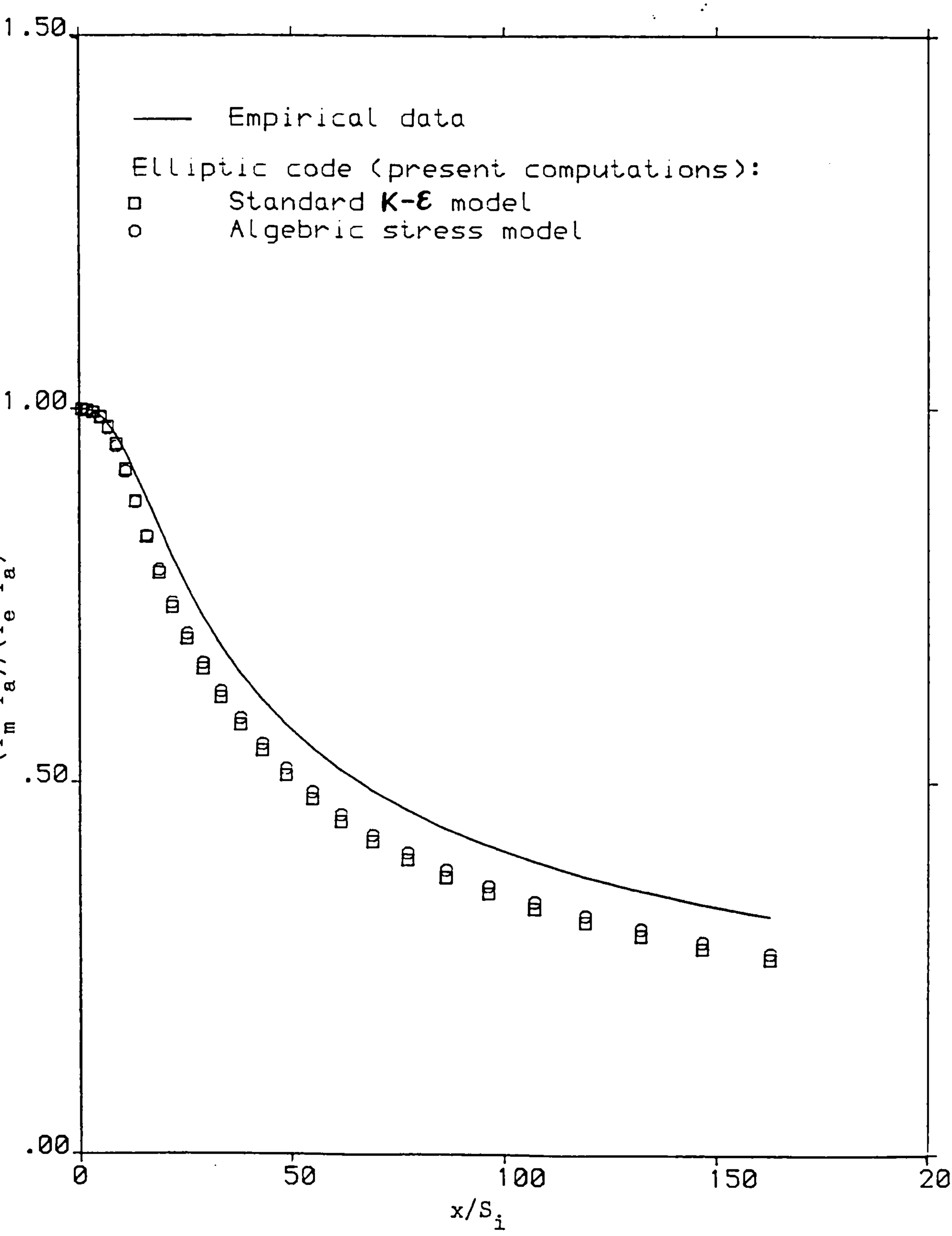

Fig. 5.6: Streamwise Development of (Tm-Ta)/(Te-Ta).

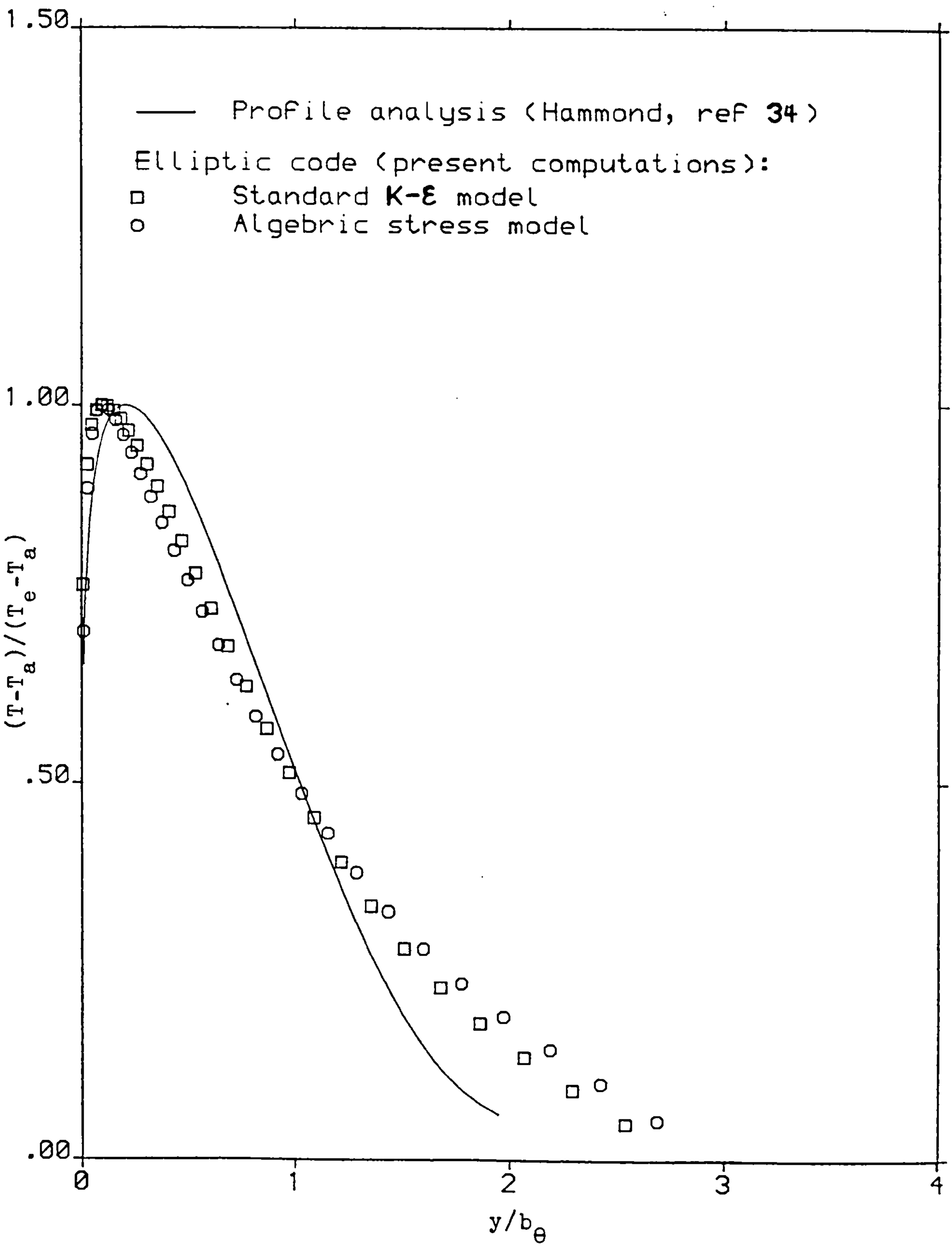

Fig. 5.7: **Cross-stream Distribution of (T-Ta)/(Tm-Ta).**

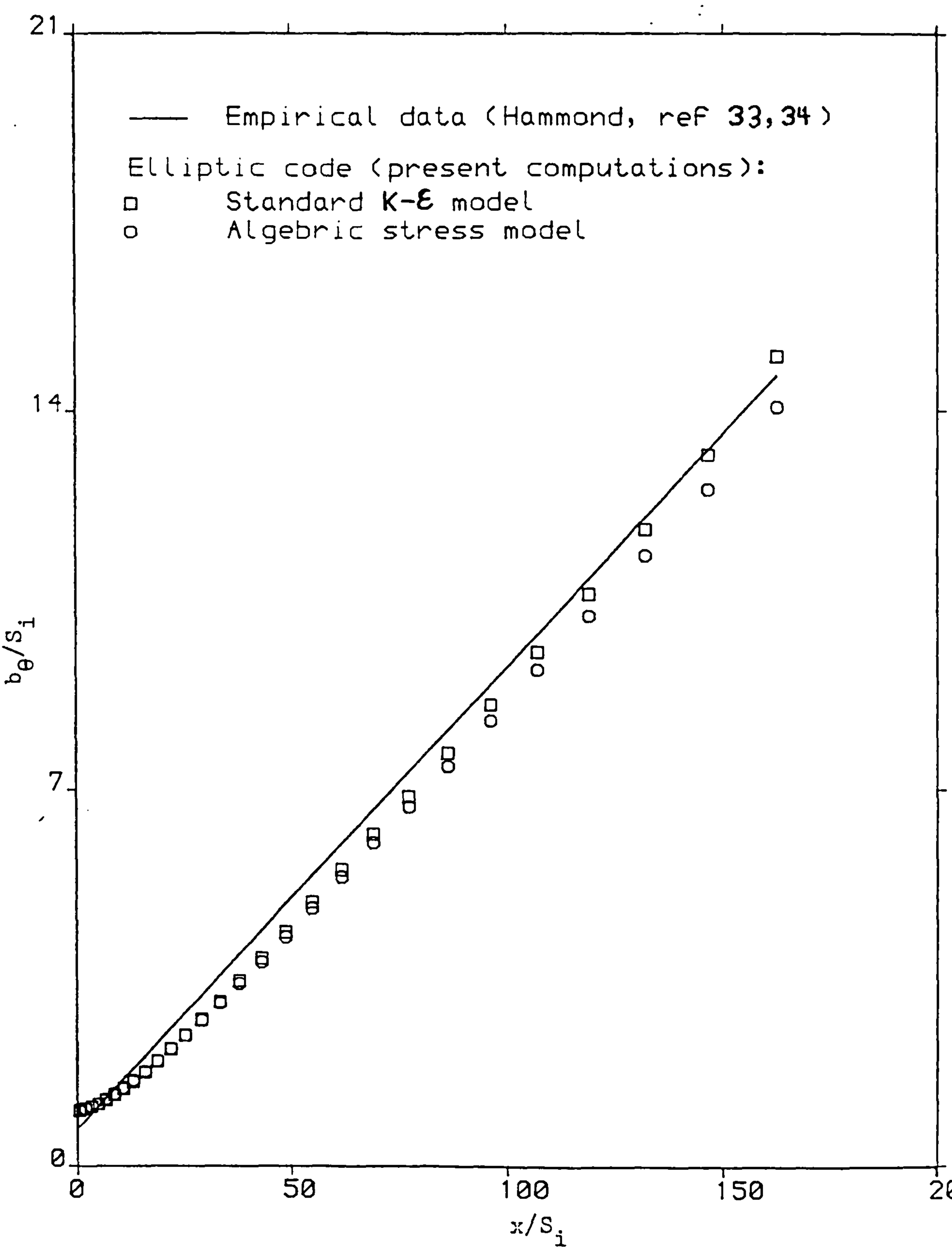

Fig. 5.8: Streamwise Development of b_θ/Si.

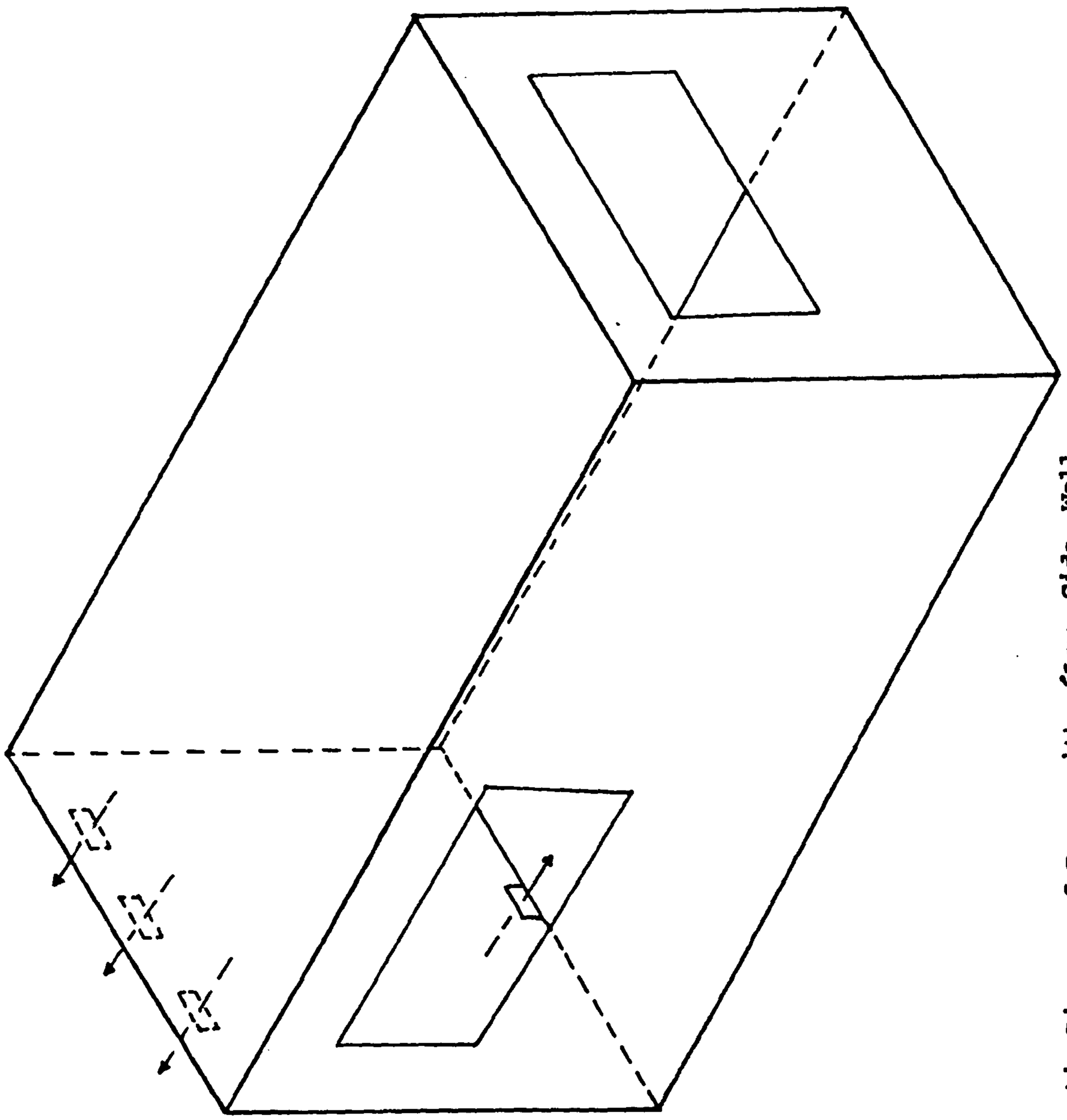

Fig. 5.9: Schematic Diagram of Room with 'Low Side Wall Register'.

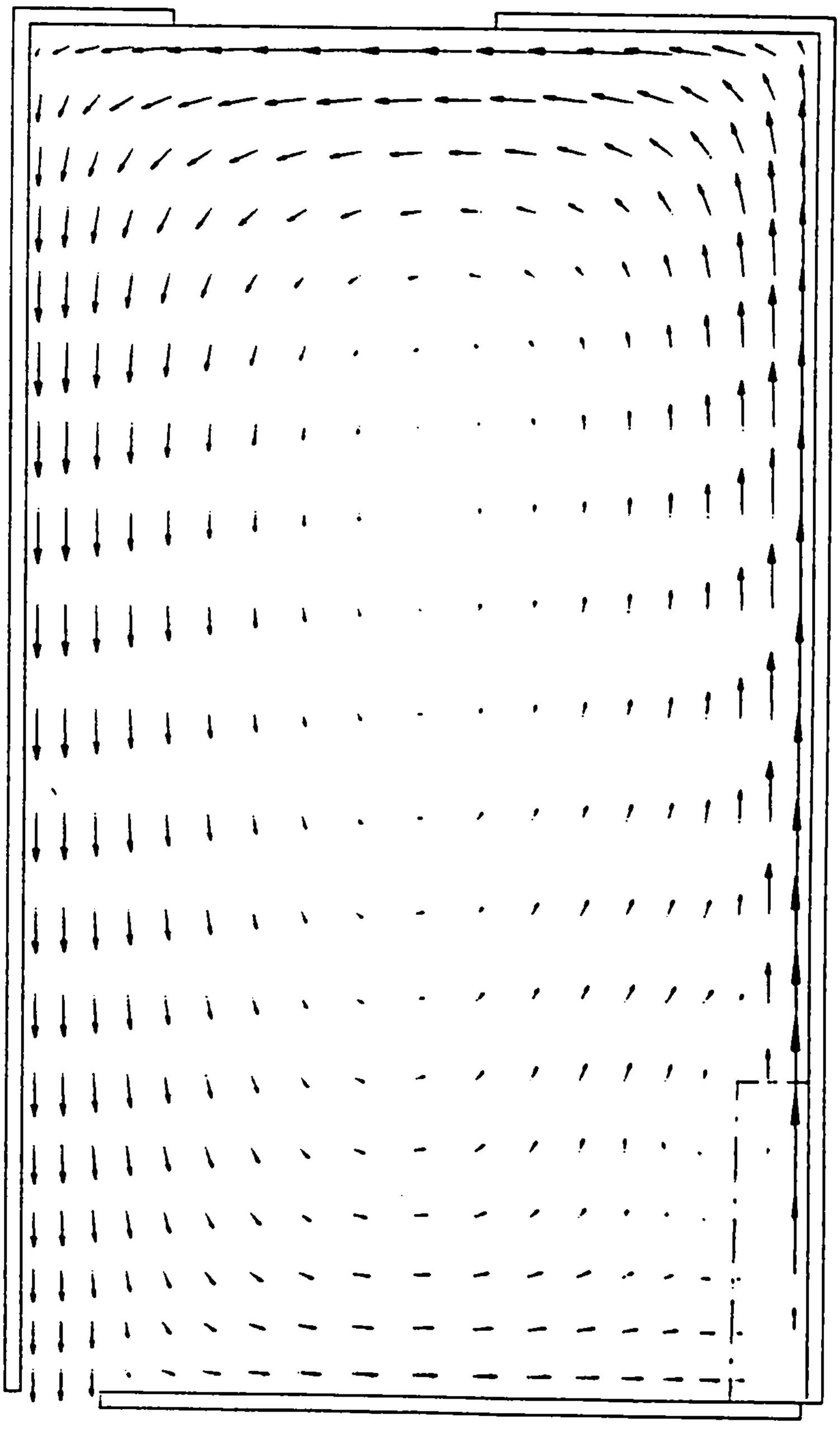

Fig. 5.10a: Predicted Flow Pattern for Case No. 1 of Table 5.2. 'Non-buoyant Version of the Elliptic Code'

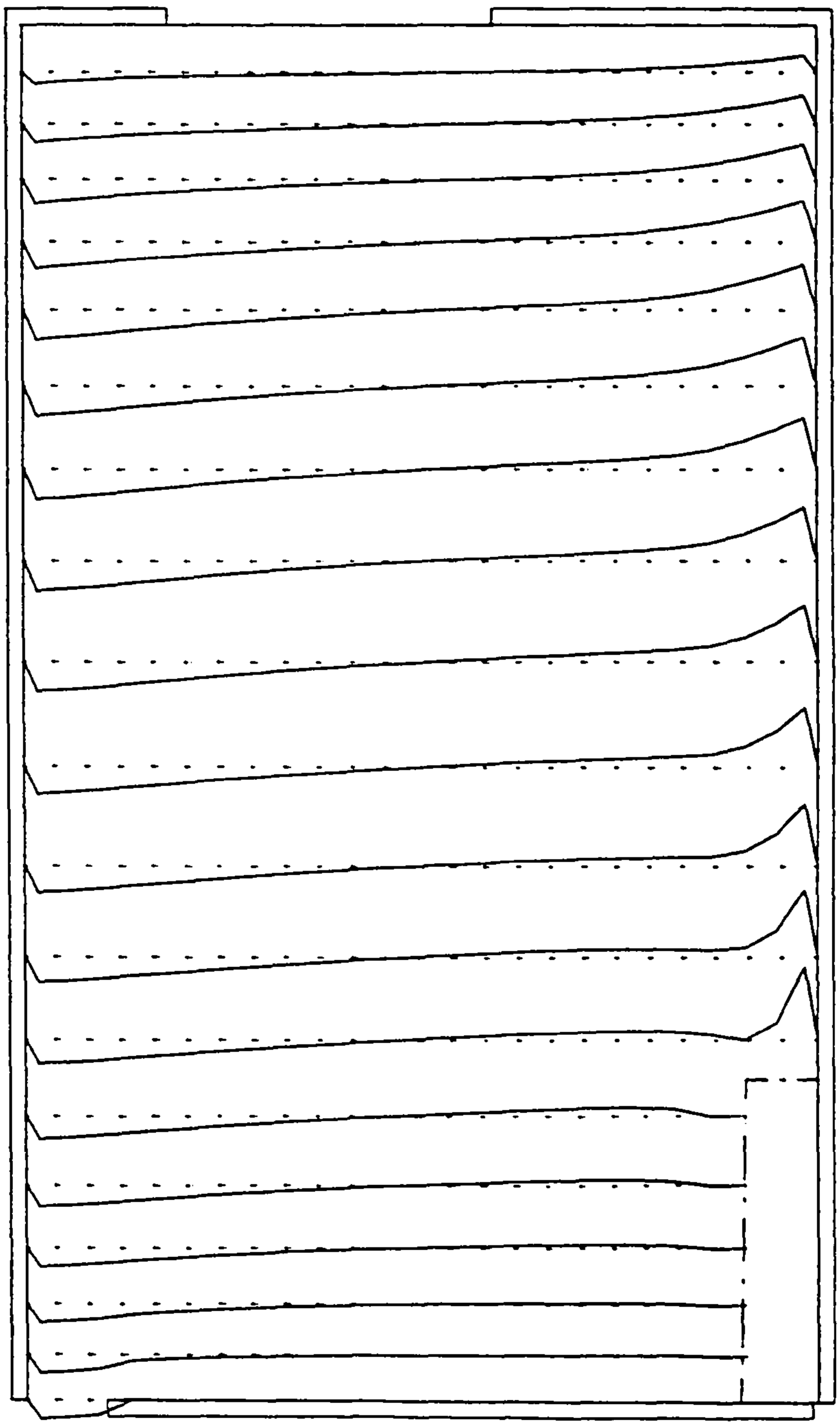

Fig. 5.10b: Predicted U-velocity for Case No. 1 of Table 5.2.
'Non-buoyant Version of the Elliptic Code'

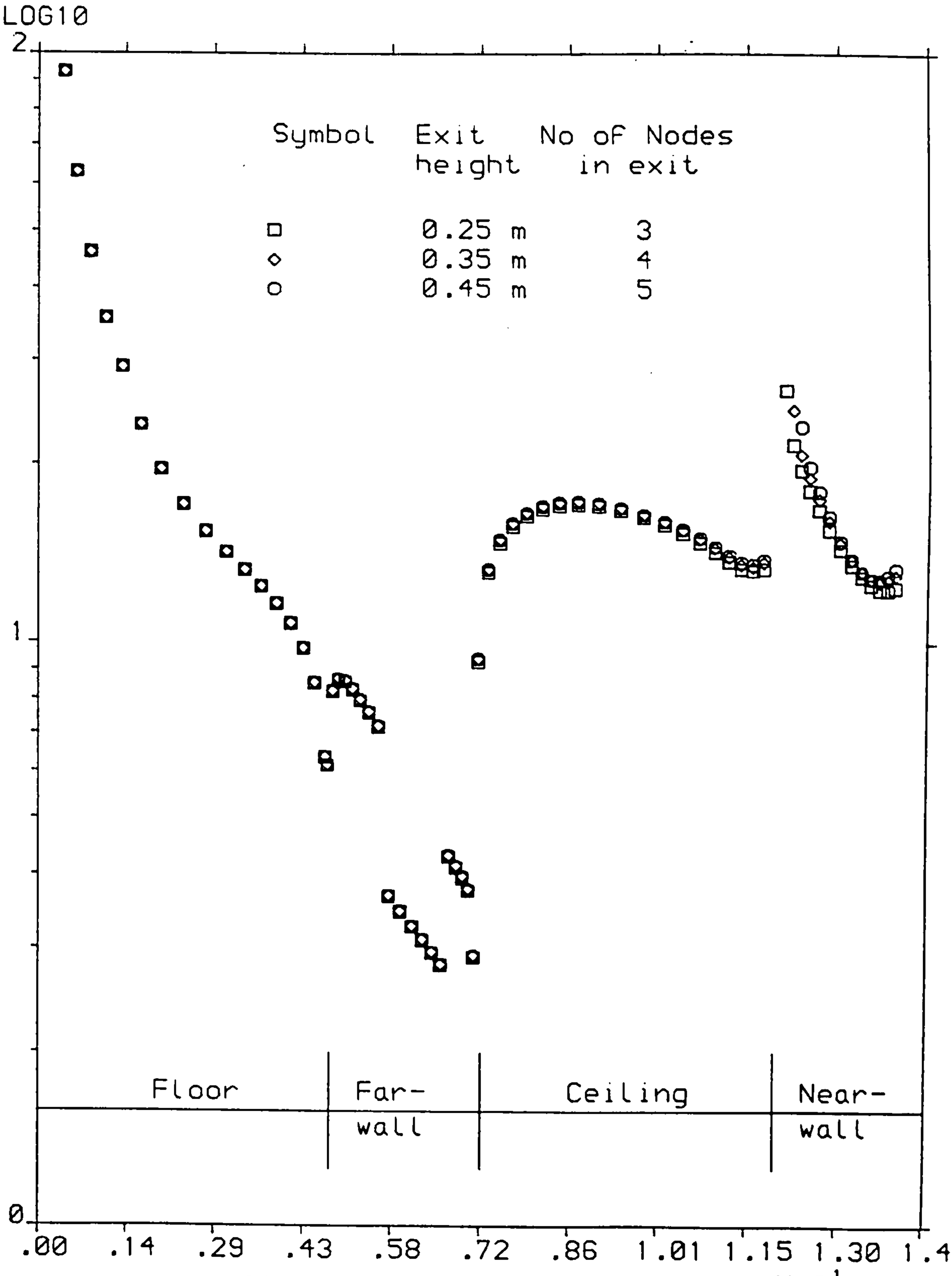

Fig. 5.10c: Computed Local Heat Transfer Coefficients- Test for Slot Outlet's Height.

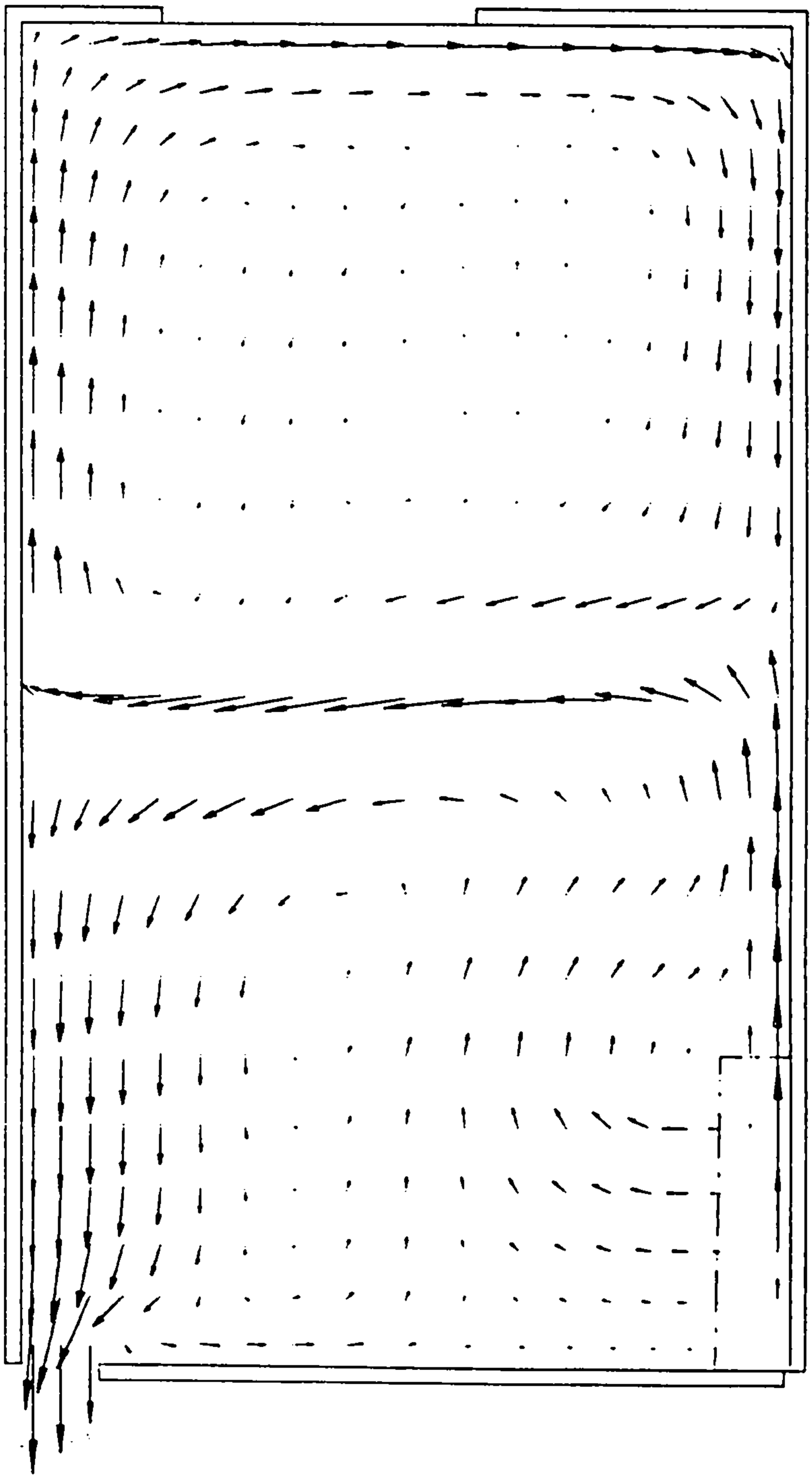

Fig. 5.11a: Predicted Flow Pattern for Case No. 1 of Table 5.2.

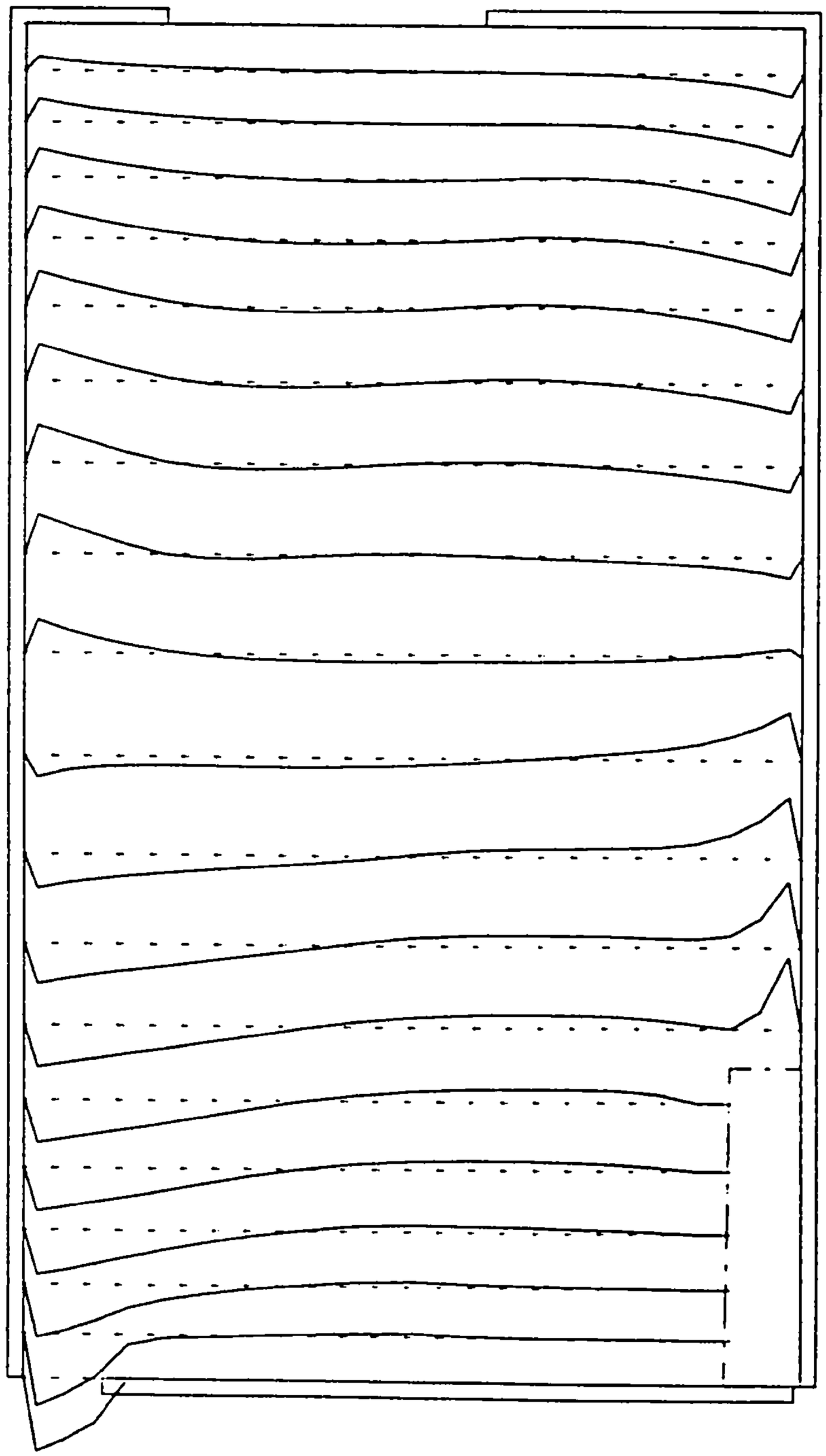

Fig. 5.11b: Predicted U-velocity Profile for Case No. 1 of Table 5.2.

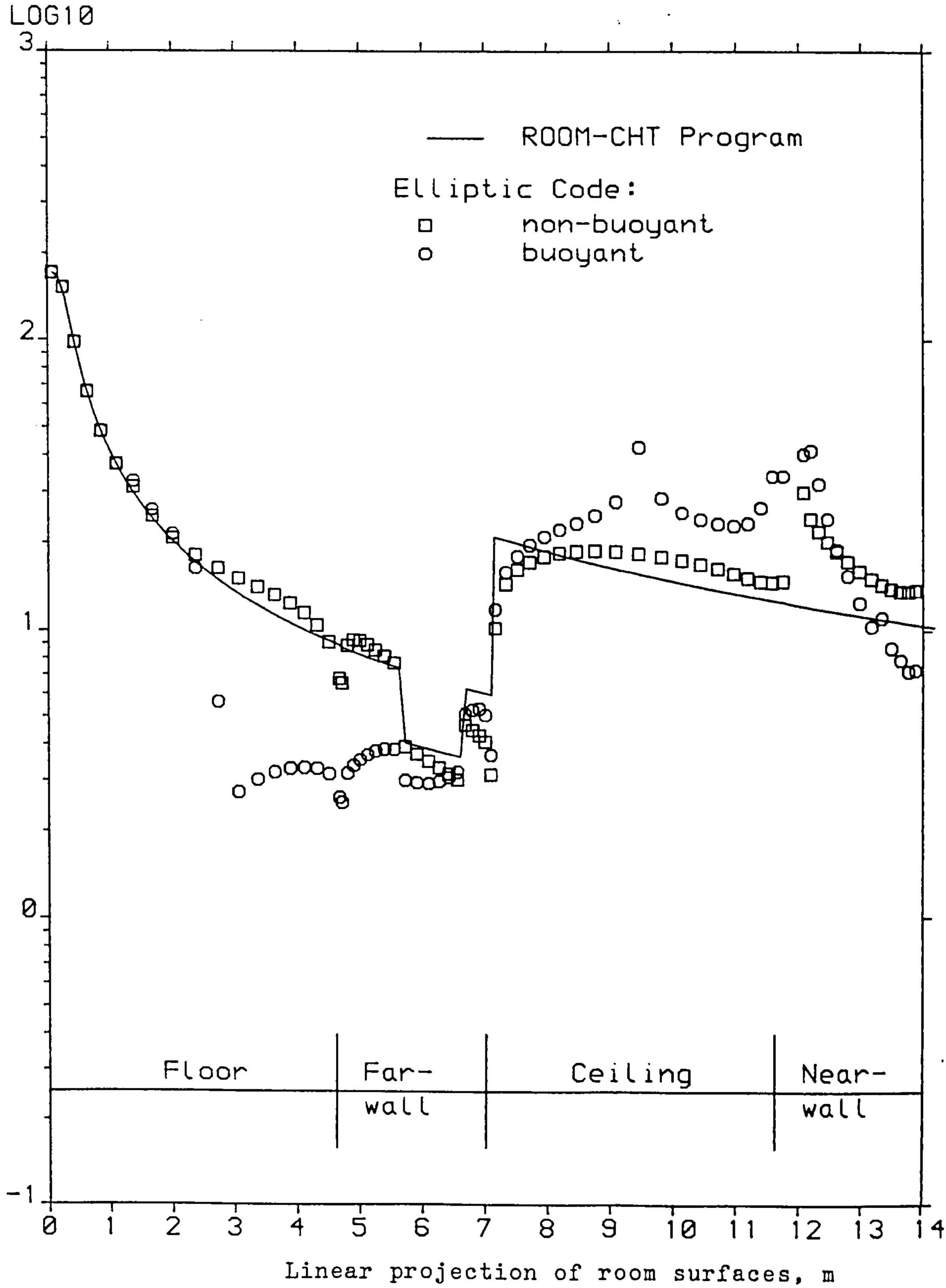

Fig. 5.11c: **Computed Local Heat Transfer Coefficients for Case No. 1 of Table 5.2.**

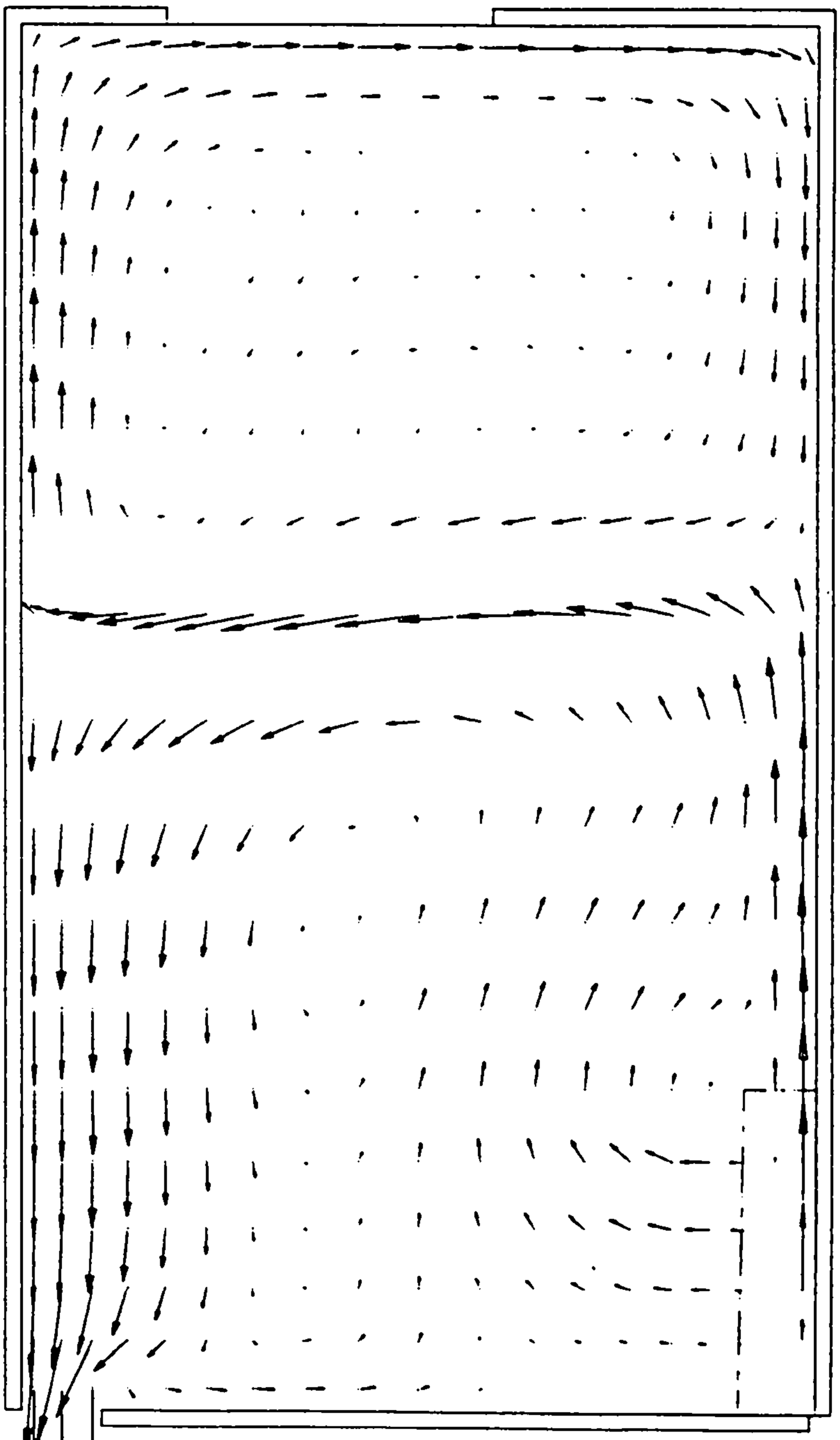

Fig. 5.12a: Predicted Flow Pattern for Case No. 2 of Table 5.2.

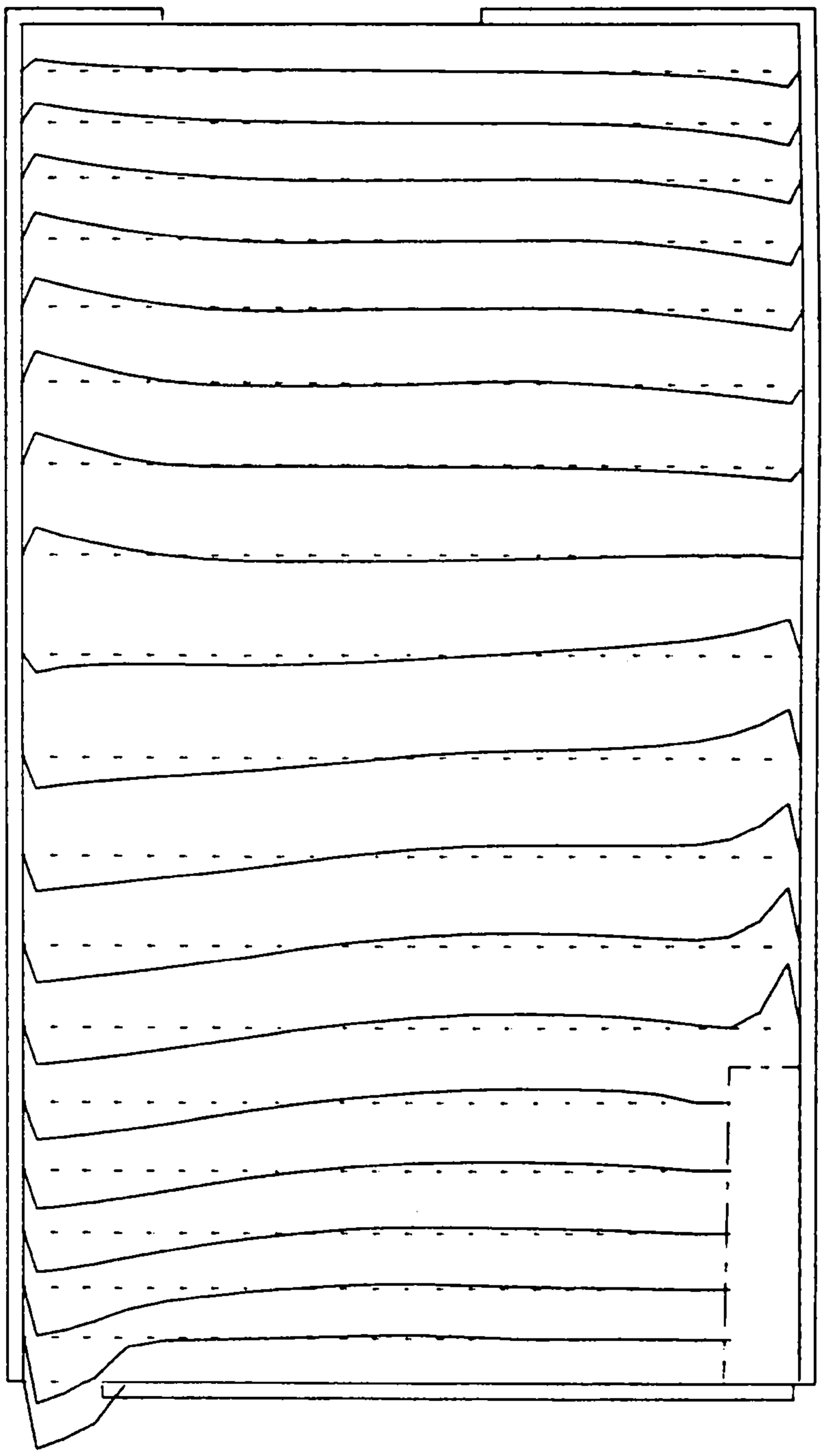

Fig. 5.12b: Predicted U-velocity Profile for Case No. 2 of Table 5.2.

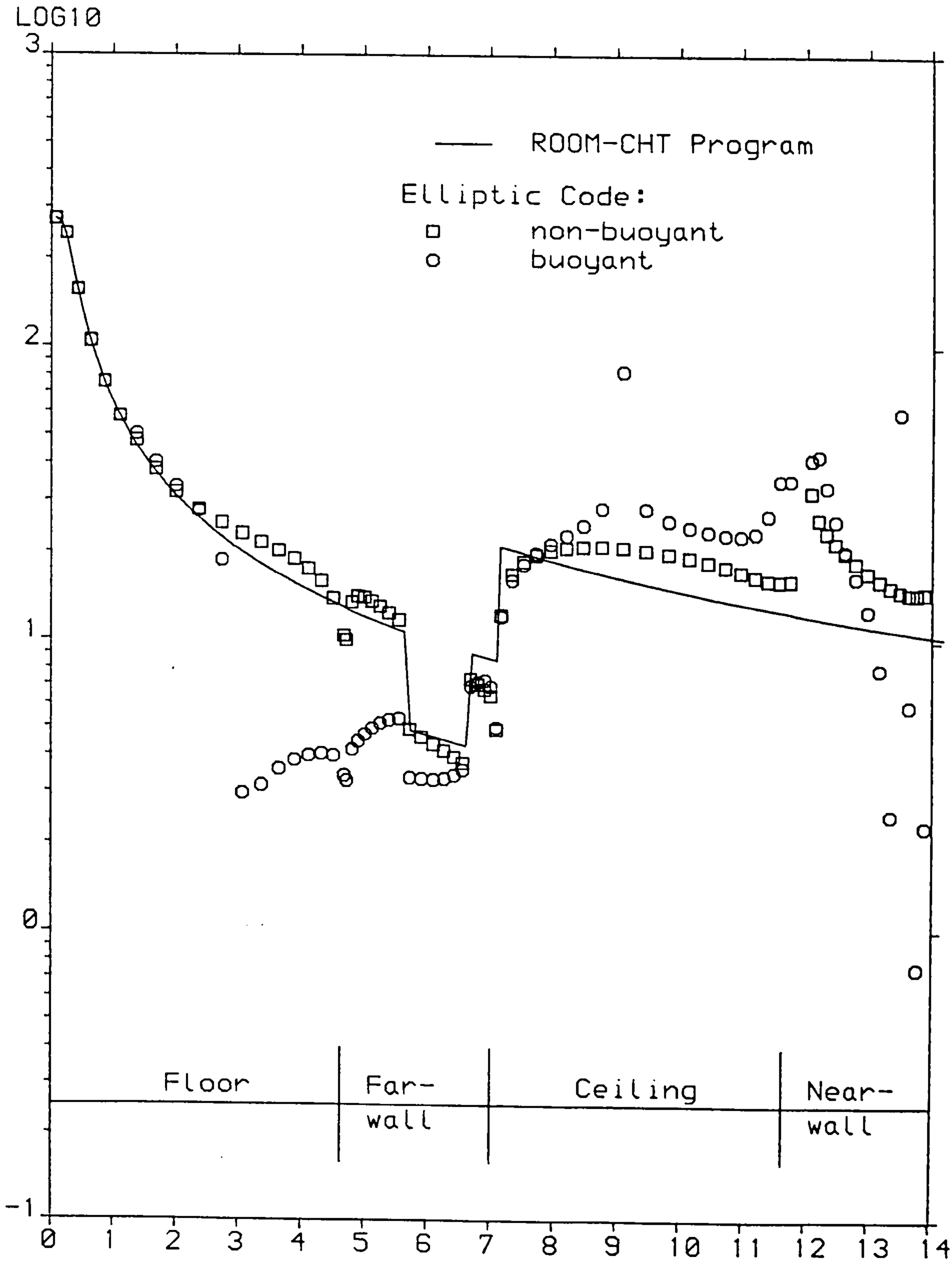

Fig. 5.12c: **Computed Local Heat Transfer Coefficients for Case No. 2 of Table 5.2.**

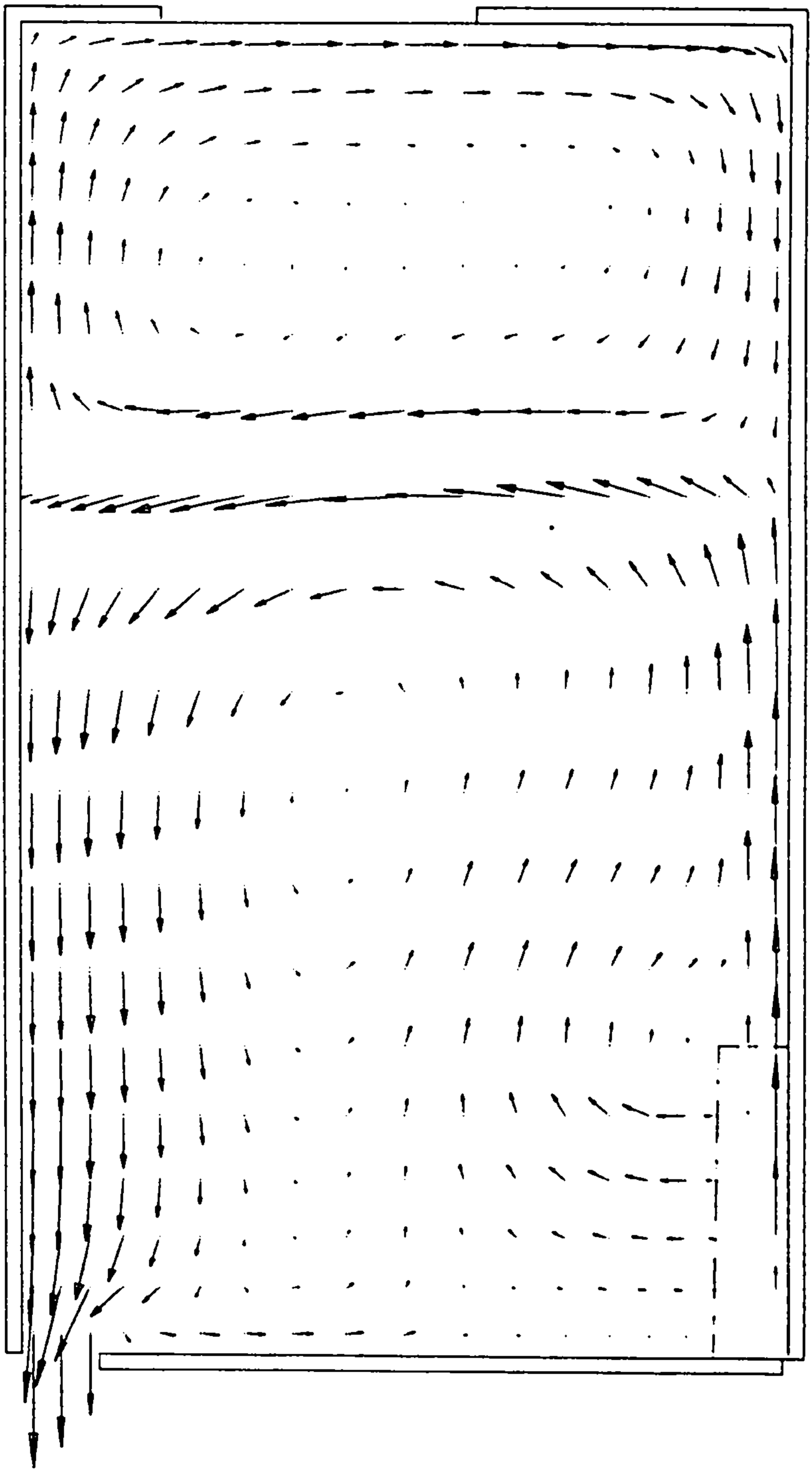

Fig. 5.13a: Predicted Flow Pattern for Case No. 3 of Table 5.2.

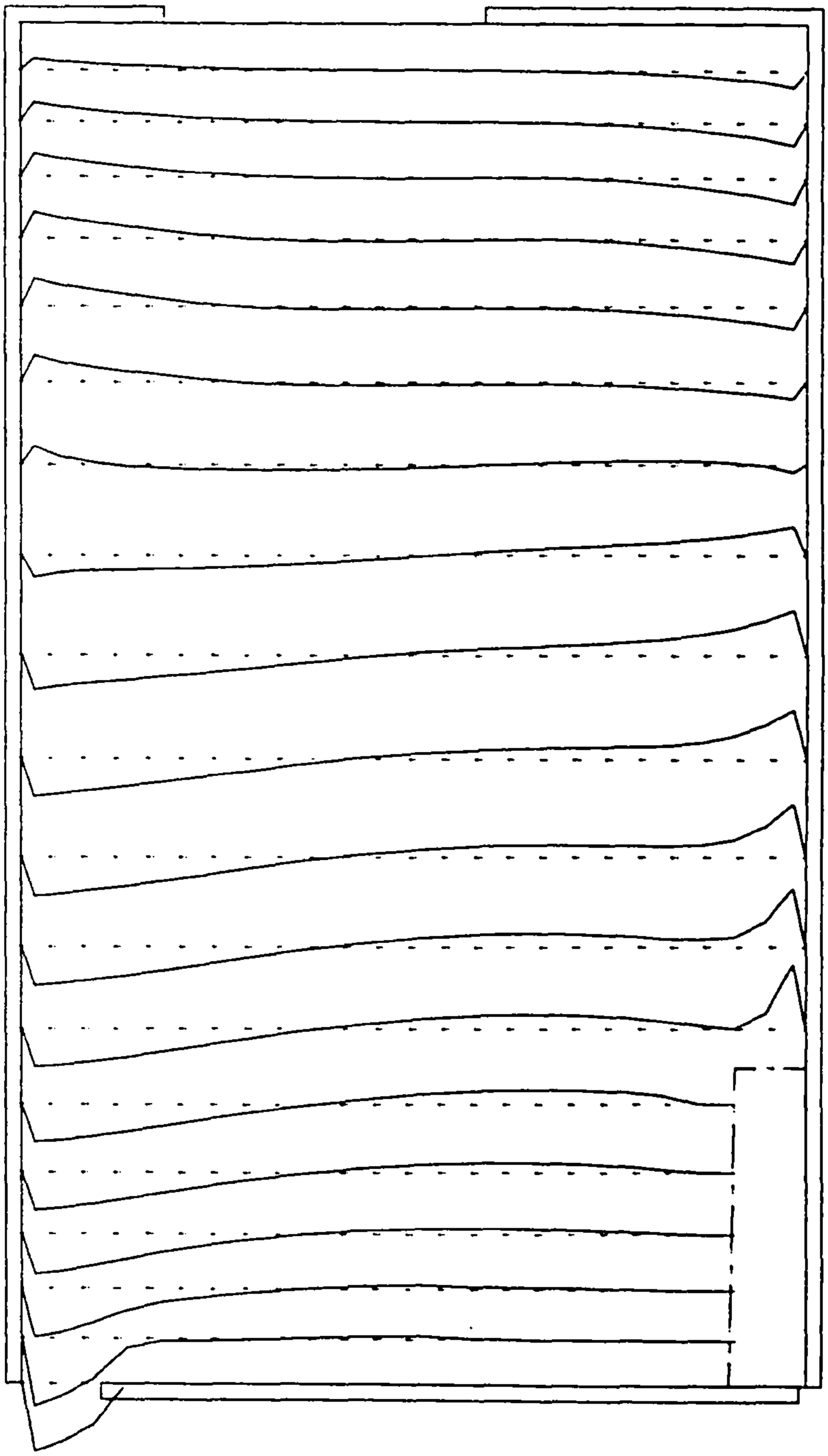

Fig. 5.13b: Predicted U-velocity Profile for Case No. 3 of Table 5.2.

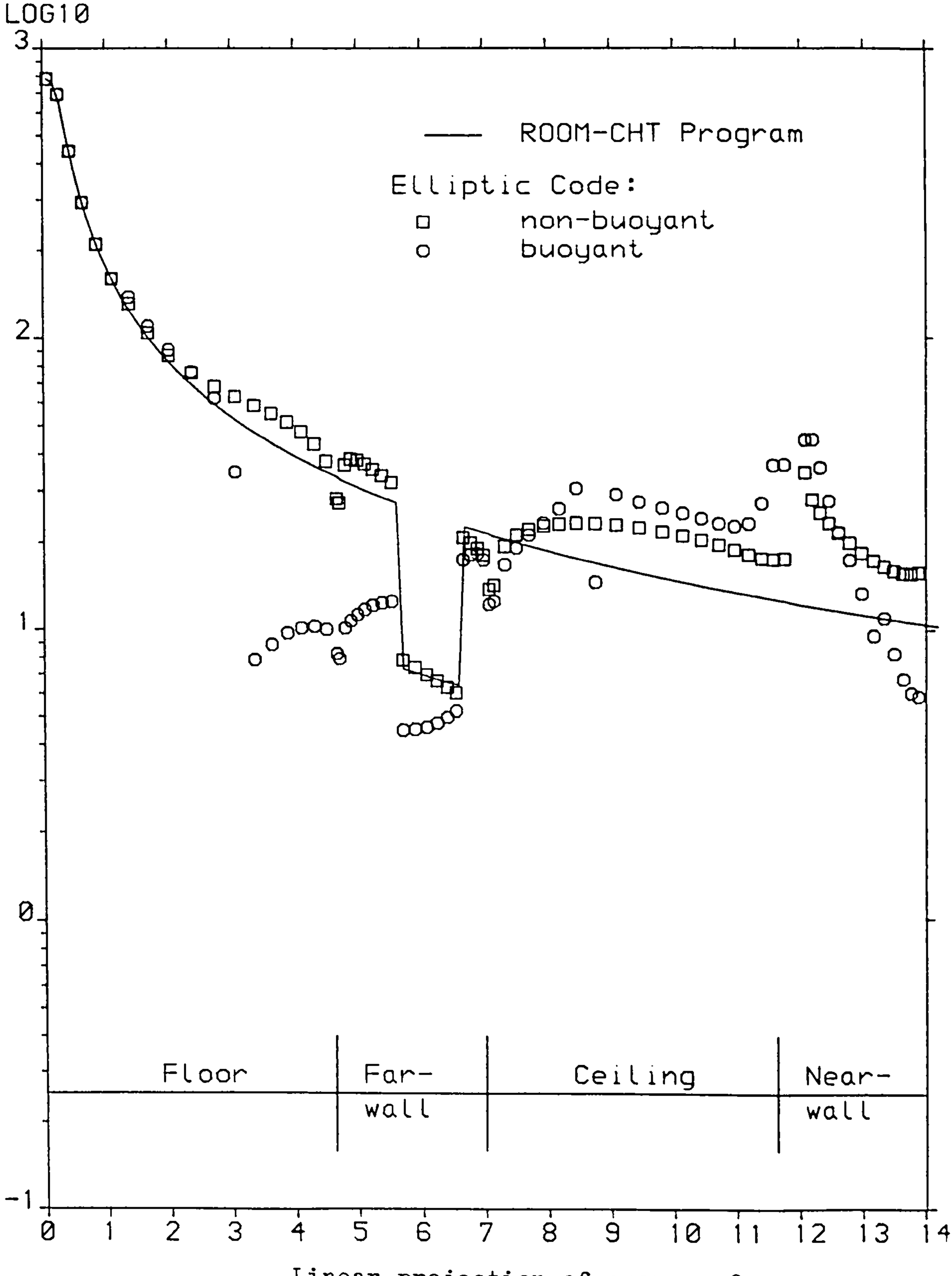

Fig. 5.13c: **Computed Local Heat Transfer Coefficients for Case No. 3 of Table 5.2.**

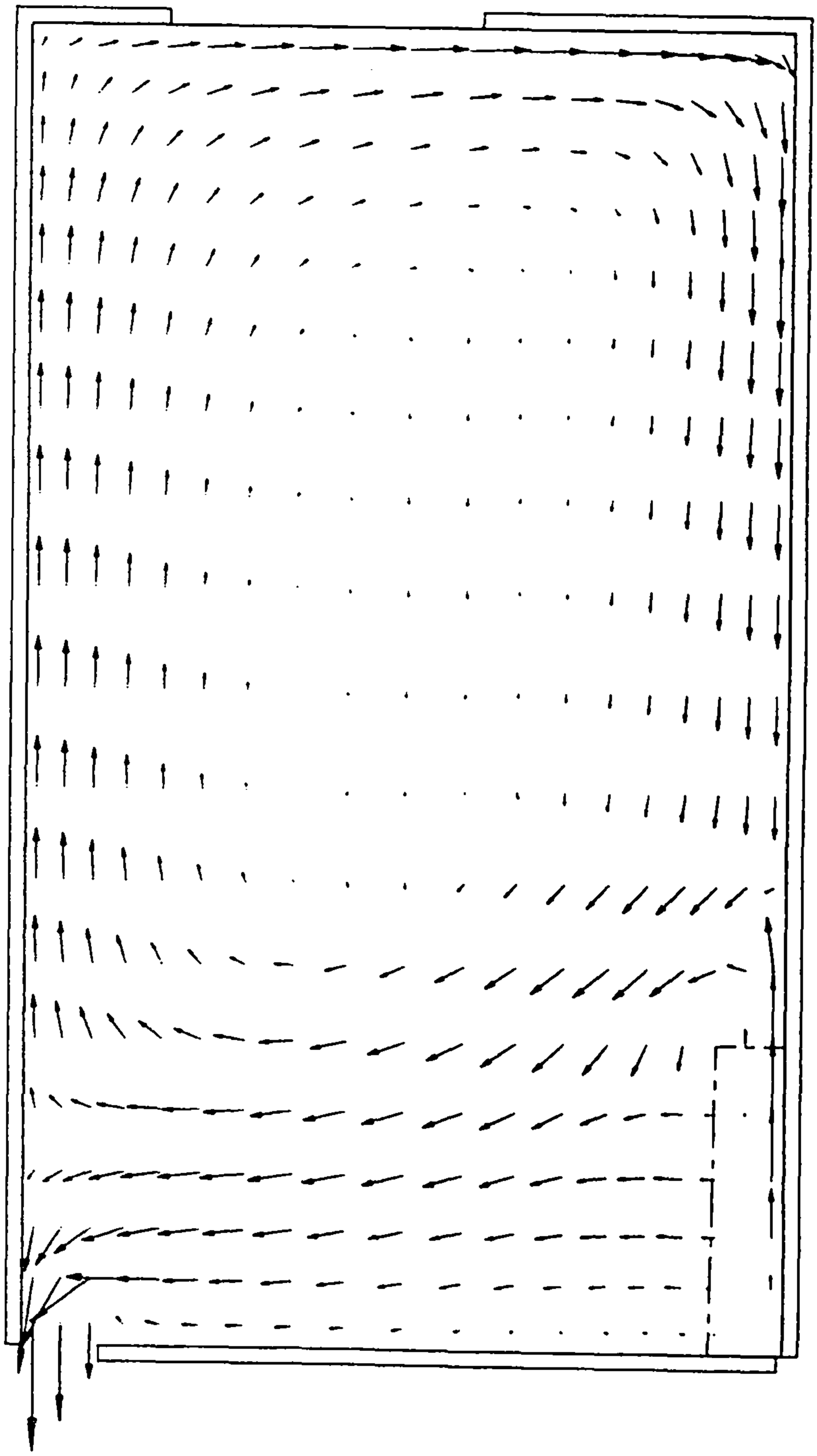

Fig. 5.14a: Predicted Flow Pattern for Case No. 1 of Table 5.3.

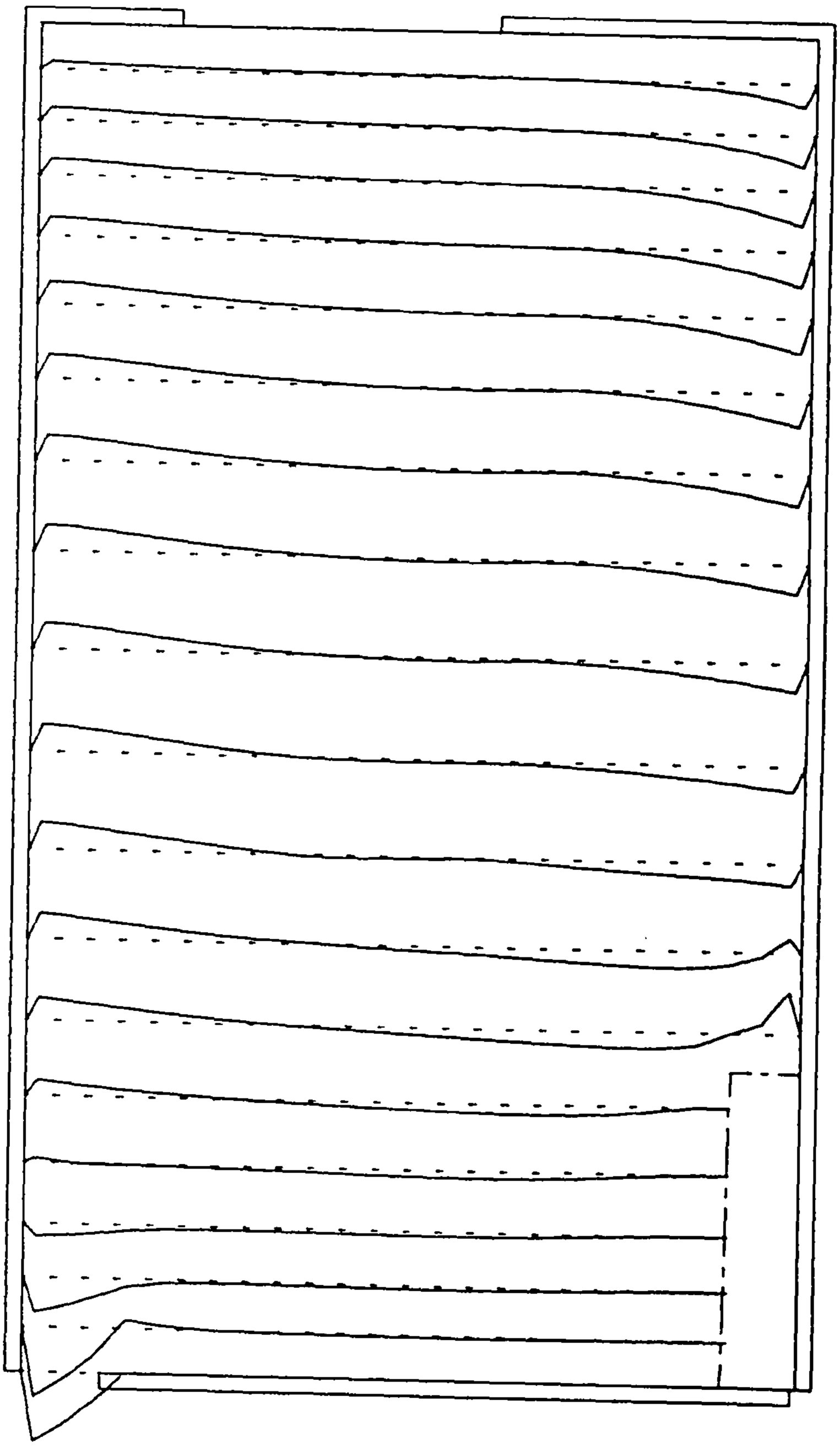

Fig. 5.14b: Predicted U-velocity for Case No. 1 of Table 5.3.

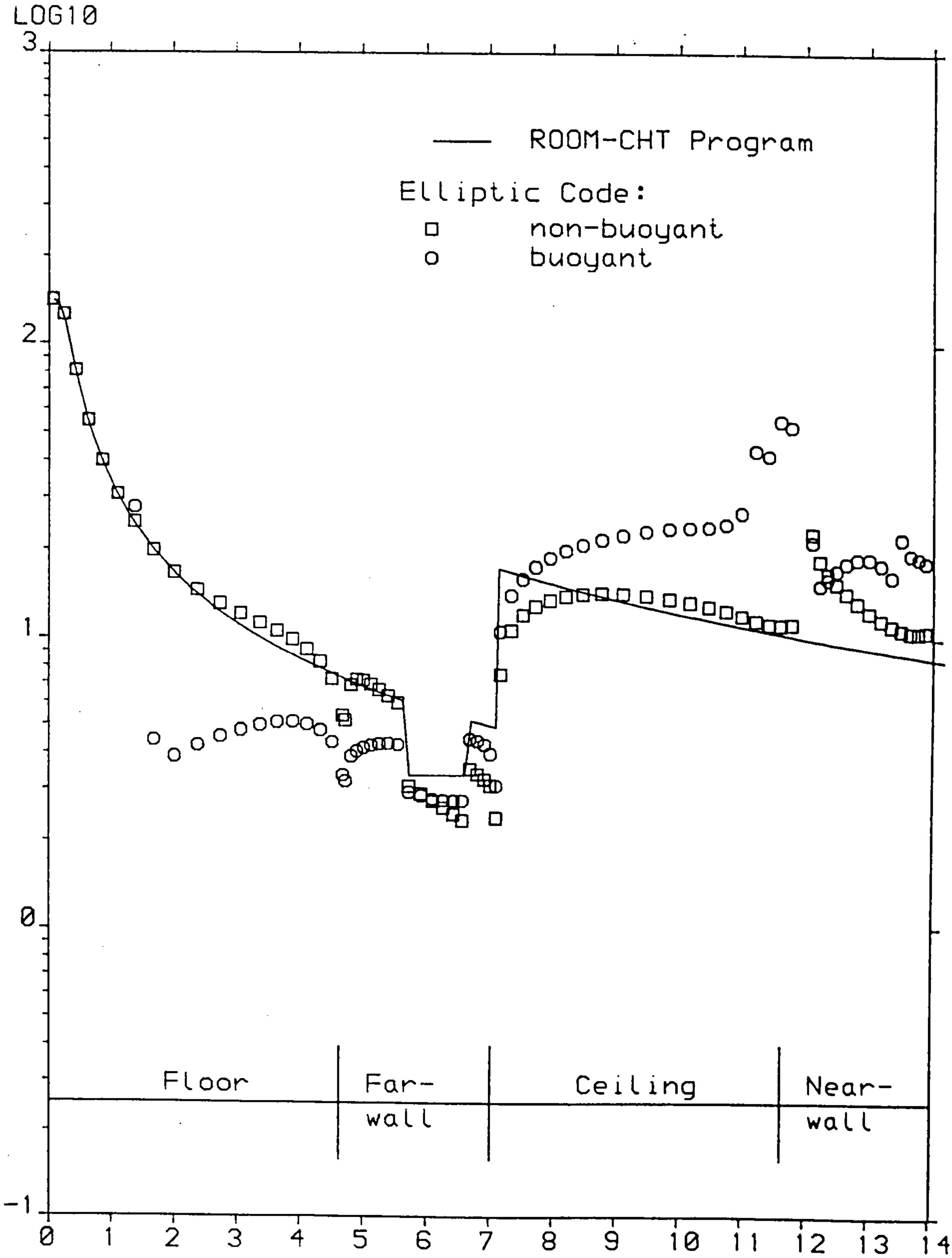

Fig. 5.14c: **Computed Heat Transfer Coefficients for Case No. 1 of Table 5.3.**

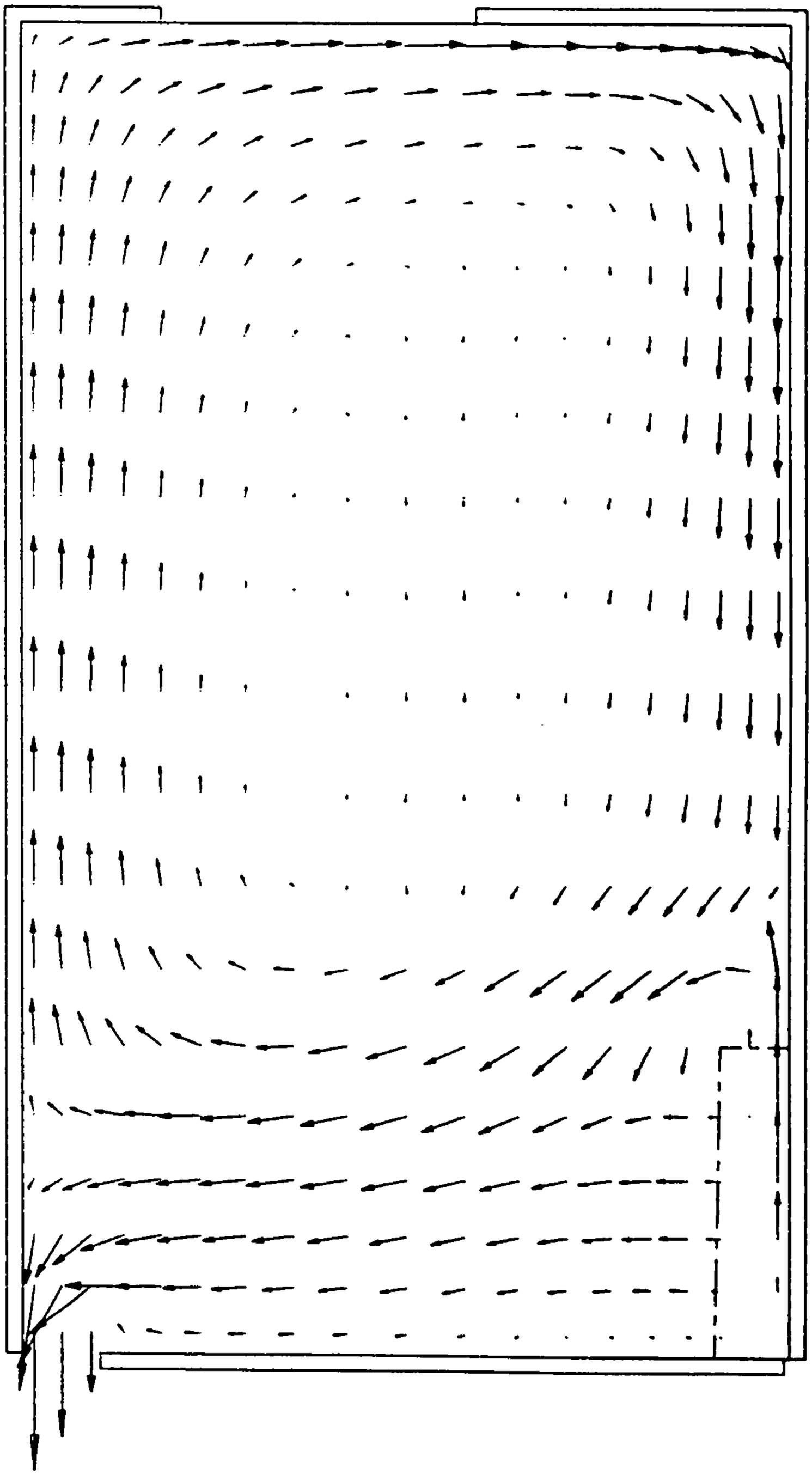

Fig. 5.15a: Predicted Flow Pattern for Case No. 2 of Table 5.3.

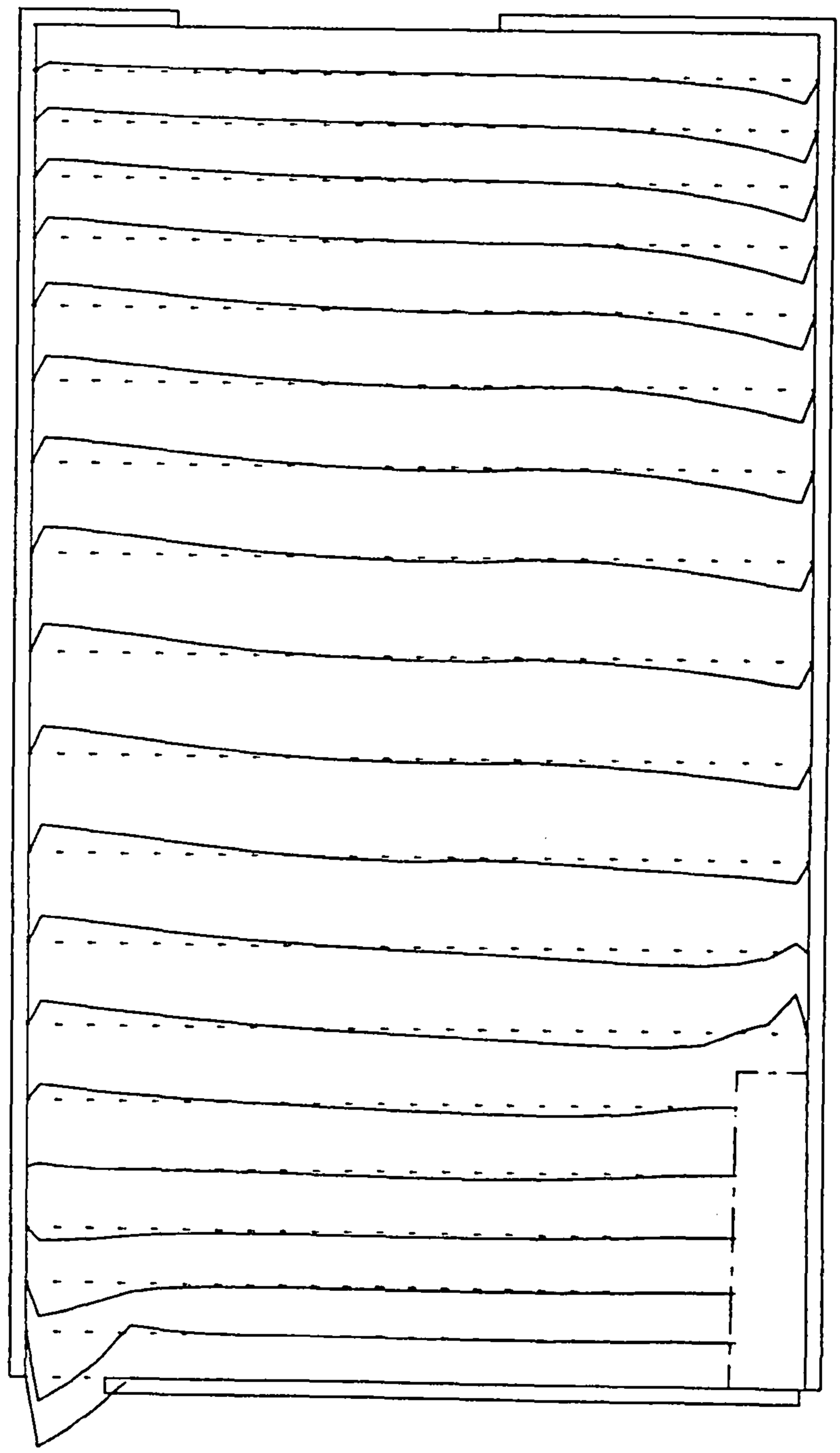

Fig. 5.15b: Predicted U-velocity Profile for Case No. 2 of Table 5.3.

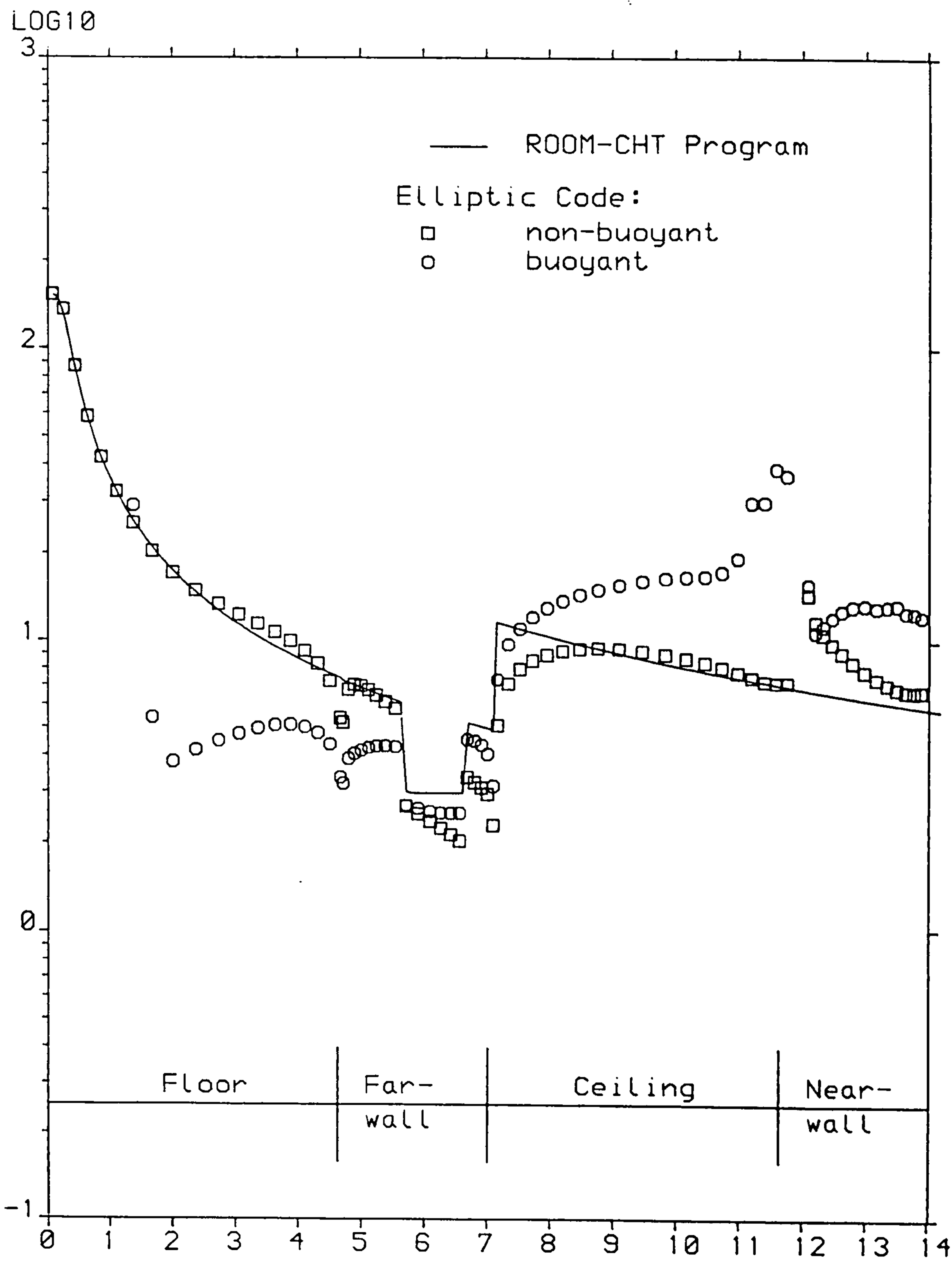

Fig. 5.15c: **Computed Heat Transfer Coefficients for Case No. 2 of Table 5.3.**

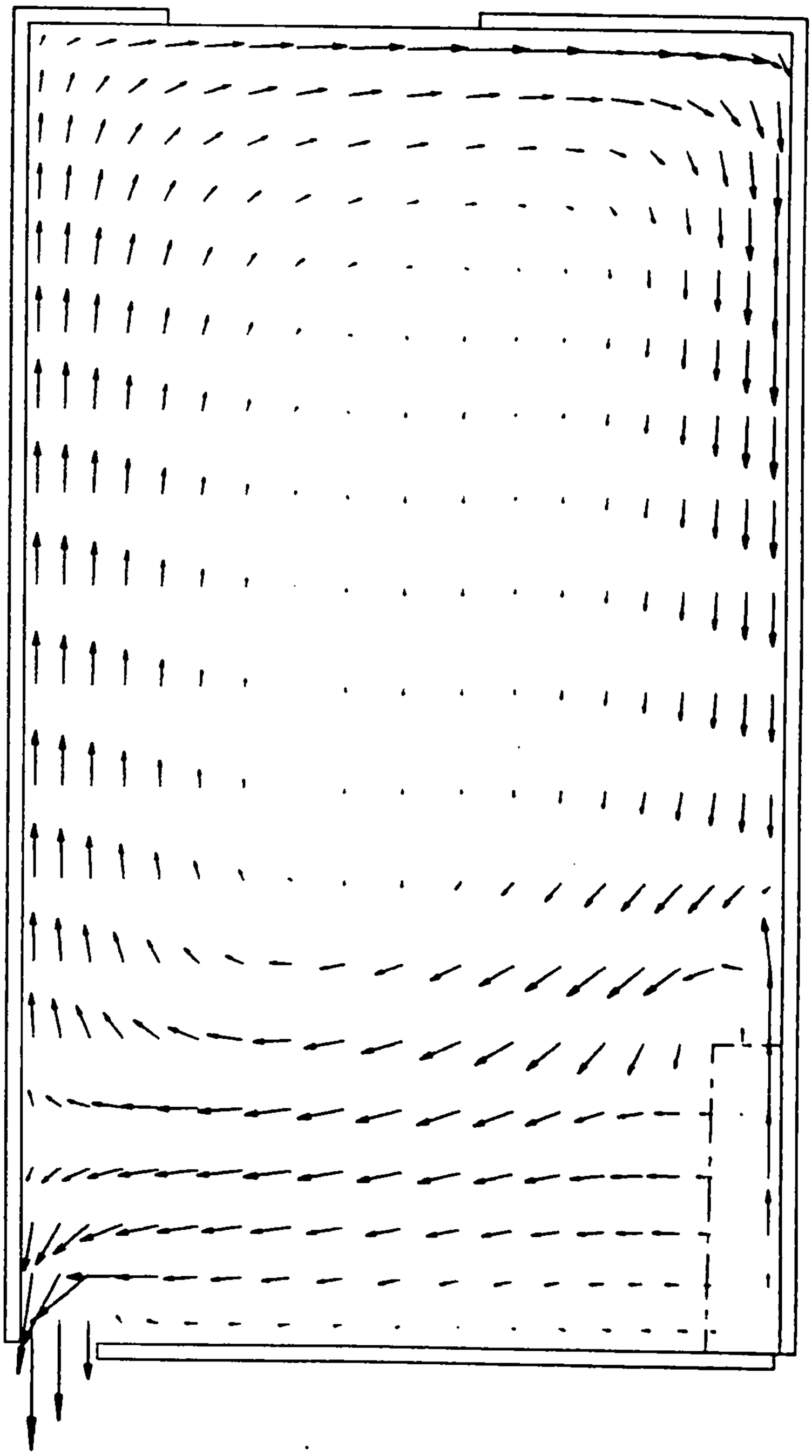

Predicted Flow Pattern for Case No. 3 of Table 5.3.

Fig. 5.16a:

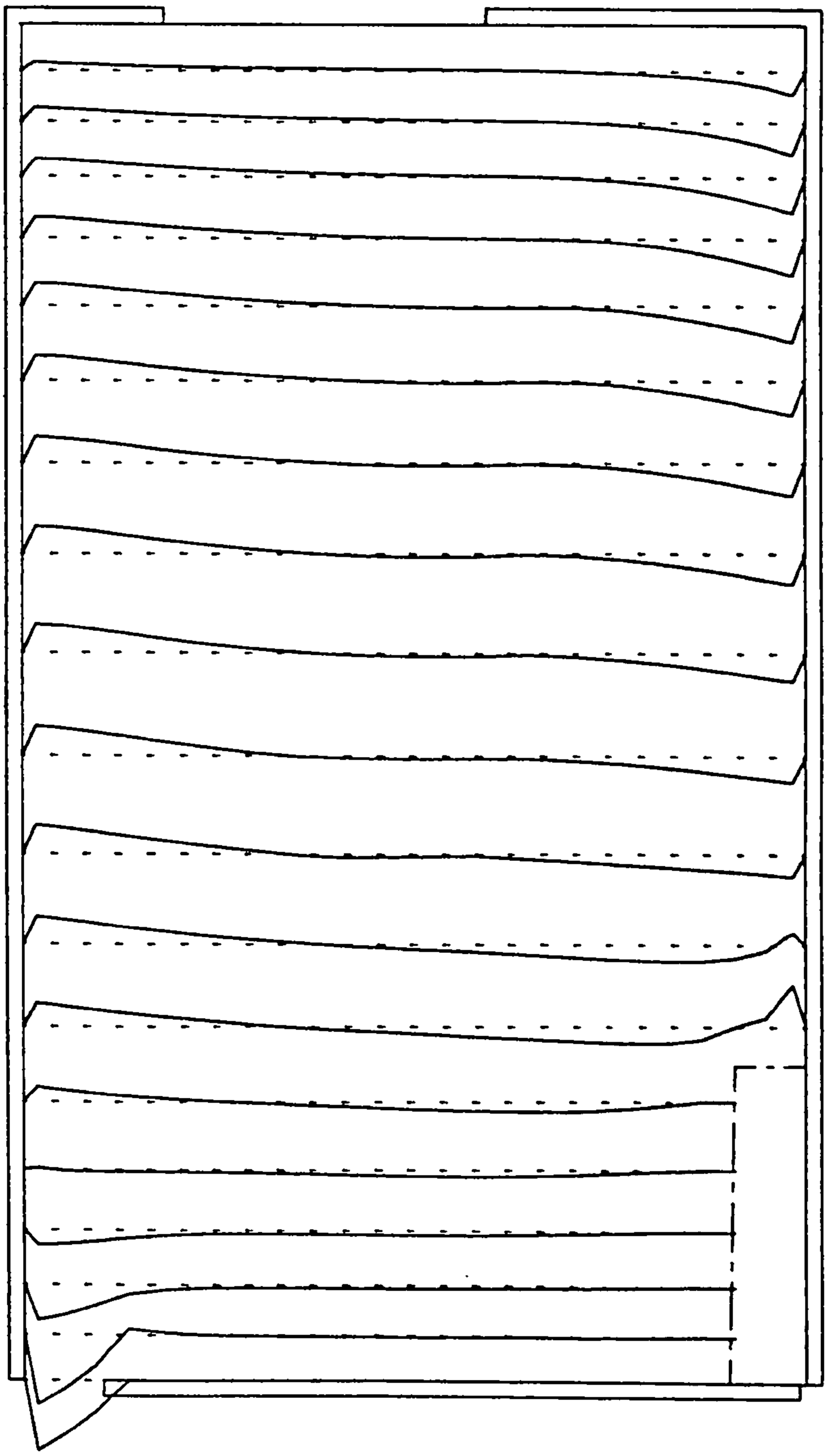

Fig. 5.16b; Predicted U-velocity Profile for Case No. 3 of Table 5.3.

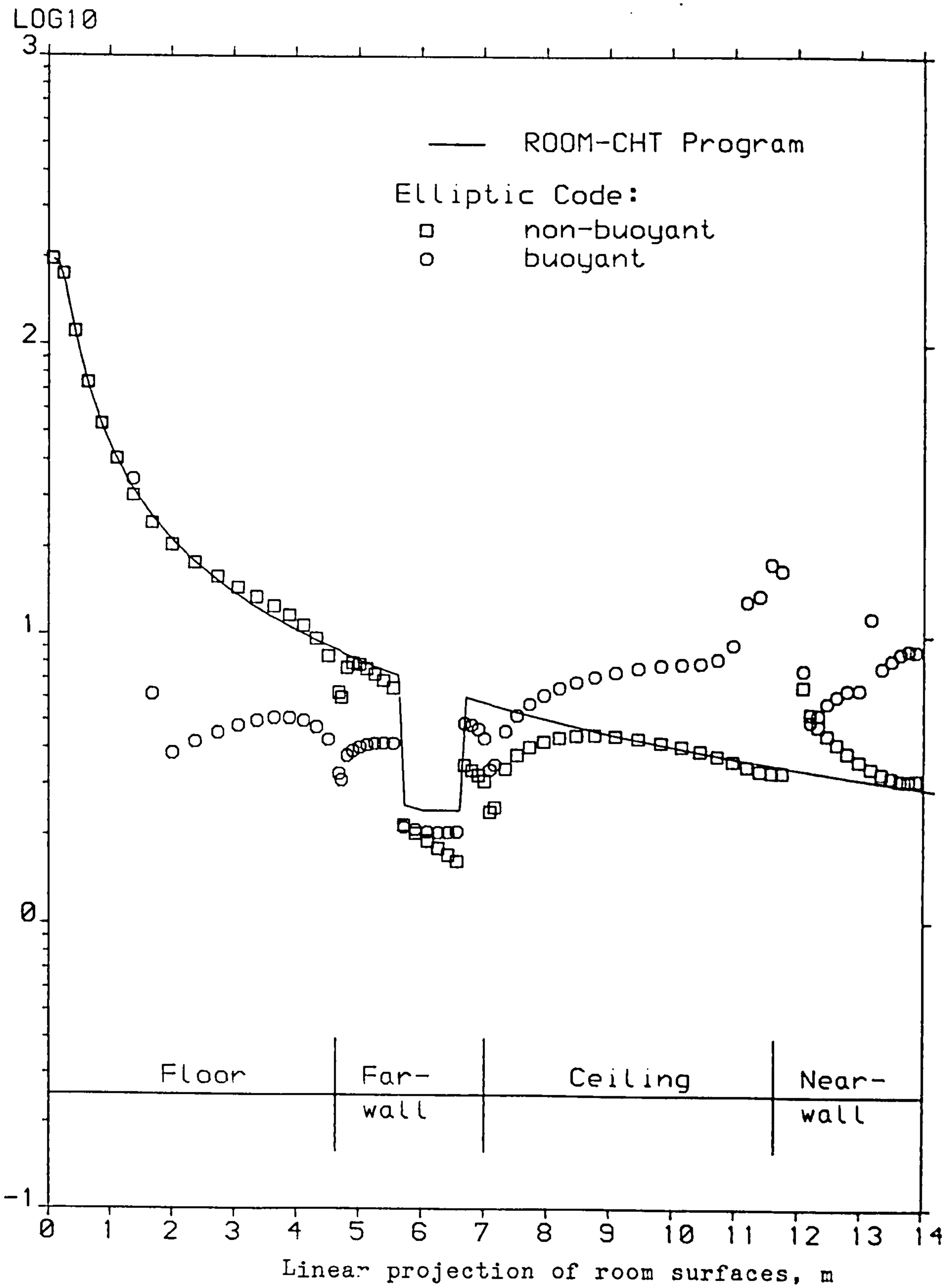

Fig. 5.16c: **Computed Heat Transfer Coefficients for Case No. 3 of Table 5.3.**

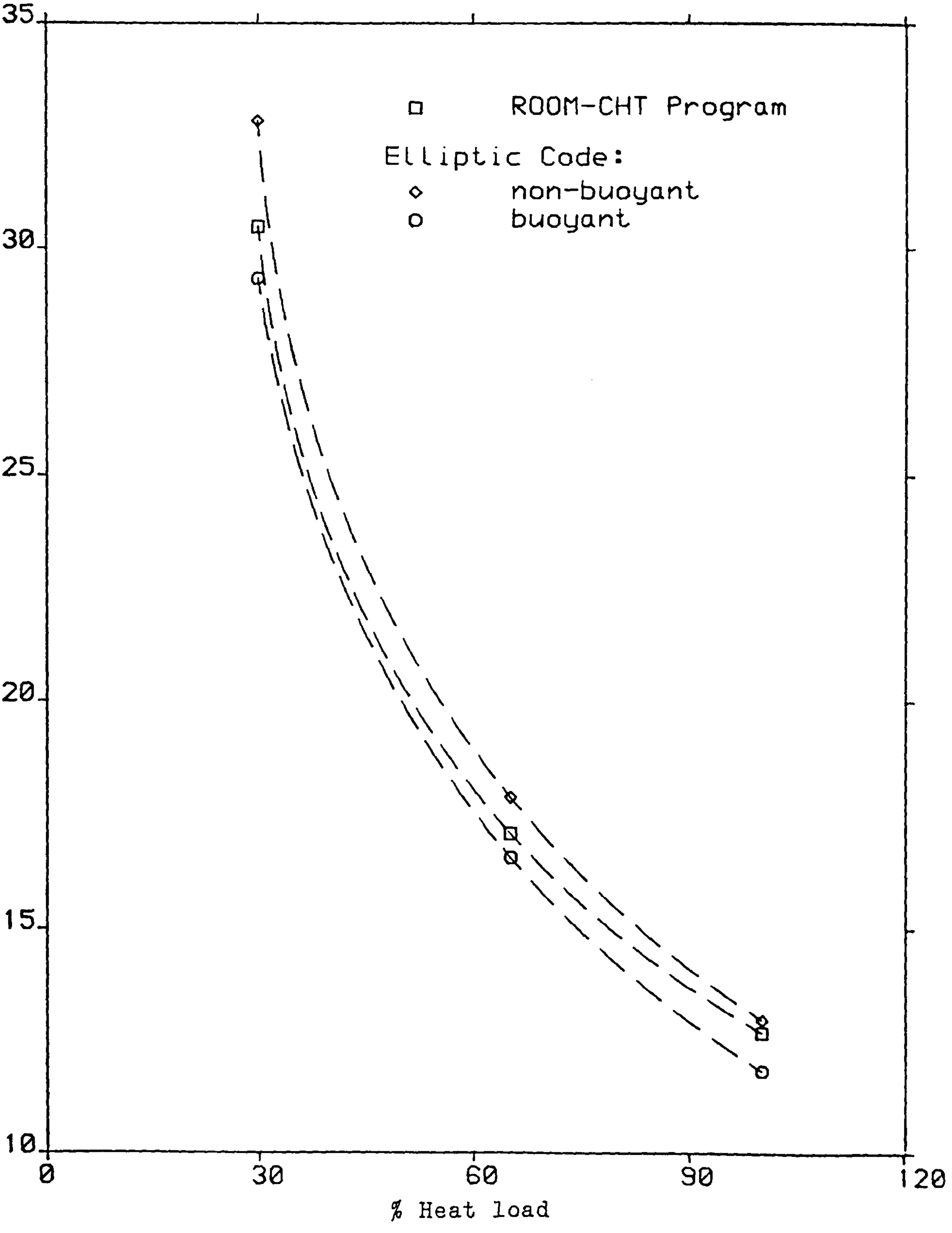

Fig. 5.17: The Dependence of the Overall, Room Averaged Convection Coefficient on the Heat Load - Cyclic Control.

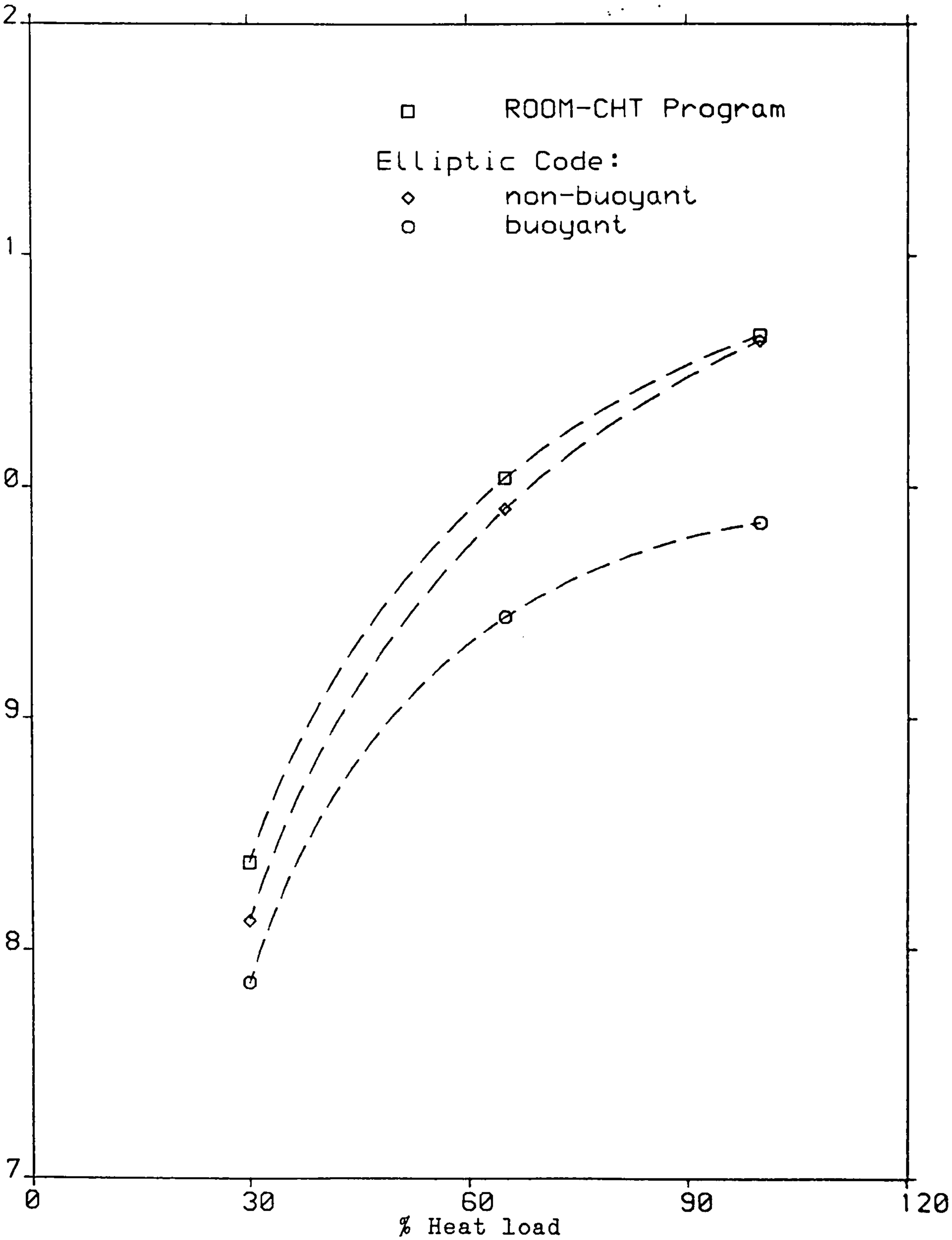

Fig. 5.18: The Dependence of the Overall, Room Averaged Convection Coefficient on the Heat Load - Modulating Control.

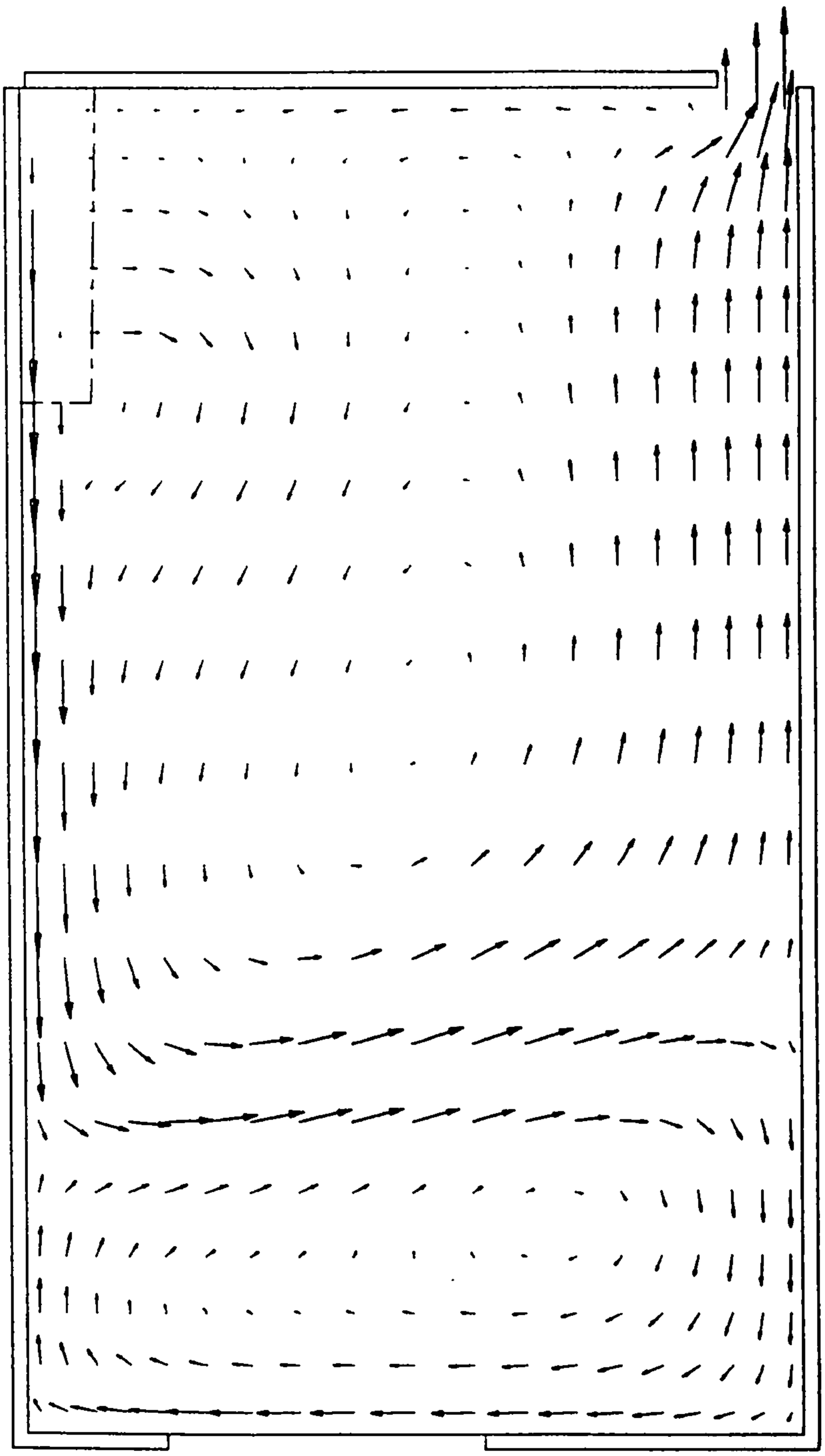

Fig. 5.19a: Predicted Flow Pattern for Structure Type 1 of Table 5.10.

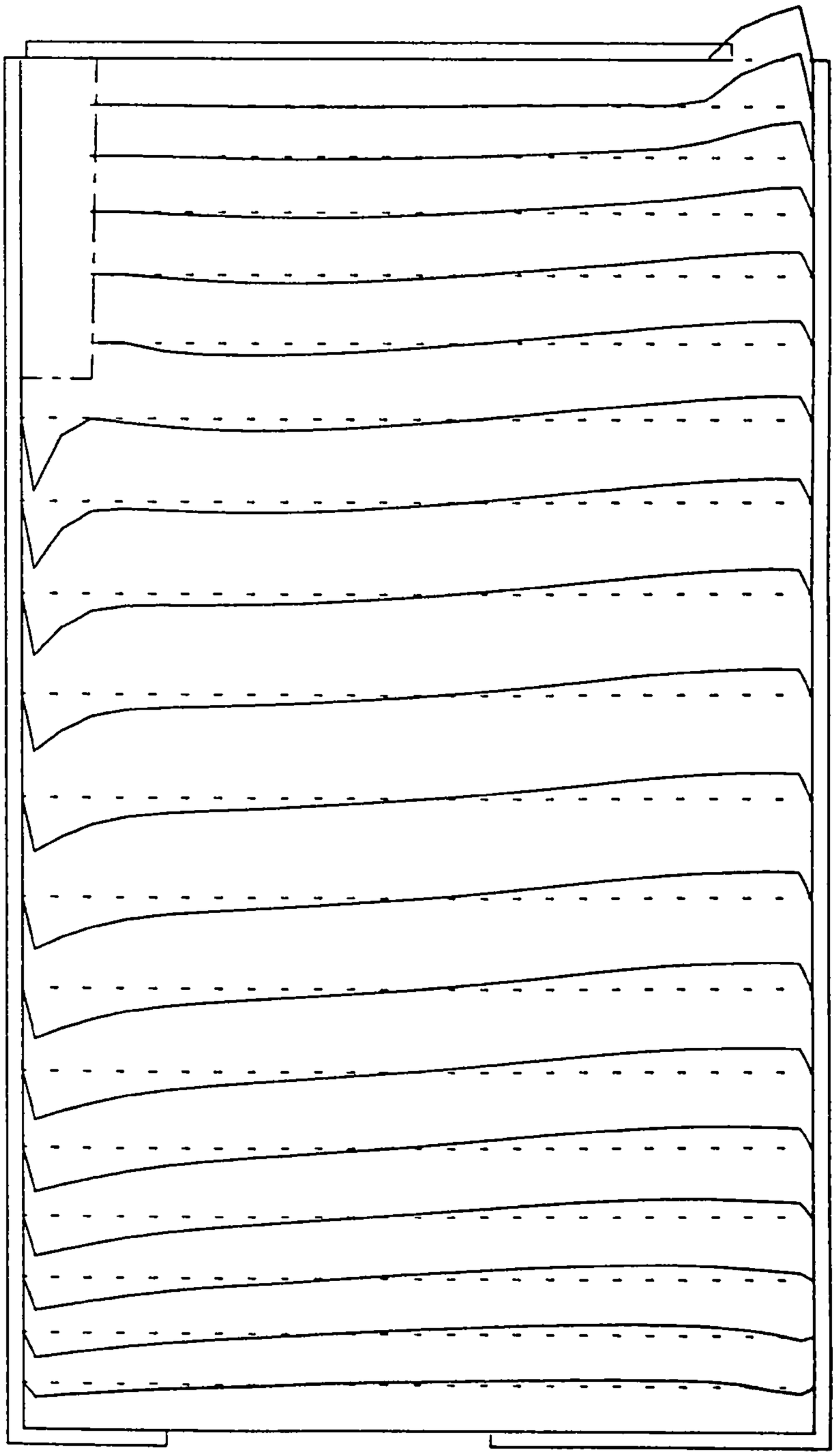

Fig. 5.19b: Predicted U-velocity Profile for Structure Type 1 of Table 5.10.

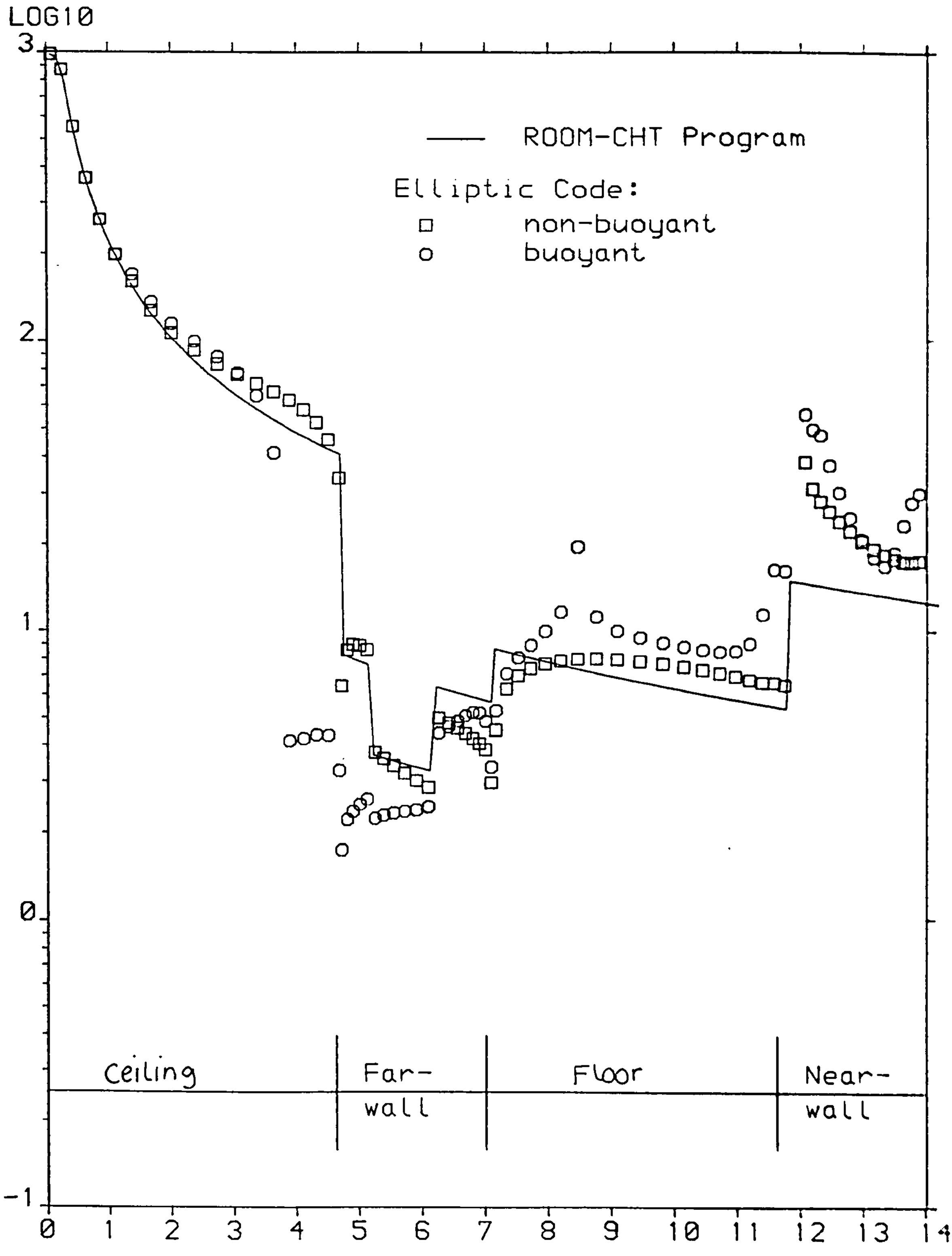

Fig. 51.9c: **Computed Heat Transfer Coefficients for Structure Type 1 of Table 5.10.**

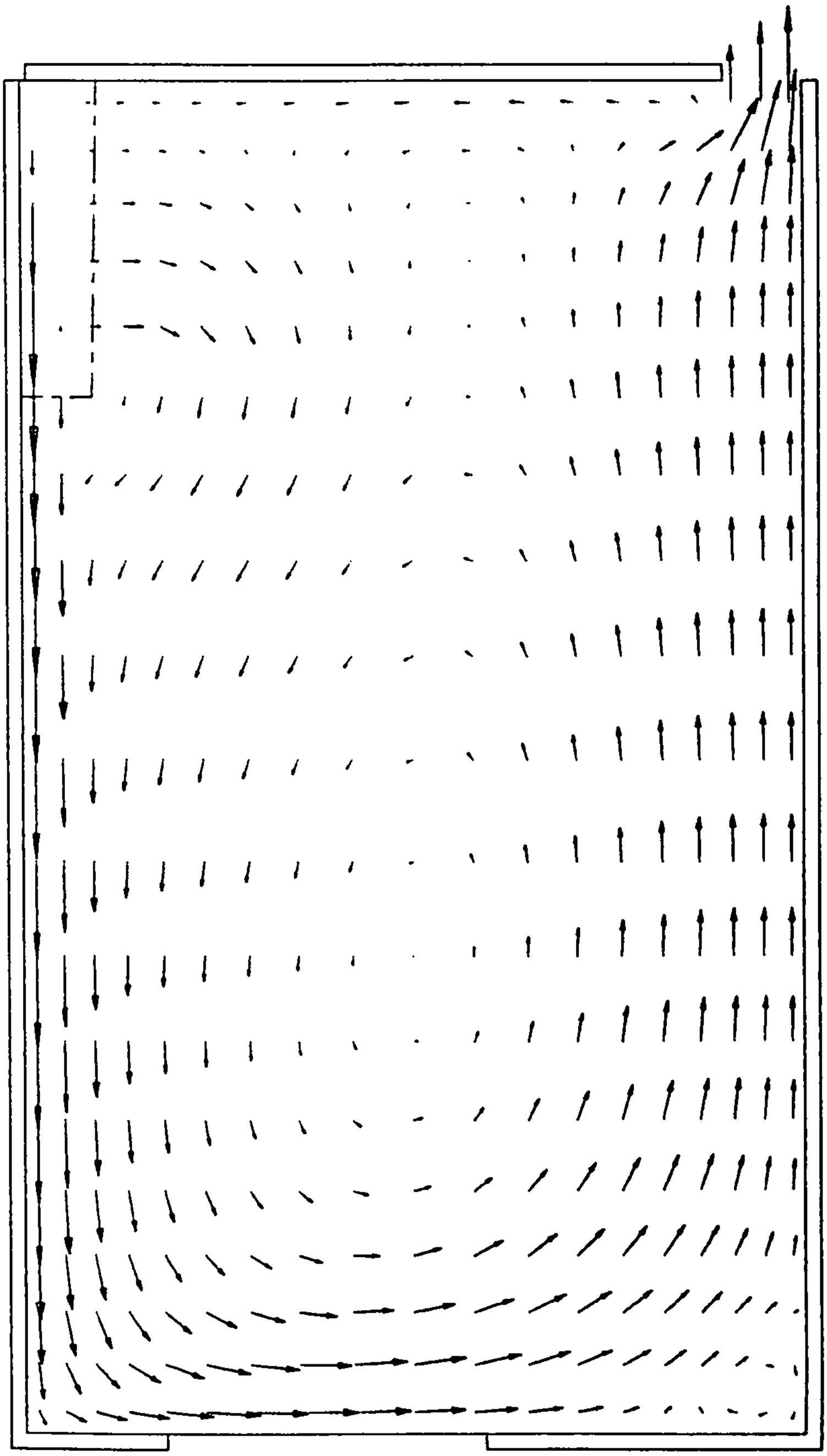

Fig. 5.20a: Predicted Flow Pattern for Structure Type 2 of Table 5.10.

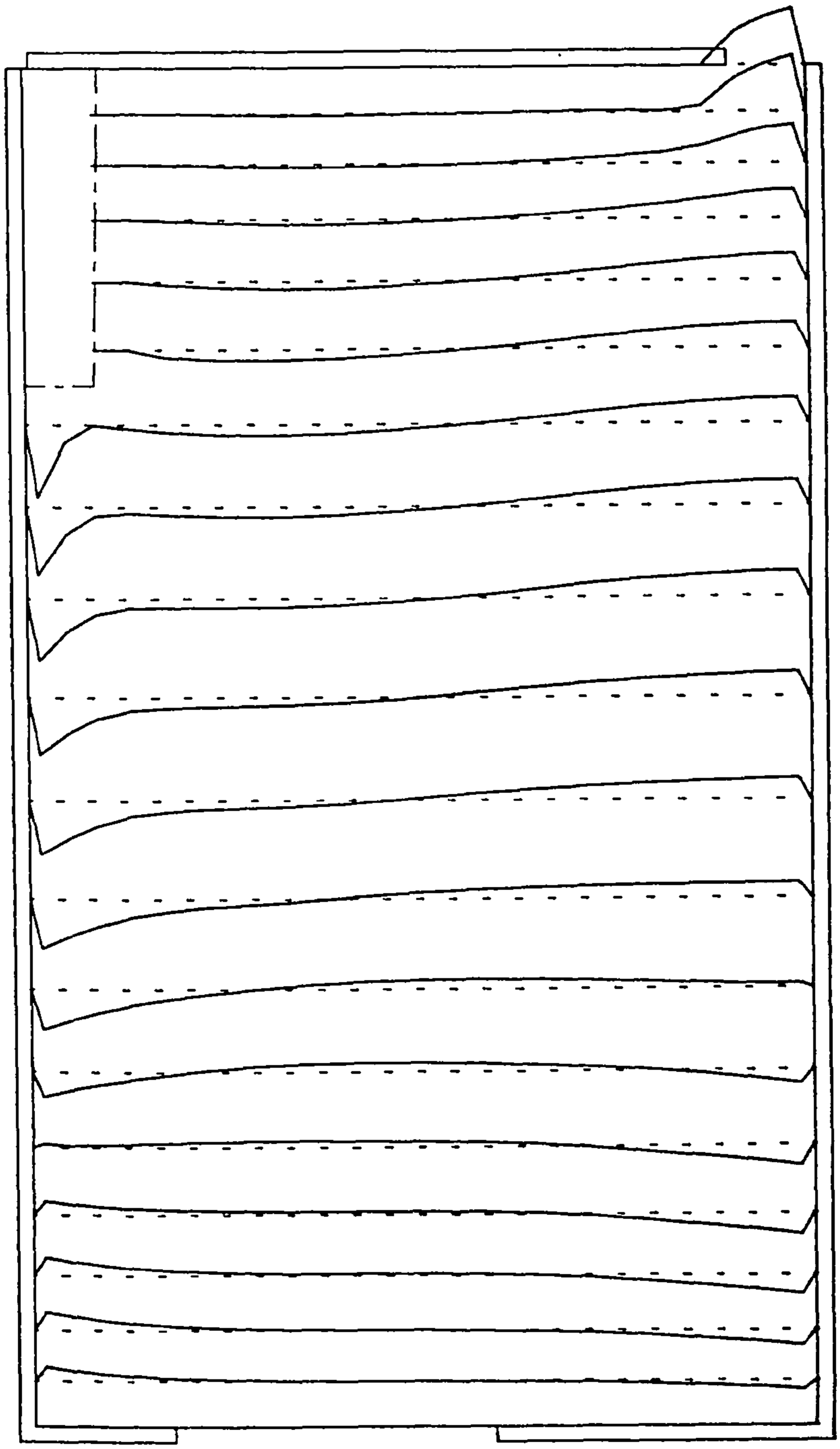

Fig. 5.20b: Predicted U-velocity Profile for Structure Type 2 of Table 5.10.

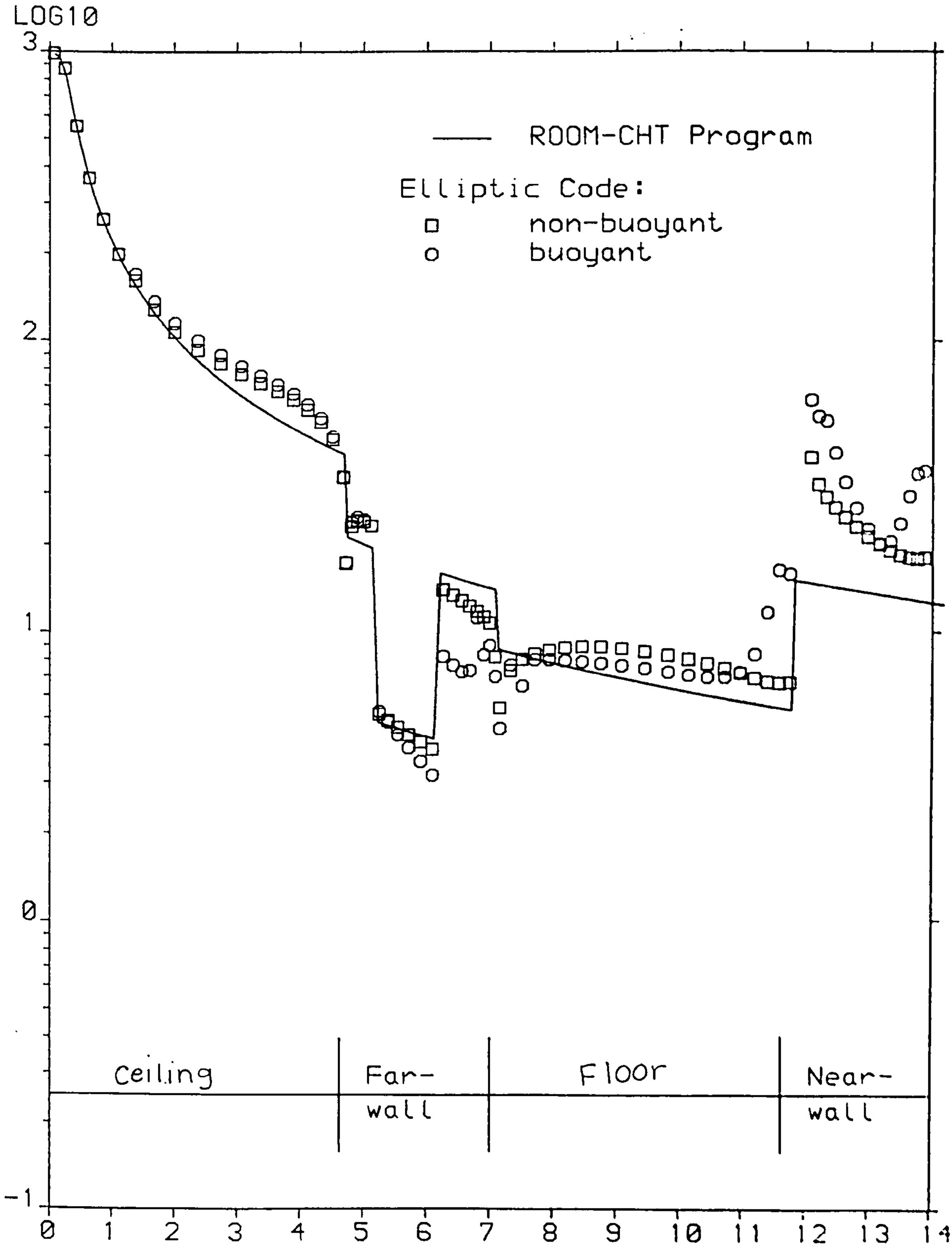

Fig. 5.20c: **Computed Heat Transfer Coefficients for Structure Type 2 of Table 5.10.**

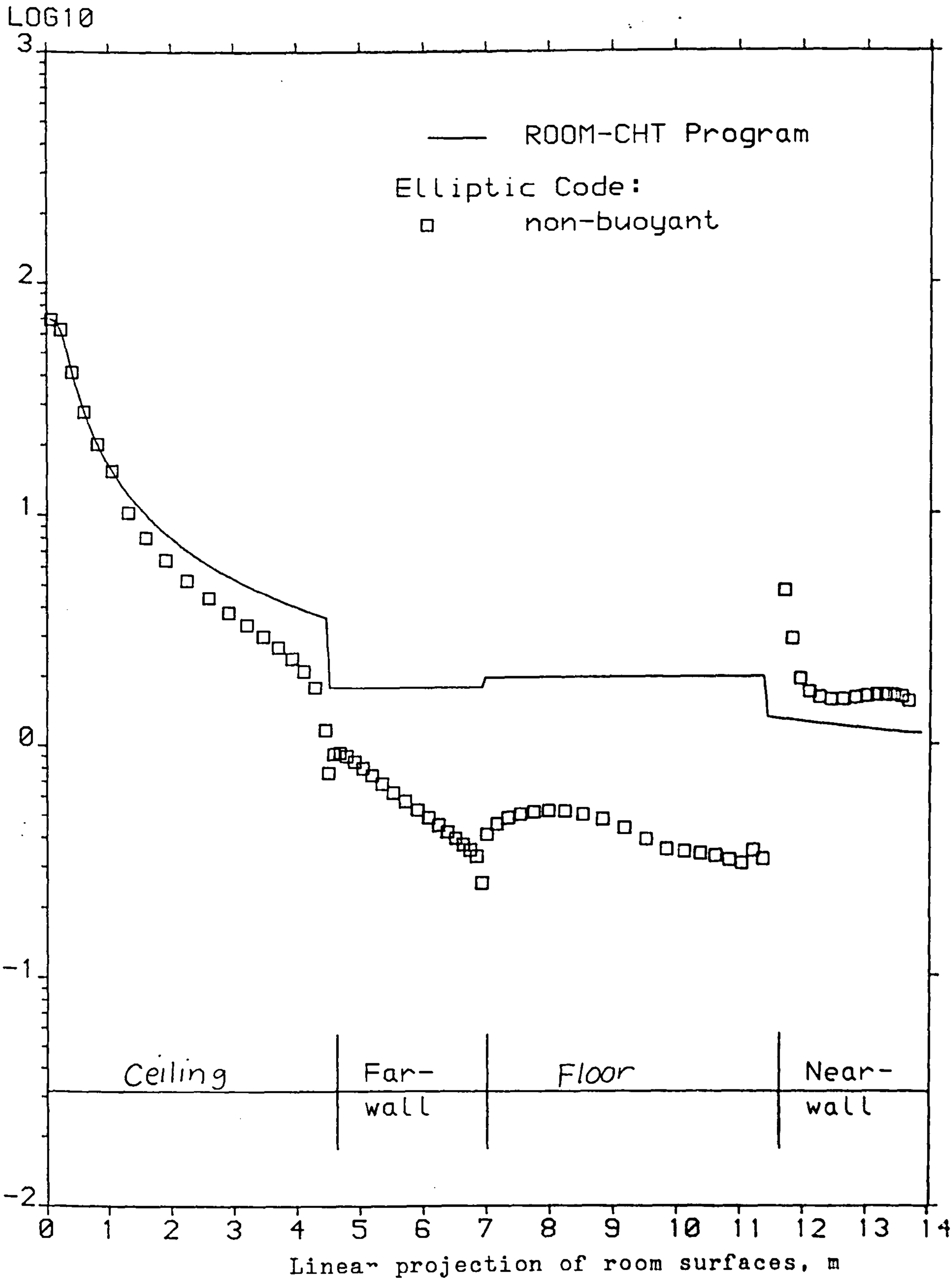

Fig. 5.21: **Computed Heat Transfer Coefficients for Conditions of 3.3 ACH of Tables 5.11 and 5.12.**

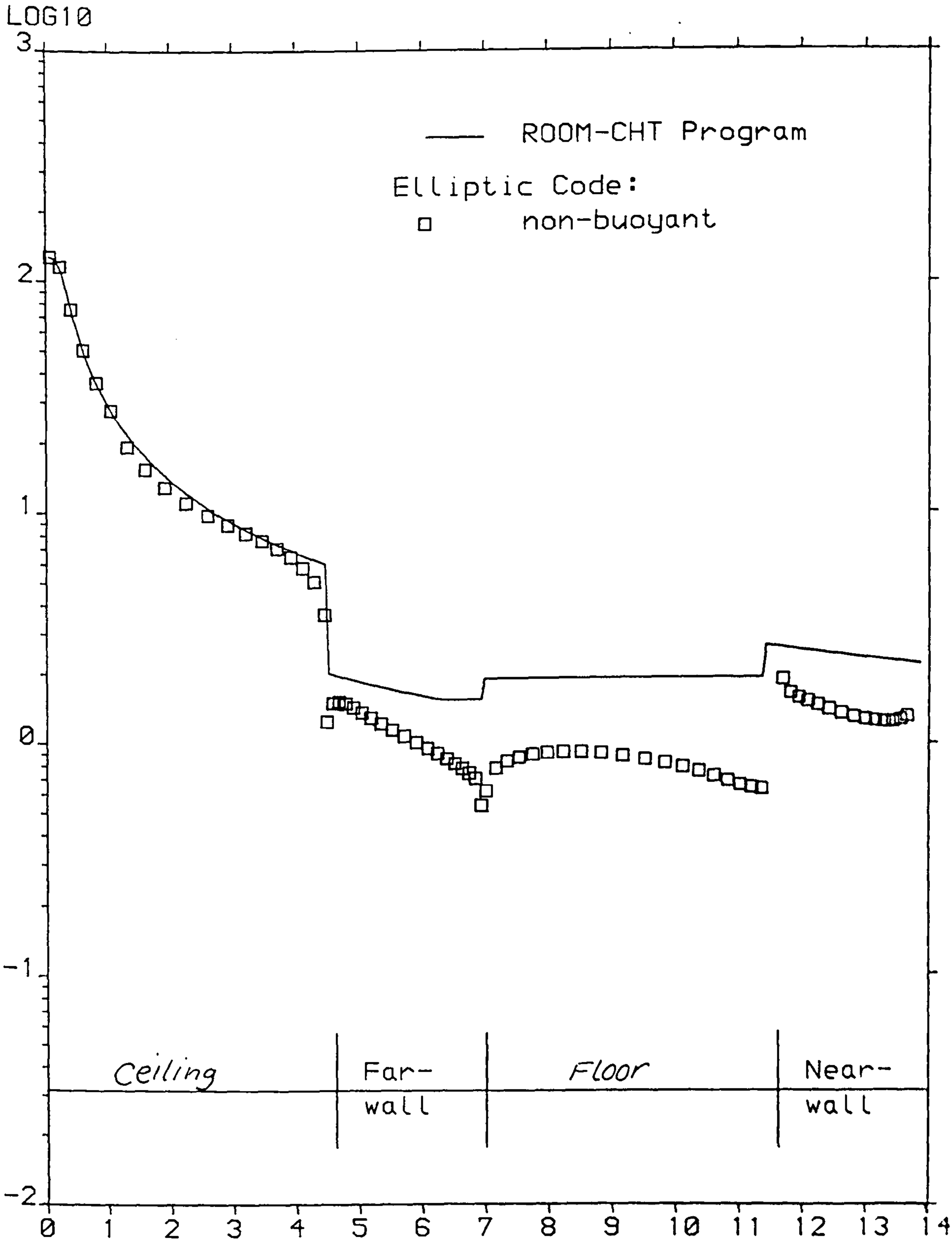

Fig. 5.22: **Computed Heat Transfer Coefficients for Conditions of 3.99 ACH of Tables 5.11 and 5.12.**

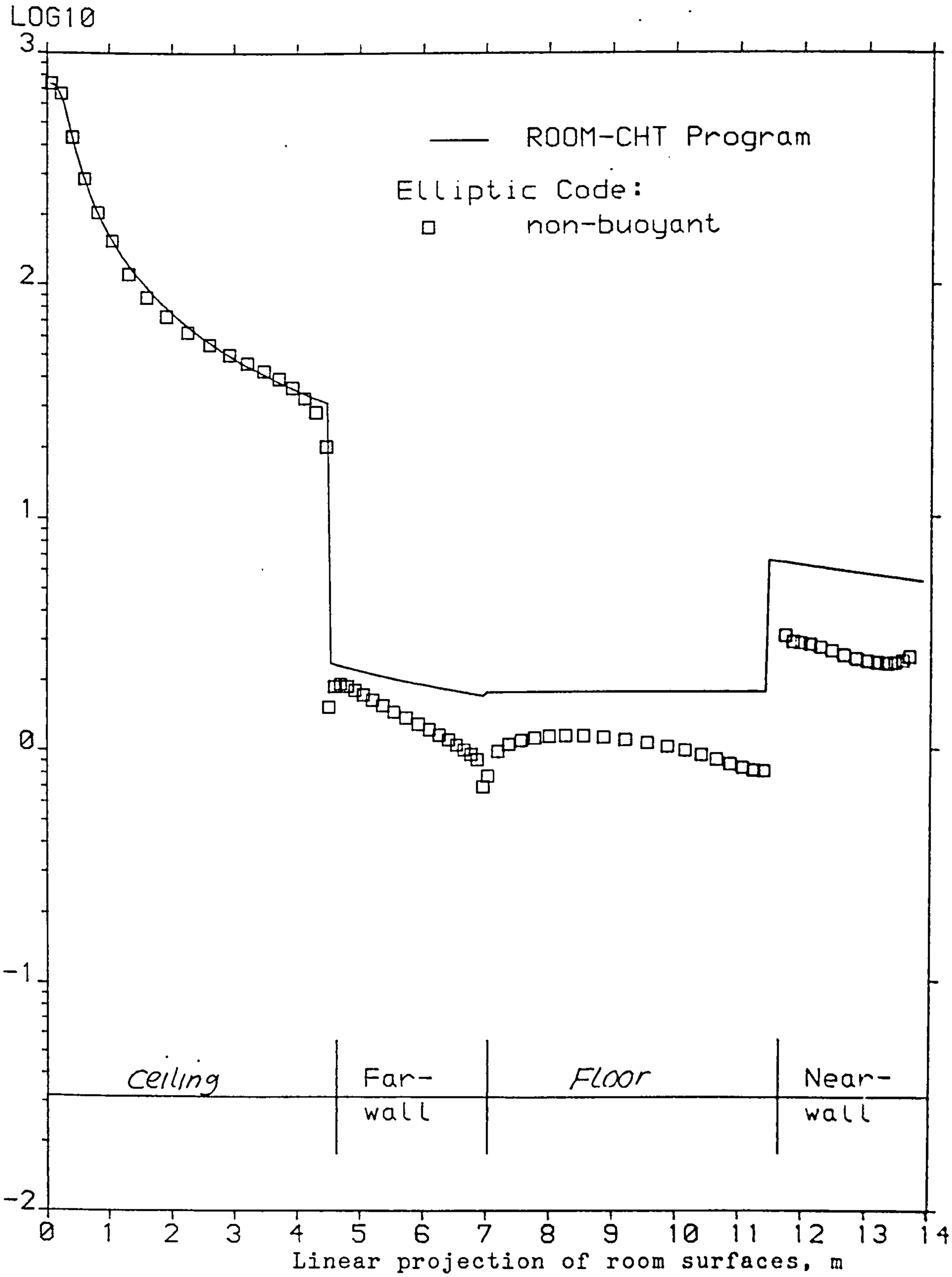

Fig. 5.23: **Computed Heat Transfer Coefficients for Conditions of 5.24 ACH of Tables 5.11 and 5.12.**

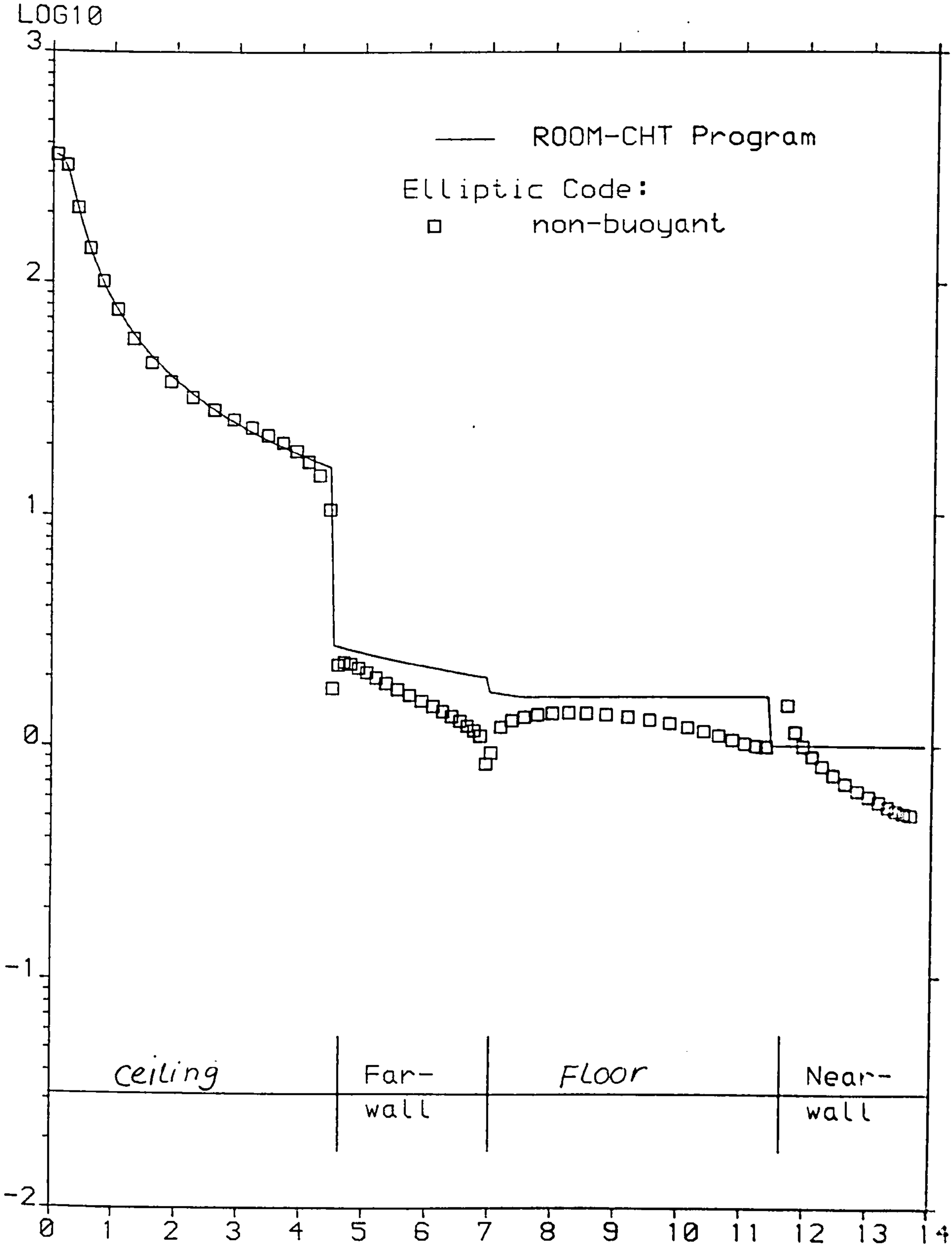

Fig. 5.24: **Computed Heat Transfer Coefficients for Conditions of 6.8 ACH of Tables 5.11 and 5.12.**

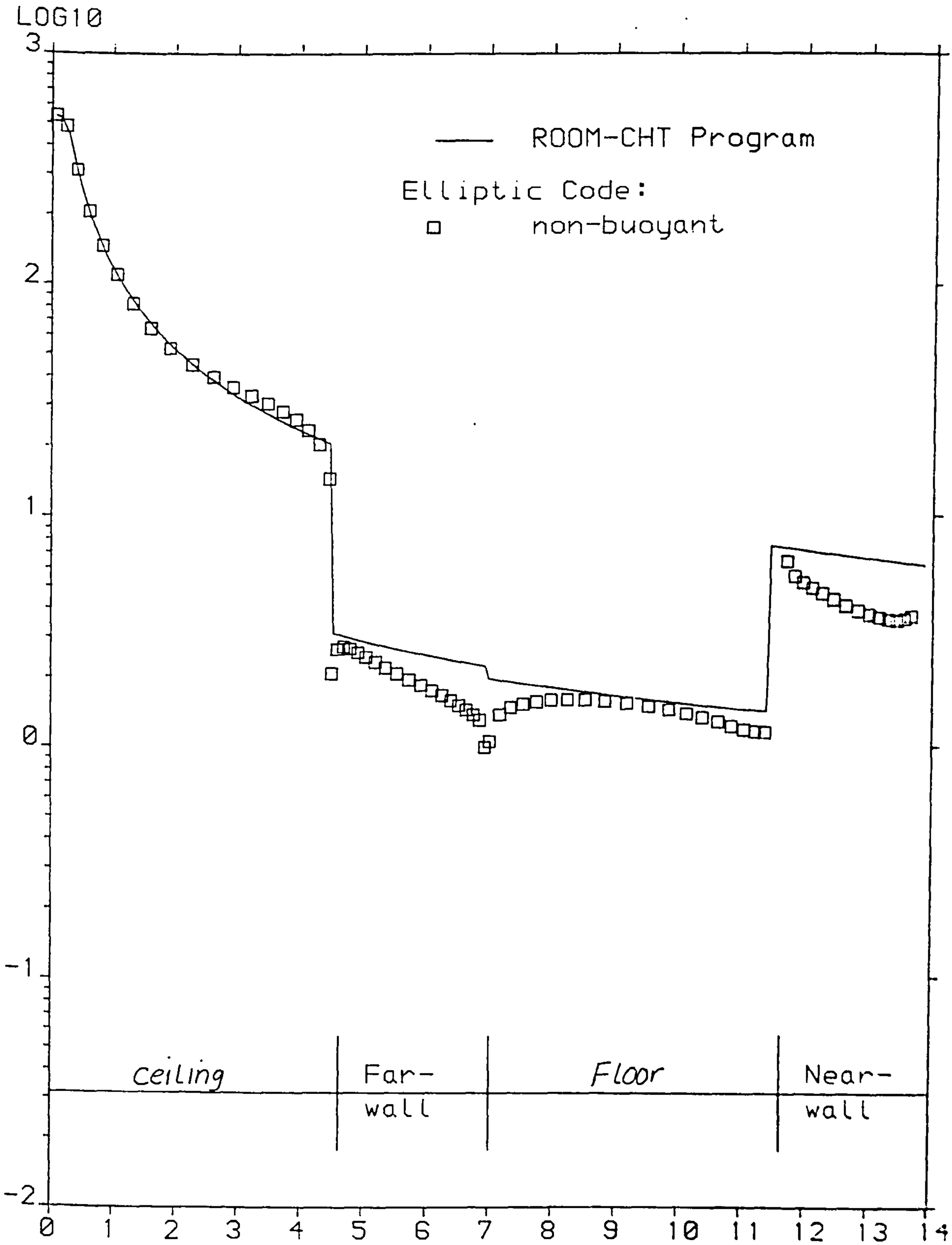

Fig. 5.25a: Computed Heat Transfer Coefficients for Conditions of 7.65 ACH of Tables 5.11 and 5.12.

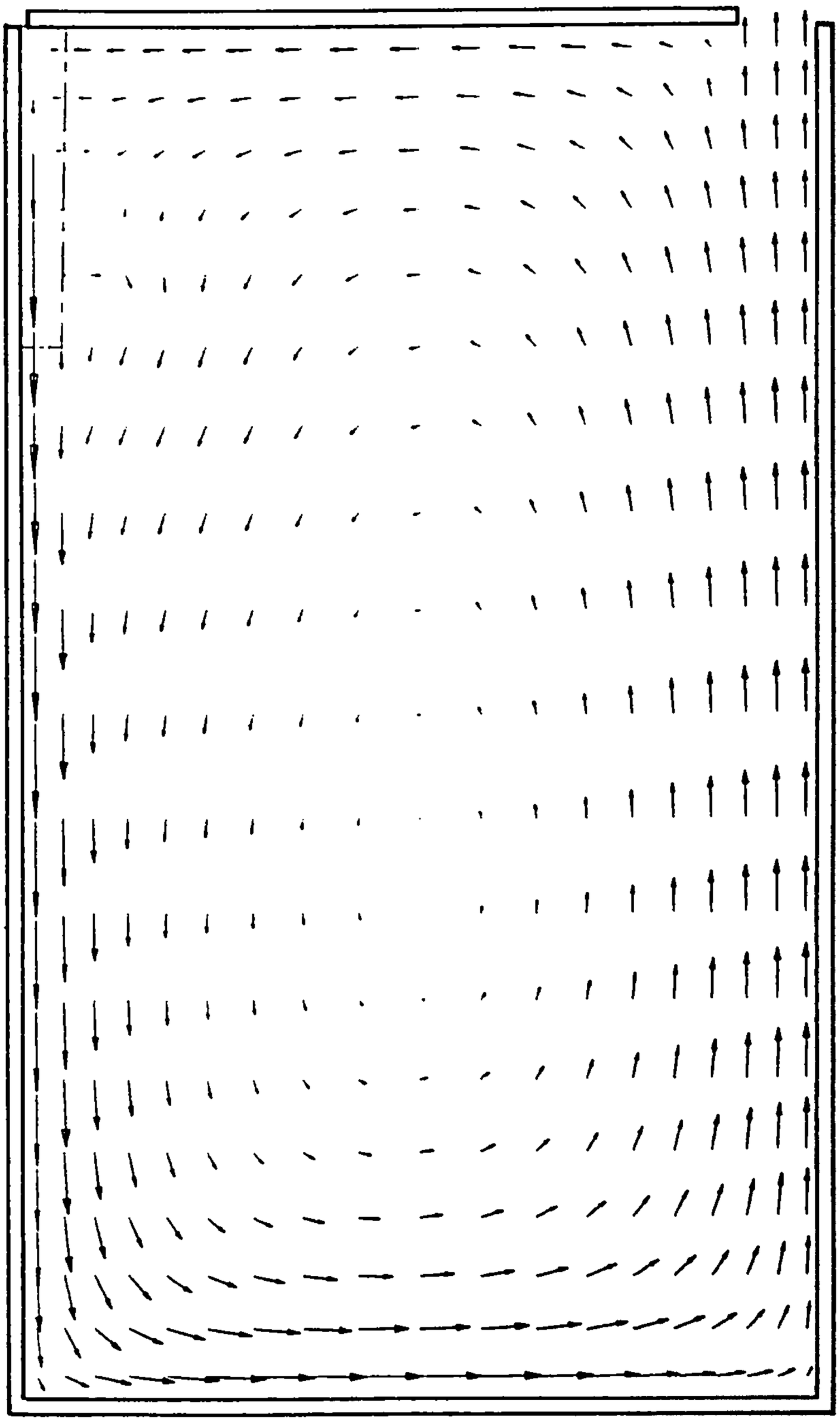

Fig. 5.25b: Predicted Flow Pattern for Conditions of 7.65 ACH of Tables 5.11 and 5.12.

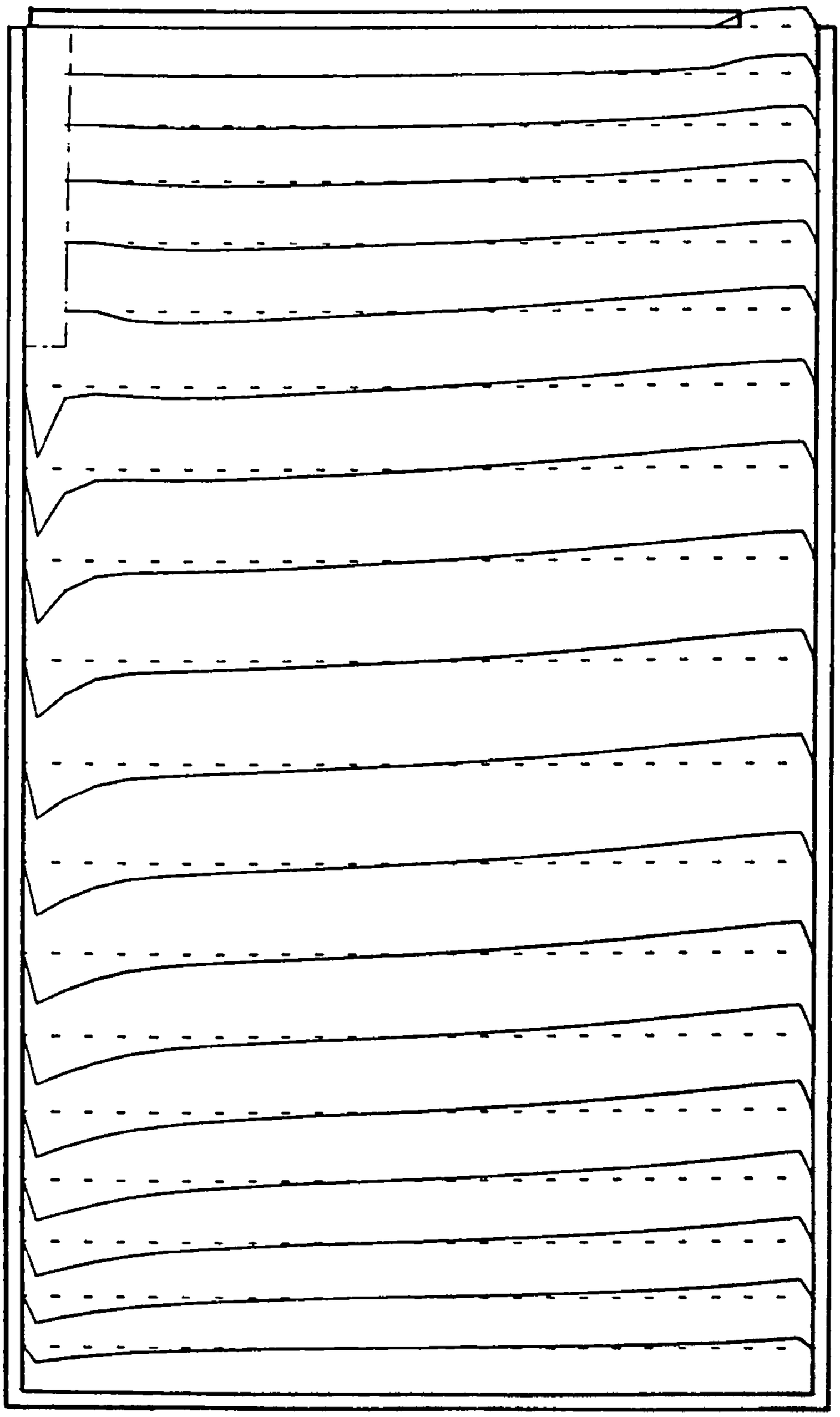

Fig. 5.25c: Predicted U-velocity Profile for Conditions of 7.65 ACH of Tables 5.11 and 5.12.

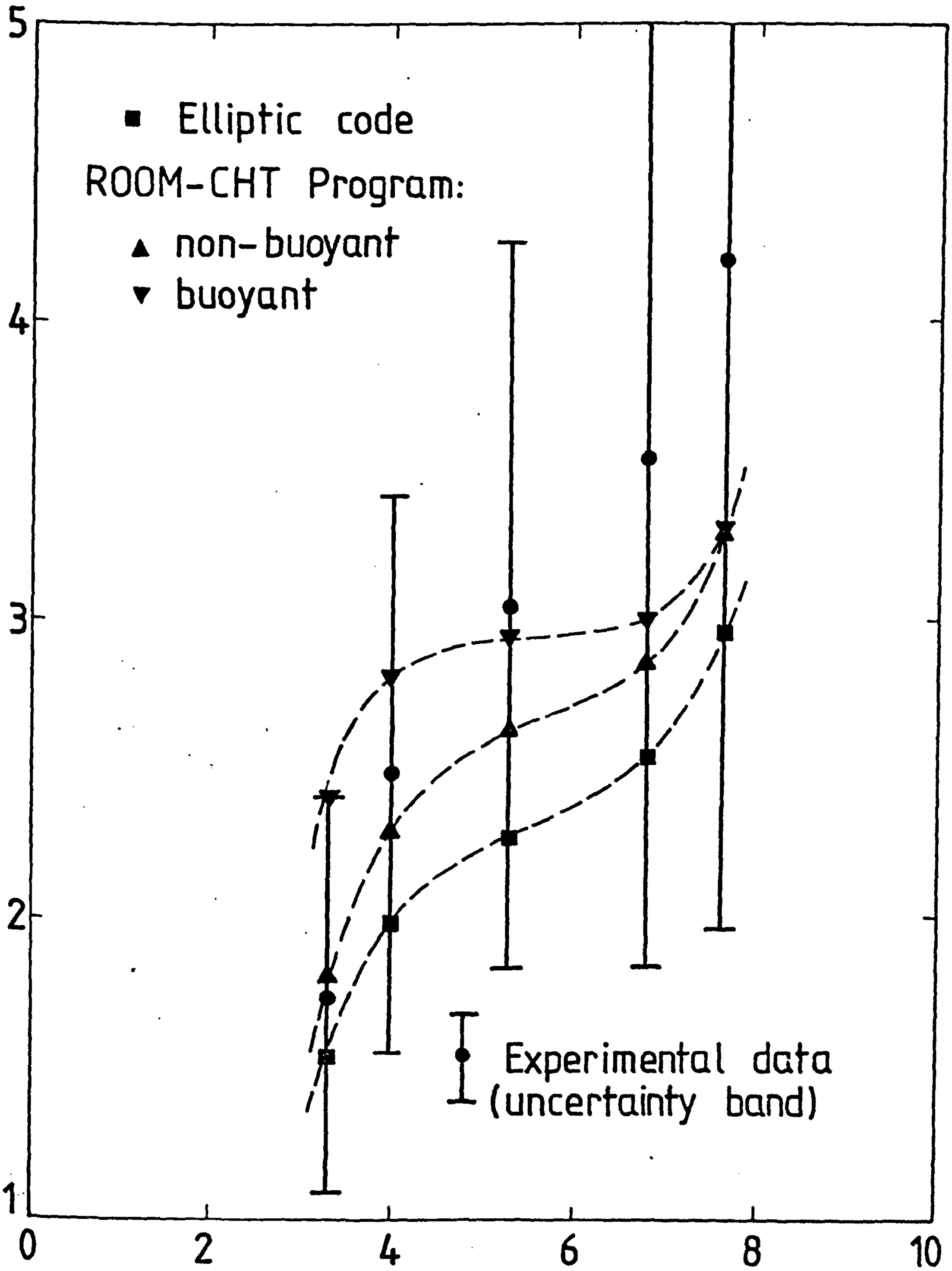

Fig. 5.26: Mechanical-ventilation Rate Dependence of the Room-averaged Convection Coefficient.

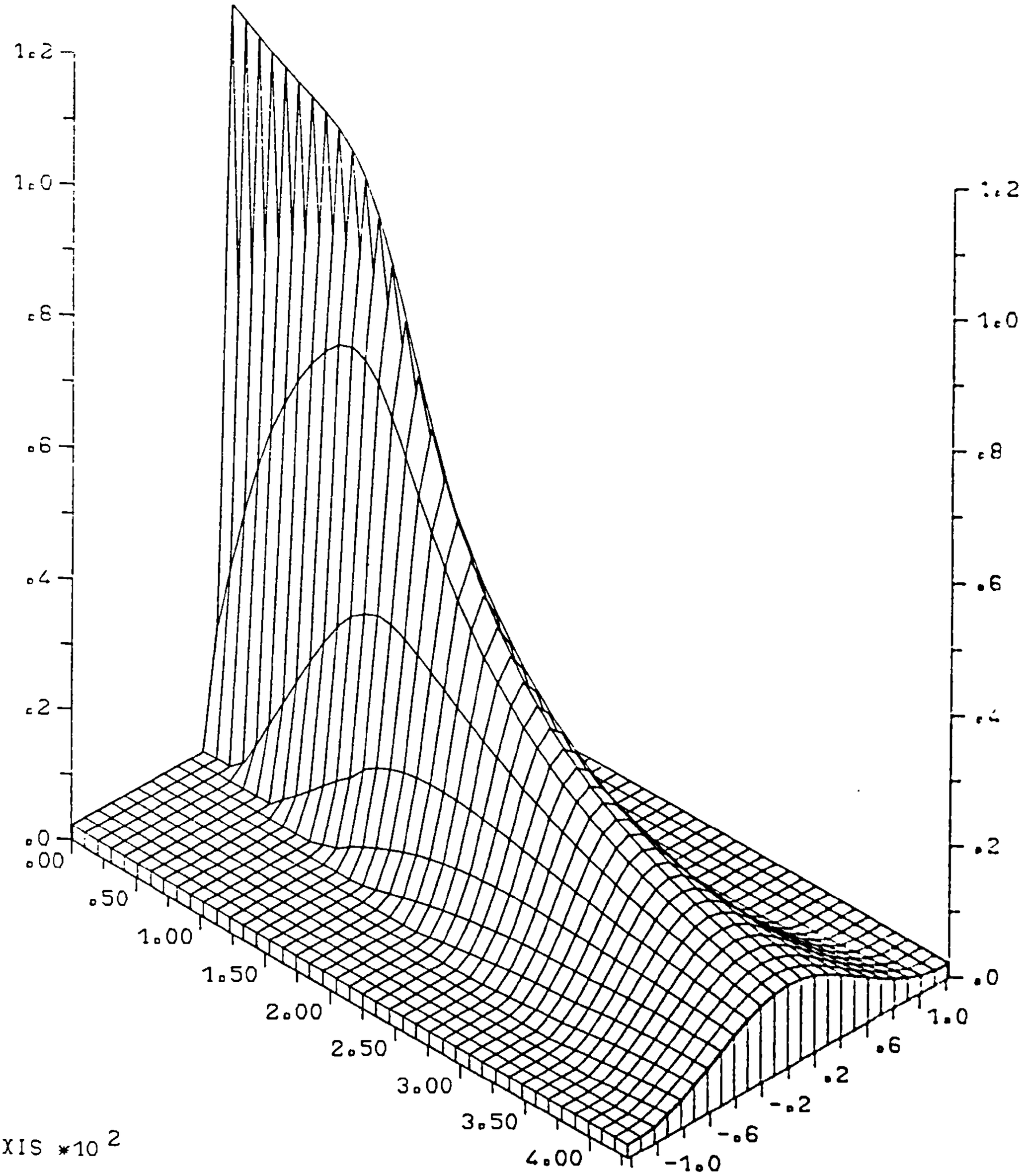

Fig. 5.27a: Three-dimensional 'Wall-jet' Heat Transfer Distribution along the Floor (hc, W/m K).

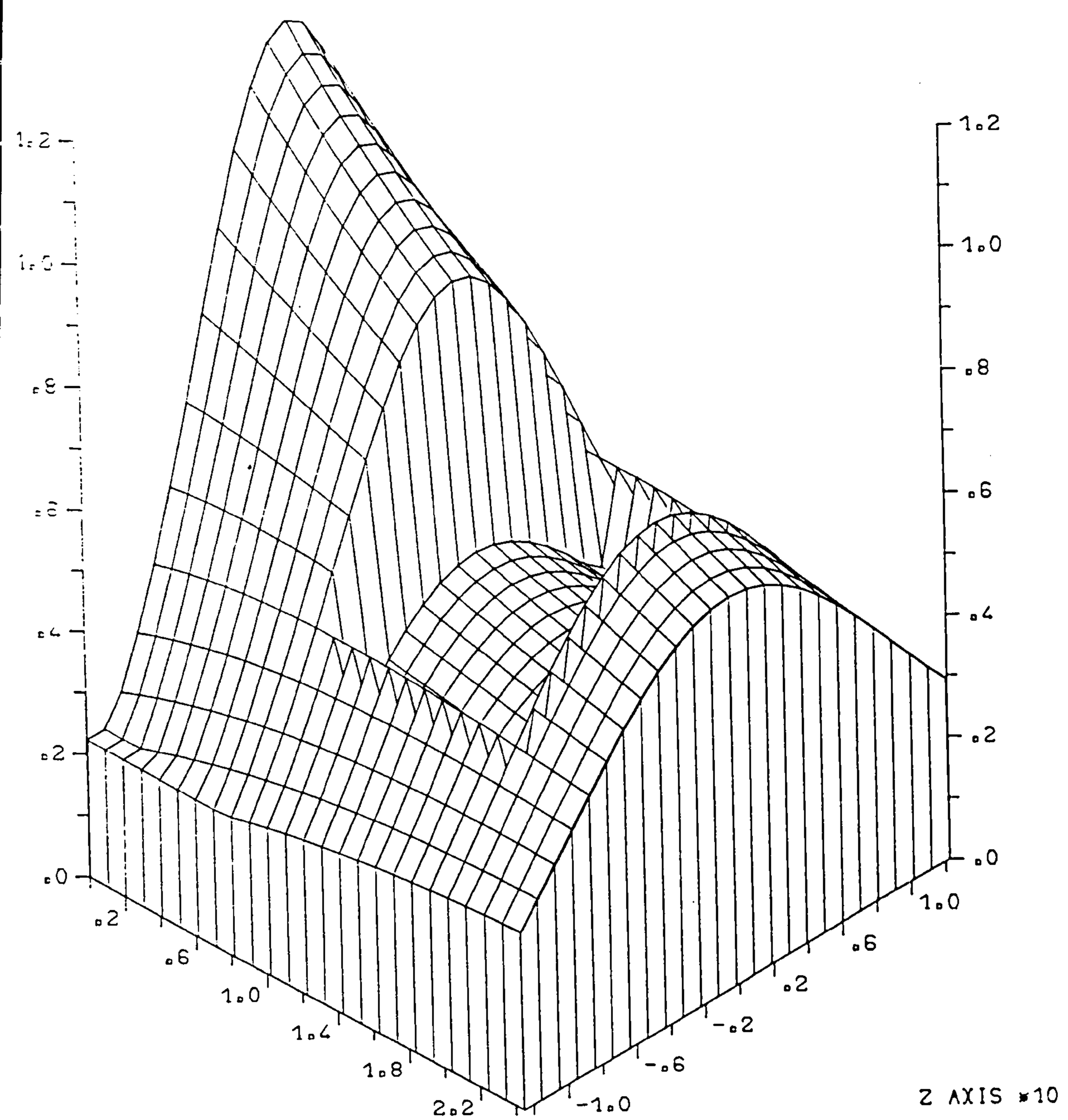

Fig. 5.27b: Three-dimensional 'Wall-jet' Heat Transfr Distribution along the Far-wall and Window (hc, W/m K).

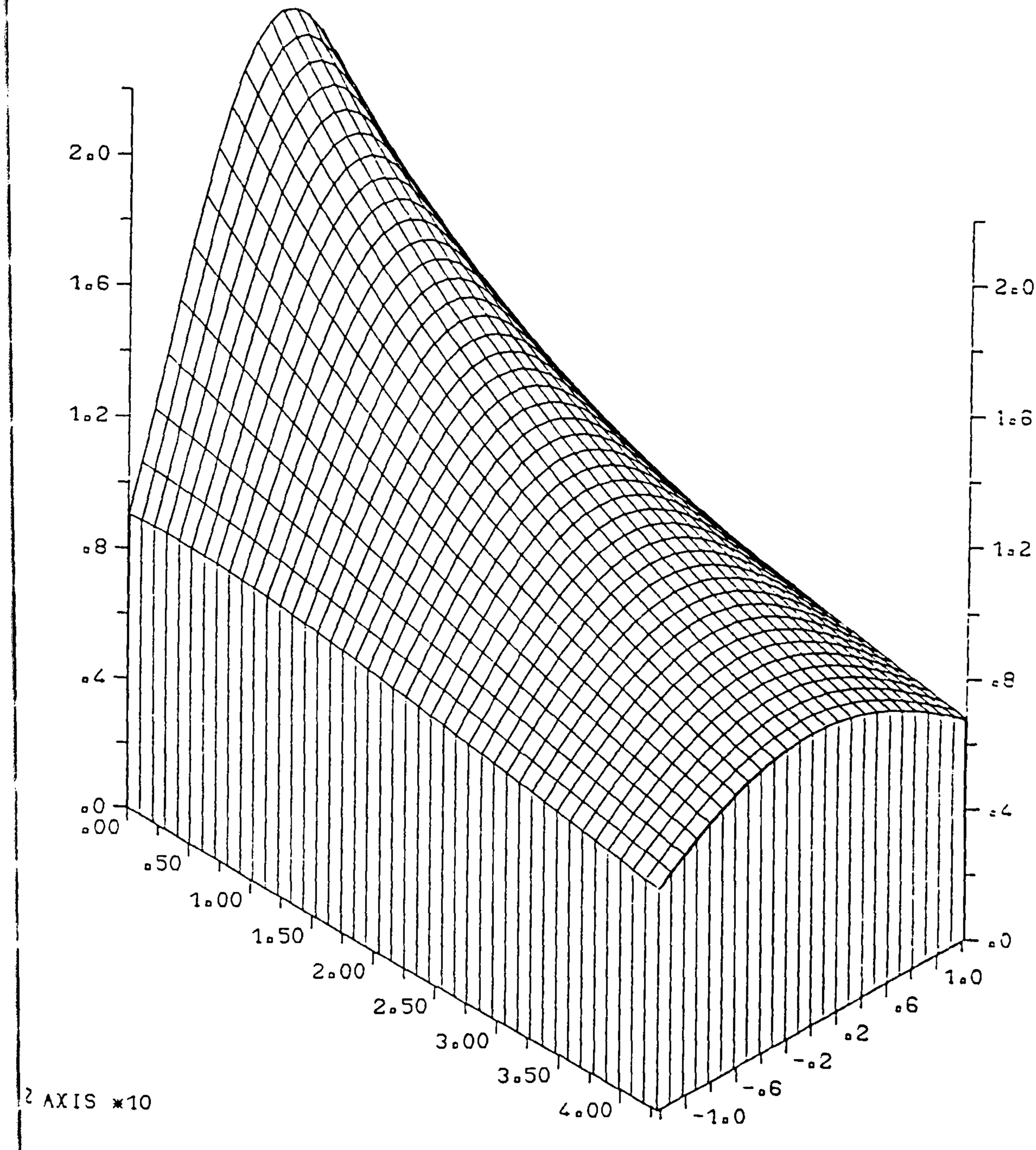

Fig. 5.27c: Three-dimensional 'Wall-jet' Heat Transfer Distribution along the Ceiling (hc, W/m K).

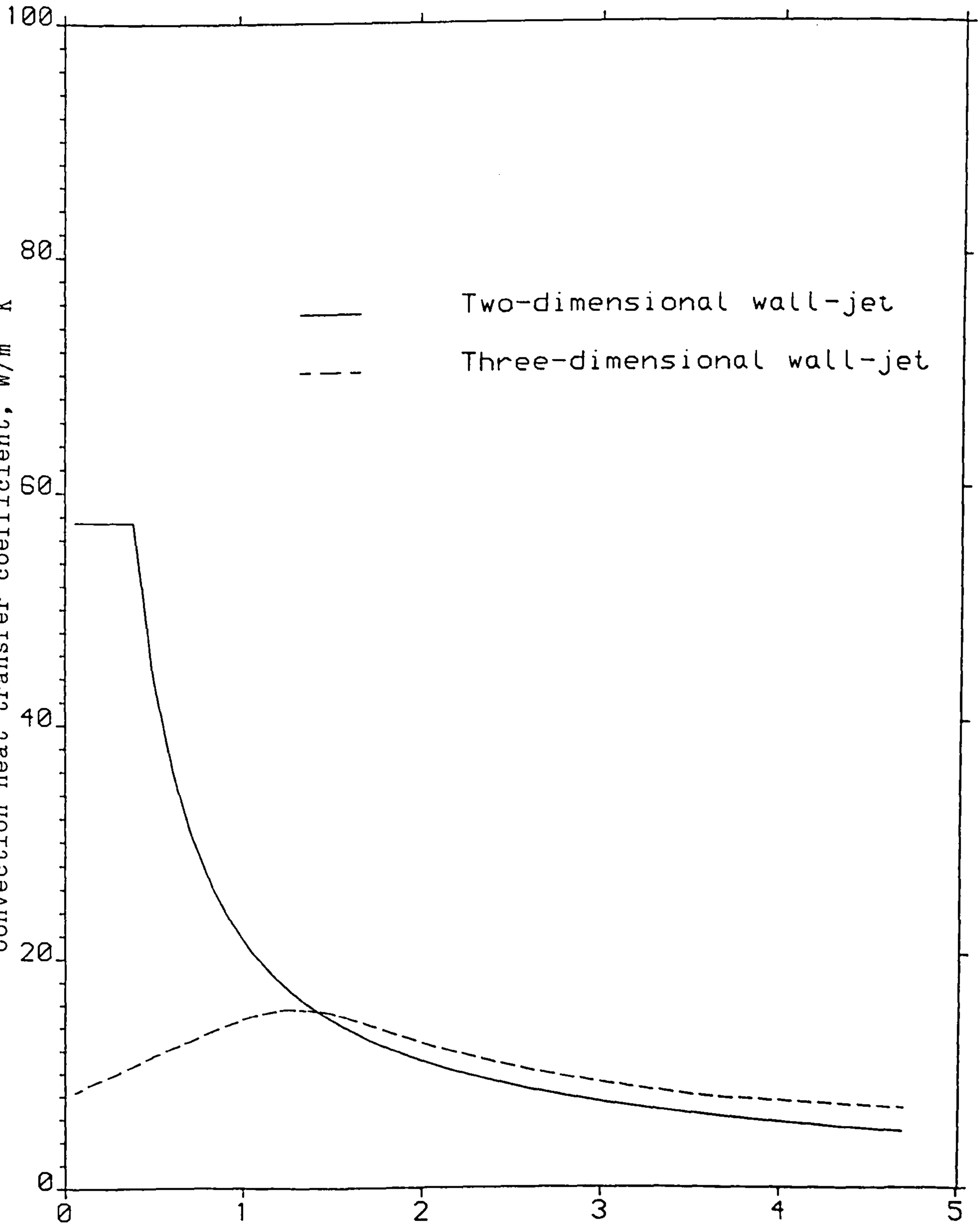

Fig. 5.28a: **Comparison of Floor Heat Transfer Distribution for Case No. 1 of Table 5.2.**

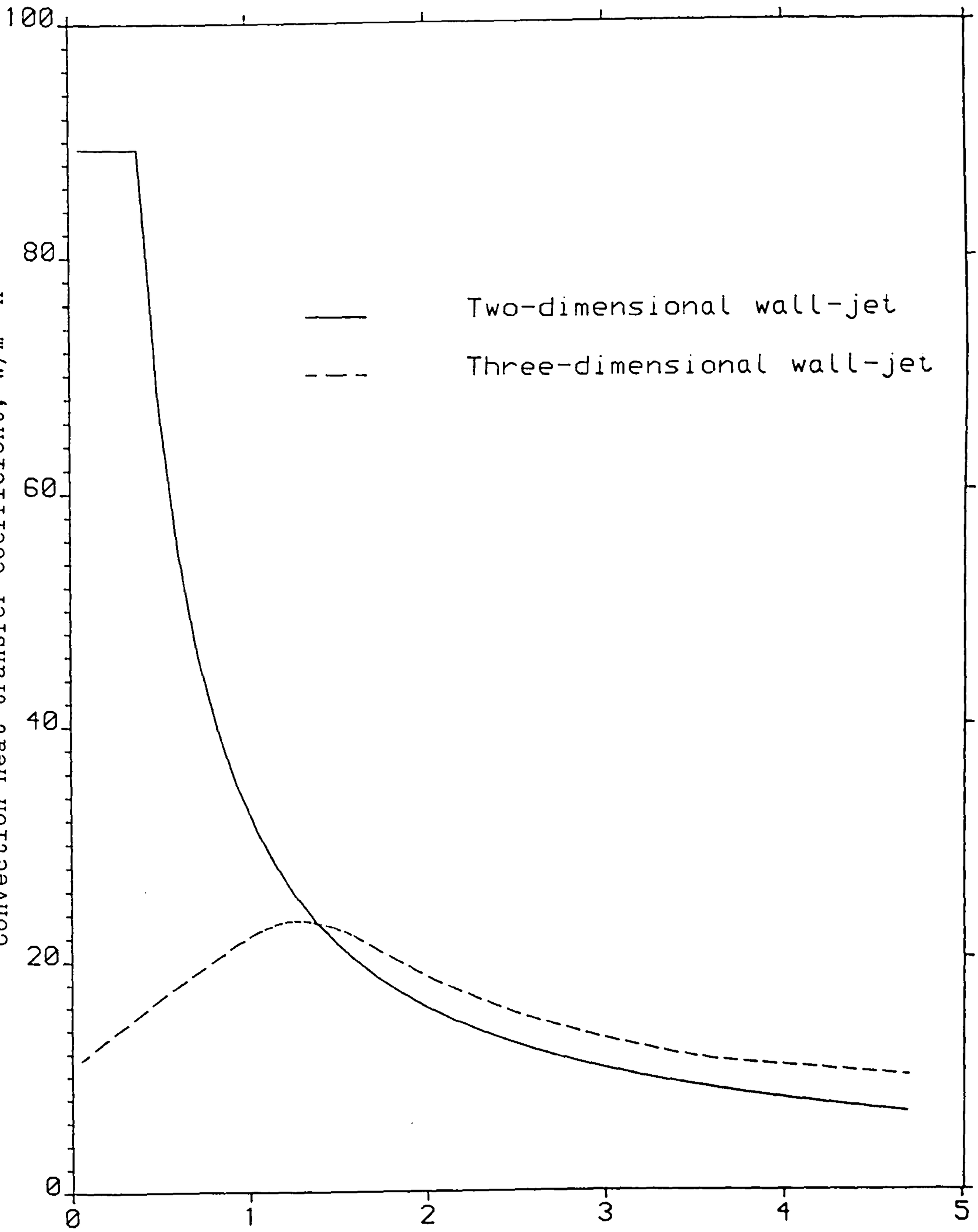

Fig. 5.28b: **Comparison of Floor Heat Transfer Distribution for Case No. 2 of Table 5.2.**

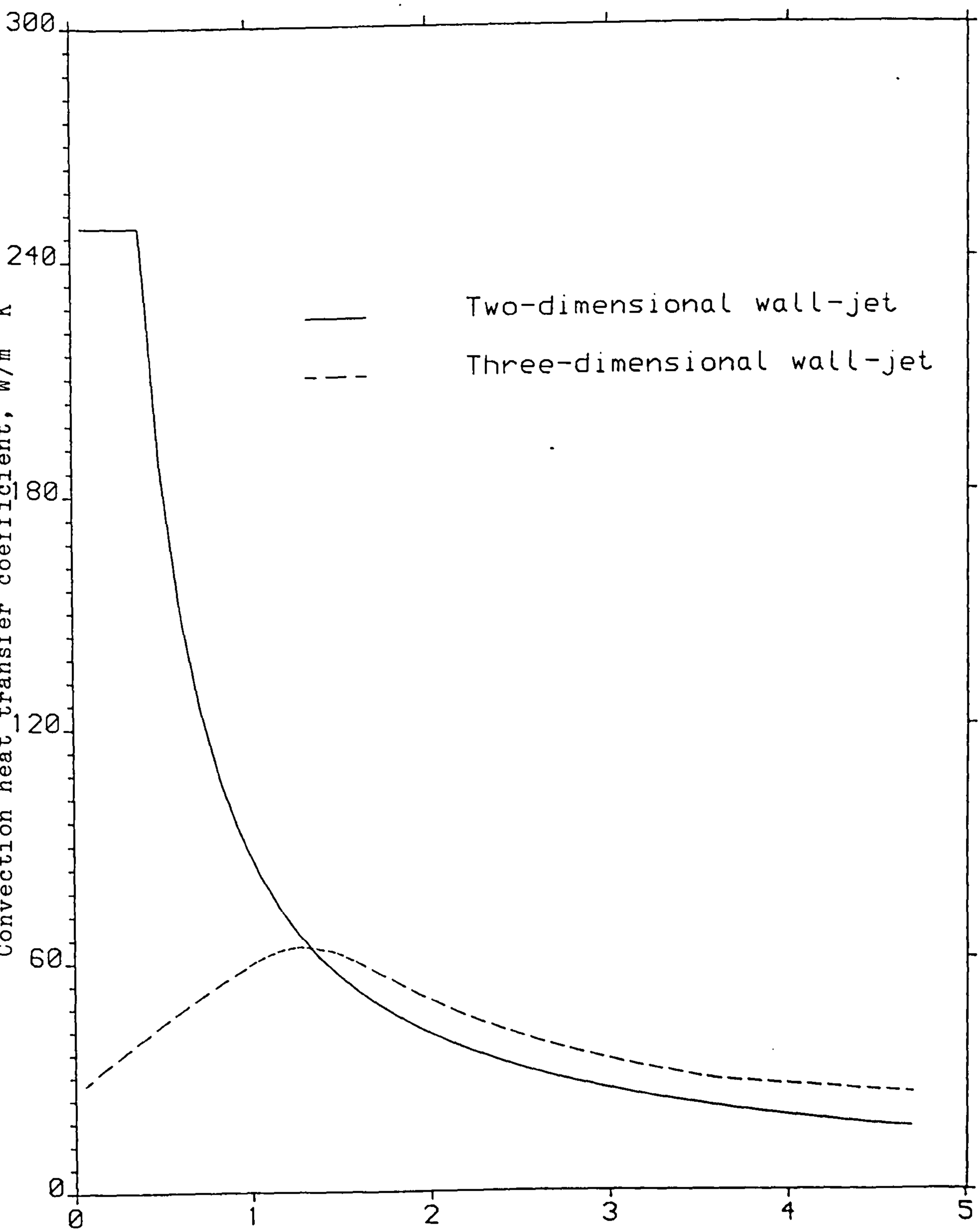

Fig. 5.28c: Comparison of Floor Heat Transfer Distribution for Case No. 3 of Table 5.2.

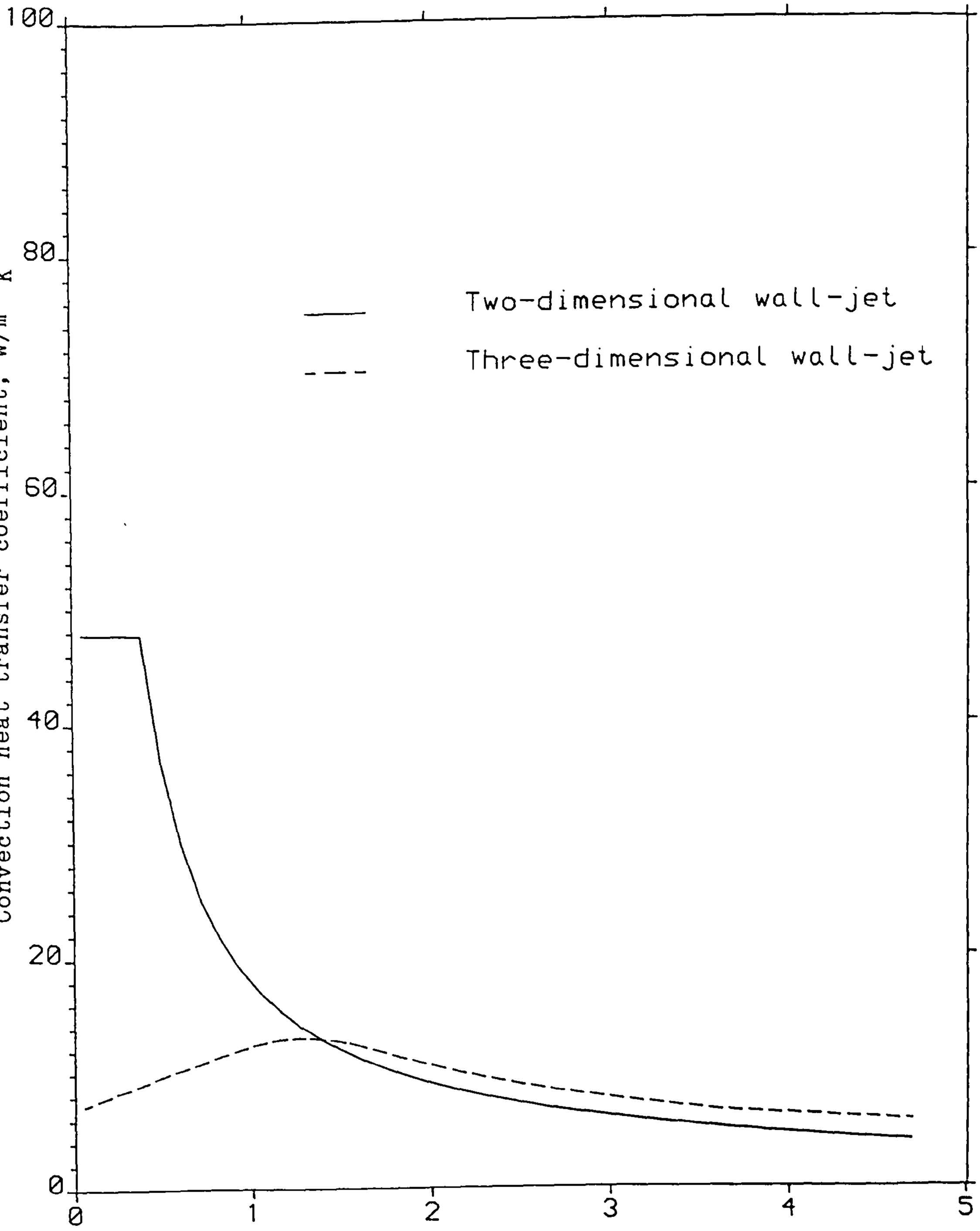

Fig. 5.29a: **Comparison of Floor Heat Transfer Distribution for Case No. 1 of Table 5.3.**

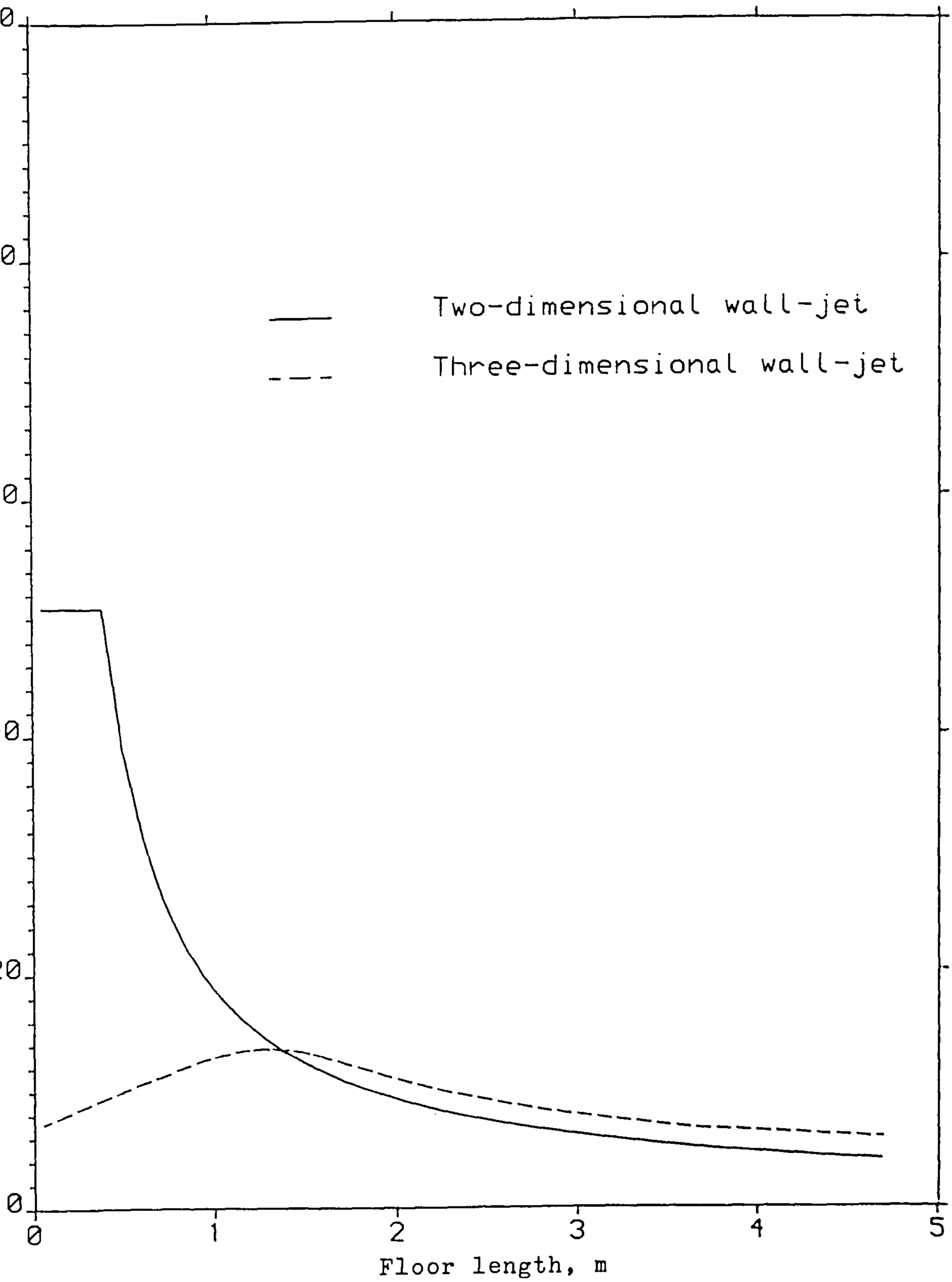

Fig. 5.29b: **Comparison of Floor Heat Transfer Distribution for Case No. 2 of Table 5.3.**

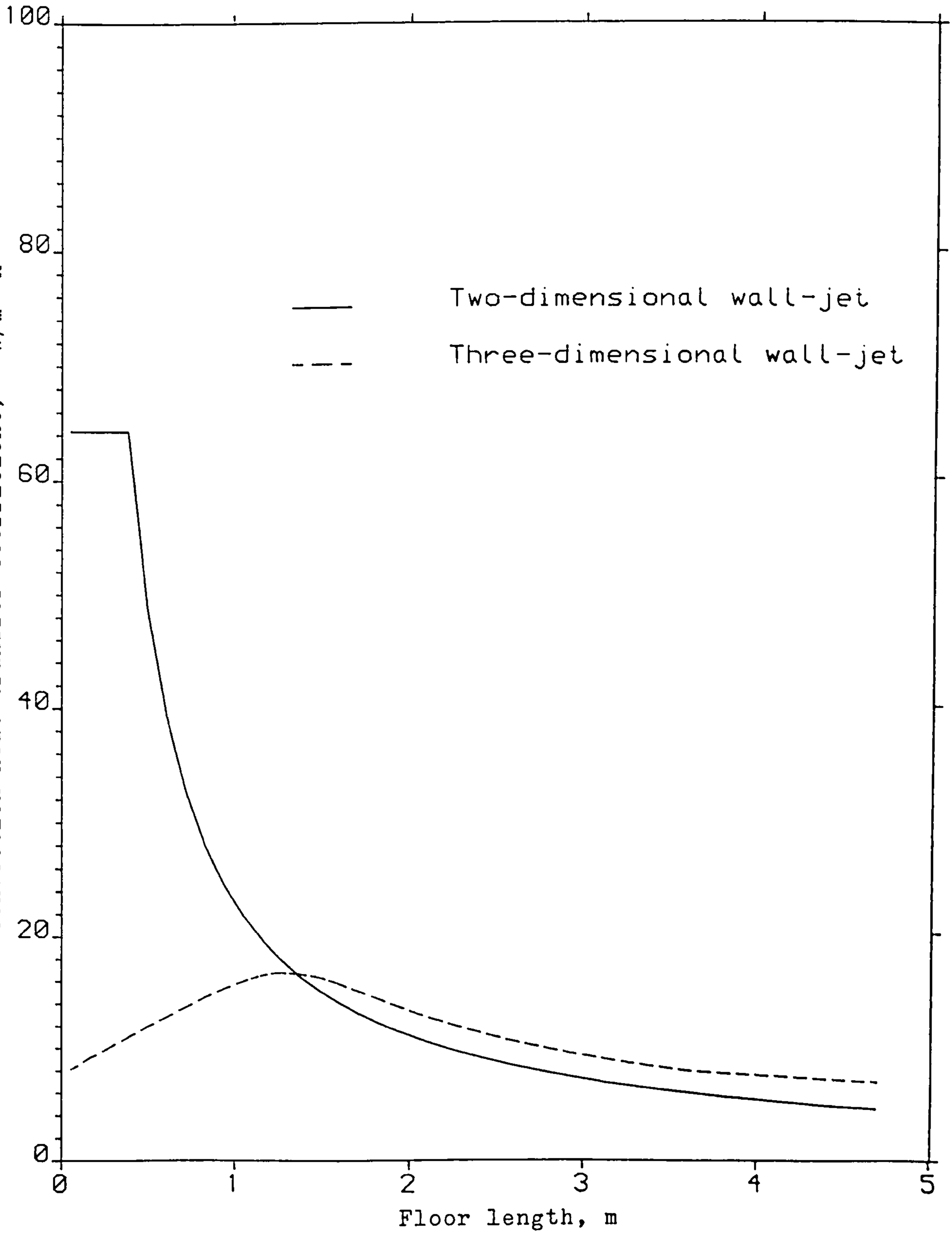

Fig. 5.29c: **Comparison of Floor Heat Transfer Distribution for Case No. 3 of Table 5.3.**

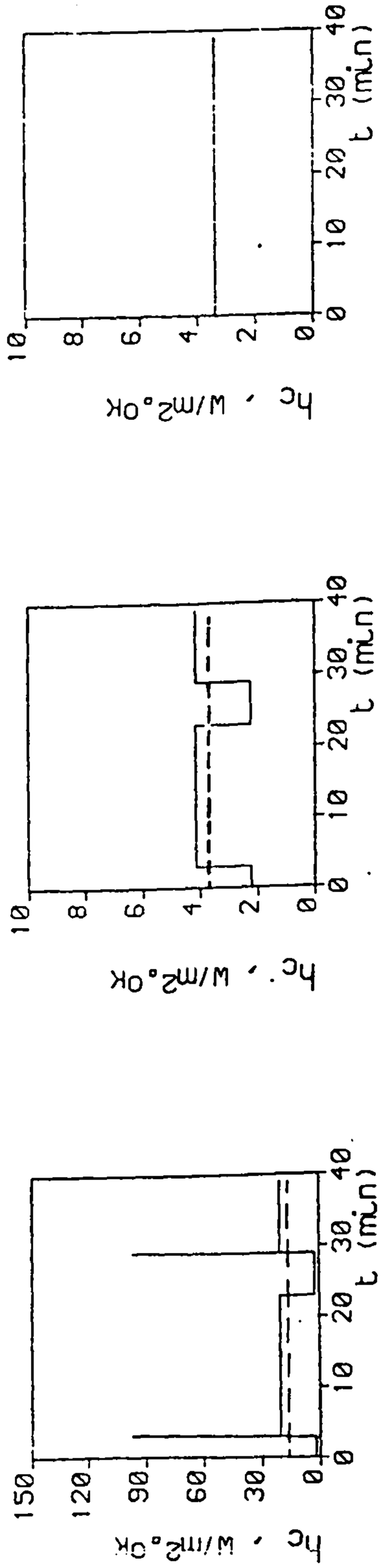

Fig. 5.30a: Time-dependent Heat Transfer for Case No. 1 of Table 5.2 (Two-dimensional version).

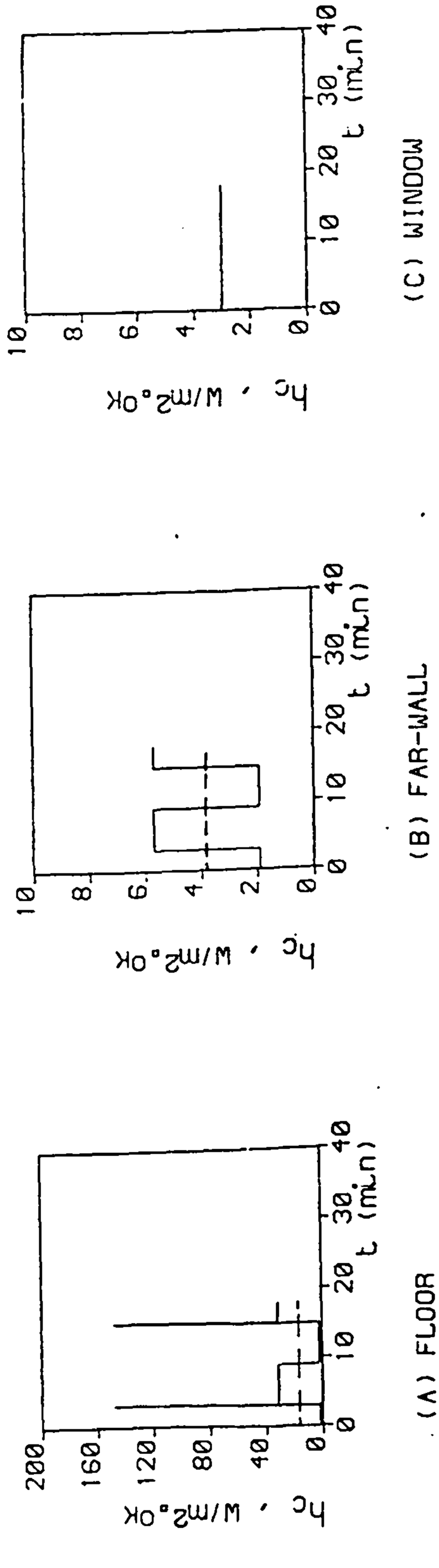

Fig. 5.30b: Time-dependent Heat Transfer for Case No. 2 of Table 5.2 (Two-dimensional version).

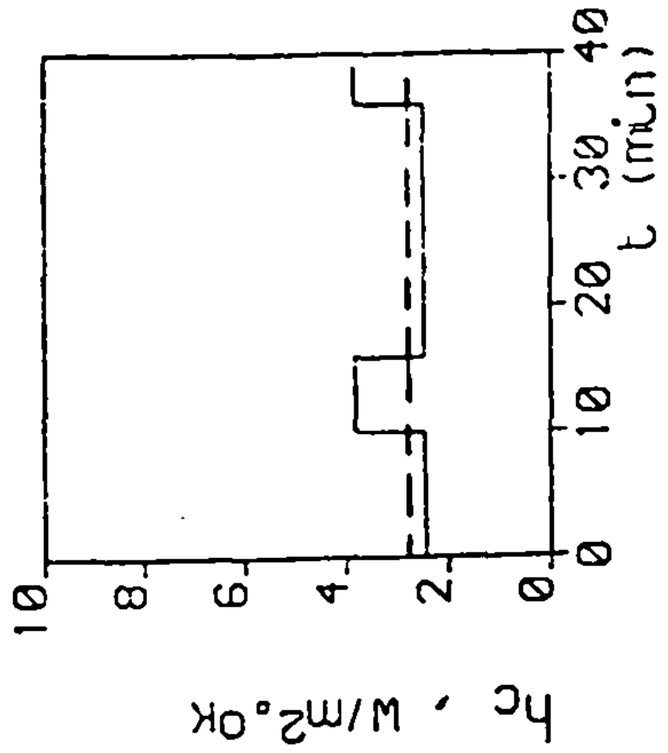

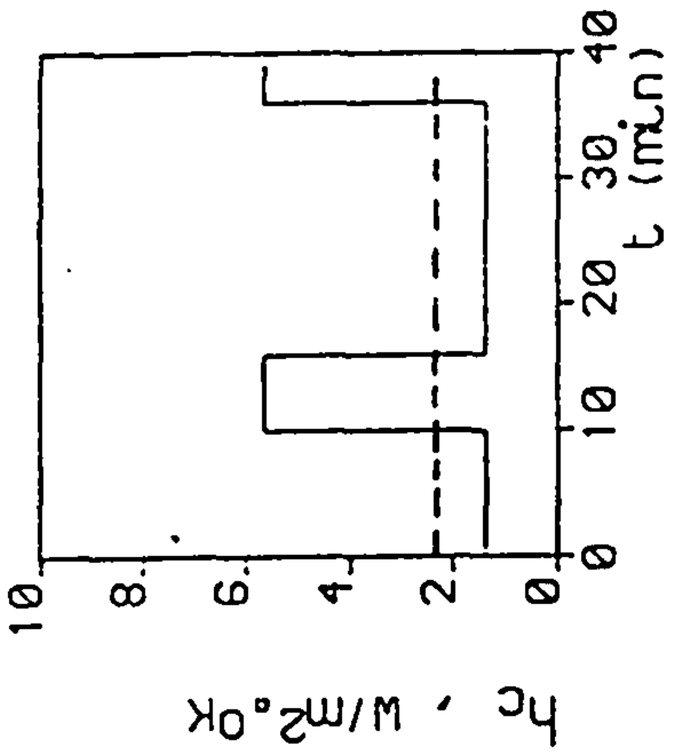

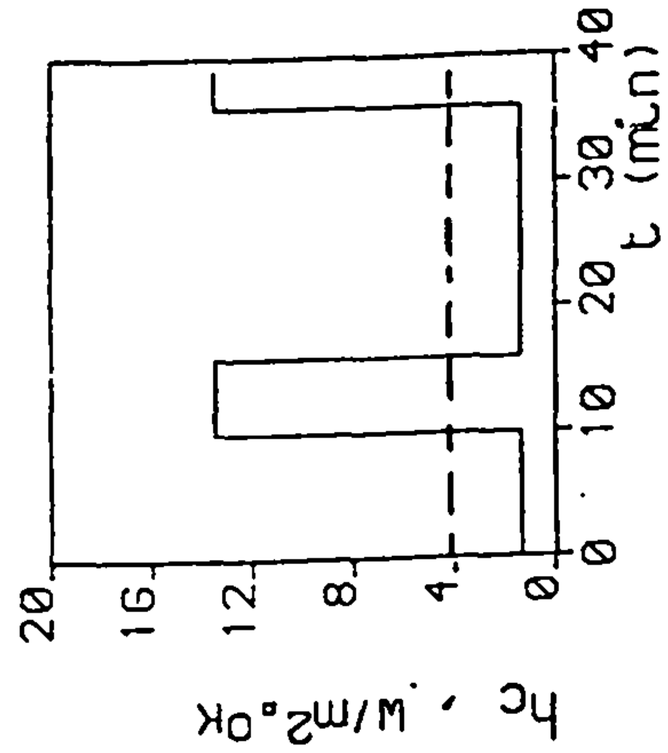

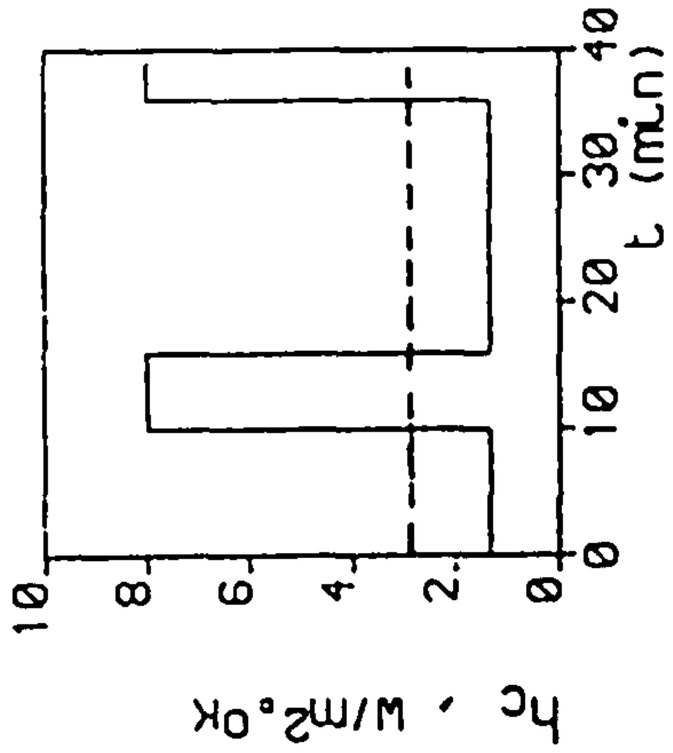

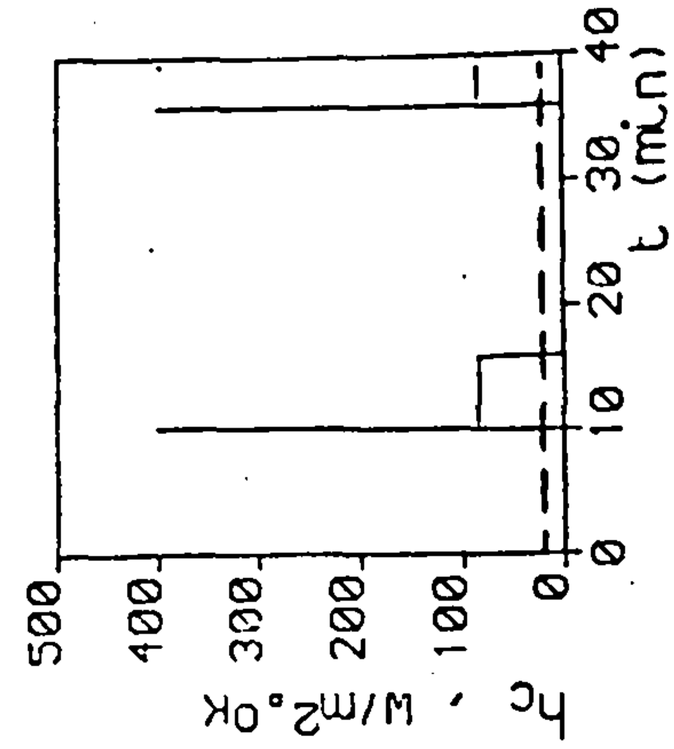

Fig. 5.30c: Time-dependent Heat Transfer for Case No. 3 of Table 5.2 (Two-dimensional version).

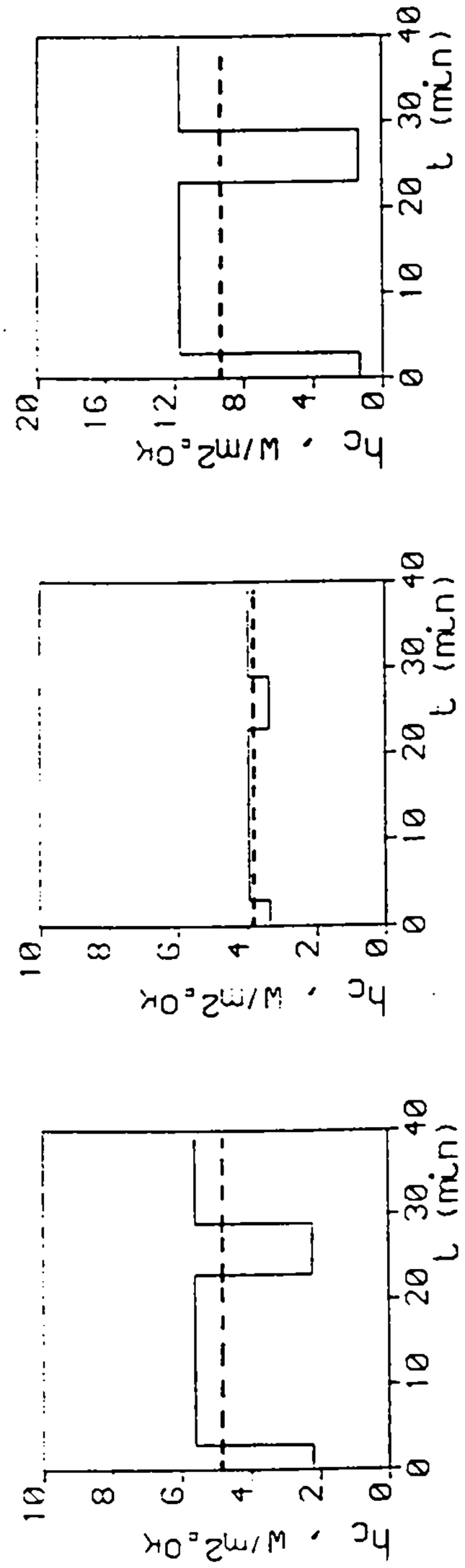

Fig. 5.31a: Time-dependent Heat Transfer for Case No. 1 of Table 5.2 (Three-dimensional version).

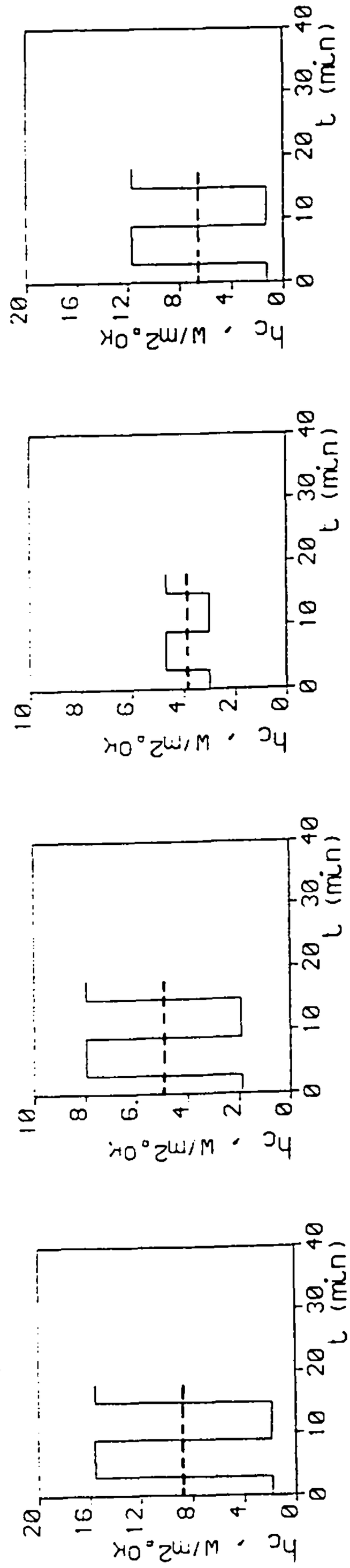

Fig. 5.31b: Time-dependent Heat Transfer for Case No. 2 of Table 5.2 (Three-dimensional version)

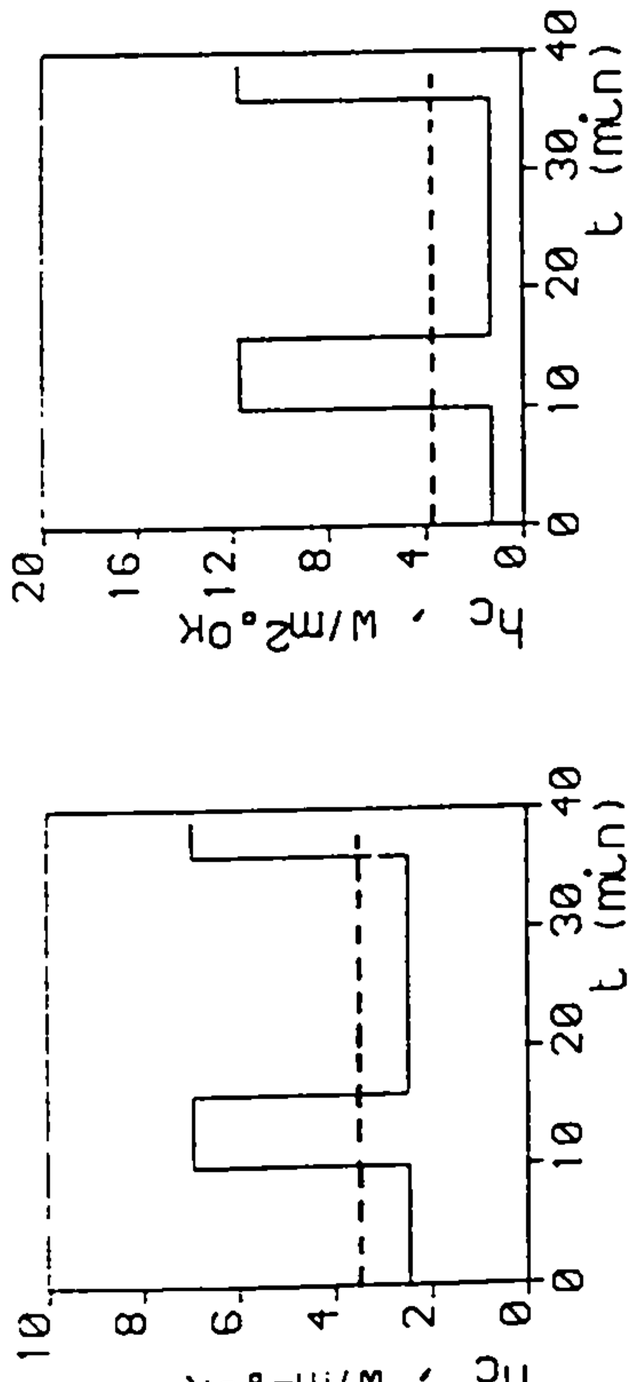

Fig. 5.31c: Time-dependent Heat Transfer for Case No. 5.2 (Three-dimensional version).

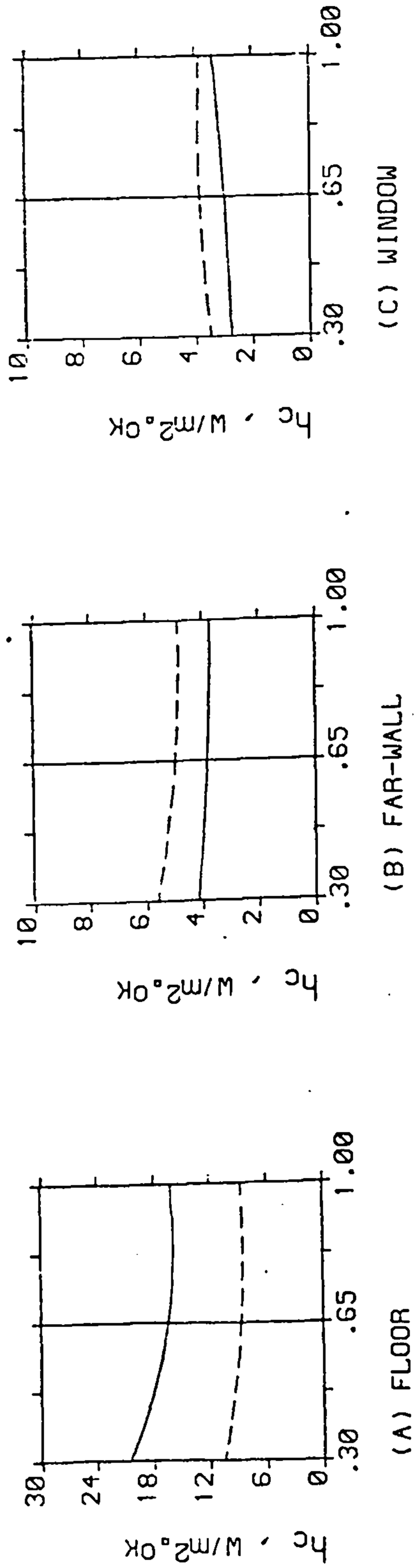

Fig. 5.32: Time-averaged Local Heat Transfer Under Cyclic Control (see table 5.2).

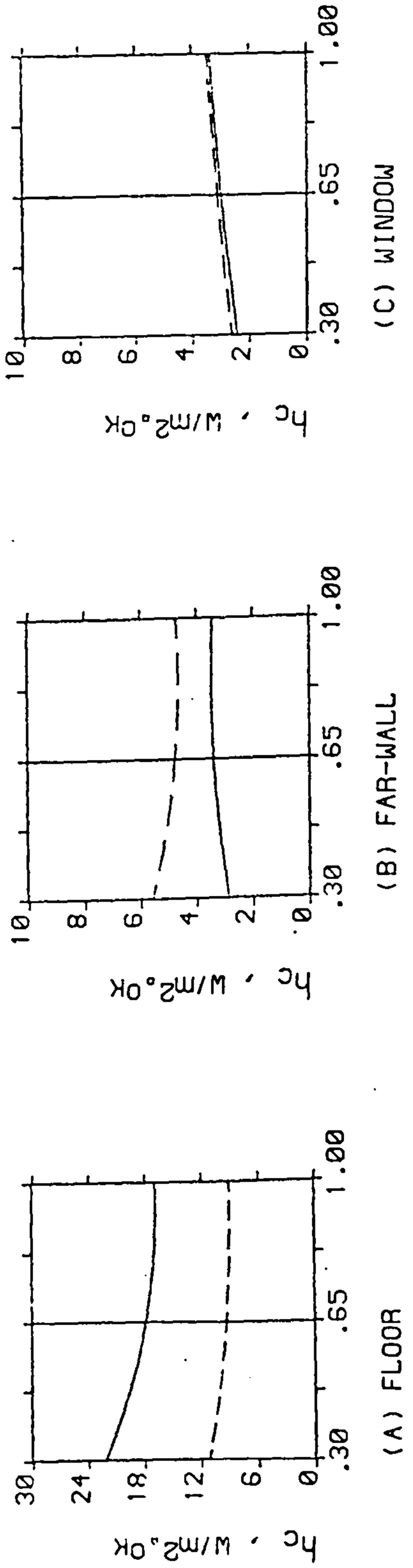

Fig. 5.33: Time-averaged Room Heat Transfer Under Modulating Control (see Table 5.3).

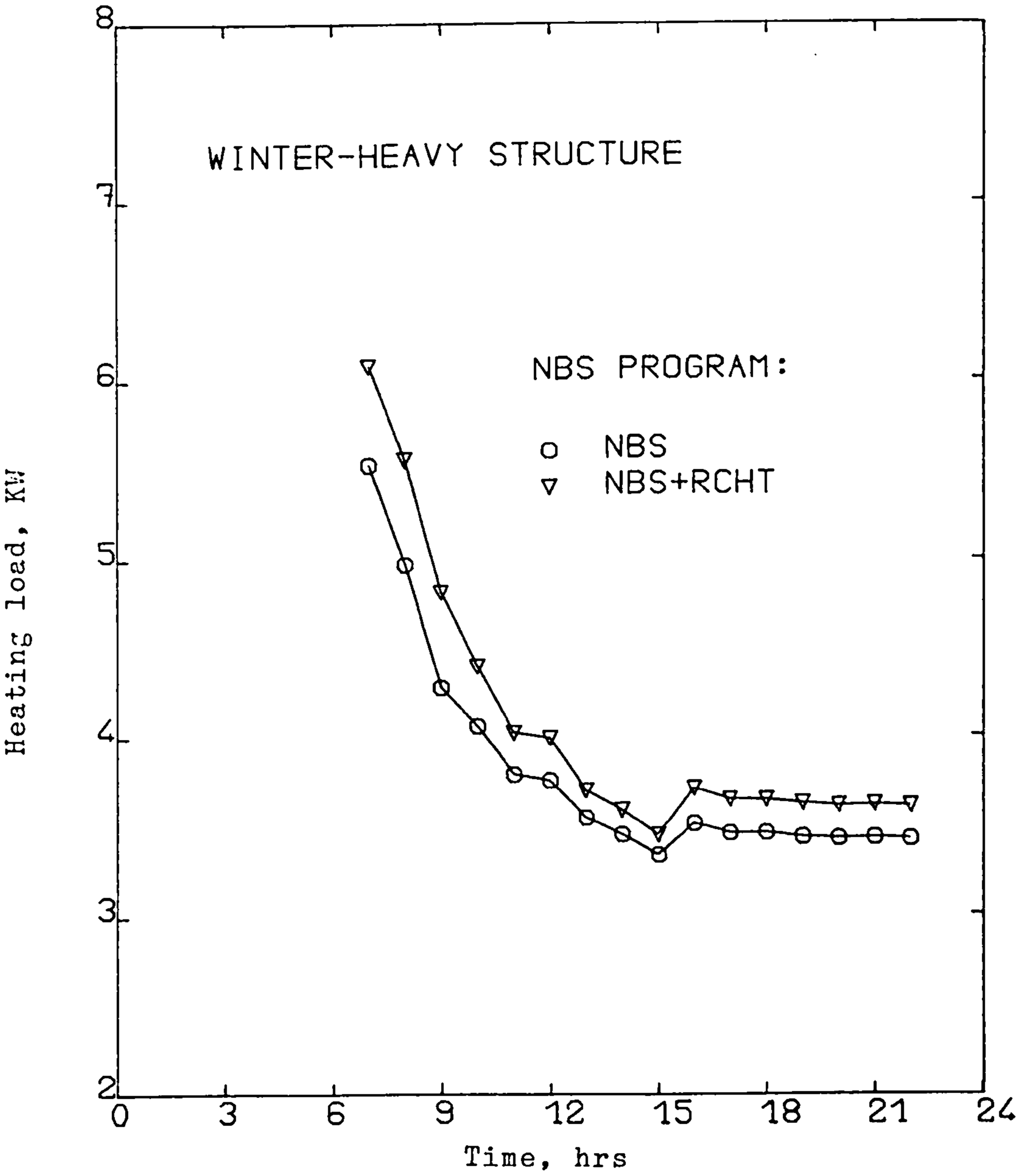

Fig. 5.34a Predicted winter heating load profile for a detached house in the UK.

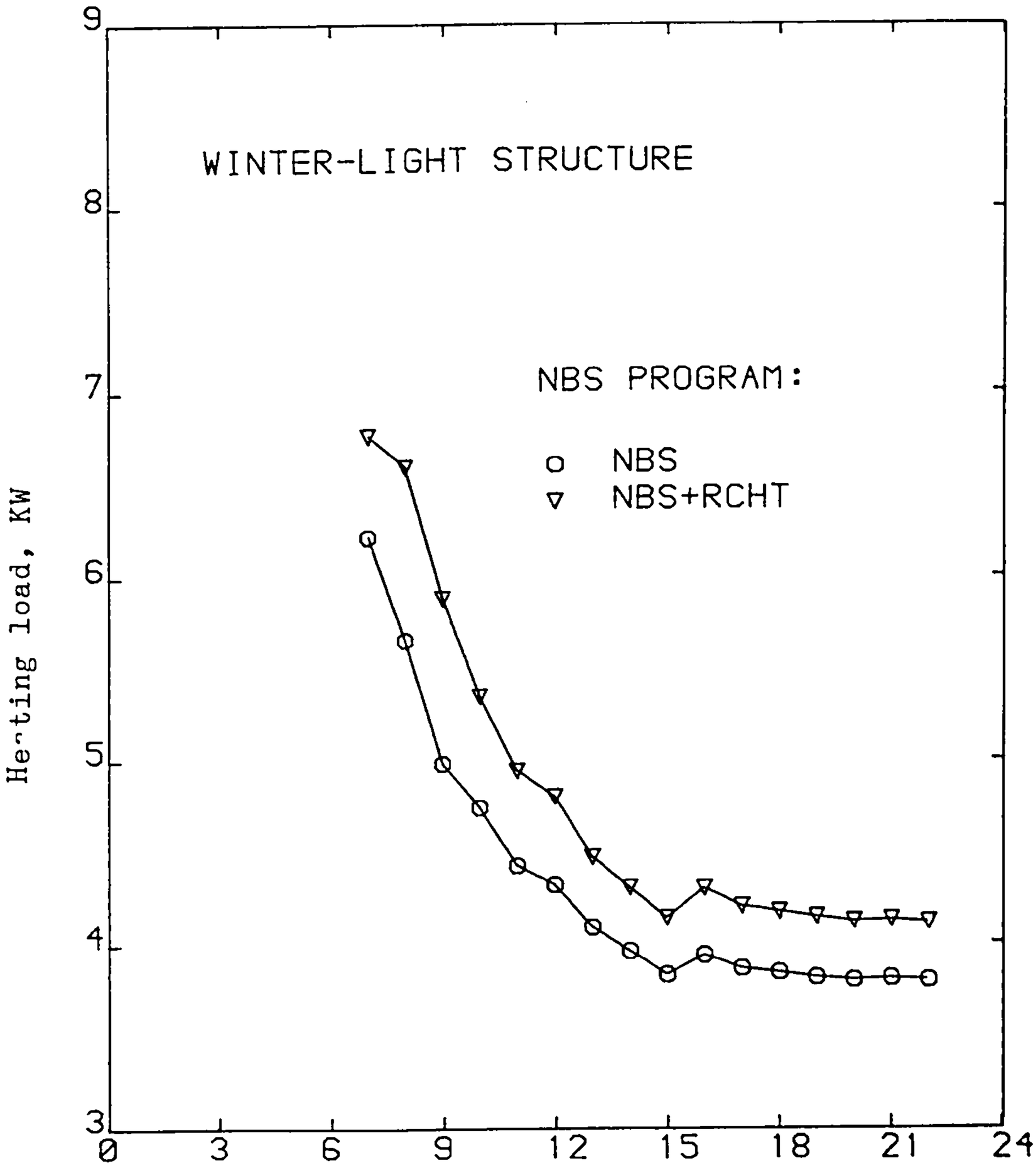

Fig. 5.34b Predicted winter heating load profile for a detached house in the UK.